New Perovskite Materials for Sensors and Low Temperature Solid Oxide Fuel Cell (LT-SOFC) Applications

Syed Munawer Bukhari

Thesis submitted to the

Faculty of Graduate and Postdoctoral Studies

In partial fulfilment of the requirements

For the PhD degree in Chemistry

Department of Chemistry

Faculty of Science

University of Ottawa

Table of Contents

List of Figures

Figure 4.9. I-V and I-P curves of the $Sm_xCe_{1-x}FeO_{3-\delta}$ (x=0.01, 0.03 and 0.05) anodes under dry methane fuel at differ.

Figure 4.10. Performance of $Sm_{1-x}Ce_xFeO_{3-\delta}$ (x=0.01-0.05) anodes under dry methane fuel for 15h. Cell powers calculated from current density obtained at an overpotential of 0.450V as a function of run time.

Figure 4.11. SEM micrographs of $Sm_{1-x}C\ e_xFeO_{3-\delta}$ (x=0.01-0.05) anodes after performance of 23h under dry methane.

Figure 5.1. XRD pattern of $Sm_{0.95}Ce_{0.05}Fe_{1-x}Co_xO_{3-\delta}$ (x =0-0.10) obtained after calcination of amorphous citrates at 850°C for 24 hours.

Figure 5.2. The weighted average ionic radii of B-cation (r_B) and normalized experimental cell volume ($V^{1/3}$) as a function of total concentration of Co (x=x′+x″).The solid line represents $V^{1/3}$ and broken lines show the weighted average ionic radii (r_B) for series 1 through 6, as described in the text.

Figure 5.3. XRD pattern of $Sm_{0.95}Ce_{0.05}Fe_{1-x}Co_xO_{3-\delta}$ (x =0-0.10) heated in 5%v/v H_2/N_2 at 700°C for 1 hour.

Figure 5.4. XRD pattern of $Sm_{0.95}Ce_{0.05}Fe_{1-x}Co_xO_{3-\delta}$ heated in 5 %v/v H_2/N_2 at 800°C for 1 hour. (a) full range XRD pattern, * indicates Sm_2O_3 phase and + indicates Fe^0, Co_3O_4 and/or Fe-Co alloy phases. (b), (c) and (d) are highlighted regions of (a). (b) shows phase separation of Sm_2O_3, (c) shows the destruction of perovskite phase and (d) shows formation of Fe^0, $Co_3O_4$and/or Fe-Co alloy phases.

Figure 5.5. XRD pattern of $Sm_{0.95}Ce_{0.05}Fe_{1-x}Co_xO_{3-\delta}$ heated in 5 %v/v H_2/N_2 at 900°C for 1 hour. (a) full range XRD pattern, * indicates Sm_2O_3 phase and + indicates Fe^0, $Co_3O_4$and/or Fe-Co alloy phases. (b), (c) and (d) are highlighted regions of (a). (b) shows phase separation of Sm_2O_3, (c) shows the destruction of perovskite phase and (d) shows formation of Fe^0, $Co_3O_4$and/or Fe-Co alloy phases.

Figure 5.6. XPS spectrum of x=0.01 showing full range spectrum, and peaks of O1s, Sm3d, Fe2p.

Figure 5.7. Electrical Conductivity of $Sm_{0.95}Ce_{0.05}Fe_{1-x}Co_xO_{3-\delta}$ sintered at 1350°C as a function of temperature. (a) and (b) shows electrical conductivity measured in air and 5% v/v H_2/N_2 respectively while 7(c) and 7(d) shows ($\sigma_R - \sigma_O$) and $\frac{\sigma_R}{\sigma_O}$ respectively as a function of temperature.

List of Tables

List of Abbreviations and Symbols

SOFC- solid oxide fuel cells

LT-SOFC- low temperature solid oxide fuel cell

XRD-X-ray diffraction

SEM-scanning electron microscopy

XPS-X-ray photoelectron spectroscopy

σ-electrical conductivity

σ_{Air}-electrical conductivity under oxidizing condition

σ_o-electrical conductivity under oxidizing condition

σ_R-electrical conductivity under reducing condition

OCP-open circuit potential

R_{CT}-charge transfer resistance

i_o-exchange current density

I-cell current

I_{max}-maximum cell current

P-cell power

P_{max}-maximum cell power

V-cell voltage

t-tolerance factor

S-sensor signal

Claims to original research

I am sole person who worked on this project. I did all experimental work and drafted all manuscripts for the publications. All work presented in this thesis is published or to be published.

1. S.M. Bukhari, J.B. Giorgi, Tuneability of $Sm_{(1-x)}Ce_xFeO_{3\pm\lambda}$ Perovskites: Thermal Stability and Electrical Conductivity, *Solid State Ionics, 180* (**2009**) 198-204
2. S.M. Bukhari, J.B. Giorgi, Effect of Cobalt doping on thermal stability and electrical conductivity of $Sm_{0.95}Ce_{0.05}Fe_{1-x}Co_xFeO_{3-\delta}$ (x=0-0.10) under oxidizing and reducing conditions, *Solid State Ionics. 181* **(2010)** 392-401
3. Syed M. Bukhari and Javier B. Giorgi, The evaluation of electrical conductivity of Ni doped $Sm_{0.95}Ce_{0.05}FeO_{3-\delta}$ on the basis of Surface morphology and composition. *Sensors and Actuators B* , 155 (**2010**) 524-537
4. Syed M. Bukhari and Javier B. Giorgi, Surface and Redox chemistry of $Sm_{0.95}Ce_{0.05}Fe_{1-x}Ni_xO_{3-\delta}$ perovskites ,*Solid State Ionics,* 194 **(2011)** 33-40
5. Syed M. Bukhari and Javier B. Giorgi, Cobalt doped $Sm_{0.95}Ce_{0.05}FeO_{3-\delta}$ for detection of reducing gases, *Journal of The Electrochemical Society*, 158 (6) J159-J164 **(2011)**
6. Syed M. Bukhari and Javier B. Giorgi, Cobalt doped $Sm_{0.95}Ce_{0.05}FeO_{3-\delta}$ for detection of reducing gases, *Electrochemical Society Trans.,* 28(20) **(2010)** 19-29
7. Syed M. Bukhari and Javier B. Giorgi, Potentials of $Sm_{0.95}Ce_{0.05}Fe_{1-x}Cr_xO_{3-\delta}$ Perovskite Materials for Gas Sensing, *ECS Trans.,* 33(8) **(2010)** 117-130
8. Syed M. Bukhari and Javier B. Giorgi, Performance of newly developed Co doped $Sm_{0.95}Ce_{0.05}FeO_{3-\delta}$ as SOFC anode material, *Electrochemical Society Trans*., 33(39) (**2011)** 81-91
9. Syed M. Bukhari and Javier B. Giorgi, Redox stability of $Sm_{0.95}Ce_{0.05}Fe_{1-x}Cr_xO_{3-\delta}$ Perovskite Materials, *Electrochemical Society Trans.*, 33(31) (**2011)** 61-74
10. Syed M. Bukhari and Javier B. Giorgi, Performance of $Sm_{0\cdot95}Ce_{0.05}Fe_{1-x}Ni_xO_{3-\delta}$ Perovskite as Anode Materials under Methane Fuel for Low Temperature Solid Oxide Fuel Cells (LT -SOFC) *Electrochemical Society Trans.,* 35(1) (**2011**) 1539-1544

11. Syed M. Bukhari and Javier B. Giorgi, Redox stability of $Sm_{0.95}Ce_{0.05}Fe_{1-x}Cr_xO_{3-\delta}$ Perovskite Materials , *Journal of The Electrochemical Society*, 158(10) H1027-H1033(**2011)**
12. Syed M. Bukhari and Javier B. Giorgi, Chemically stable and coke resistant Ce doped $SmFeO_3$ perovskite materials for solid oxide fuel (SOFC) anode applications, submitted to *Journal of Power Sources* (**2011**)

In preparation

1. Syed M. Bukhari and Javier B. Giorgi, Hydrogen detection by reduced Ni doped $Sm_{0.95}Ce_{0.05}FeO_{3-\delta}$ perovskite bases sensors [in preparation for *Sensors and Actuators B*]
2. Syed M. Bukhari and Javier B. Giorgi, Performance of newly developed Co doped $Sm_{0.95}Ce_{0.05}FeO_{3-\delta}$ as SOFC anode material [in preparation for *Journal of The Electrochemical Society*]
3. Syed M. Bukhari and Javier B. Giorgi, Performance of $Sm_{0.95}Ce_{0.05}Fe_{1-x}Ni_xO_{3-\delta}$ Perovskite as Anode Materials under Methane Fuel for Low Temperature Solid Oxide Fuel Cells (LT -SOFC) [in preparation for *Journal of The Electrochemical Society*]

Summary

This work involved the development of new perovskite oxides based on $SmFeO_3$ and testing their performances as sensors for reducing gases (H_2, CO & CH_4) and as anode materials for dry methane oxidation in solid oxide fuel cells. The new perovskite oxide materials with formula $Sm_{0.95}Ce_{0.05}Fe_{1-x}M_xO_{3-\delta}$ (M= Co, Ni & Cr) were synthesized by a sol gel method using citric acid as a complexing agent. The resulting materials were characterized by using a battery of techniques including XRD, XRF, XPS, SEM and electrochemical methods.

Sensing experiments revealed that both cobalt doped and Cr doped materials can detect H_2, CO and CH_4 in air at different temperatures including room temperature. The Ni doped materials did not prove good candidates as sensors. However, their reduction treatment studies showed the formation of metallic nanoparticles on the surface which deeply influence their electrical conductivity as well as sensing ability. Consequently, this modification in surface structure and chemical composition enabled them to sense hydrogen gas at 300^oC very effectively. The response of sensors based on these reduced materials was measurable and reversible.

Some materials were also selected on the basis of their reduction stability and electrical properties, and their electrochemical performances were evaluated as SOFC anodes under dry methane and dry hydrogen fuels separately. The performance tests as SOFC anode revealed that the best anode material for the oxidation of dry hydrogen fuel is $Sm_{0.95}Ce_{0.05}FeO_{3-\delta}$. Furthermore, $Sm_{0.95}Ce_{0.05}FeO_{3-\delta}$ proved to be coke resistant anode under dry methane fuel and exhibited reasonably low charge transfer resistance values at temperatures between 600-700^oC. The doping of Co and Ni at the B-site of $Sm_{0.95}Ce_{0.05}FeO_{3-\delta}$ found to be very effective in further improving its performance as SOFC anode towards oxidation of dry methane fuel at the lower temperatures.

Acknowledgements

I would like to express my heartfelt gratitude to my research supervisor, Professor Dr. Javier B. Giorgi, for his excellent guidance and continuous encouragement during my course of thesis research. I would also like to thank Dr. Paul Mayer and Dr. Christian Detellier for being a part of my committee.

I would like to extend my regards to former and current members of Javier's group for their support and useful suggestions. I would also like to thank Dr. Yun for helping me on SEM/EDS, Sander Mommers for collecting all XPS data and Dr. Wendy Pell for useful discussions and suggestions on the electrochemical measurements.

Finally, I would like to dedicate this work to my family especially my wife, Syeda Asia, who has always encouraged and unreservedly supported me for whatever I do. Thank you.

1. Introduction

1.1 Perovskites

1.1.1 Origin of the Perovskite

Perovskites are solid materials (ceramics) which contain metallic cations (at least two) and anions (usually oxide). Perovskites take their name after the mineral $CaTiO_3$ which was first discovered by scientist Gustav Rose in 1839 from the Ural Mountains of Russia. He named this mineral ($CaTiO_3$) as Perovskite after the famous Russian mineralogist Count Lev Aleksevich Von Perovski [1]. Since then, all those solid materials which have a structure similar to the $CaTiO_3$ mineral are grouped into the family known as perovskites. Due to this reason, $CaTiO_3$ is referred as the "founding father" of perovskites. It is important to note that the ideal cubic perovskite structure is not very common. Most importantly, the crystal structure of the mineral $CaTiO_3$ perovskite itself is orthorhombic at room temperature instead of cubic due to a slight distortion. This slight distortion has been explained in terms of the smaller ionic radius of Ca^{+2} which favours the orthorhombic phase [2]. However, the cubic phase of $CaTiO_3$ perovskite does exist at higher temperatures.

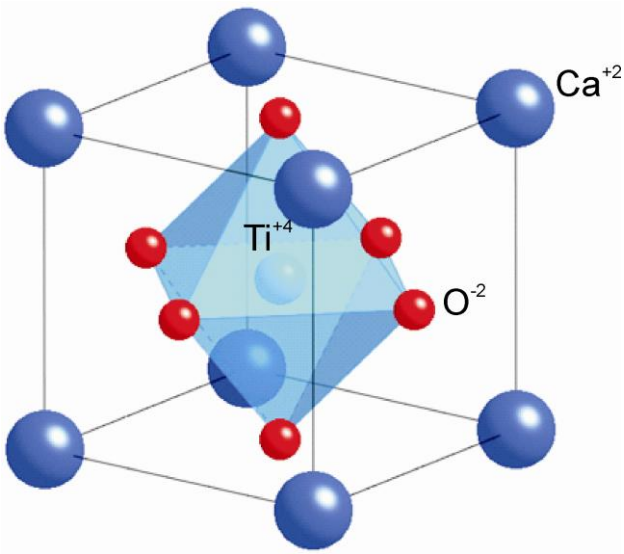

Figure 1.1. Ideal perovskite structure of $CaTiO_3$.

1.1.2 Structure of the Perovskites

The perovskite type structure is one of the most common structures found in solid-state inorganic chemistry. The general stoichiometry of the perovskite structure is represented by formula ABX_3 where A and B are cations while X is an anion which bonds to both cations. The position A in the structure is mostly occupied by an alkaline, alkaline earth or rare earth (Ln) ions while the B site is usually occupied by a transition metal ion [3-6]. The majority of the perovskite compounds contain oxygen as anions and are called perovskite oxides (ABO_3). Generally, the A-site cation is bigger than the B-site cation. In the ideal cubic symmetry, the B-site cation is surrounded by 6 oxygen atoms forming an octahedron (BO_6) while the A-site cation is bonded to 12 oxygen atoms (Figure 1.2).

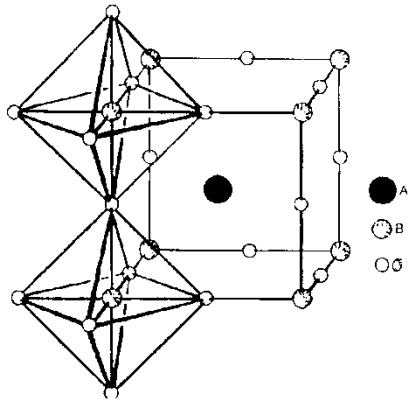

Figure 1.2. Structure of an ideal perovskite ABO_3. Note that the BO_6 octahedron are sharing corner and extending in three dimension to form network [7].

It is evident from the literature that a cubic perovskite can transform into other crystal structures through tilting of the octahedral BO_6 [7, 8]. This tilting causes a distortion in the crystal structure and could happen due to different reasons, including variations in the relative size and/or oxidation state of the A or B cations. The resulting structures due to distortion i.e., octahedral BO_6 tilting, are closely related to the cubic perovskite. There are 15 different kinds of structures including cubic and all compounds exhibiting these structures belong to the perovskite index.

1.1.3 Tolerance factors of the Perovskites

For perovskites, the size and coordination preferences of three or more ions must be satisfied simultaneously by the structure. Nevertheless, it is hardly ever that all these preferences can be accommodated perfectly. Goldschmidt (1920s) illustrated the ionic size dependence of the perovskite structure by deriving a relationship between the radii of the various ions [9]. This relationship is called tolerance factor which is represented by symbol 't'. This tolerance factor indicates the compatibility of a given set of ions with the ideal cubic perovskite structure.

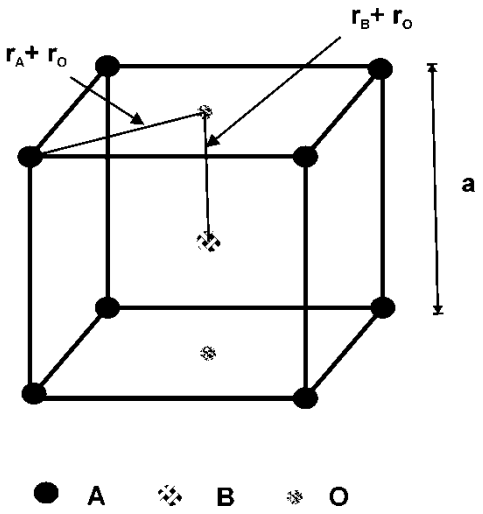

Figure 1.3. The relationship of ionic radii in ABO_3 perovskites.

The tolerance factor 't' can be derived by considering the anion-cation contacts in the ideal cubic perovskite and their relation to the lattice parameter (Figure 1.3). The oxygen anions (O) separate both A-site cations and B-site cations. The lattice constant can be determined by the sum of the ionic radii of the B-site cation and oxygen anion (Eq. 1.1).

$$a = 2 \times B - O = 2 \times (r_B + r_O) \quad (1.1)$$

where a is the unit cell parameter, B-O is the bond length between a B-site cation and oxygen anions and r_B and r_O are the ionic radii of the B-site cation and an oxygen anion, respectively.

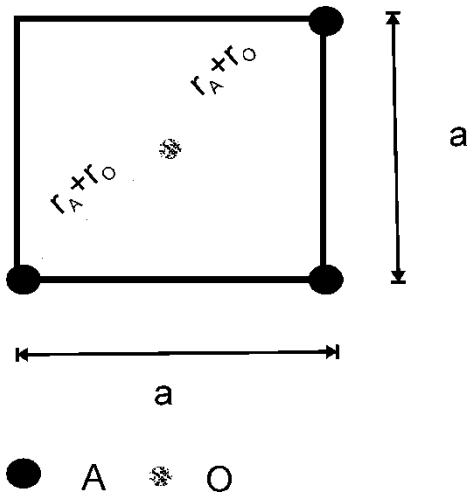

Figure 1.4. The contact distance between an A-site cation and an oxygen anion in the diagonal plane.

Since the A-site cation and the oxygen anion are diagonal to each other, the unit cell parameter will not be equal to the sum of ionic radii of the A-site cation and the oxygen anion along this plane. So, in order to determine the exact unit cell parameter 'a' in terms of contact distances, the Pythagoras theorem can be used. For the triangle shown in Figure 1.4, the Pythagoras theorem can be written as (Eq. 1.2).

$$(Base)^2 + (Perp)^2 = (Hyp)^2 \quad (1.2)$$

$$a^2 + a^2 = (2 \times A - O)^2 \quad (1.3)$$

$$2a^2 = (2 \times A - O)^2 \quad (1.4)$$

$$a^2 = \frac{(2 \times A - O)^2}{2} \quad (1.5)$$

$$a = \sqrt{\frac{(2 \times A - O)^2}{2}} \quad (1.6)$$

$$a = \frac{2}{\sqrt{2}} \times A - O \quad (1.7)$$

$$a = \frac{\sqrt{2} \times \sqrt{2}}{\sqrt{2}} \times A - O \tag{1.8}$$

$$a = \sqrt{2} \times A - O \tag{1.9}$$

$$a = \sqrt{2} \times (r_A + r_O) \tag{1.10}$$

where a is the unit cell parameter, A-O is the bond length between an A-site cation and an oxygen anion and r_A and r_O are the ionic radii of the A-site cation and oxygen anions, respectively. For yielding the ideal perovskite structure, the contact distance for both the A-site and the B-site cations must equal to each other. Hence,

$$2 \times (r_B + r_O) = \sqrt{2}(r_A + r_O) \tag{1.11}$$

In view of the fact that ionic radii are not fixed values, some variation in the ion separations from ($r_+ + r_-$) are always expected in any crystal structure. To account this, we have to introduce another factor in above relation called the tolerance factor t.

$$2 \times t \times (r_B + r_O) = \sqrt{2}(r_A + r_O) \tag{1.12}$$

$$t = \frac{\sqrt{2}(r_A + r_O)}{2(r_B + r_O)} \tag{1.13}$$

$$t = \frac{\sqrt{2}(r_A + r_O)}{\sqrt{2} \times \sqrt{2}(r_B + r_O)} \tag{1.14}$$

$$t = \frac{r_A + r_O}{\sqrt{2}(r_B + r_O)} \tag{1.15}$$

So, the ratio of the bond length of A-O bond to the bond length of B-O bond is called Goldschmidt tolerance factor ‘t’. For an ideal perovskite, geometrically, the ratio of the bond

length of A-O bond to the bond length of B-O bond is $\sqrt{2}:1$. Accordingly, if the bond length is approximately presupposed equal to the sum of two ionic radii, the t-value of the ideal perovskite should be equal to 1.0. However, if the cations are either too big or too small to fit in their designated site, the tolerance factor 't' will deviate from the unity. And this will indicate the stress present in the perovskite structure.

According to the Goldschimdt's experimental findings, the values of tolerance factor 't' for the most cubic perovskites are in the range 0.8-0.9 and perovskites with distorted structure exist in a somewhat wider range of tolerance factor 't' [9, 10]. Goldschimdt's tolerance factor is a very widely used principle for the estimation of formability of the perovskite structure. Up till now, all known compounds with perovskite structure have 't' values in the range of 0.75-1.00[7, 11, 12]. Table 1.1 summarizes the ranges of tolerance factors and corresponding perovskite variants with the possible structures of the known perovskites.

Table 1.1. Tolerance factor t, validity ranges and corresponding perovskite variants [13]

t-values	**Effect**	**Possible structures**
>1	A-site cations are too large to fit into their interstices	Hexagonal perovskite (e.g. $BaNiO_3$)
~0.9-1.0	Both A-site and B-site cations fit exactly into their allotted sites (Ideal condition)	Cubic Perovskites (e.g. $SrTiO_3$)
0.75-0.9	A-site cations are too small to fit into their allotted sites	Several possible structures including • Orthorhombic perovskites (e.g. $SmFeO_3$) • Rhombohedral Perovskites (e.g. $LaAlO_3$)
< 0.71	Both A-site cations and B-site cations are of same size	Possible close-packed structures • Correndum structure (disordered arrangement of cations e.g. $LiNbO_3$) • Ilmenite structure (ordered arrangement within sheets e.g. $FeTiO_3$) • $KNbO_3$ structure (sheetwise ordered arrangement)

1.1.4 Oxygen nonstoichiometry of the Perovskites

In view of the fact that the perovskite oxides consist of cations and oxide ions, they should satisfy the electro-neutrality condition in addition to ionic radii requirements. The electro-neutrality condition means, the sum of charges of A-site cations and B-site cations must be equal to total charge of oxygen anions. This is accomplished by means of appropriate charge distribution on A-site and B-site cations. On this basis, the simple oxide ABO_3 systems can be classified into three types (Table 1.2).

Table 1.2. Classification of ABO_3 Perovskite oxides based on cationic valency.

Class	**Electro-neutrality**	**Examples**
$A^{1+}B^{5+}O_3$	1+5=3(-2)	$NaWO_3$
$A^{2+}B^{4+}O_3$	2+4=3(-2)	$SrTiO_3$
$A^{3+}B^{3+}O_3$	3+3=3(-2)	$SmFeO_3$

These three types alone cover a large number of perovskite oxides. Moreover, partial substitutions are allowed at A-site, B-site and/or both A-site and B-site which produce a series of compounds while preserving the perovskite structure. It is common that the partial substitutions result in defective perovskites due to deficiencies of cations at the A-site or B-site or of oxygen anions. However, the oxygen deficiencies i.e., oxygen vacancies are more frequent than those of cation vacancies. Oxygen vacancy formation in perovskite oxide materials is very important because it produces diversity in the properties and thereby increasing their technological applications [14-16]. The oxygen vacancies are produced when a cation is substituted by another cation with a smaller charge. For example, if a divalent cation is partially substituted at the A-site of a $A^{3+}B^{3+}O_3$ perovskite, then the oxygen vacancies will be produced to compensate the charge and the resulting perovskite will have less oxygen i.e., $A^{3+}_{1-x}A'^{2+}_{x}B^{3+}O_{3-\delta}$ [17, 18]. Similarly, oxygen vacancies can also be induced in the perovskite structure by partial substitution of a cation (for instance, divalent) at the B-site in $A^{3+}B^{3+}O_3$ and the resulting perovskite composition will be $A^{3+}B^{3+}B'^{2+}O_{3-\delta}$[19,

20]. The perovskite system can be made even more oxygen deficient and complicated by doing substitutions at both A-site and B-site at the same time i.e., $A^{3+}_{1-x}A'^{2+}_{x}B^{3+}_{1-y}B'^{2+}_{y}O_{3-\delta}$ [21, 22]. Since perovskite oxides are highly tolerant to oxide vacancies, multiple substitutions have been reported at both A-site and B-site [23].

1.2. Applications of Perovskite Oxides

Perovskite type oxides (ABO_3) form an important class of materials which have great diversity in their properties. Their diverse properties are due to the fact that around 90% of the metallic natural elements are stable in the perovskite oxide structure and also from the possibility of synthesizing multi-component perovskite by partial substitution of cations in position A and B giving rise to substituted compounds with complex formula $A_{1-x}A'_{x}B_{1-y}B'_{y}O_3$. These characteristics account for their large variety of properties like optical, mechanical, electrical, magnetic, and catalytic properties. Due to these reasons, they have found numerous technological applications, e.g. in solid oxide fuel cells as electrode materials (i.e., cathode, anode and electrolyte) [24-28], chemical sensors[6, 22, 29-33], oxygen permeating membranes[34] and as catalysts for oxidation of hydrogen, CO, hydrocarbons and NO_x decomposition[5, 35-37]. Since the focus of this thesis is to study the performance of newly developed perovskite oxides as solid oxide fuel cell anodes and as gas sensors for the reducing gases, only these two applications will be discussed in detail in upcoming sections.

1.2.1. Gas sensors

1.2.1.1. Introduction

In the present time, living standards have dramatically increased due to the advancement in technology and industry. This development has been accompanied by a variety of serious environmental problems including emission of toxic pollutants (NO_x, SO_x, HCl, CO_2, volatile organic compounds etc.) from industries, homes and automobiles. These noxious environmental pollutants have caused serious concerns, such as acid rain, ozone depletion and greenhouse effect (Table 1.3).

Table 1.3. Global environmental problems and related substances.

Environmental problems	**Related substances**
Acid Rain	NO_x, SO_x, HCl
Greenhouse effect	CO_2, CH_4, N_2O, O_3,Fluorocarbon
Ozone layer depletion	Fluorocarbon, Halocarbon
Offensive odour	H_2S, NH_3

There is also an increasing demand of environmental monitoring of research facilities and industrial work place areas to ensure the safety of the workers. For example, methane reduces the oxygen concentration in the atmosphere, if the oxygen concentration drops to less than 12% it can cause unconsciousness and death may occur without any warning. Similarly, as little as 5%H_2 in air can produce an explosion with a tiny spark at room temperature. In view of the fact that types and quantities of environmental pollutants have increased dramatically, developing methods to monitor and control these chemical agents has become very important and challenging.

To prevent or minimize the damage caused by hazardous gases, monitoring and controlling systems are required that can detect and quantify these noxious chemical substances in the environment with very high efficiency and precision. So far, the measurements of the concerned gases have been done by using different analytical instruments such as Gas chromatography, UV spectrophotometers and mass spectrometers. Although these instruments can give a precise analysis, their bulky size, high cost and time-consuming measurements have restricted their widespread use. In contrast to analytical instruments, gas sensors are more compact and robust. The lower cost and versatile application of gas sensors have made them a very effective alternative. There are two main groups of applications i.e., single gas sensors and multiple gas sensors. Single gas sensors can detect only one gas such as NO_x, NH_3, O_3, CO, CH_4, H_2, SO_2 etc., while multiple gas sensors are the modern gas sensing devices designed to analyse complex environmental mixtures containing different gases. The multiple gas sensors are often referred to as

electronic noses. Some applications of gas sensors and electronic noses are summarized in Table 1.4.

Table 1.4. Example applications of gas sensors and electronic noses[38].

Field	**Applications**
Safety	• Fire detection • Leak detection • Toxic/flammable/explosive gas detection • Boiler control • Personal gas monitor
In door air quality	• Air purifiers • Ventilation control • Cooking control
Environmental quality	• Weather stations • Pollution monitoring
Automobiles	• Car ventilation control • Filter control • Gasoline vapour detection • Alcohol breath tests
Food	• Food quality control • Process control • Packaging quality control (off-colours)
Industrial production	• Fermentation control • Process control
Medicine	• Breath analysis • Disease detection

1.2.1.2. Solid state gas sensors

By definition, a solid state gas sensor is based on a material which functions as a filter, transducer and amplifier selectively converting a microscopic chemical reaction into a macroscopic signal.

Solid state gas sensors are among those types of gas sensors which are currently well established and are in commercial applications. The solid state gas sensors are of enormous interest for industrial and scientific world due to their many advantages such as small size, lower cost, relatively high sensitivity towards very low concentration and the possibility of on-line operation. For these reasons, presently, much attention has been paid on the research and development of solid state gas sensors. There are many types of solid state gas sensors which are in commercial use both domestically and industrially. Every type of solid state gas sensor detects the target gases due to a physical effect. A brief summary of different types of solid state gas sensors and their bases of detection for the target gases is given in Table 1.5.

Table 1.5. Types of solid state gas sensors with the corresponding physical change used as gas detection principle[38].

	Type of devices	**Physical change**
1	Semiconductor gas sensors	Electrical conductivity
2	Field effect gas sensors: Diodes, transistors, Capacitors	Work function (electrical polarisation)
3	Piezoelectric sensors: Quartz microbalance (QMB), Surface acoustic wave (SAW), Microcantilevers	Mass
4	Optical sensors (fibre optic or thin film)	Optical parameters: Surface Plasmon Resonance (SPR), reflection, interferometry, absorption, fluorescence, refractive index or optical path length
5	Catalytic gas sensors: Seebeck effect, pellistors, semistors	Heat or temperature
6	Electrochemical gas sensors: Potentiometric, Amperometric	Electromotive force (EMF) or electric current in a solid state electrochemical cell

1.2.1.3. Semiconductor gas sensors

Those solid state gas sensors in which the sensitive layer is made up of a semiconductor material are called semiconductor gas sensors (SGS). The SGS are one of the most promising devices which can detect different types of target gases with very high sensitivity and stability due to their mixed electronic and ionic conducting nature. Additionally, these are cheaper, reliable, robust, light weight and consume lower power. At present, there are three types of SGS devices viz. pellets, thin- and thick-film types.

SGS based on metal oxides such as SnO_2, TiO_2, ZnO, etc. [39-46] have been developed for detection and control of different gases including CO, H_2, NH_3 and H_2S. Although, most of the commercially available SGS devices are based on SnO_2, there are some issues that require improvement like reduced sensitivity, poor reproducibility, and low stability under reducing condition. Sensor devices based on ZnO suffered from some limitations such as high working temperature 400-500^oC, poor gas selectivity and comparatively low gas sensitivity[47]. Similarly, TiO_2 based sensing devices also have some issues like: (i) They have very low[39] and even null[41] sensitivity at above 400^oC; (ii) They are restricted to an operating temperature lower than 300^oC due to oxidation of Ti metal. So, clearly, there is a demand of searching some new materials.

It is evident from literature that perovskite oxides (ABO_3) can be used as gas sensors because they are capable of catalytic activity involving oxidation-reduction reactions. More importantly, substitution at the A-site and/or the B-site can easily be done to get new sensor materials with desirable sensitivity and selectivity for particular applications [32, 48-51].

$SmFeO_3$ is a p-type semiconductor perovskite type oxide[52]. It has been previously examined for the detection of various oxidising gases such as O_3 and NO_2. Furthermore, partial substitutions of Co, Ni and Mg at B-site have been reported which not only improve the sensitivity towards O_3 and NO_2 but also enable $SmFeO_3$ to detect some other gases such as ethanol, propane and acetone (Table 1.6). The resulting perovskite oxides are also p-type, like $SmFeO_3$, and possess good sensitivity towards these gases. However, $SmFeO_3$ has rarely been explored for the detection of strong reducing gases like H_2 due to two main reasons. First, it has very low electrical conductivity under reducing gas atmospheres due to its p-type

electrical behaviour[53]. Second, it tends to show phase separation when exposed to strong reducing gases[54]. Thus to use $SmFeO_3$ for detection of strong reducing gases, there is a need to tune its properties.

Table 1.6. $SmFeO_3$ based perovskite oxides for detection of oxidizing gases.

Perovskite Type oxide	**Target gas**	**Reference**
$SmFeO_3$	NO_2,CO,O_3	[55-59]
$SmFe_{1-x}Co_xO_3$	Ethanol, NO_2,O_3	[51, 53]
$SmFe_{1-x}Ni_xO_3$	Ethanol	[32]
$SmFe_{1-x}Mg_xO_3$	Acetone	[60]

1.2.2. Solid Oxide Fuel Cells (SOFC)

1.2.2.1. Introduction

Fuel cells are electrochemical devices which convert chemical energy of fuels into electrical energy with very high efficiency and minimum noxious waste emission. Being a very important technology, they are currently catching tremendous interest due to:

I. They have great potential for power generation in stationary, portable and transport applications.

II. There is an increasing demand for sustainable energy resources.

However, the requirement of pure hydrogen or hydrogen-rich fuel and high fabrication cost are two major obstacles in the commercial application of fuel cells. The last two decades have been spent in developing materials with improved properties which can made fuel cells a viable commercial competitor of conventional power generation.

William Grove (1839), first time demonstrated the concept of fuel cells [61]. He was studying the electrolysis of water by using platinum electrodes. During his experiments, he observed that when the current was switched off, a small amount of current flowed through the circuit in the opposite direction as a result of reaction between the electrolysis products (i.e., hydrogen and oxygen), catalyzed by the platinum electrodes. He predicted that this setup can be combined in series to build a gaseous voltaic battery [62]. Mond and Langer (1889), 50 years after Grove's gas battery, developed their device consisting of porous

platinum black electrode structures and an electrolyte supported on a porous non conducting diaphragm[63]. They called their device, for the first time, a ‘fuel cell’.

Different types of fuel cells have been developed which mainly differ in the nature of the electrolyte. However, the basic principle of operation for all types of fuel cell is same as depicted in Figure 1.5. All fuel cells consist of three main parts i.e., cathode, anode and electrolyte. Generally, both cathode and anode are porous and electrically conducting while the electrolyte is dense (i.e., non-porous) and electronically insulating but ion-conducting.

The fuel is fed on the anode side of the cell, which is also called the fuel electrode while the cathode is referred to as an air electrode because air is introduced on this side of the cell as an oxidant. At the anode, a fuel such as hydrogen is oxidised into protons and electrons. These electrons make the anode negative; the negative electrode. At the cathode, oxygen takes electron and reduces to oxide ions, for that reason the cathode act as positive electrode.

Depending upon nature of the conducting ions, the electrolytes are of two kinds i.e., proton-conductor and oxide-ion conductor. If the electrolyte is an oxide ion conductor then the oxide ions move from cathode to anode and water forms on the anode due to the reaction between oxide ions and protons. While if the electrolyte is a proton conductor then the protons flow from anode to cathode and water will be formed on the cathode cathode side. In both cases, the electrons travel round an external circuit and deliver electrical power.

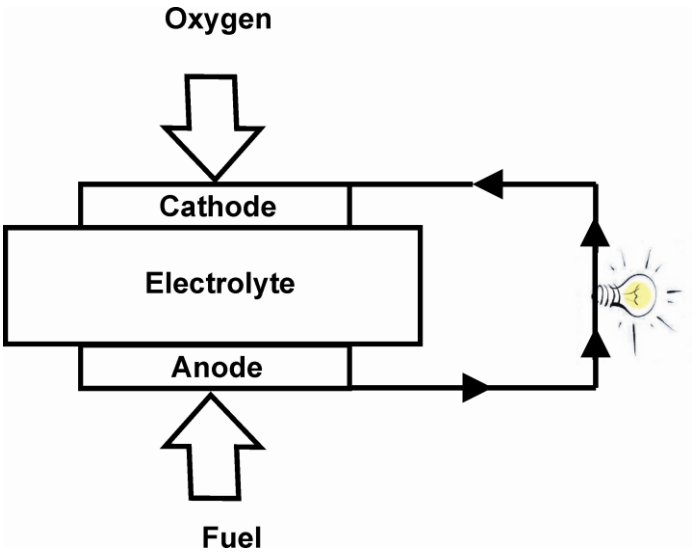

Figure 1.5. Schematic showing basic operating principle of a fuel cell.

There are five main types of fuel cells i.e., polymer electrolyte membrane (PEM), alkaline fuel cell (AFC), Phosphoric acid fuel cell (PAFC), molten carbonate fuel cell (MCFC) and solid oxide fuel cell (SOFC). The comparison of these five important fuel cell types is summarised in Table 1.7. The most obvious difference in characteristics between types of fuel cell is the operating temperature. The operating temperature has a direct effect on the applications for which particular fuel cell types are most suited. It is generally considered that PEM and SOFC are most likely to succeed in achieving widespread commercial applications.

Table 1.7. Comparison of fuel cell technologies[64]

Fuel Cell Type	Common Electrolyte	Operating 'T'	Efficiency	Applications	Advantages	Disadvantages
Polymer Electrolyte Membrane (PEM)	Perfluoro sulfonic acid	50-100^{o}C	60% transportation 35% stationary	Backup power Portable power Transportation Distributed generation	Low Temperature Quick start-up	Expensive catalysts Sensitive to fuel impurities Low T waste heat
Alkaline Fuel Cell (AFC)	KOH_{aq} soaked in a matrix	90-100^{o}C	60%	Military Space	High performance Low cost components	Sensitive to CO_2 in fuel and air Electrolyte management
Phosophoric Acid Fuel Cell (PAFC)	H_3PO_4 soaked in a matrix	150-200^{o}C	40%	Distributed generation	Suitable for CHP High tolerance to fuel impurities	Pt catalyst Long start up Low current and power
Molten Carbonate Fuel Cell (MCFC)	Solution of M_2CO_3 (M=Li, Na ,K) soaked in a matrix	600-700^{o}C	45-50%	Electric utility Distributed generation	High efficiency Fuel flexibility Suitable for CHP Can use variety of catalysts	High T corrosion and break down of cell components Long start up time Low power density
Solid Oxide Fuel Cell (SOFC)	Yttria stabilized zirconia (YSZ)	700-1000^{o}C	60%	Auxiliary power Electric utility Distributed generation	High efficiency Fuel flexibility Suitable for CHP & CHHP Can use variety of catalysts Solid electrolyte Hybrid/GT cycle	High T corrosion and break down of cell components Long start up time Coke/Sulphur poisoning of anode catalysts

1.2.2.2. Basic operating principle of a SOFC

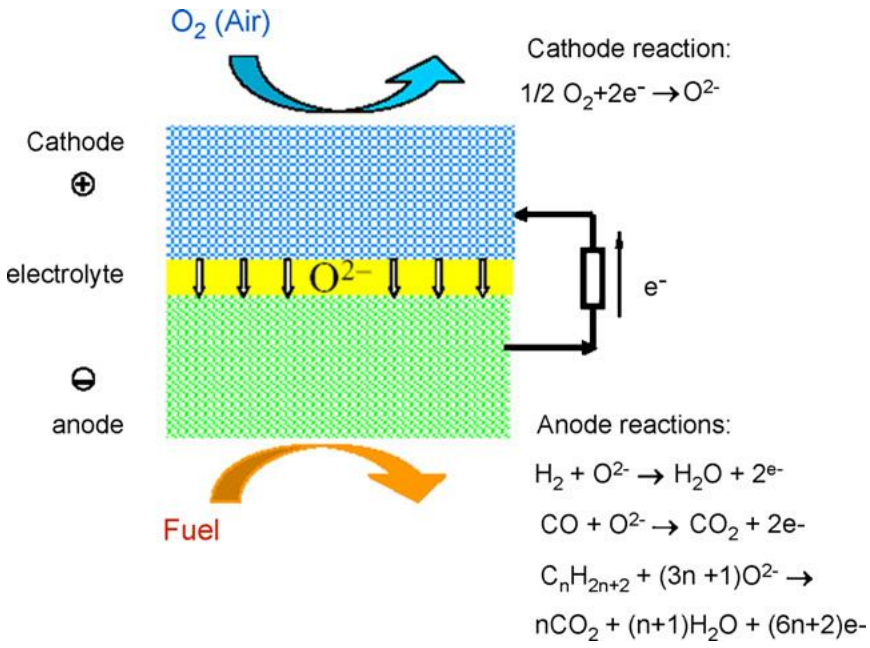

Figure 1.6. Schematic diagram showing the operating principles of a solid oxide fuel cell

The working principle of a solid oxide fuel is shown in Fig. 1.6. At the cathode, molecular oxygen is reduced to oxide ions using electrons from the external circuit The ions pass through the solid electrolyte to the anode, where they react with the fuel, generally hydrogen and carbon containing fuels, producing water and carbon dioxide, as well as heat and electricity.

1.2.2.3. Materials requirements for SOFC

The solid oxide fuel cell (SOFC) is also known as a ceramic fuel cell because it is made up of a solid ceramic electrolyte. The solid ceramic electrolyte is an oxide ion conductor and usually it is a metal oxide. The solid electrolyte of a SOFC must possess the following important characteristics.

I. Gas leakage proof (i.e., dense enough to separate the air and fuel compartments).
II. High oxide ion conductivity (to allow easy migration of oxide ions).

III. Electronically insulator (to prevent short circuiting between cathode and anode electrode)
IV. Chemically stable i.e., maintain these properties over a wide range of the partial pressure of oxygen (~ 1 atm to 10^{-20}).

The operational temperature of SOFC is largely dependent on the ionic conductivity of the electrolyte. The most commonly used electrolyte is Yttria-stabilized Zirconia (YSZ) which requires a very high temperature (800-1000^{o}C) to achieve sufficient ionic conductivity required for transportation of oxide ions[65]. Some other oxides like SDC, GDC and LSGM are also under considerations which have reasonably high ionic conductivity and can enable SOFCs to operate at lower temperature (500-700^{o}C)[66, 67].

The cathode electrode operates in an oxidising environment of air or oxygen and causes to reduce molecular oxygen into oxide ions. The cathode materials in solid oxide fuel cells must meet the following requirements.

I. High electronic conductivity
II. Chemical and structural stability
III. Compatible (thermal expansion coefficient must match well) with other cell components (the electrolyte and interconnect).
IV. No reactivity with the electrolyte and interconnection with which the cathode comes into contact.
V. Adequate porosity which must enable the transport of molecular oxygen from the gas phase to the cathode/electrolyte interface

The common cathode material is Sr-doped $LaMnO_3$[68] which is a p-type perovskite and stable in air and oxidizing atmospheres. In addition, there are lots of mixed ionic-electronic conductors (MIEC), which can be used as cathodes, such as, $La_{0.6}Sr_{0.4}Fe_{0.8}Co_{0.2}O_3$ [69, 70] and $Ba_{0.5}Sr_{0.5}Fe_{0.8}Co_{0.2}O_3$ [71].

The anode electrode is the site in SOFCs where oxidation of the fuel occurs, which leads to the production of electric current. An effective anode of SOFC must possess following characteristics.

I. Stable under the strong reducing environment of the fuel.
II. Good electronic conductor.

III. Good catalytic activity towards fuel oxidation

IV. Sufficient porosity to allow the transport of the fuel to and the transport of the fuel oxidation products away from the electrolyte/anode interface where fuel oxidation reaction takes place.

V. Compatible with other cell components (i.e., electrolyte and interconnect)

The conventional anode material is a Ni/YSZ composite which possesses very high electronic conductivity and exhibit excellent electrochemical performance in hydrogen fuel. In addition, other mixed ionic and electronic conducting oxides have also been used as anodes such as LSCF [72], doped $LaCrO_3$ [26, 37] and doped $SrTiO_3$[25, 73-75].

1.2.2.3. Anode materials for direct hydrocarbon SOFC

The state of art of the SOFC is to use Ni/YSZ composite anodes. In these cermet anodes, Ni provides electronic conductivity and catalytic activity both for direct oxidation and steam reforming of methane. The YSZ, in these cermets, perform two functions. Firstly, it allows the diffusion of the oxide ion to the reactive sites. Secondly, it provides a structural support to Ni particles and prevents their sintering. No doubt, these Ni/YSZ composite anodes exhibit excellent performance in hydrogen fuel, however, when exposed to hydrocarbon fuels, they are quickly poisoned due to coke formation. Furthermore, their performance suffers drastic degradation due to sintering of Ni particles over time. Although, this coking can be reduced by a internal steam reforming process, it results in some issues like reduction in fuel efficiency, lowering in OCV and complications in the system due to the requirement of additional heating required for the conversion of water into steam. Therefore, there is a considerable interest in developing new anode materials for the direct conversion of hydrocarbon fuels into electrical power with high efficiency and without coking problems.

There are three possible approaches which have been suggested to tackle the problem of coke formation while using hydrocarbon fuels directly in SOFC [76-78]. Firstly, coke formation can be reduced substantially by lowering the operational temperature while using conventional Ni/YSZ composite anodes[79]. The reason behind this is that at the intermediate temperatures, the rate of cracking of methane fuel to form coking on the anode is lower while the reaction of oxygen anions with methane to produce steam increases. The steam, thus formed, helps in removing coke deposited on the anode surface. However, this

approach ends up in the lowering of cell powers due to the increase in electrode polarization resistances.

Secondly, coke formation can be avoided by replacing Ni cermets with composites containing Cu and ceria [80-84]. In these composites, copper provides only electronic conduction to the anode while ceria provides catalytic activity due to its mixed electronic and ionic conducting nature. From the catalysis point of view Cu is inactive; however, it has been found that Cu does promote gas phase pyrolysis reactions which still form tar containing polyaromatics on Cu cermets. These polyaromatics enhance the anode performance by providing additional electronic conductivity.

Thirdly, direct utilization of hydrocarbons in SOFC can be made possible by looking for alternative anode materials with mixed electronic and ionic conductivity, since these are less likely to promote carbon formation. The perovskite oxides (ABO_3) are amongst the MIEC materials which have also been investigated as SOFC anodes for the direct oxidation of hydrocarbon fuels. Among these materials chromites and titanates have received considerable attention due to their reduction stability in reducing conditions[76, 85]. However, under dry methane fuel, they suffered from coking problems and therefore, they are always tested under wet methane fuel (3% steam)[78, 86]. So clearly, there is still need of developing new perovskite anode materials that should possess good performance under dry methane fuel without coke poisoning issues in SOFC.

1.3. Scope

This thesis deals with the development and characterization of new perovskite type oxides that will address the sensing issues of reducing gases at lower temperatures and the coking problems of SOFC anodes under dry methane fuel condition. The intention was to develop new perovskite oxide materials that should exhibit good performance as the sensors for the detection of reducing gases i.e., H_2, CO and CH_4; and coke resistant quality under dry methane fuel. To achieve these goals, $SmFeO_3$ perovskite was selected because it contains samarium oxide and iron oxide which are amongst the promising catalysts for hydrocarbon oxidation. However, the p-type electrical behaviour and reduction stability issues were key reasons due to which $SmFeO_3$ was not successful candidate as sensor for the detection of reducing gases and for SOFC anodes. So, tuning of $SmFeO_3$ properties was one of the

important tasks in this work. Chapter 3 describes the tuning of $SmFeO_3$ properties by Ce doping at the A-site. The evaluation of the resulting $Sm_{1-x}Ce_xFeO_{3-\delta}$ (x=0-0.05) perovskites as anode is illustrated in Chapter 4. $Sm_{0.95}Ce_{0.05}FeO_{3-\delta}$ proved to be the best anode material in this series under both dry hydrogen and dry methane fuels. Therefore, $Sm_{0.95}Ce_{0.05}FeO_{3-\delta}$ was used as the starting material to produce other perovskite series by doing partial substitutions of other cations at the B-site. The effect of Co doping on the reduction stability and electrical conductivity of $Sm_{0.95}Ce_{0.05}FeO_{3-\delta}$ is summarized in Chapter 5. The performance of cobalt $Sm_{0.95}Ce_{0.05}FeO_{3-\delta}$ as sensors for the detection of H_2, CO and CH_4 is described in Chapter 6.The relation of anode performance with the cobalt concentration is depicted in Chapter 7. To enhance the catalytic properties, partial doping of Ni was also done at the B-site and the properties of the resulting nickel doped perovskite materials are illustrated in Chapter 8. The effect of reduction treatments on electrical conductivity and sensing properties is described in Chapter 9 and 10. The candidacy of Ni doped $Sm_{0.95}Ce_{0.05}FeO_{3-\delta}$ as anode was examined and shown in Chapter 11. The effect of partial substitution of Cr at the B-site was also explored. Chapter 12 and 13 describes the characterization and sensing results of the Cr doped $Sm_{0.95}Ce_{0.05}FeO_{3-\delta}$ perovskite oxides respectively.

1.4. References

[1] Data Sheet for Perovskite ($CaTiO_3$). Mineral Data Publishing, version 1 (2005).

[2] F. Erazo, A. Stashans, Int. J. Quant. Chem. 87 (2002) 225-231.

[3] R. Ganguly, I.K. Gopalakrishnan, J.V. Yakhmi, J. Phys. Condens. Matter. 12 (2000) L719-L722.

[4] N.G. Eror, D.M. Smyth, J. Eletrochem. Soc. 128 (1981) 1762-1769.

[5] P. Ciambelli, S. Cimino, S.D. Rossi, L. Lisi, G. Minelli, P. Porta, G. Russo, Appl. Catal. B. 29 (2001) 239-250.

[6] S.M. Bukhari, J.B. Giorgi, Sens. Actuators B. 155 (2010) 524-537.

[7] L.Q. Jiang, J.K. Guo, H.B. Liu, M. Zhu, X. Zhou, P. Wu, C.H. Li, J. Phys. Chem. Solids. 67 (2006) 1531-1536.

[8] A.M. Glazer, Acta cryst. A13 (1975) 756-762.

[9] V.M. Goldschmidt, Oslo, Naturwissenschaften. 14 (1926) 477.

[10] A.S. Bhalla, R. Guo, R. Roy, Mater. Res. Innovat. 4 (2000) 3-26.

[11] M.A. Pena, J.L.G. Fierro, Chem. Rev. 101 (2001) 1981-2017.

[12] C. Li, K. Chi, K. Soh, P. Wu, J. Alloys Compd. 372 (2004) 40-48.

[13] C. Schinzer, 1998.

[14] H. Peng, J. Kui-Juan, L. Hui-Bin, J. Jin-Feng, Q. Jie, H. Chun-Lian, Y. Guo-Zhen, Chinese Physics Letters. 26 (2009) 027301.

[15] V.-A.T. Dam, W. Olthuis, P. Bergveld, A.v.d. Berg, The 13th International Conference on Solid-State Sensors, Actuators and Microsystems, IEEE, Seoul, Korea, 2005, pp. 1840-1843.

[16] H.Z. Guo, A. Gupta, J. Zhang, M. Varela, S.J. Pennycook, Appl. Phys. Lett. 91 (2007) 202509.

[17] T. Bak, J. Nowotny, M. Rekas, C.C. Sorrell, J. Phys. Chem. Solids. 62 (2001) 731-735.

[18] A. Fossdal, M. Menon, I. Waernhus, K. Wiik, M.-A. Einarsrud, T. Grande, J. Am. Ceram. Soc.,. 87 (2004) 1952-1958.

[19] G.C.d. AraujO, S. Lima, M.d.C. Rangel, V.L. Parola, M.A. Pena, J.L.G. Fierro, Catal. Today. 107-108 (2005) 906-912.

[20] C.d.l. Calle, J.A. Alonso, A. Aguadero, M.T. Fernandez-Diaz, Dalton Trans. (2009) 4104-4114.

[21] A. Berenov, H. Wood, A. Atkinson, J. Electrochem. Soc. 154 (2007) B1362-B1367.

[22] Y.L. Chai, D.T. Ray, H.S. Liu, C.F. Dai, Y.H. Chang, Mater. Sci. Eng. A. 293 (2000) 39-45.

[23] T. Ishihara, H. Furutani, M. Honda, T. Yamada, T. Shibayama, T. Akbay, N. Sakai, H. Yokokawa, Y. Takita, Chem. Mater. 11 (1999) 2081-2088.

[24] A. Babaei, L. Zhang, S.L. Tan, S.P. Jiang, Solid State Ionics. 181 (2010) 1221-1228.

[25] J. Canales-Vazquez, J.C. Ruiz-Morales, D. Marrero-Lopez, J. Pena-Martinez, P. Gomez-Romero, J. Power Sources. 171 (2007) 552-557.

[26] L. Deleebeeck, J.L. Fournier, V. Birss, Solid State Ionics. 181 (2010) 1229-1237.

[27] A. El-Himri, D. Marrero-Lopez, J.C. Ruiz-Morales, J. Pena-Martínez, P. Nunez, J. Power Sources. 188 (2009) 230-237.

[28] C. Fu, K. Sun, N. Zhang, X. Chen, D. Zhou, Electrochim. Acta. 52 (2007) 4589-4594.

[29] J.W. Fergus, Sens. Actuators B. 122 (2007) 683-693.

[30] J.W. Fergus, Sens. Actuators, B. 123 (2007) 1169-1179.

[31] C.R.M. Emilio Delgado, Mater. Lett. 60 (2006) 1613-1616.

[32] L. Chen, J. Hu, S. Fang, Z. Han, M. Zhao, ZhanleiWu, X. Liu, H. Qin, Sens. Actuators B. 139 (2009) 407-410.

[33] J. Cerda, J. Arbiol, G. Dezanneau, Sens. Actuators B. 84 (2002) 21-25.

[34] C.H. Chen, H. Kruidhof, H.J.M. Bouwmeester, A.J. Burggraaf, J. Appl. Electrochem. 27 (1997) 71-75.

[35] L. Fornia, C. Oliva, T. Barzetti, E. Selli, A.M. Ezerets, A.V. Vishniakov, Appl. Catal. B. 13 (1997) 35-43.

[36] S.O. Choi, S.H. Moon, Catal. Today. 146 (2009) 148-153.

[37] X.J. Chen, Q.L. Liu, K.A. Khor, S.H. Chan, J. Power Sources. 165 (2007) 34-40.

[38] S. Capone, A. Forleo, L. Francioso, R. Rella, P. Siciliano, J. Spadavecchia, D.S. Presicce, A.M. Taurino, J. Optoelect. Adv. Mater. 5 (2003) 1335-1348.

[39] H.-S. Kim, W.-T. Moon, Y.-K. Jun, S.-H. Hong, Sens. Actuators B. 120 (2006) 63-68.

[40] C. Lu, Z. Chen, Sens. Actuators B. 140 (2009) 109-115.

[41] H. Tang, K. Prasad, R. Sanjines, F. Levy, Sens. Actuators B. 26-27 (1995) 71-75.

[42] N. Barsan, R. Grigorovici, R. Ionescu, M. Motronea, A. Vancu, Thin Solid Films. 171 (1989) 53-63.

[43] K. Jain, R.P. Pant, S.T. Lakshmikumar, Sens. Actuators B. 113 (2006) 823-829.

[44] S.W. Lee, P.P. Tsai, H. Chen, Sens. Actuators B. 67 (2000) 122-127.

[45] N.J. Dayan, S.R. Sainkar, R.N. Karekar, R.C. Aiyer, Thin Solid Films. 325 (1998) 254-258.

[46] W. Cheng, X. Ma, J. Phys.: Conference Series. 152 (2009) 012039.

[47] A.B. Bodade, A.M. Bendea, G.N. Chaudhari, Vacuum. 82 (2008) 588-593.

[48] X. Liu, J. Hu, B. Cheng, H. Qin, M. Jiang, Current Appl. Phys. 9 (2009) 613-617.

[49] G.N. Chaudharia, N.N. Gedam, S.V. Jagtap, S.V. Manorama, Talanta. 77 (2009) 1675-1679.

[50] J. Zosel, D. Franke, K. Ahlborn, F. Gerlach, V. Vashook, U. Guth, Solid State Ionics. 179 (2008) 1628-1631.

[51] M. Zhao, H. Peng, J. Hu, Z. Han, Sens. Actuators B. 129 (2008) 953-957.

[52] H. Aono, M. Sato, E. Traversa, M. Sakamoto, Y. Sadaoka, J. Am. Ceram. Soc. 84 (2001) 341-347.

[53] Y. Itagaki, M. Mori, Y. Hosoya, H. Aono, Y. Sadaoka, Sens. Actuators, B. 122 (2007) 315-320.

[54] S.M. Bukhari, J.B. Giorgi, Solid State Ionics. 180 (2009) 198-204.

[55] H. Aono, E. Traversa, M. Sakamoto, Y. Sadaoka, Sens. Actuators B. 94 (2003) 132-139.

[56] G. Martinelli, M.C. Carotta, M. Ferroni, Y. Sadaoka, E. Traversa, Sens. Actuators B. 55 (1999) 99-110.

[57] Y. Hosoya, Y. Itagaki, H. Aono, Y. Sadaoka, Sens. Actuators, B. 108 (2005) 198-201.

[58] E. Traversa, Y. Sadaoka, M.C. Carotta, G. Martinelli, Sens. Actuators B. 65 (2000) 181-185.

[59] E. Traversa, S. Villanti, G. Gusmano, J. Am. Ceram. Soc. 82 (1999) 2442-2450.

[60] X. Liu, J. Hu, B. Cheng, H. Qin, M. Jiang, Sens. Actuators B. 134 (2008) 483-487.

[61] W.R. Grove, Phil. Mag., Ser. 3. 14 (1839) 127.

[62] W.R. Grove, Phil. Mag., Ser. 3. 21 (1843) 417.

[63] L. Mondon, C. Langer, Proc. R. Soc. London. 46 (1889) 296.

[64] http://www.houghton.edu/academics/science_honors/Assignments/in-class/Fuel%20cell%20comparison.pdf.

[65] X. Ge, X. Huang, Y. Zhang, Z. Lu, J. Xu, K. Chen, D. Dong, Z. Liu, J. Miao, W. Su, J. Power Sources. 159 (2006) 1048-1050.

[66] D. Xu, X. Liu, D. Wang, G. Yi, Y. Gao, D. Zhang, W. Su, J. Alloys Comp. 429 (2007) 292-295.

[67] S. Zha, W. Rauch, M. Liu, Solid State Ionics. 166 (2004) 241-250.

[68] H. Nie, W. Huang, T.-L. Wen, H. Tu, Z. Zhan, J. Mater. Sci. Lett. 21 (2002) 1951-1953.

[69] D. Berger, C. Matei, s. Stoleriu, Rev. Roum. Chim. 55 (2010) 653-658.

[70] J.M. Serra, S. Uhlenbruck, W.A. Meulenberg, H.P. Buchkremer, D. Stover, Topics in Catalysis. 40 (2006) 123-131.

[71] J. Dailly, S. Fourcade, A. Largeteau, F. Mauvy, J.C. Grenier, M. Marrony, Electrochim. Acta. 55 (2010) 5847-5853.

[72] J.C.F. II, S.S.C. Chuang, Catal. Commun. 10 (2009) 772-776.

[73] Q.X. Fu, F. Tietz, D. Stöver, J Electrochem. Soc. 153 (2006) D74-D83.

[74] M.D. Gross, K.M. Carver, M.A. Deighan, A. Schenkel, B.M. Smith, A.Z. Yee, J Electrochem. Soc. 156 (2009) B540-B545.

[75] S. Hui, A. Petric, J. Eur. Ceram. Soc. 22 (2002) 1673-1681.

[76] S. Tao, J.T.S. Irvine, The Chemical Records. 4 (2004) 83-95.

[77] A. Atkinson, S. Barnett, R.J. Gorte, J.T.S. Irvine, A.J. McEvoy, M. Mogensen, S.C. Singhal, J. Vohs, Nature Materials. 3 (2004) 17-27.

[78] C. Sun, U. Stimming, J. Power Sources. 171 (2007) 247-260.

[79] E.P. Murray, T. Tsai, S.A. Barnett, Nature. 400 (1999) 649-651.

[80] S. Park, J.M. Vohs, R.J. Gorte, Nature. 404 (2000) 265-267.

[81] S. McIntosh, J.M. Vohs, R.J. Gorte, Electrochim. Acta. 47 (2002) 3815-3821.

[82] S. Park, R. Craciun, J.M. Vohs, R.J. Gorte, J. Electrochem. Soc. 146 (1999) 3603-3605.

[83] C. Lu, W.L. Worrell, R.J. Gorte, J.M. Vohs, J. Electrochem. Soc. 150 (2003) A354-A358.

[84] B.C.H. Steele, P.H. Middleton, R.A. Rudkin, Solid State Ionics. 40/41 (1990) 388-393.

[85] J.W. Fergus, Solid State Ionics. 177 (2006) 1529-1541.

[86] S. Primdahl, J.R. Hansen, L. Grahl-Madsen, P.H. Larsen, J. Electrochem. Soc. 148 (2001) A74-A81.

2. Experimental Considerations

2.1. Summary

While the aim of this thesis work was to develop new perovskite oxide materials and examine their suitability for the use as sensors and anodes of solid oxide fuel cells, it was essential to know about their principal properties such as crystalline phase of as synthesized, sintered and reduced materials, their elemental chemical compositions, oxidation states of various metals in bulk as well as on the surface and microstructures of powders and sintered materials. This chapter will only give a brief overview of each characterization technique; however, these will be discussed in detail in upcoming chapters for each series of materials.

The considerations for testing electrochemical performances of each material as anode are also included in this chapter. These include selection of operational temperature range, assortment of materials for the anode testing, fuel types and also parameters for electrochemical tests like impedance and chronoamperometry experiments. This chapter does not include the specific procedures for the synthesis and performance details as sensors and anodes but assesses the general methodologies.

2.2. Material characterization

2.2.1. X-ray Fluorescence (XRF)

The quantitative elemental composition of each perovskite powder prepared in this work was mainly determined by X-ray fluorescence (Philips PW2400/00). In XRF analysis, the calibration standards were used to get calibration curves. Mixtures of metal oxides with known concentration were used as calibration standards which first were thoroughly mixed and then pressed along with Paraffin binder (Spex) to form pellets. These pellets were used to determine the Kα peak heights of each metal present in the calibration standards. Similarly, the powders under study were pelleted and the Kα peak heights of each metal were determined. The comparison between the Kα peak height of each metal present in calibration standard and powder gave the calibration curve.

2.2.2. X-ray diffraction (XRD)

X-ray diffraction was an important tool used for the characterization of each perovskite oxide series. Diffractograms of all materials were obtained by using a S Phillips PW 1830 instrument. Each diffractogram gives information about the position and intensity of different

peaks. From peak position and intensity, very important information about materials can be obtained such as phase composition, crystallite sizes and lattice parameters. In the present work, the phase composition was determined by comparing all diffractograms with the diffractogram of standard $SmFeO_3$. The crystallite sizes were established from the peak width of selected peaks as obtained by peak fitting and analysed using the Scherrer equation[1]. Peak fitting was carried out by using Jade 6.1 software[2]. The determination of lattice parameters depends on the 2Theta values of each peak which can be significantly affected by the instrumental and experimental imperfections. Therefore, SrO/LaB_6 was used as a reference standard material to correct the peak positions and errors in lattice parameter determination were minimized.

2.2.3. X-ray photoelectron spectroscopy (XPS)

The chemical state and relative abundance of the elements in the surface of all samples were revealed by X-ray photoelectron spectroscopy (XPS; Kratos AXIS Ultra^{DLD} 39-306l). The peaks for $Sm3d_{5/2}$, $Ce3d_{5/2}$, $Fe2p_{3/2}$,$Co2p_{3/2}$, $Cr2p_{3/2}$, $Ni2p_{3/2}$ and O1s core levels were used for identification of oxidation states and for quantification. The XPS spectra were analyzed and quantified by using CasaXPS software[3]. All spectra were calibrated by using the B.E. of the C1s level set at 284.8eV. A nonlinear background subtraction (Shirley) was used to fit all peaks.

2.2.4. Scanning Electron Microscopy and Energy Dispersive X-ray spectroscopy (SEM & EDS)

The microstructure analysis of as synthesized powders; pellets before and after reduction treatments and anode surfaces before and after performances was carried out by using Scanning Electron Microscopy (SEM, JEOL JSM-7500F). Although, all materials were non-conductive in nature, the SEM imaging was performed without doing any surface coating because it can impede the observation of fine surface features. To prevent significant charging effects, a lower acceleration voltage of 9 kV was used during SEM imaging. The elemental composition of particles formed on the surface of sintered samples after the reduction treatments was also determined by using Energy dispersive X-ray spectroscopy in combination with the SEM.

2.3. Electrical conductivity measurements

The electrical conductivity measurement was the key tool used for the determination of electrical behaviour of the materials under study. The measurement of electrical conductivities was initially done by both two probe and four probe DC methods. The values obtained by both

methods were in good agreement to each other. However, the four probe DC method was adopted preferably because of minimum contact resistance and more accuracy.

2.4. Electrochemical measurements

2.4.1. Button cell fabrication

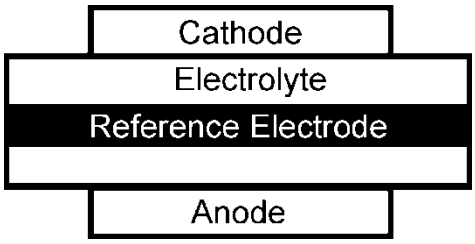

Figure 2.1. Schematic of button cell showing three electrode geometry[4].

Electrolyte supported button cells with a three electrode geometry were fabricated. The following objectives defined the design:

i. To reduce the cross talk between reference and counter electrode
ii. To reduce the alignment problem of counter and working electrode
iii. To increase the effective surface area of electrode
iv. To provide firm contact of electrodes with electrolyte surface

To achieve first three goals, the design of the button cell was modified from previous versions used in the group. In the new design, a thick electrolyte was made. The reference electrode was wrapped around the electrolyte pellet while the working and counter electrodes were placed on the bottom and top of the electrolyte, respectively. A series of sintering temperatures (1000-1400^{o}C) were tested for optimal adhesion of the electrodes to the electrolyte. Lower temperatures (800-1000^{o}C) yielded poor adhesion. The sintering temperature of 1400^{o}C proved to be most effective in fixing the working electrode to the electrolyte.

2.4.2. Button cell sealing

A Pyrex ring was used to seal the button cell at the top of a supporting alumina tube. To optimize the sealing conditions, the sealing was done at different temperatures (700-950^{o}C) for 1 hour. The testing results showed that 950^{o}C is the best temperature for sealing. Therefore, in all

SOFC testing, the button cell was sealed by partially melting the Pyrex ring at 950^{o}C for one hour without gas flow.

2.4.3. Operational conditions

While the aim of this work was to test the anode materials for low temperature SOFC applications, all anodes were tested in the temperature range of 450-700^{o}C.

The effect of flow rate of fuel gas on OCP (open circuit potential) was also studied. The open circuit potential is the voltage difference between the cathode and the anode of SOFC when there is no external load connected i.e., the circuit is open or broken. The results showed that the OCP did not change significantly while changing flow rate from 50 sccm to 100 sccm at different temperatures. Thus a lower flow rate of 50 sccm was selected for the experiments.

2.4.4. Selection of experiments

Since the focus of this research was to study the kinetics of different anode materials under both dry hydrogen and dry methane fuel, it was decided to measure OCP, I-V, P-I and electrochemical impedance (at OCP) at all operational temperatures under both dry hydrogen and dry methane fuel separately.

2.5. Sensor Measurements

Gas sensor experiments were carried out by making solid state sensors in the form of rectangular pellets. The response of each sensor was measured by measuring change in electrical conductivity on introducing a target gas in the carrier gas. The sensor signal is defined by following formula[5]:

$$S(\%) = 100 \times \left(\frac{\sigma_{gas} - \sigma_{Air}}{\sigma_{Air}} \right) \qquad (2.1)$$

2.6. References

[1] I. MDI Jade 6.1 Software Materials Data. Serial#MDI-R97738 (2002).
[2] I. MDI Jade 6.1 Software Materials Data. Serial#MDI-R97738 (2002).
[3] N. Fairley, Casa XPS version 2.3.13 Dev73 (2007).
[4] S.M. Bukhari, J.B. Giorgi, J Power Sources. submitted May (2011).
[5] S.M. Bukhari, J.B. Giorgi, J. Electrochem. Soc. 158 (2011) J159-J164.

3. Synthesis and characterization of $Sm_{1-x}Ce_xFeO_{3-\delta}$ perovskites

The contents of this chapter have been published as: Syed M. Bukhari and Javier B. Giorgi, Solid State Ionics, 180 (2009) 198-204

Abstract

Trimetallic perovskite oxides, $Sm_{1-x}Ce_xFeO_{3-\delta}$ (x =0-0.05), were prepared by thermal decomposition of amorphous citrate precursors followed by calcinations. The material properties of the substituted perovskites were characterized by X-ray diffraction (XRD), X-ray florescence spectroscopy (XRF), scanning electron microscopy (SEM) and X-ray photoelectron spectroscopy (XPS). The doped materials exhibited a single perovskite phase in air up to 1350^oC and have specific surface areas in the range of 2.696-8.665m^2/g. In reducing atmosphere (5%v/vH_2/N_2), the un-substituted perovskite (x=0) decomposed into two phases while the ceria stabilized materials (x=0.01, x=0.03, x=0.05) remained in a single phase as revealed by XRD analysis. Their conductivities were measured by the four point probe method in air and in dilute hydrogen (5%v/vH_2/N_2), separately. The ceria substituted materials show increased stability versus reduction and phase separation for a wide temperature range (up to 1000^oC). Although undoped $SmFeO_3$ has higher conductivity under oxidizing conditions than ceria doped $SmFeO_3$ due its p-type nature, the situation is reversed in reducing conditions. The ceria substituted perovskites ($Sm_{1-x}Ce_xFeO_{3-\delta}$, x =0-0.05) showed higher conductivity in reducing than in oxidizing conditions, suggesting that ceria doping at the A-site has changed the $SmFeO_3$ from p-type to n-type semi-conducting behavior.

3.1. Introduction

Rare-earth orthoferrites ($LnFeO_3$) have found extensive applications in the electro-ceramic industry. These materials are mixed ion electron conductors (MIEC), which makes them good candidates for solid oxide fuel cell (SOFC) materials [1-3], for catalytic partial oxidation of methane (CPOM) [4-6], and for gas sensors [7-9].

Orthoferrites belong to the perovskite family of mixed oxides with the general formula ABO_3. These materials are of great interest because their properties can easily be tailored by partial substitution at the A-site, the B-site, or at both A- and B-sites [10]. The partial substitutions at A- and B-sites create structural defects such as oxygen vacancies which

greatly affect properties like electrical conductivity and thermal stability under oxidizing and reducing conditions [1, 7, 11]. The thermal stability of perovskites is also determined by the nature of the cations at the A- and B-site positions. Their stability can be estimated by calculating a tolerance factor "t" (Goldschmidt factor) based on the ionic radii of cations and oxide ions (O^{-2}) present in the perovskite lattice (Eq. 3.1) [10, 12, 13].

$$t = \frac{r_A + r_O}{\sqrt{2}(r_B + r_O)} \tag{3.1}$$

where r_A is ionic radius of the A, r_B is the ionic radius of B and r_O is the ionic radius of oxygen in the lattice. Perovskites with values of "t" between 0.75 and 1.0 are typically stable.

The rare-earth orthoferrites have been used in resistance type sensors. The working principle of these sensors is that the reaction of gas with surface oxygen changes the conductivity of the material. However, the application of gas sensors is limited by the stability of the perovskite phase in a reducing atmosphere at high temperatures [10] and therefore more stable materials are being sought.

$SmFeO_3$ is one of the rare-earth orthoferrites which has been reported as a potential gas sensor for O_3, CO and NO_2 detection due to its highly gas-sensitive electrical properties. The good sensitivity of $SmFeO_3$ in these sensors has been explained in terms of their greater number of gas adsorption sites on the surface, which has been attributed to surface segregation of Sm ions [14]. $SmFeO_3$ is a p-type semiconductor and therefore its electrical conductivity is high in oxidizing atmosphere and lowers in reducing atmosphere [7, 8, 14], making it suitable for detecting oxidative gases like ozone and NO_2 and reducing gases like CO. In the current work the authors have tried to improve the thermal stability and electrical conductivity in reducing atmosphere by partial substitution of the A site in $SmFeO_3$ by Ce. The increase in size of the A-cation (replacing Sm for Ce) is thought to improve the thermal stability and the electrical conductivity in reducing conditions [1, 10, 15]. However, the limited solubility of Ce is an issue. It has been found that the Ce has very low solubility at A-site in perovskite (ABO_3) structures, though the solubility is dependent on the nature of the B-metal [15, 16].

There is precedent in the literature for the tuning of physical properties of perovskites by minor substitutions. The perovskite structure of undoped $SrMnO_3$ is stable above 1400°C but this structure becomes unstable at room temperature. However the partial substitution of Ce for Sr in $SrMnO_3$ stabilizes the perovskite structure down to room temperature. The conductivity of the undoped $SrMnO_3$ is lower than that of $La_{0.8}Sr_{0.2}MnO_3$ (LSM, 175 $S.cm^{-1}$ at 1000°C) but on Ce substitution ($Sr_{0.7}Ce_{0.3}MnO_3$) its conductivity becomes higher, 290 $S.cm^{-1}$ at 1000^oC [17, 18]. Similarly, undoped $SrCoO_{3-\delta}$ shows phase instability[19] which is responsible for severe degradation in electrical properties. Doping with Ce inhibits the structural change and improves the electrical conductivity. The conductivity of $Sr_{1-x}Ce_xCoO_{3-\delta}$ (x=0.15) is found to be over 500 Scm^{-1} at 350-400 °C, much higher than undoped $SrCoO_{3-\delta}$.

From the literature it is evident that Ce containing perovskites have shown potential for catalytic oxidation processes. Ceria doped $LaCoO_3$ has shown high catalytic oxidation activity towards CO and CH_4 [16], and ceria doped $LaNiO_3$ has been reported to show good potential for auto-thermal reforming [15]. According to Aidu Qi *et al*. [15], the introduction of Ce at La in $LaNiO_3$ improves the thermal stability and tolerance towards coke formation and sulfur poisoning. Similarly, Giammakas et al. [20] have reported that $La_{0.8}Ce_{0.2}FeO_3$ and $La_{0.8}Ce_{0.1}Sr_{0.1}FeO_3$ show very high catalytic activity toward the NO+CO reaction. Studies of the versatility and reactivity of $Sm_{1-x}Ce_xFeO_{3-\delta}$ perovskite materials described in this work are described in subsequent chapters.

In the present chapter, we have investigated the effect of ceria doping on $SmFeO_3$. The doped perovskites were synthesized with increasing amounts of ceria (nominally $Sm_{1-x}Ce_xFeO_{-\delta}$, x = 0 - 0.10). Phase purity, structure, thermal stability and conductivity were determined using X-ray diffraction (XRD), X-ray photoelectron spectroscopy (XPS), Scanning electron microscopy (SEM) and 4-point conductivity measurements. Material properties are discussed as a function of ceria doping and temperature.

3.2. Experimental

3.2.1. Synthesis

Ceria doped samarium iron oxide materials were prepared by thermal decomposition of the amorphous citrate precursors. This technique allows homogeneous dispersion of the precursor salts and it lowers the calcination temperature required for the perovskite structure

formation, as compared to solid state techniques. The lower calcination temperature prevents the materials from sintering and helps in producing a high surface area material. For the preparation of $Sm_{1-x}Ce_xFeO_{3-\delta}$, samarium nitrate ($Sm(NO_3)_3 \cdot 6H_2O$, AlfaAesar, 99.9%), cerium nitrate ($Ce(NO_3)_3 \cdot 6H_2O$, AlfaAesar, 99.5%), iron nitrate ($Fe(NO_3)_3 \cdot 9H_2O$, AlfaAesar, >98%) and citric acid monohydrate (minimum 99.0%) were used as precursors. Samarium nitrate, cerium nitrate and iron nitrate were weighed separately according to the desired stoichiometric ratio of the three metals (Sm_{1-x} + Ce_x : Fe = 1:1) and were then dissolved in de-ionized water to prepare their solutions. Solutions were mixed and the resulting solution was added to aqueous citric acid such that the metal to citric acid ratio was 1:1. Water was evaporated at 100 °C until the amorphous citrate precursors were dried and the material was then ground and finally calcined at 850°C for 24 hours to form the perovskite phase.

3.2.2. Characterization

X-ray diffraction (XRD, Phillips PW 1830) analyses were carried out to determine the phase composition and crystallite sizes using CuK_α radiation with a wavelength of 1.54 Å. The scans were measured in the range of $2\theta = 13^o$ to 90^o at a scan rate of 0.02 ^{o}/sec. The crystalline phase was assigned using the Powder Diffraction File database (ICDD/JCPDS, 2001, Dataset 1-99). Lattice parameters were measured after theta calibration with SrO as the internal standard. Peak refinements were performed using Jade 6.1.

The stoichiometry of the perovskite was determined by X-ray fluorescence (Philips PW2400/00). Quantities of Sm, Ce and Fe in each sample were determined using a calibration curve consisting of a concentration gradient of Sm_2O_3, CeO_2 and Fe_2O_3.

The surface morphology of each sample was observed by scanning electron microscopy (SEM, JEOL JSM-7500F) while the surface chemical states and composition of each sample were measured by X-ray photoelectron spectroscopy (XPS; Kratos AXIS Ultra^{DLD} 39-306l), using a monochromatic Al anode. The BET surface areas of all samples were determined by using a Quantachrome Autosorb 1-C instrument using nitrogen as the vector gas.

Conductivities of each perovskite were measured using a four-probe DC method in air and in 5 %v/v H_2/N_2 in the temperature range of 25°C -1000°C. For these measurements, the materials were pelleted by uniaxially pressing 2 g of powder perovskite to 15000 lbs and sintering the pellet in air to 1350°C for 4 hours with a ramp of 2 °C/min during heating and cooling. During conductivity measurements in both air and flowing 5%v/v H_2/N_2, the pellets

were initially maintained at 1000°C for half an hour to achieve equilibrium. Current measurements were performed during cooling (1000°C to 25 °C) and heating (25°C to 1000°C) to ensure overlapping curves which indicate equilibrium conditions.

3.3. Results and discussion

3.3.1. Bulk structure

Upon synthesis, the quantitative elemental composition of the prepared perovskites was experimentally determined using X-ray fluorescence. Table 3.1 shows the quantification of $Sm_{1-x}Ce_xFeO_{-\delta}$ obtained from X-ray florescence spectroscopy. The calibration curve was obtained by using CeO_2, Fe_2O_3 and Sm_2O_3, which were obtained by thermal decomposition of $Ce(NO_3)_3.6H_2O$, $Fe(NO_3)_3.9H_2O$ and $Sm(NO_3)_3.6H_2O$, respectively.

The experimentally obtained stoichiometric ratios between metal atoms match the expected composition based on synthesis quantities. The oxygen composition is obtained indirectly, from the balance of the sample mass and the percent composition of all metals. The discrepancy relative to the expected composition is 1-4 %. The concentration of oxygen is expected to vary as a function of sample history due to the ionic-conducting abilities of this perovskite series.

Table 3.1. Elemental quantification of $Sm_{1-x}Ce_xFeO_{3-\delta}$obtained from XRF.

$Sm_{1-x}Ce_xFeO_{3-\delta}$	% w/w Sm[a]	% w/w Ce[a]	% w/w Fe[a]	Experimental Stoichiometric ratio Sm : Ce : Fe : O[b]
x=0	59.25	0	21.59	1.00 : 0.00 : 0.983 : 3.09
x=0.01	58.36	0.56	21.81	0.99 : 0.01 : 0.992 : 3.10
x=0.03	57.51	1.67	21.93	0.97 : 0.03 : 0.997 : 3.01
x=0.05	56.23	2.78	21.68	0.95 : 0.05 : 0.985 : 3.06

[a]Measured by XRF using a calibrations curves of the corresponding oxides. Values are given as % w/w of the overall sample.
[b]Oxygen cannot be measured directly. The oxygen content is calculated from the balance of the sample weight.

The crystal structure of the synthesized perovskites was determined using powder X-ray diffraction. Figure 3.1 shows the XRD pattern of $Sm_{1-x}Ce_xFeO_{3-\delta}$ with x=0, 0.01, 0.03, 0.05, 0.07 and 0.10. Comparison with the standard JCPDS card # 39-1490 indicates an orthorhombic symmetry from the Pnma (62) space group. A phase separation of CeO_2 was detected for $x \geq 0.07$, which indicated that the solubility limit of CeO_2 was between 5 and 7 mol%. There are different factors that govern the solubility limit of a dopant in a perovskite system. One of the commonly used factors to explain the solubility limit, is the tolerance factor of the resulting perovskite which explains geometrically to what extent the ionic radii of the dopant distorts the structure [21]. However, the formation of a solid solution is governed by the Gibbs energy of solubilization, which takes into account enthalpic and entropic contributions of the substitution. The determination of these quantities is beyond the scope of this work.

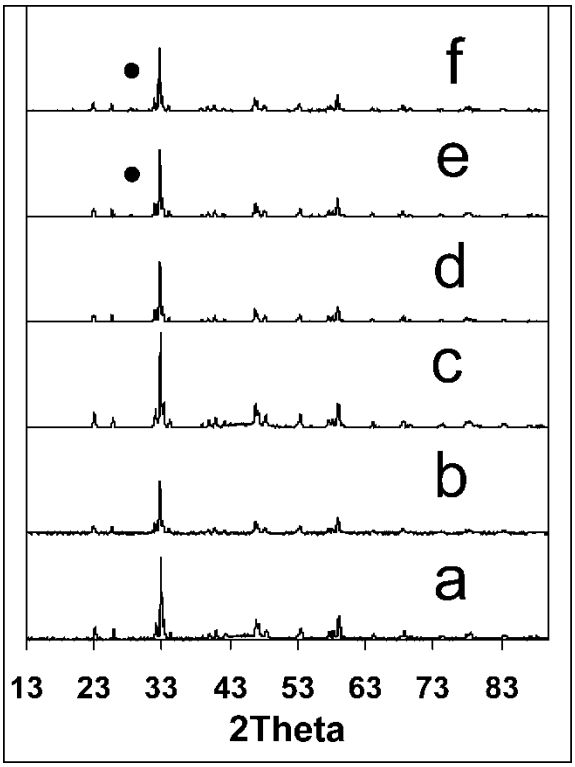

Figure 3.1. XRD patterns of $Sm_{1-x}Ce_xFeO_{3-\delta}$ sintered in air for 24 hours at 850^0C. a) x = 0; b) x = 0.01; c) x = 0.03; d) x = 0.05; e) x = 0.07; f) x = 0.10. ● indicates peaks of a separate CeO_2 phase.

XRD peak positions and full-width-half-maxima were used to determine cell parameters and crystallite sizes for all the perovskites. Additionally, densities were calculated from the obtained unit-cell volume according to equation 3.2 [22]. Table 3.2 shows the calculated values.

$$D(\,gcm^{-3}\,) = \frac{W \times Z}{V \times 0.6022169} \tag{3.2}$$

Table 3.2. Calculated cell parameters, theoretical densities, cell volumes and crystallite sizes from XRD data of $Sm_{1-x}Ce_xFeO_{3-\delta}$ calcined at 850^0C for 24 hours

$Sm_{1-x}Ce_xFeO_{3-\delta}$	Crystallite Size (Å)	a (Å)	b (Å)	c (Å)	Volume ($Å^3$)	Density (g/cm^3)
x=0	596	5.606	7.751	5.409	235.019	7.184
x=0.01	530	5.592	7.719	5.390	232.668	7.256
x=0.03	816	5.588	7.723	5.393	232.712	7.248
x=0.05	627	5.600	7.718	5.413	233.927	7.204

In equation 3.2, 'W' is the formula mass, 'Z' is number of formula units per crystal and 'V' is the volume calculated from unit-cell constants. For $SmFeO_3$ in the orthorhombic phase, the value of 'Z' is 4[23]. From the relative sizes of Sm^{+3} and Ce^{+3} cations, a straight substitution was expected to produce a gradual increase in volume from x=0 to x=0.05. However, the experimental results show a volume decrease from x = 0 to x = 0.01 followed by volume increases for higher Ce content. The volume of all $Sm_{1-x}Ce_xFeO_{3-\delta}$ was found to be smaller than that of $SmFeO_3$, which can be attributed to the presence of some A-cations in the +4 state. In order to explain this trend of volume we calculated the average radii of the A cation, r_A(avg), by using different concentrations and concentration trends of Sm^{+3}, Sm^{+4}, Ce^{+3}, and Ce^{+4}. Representative results of these calculations were compared with the volume (as $V^{1/3}$) in Figure 3.2 and plotted as a function of total concentration of Ce (x).

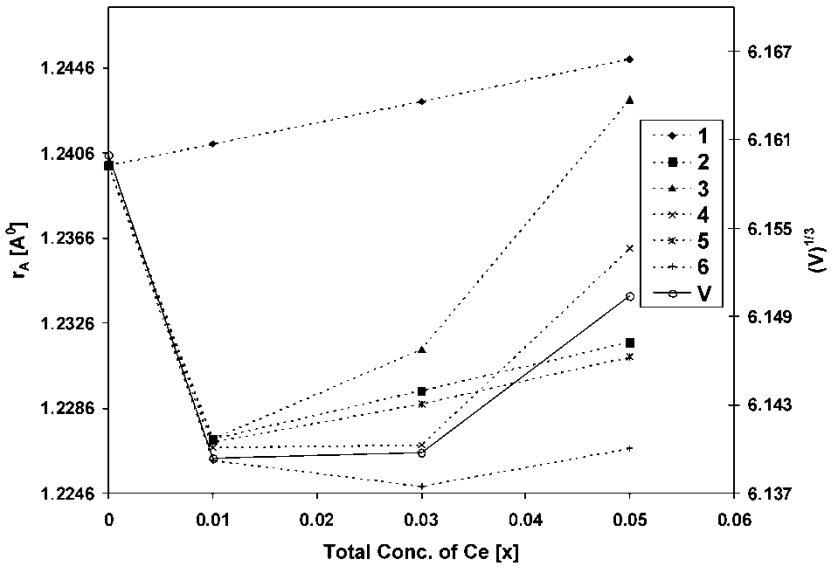

Figure 3.2. Average ionic radii of A-cation (r_A) and normalized cell volume ($V^{1/3}$) as a function of total concentration of Ce($x = x' + x''$). The solid line represent $V^{1/3}$ and broken lines are representing average ionic radii ($r_{A)}$. The compositions corresponding to different series are:

(1) $Sm^{+3}_{1-x'}Ce^{+3}_{x'}FeO_3 (x' = 0-0.05)$,

(2) $Sm^{+3}_{1-y-x'}Sm^{+4}_{y}Ce^{+3}_{x'}FeO_3 (x' = 0-0.05, y = 7\%Sm^{+3})$

(3) $Sm^{+3}_{1-y-x'}Sm^{+4}_{y}Ce^{+3}_{x'}FeO_3 (x' = 0-0.05, y = 7\%-1\%Sm^{+3})$

(4) $Sm^{+3}_{1-y-x'-x''}Sm^{+4}_{y}Ce^{+3}_{x'}Ce^{+4}_{x''}FeO_3 (x' + x'' = 0-0.05, x'' = 0-70\%Ce^{+3}, y = 7-1\%Sm^{+3})$

(5) $Sm^{+3}_{1-y-x'-x''}Sm^{+4}_{y}Ce^{+3}_{x}\ Ce^{+4}_{x''}FeO_3 (x' + x'' = 0-0.05, x'' = 7\%Ce^{+3}, y = 7\%Sm^{+3})$

(6) $Sm^{+3}_{1-y-x'-x''}Sm^{+4}_{y}Ce^{+3}_{x'}Ce^{+4}_{x''}FeO_3 (x' + x'' = 0-0.05, x'' = 50\%Ce^{+3}, y = 7\%Sm^{+3})$

The compositional trends can be divided into three categories. Series 1 does not contain +4 cations and shows the expected increase in r_A(avg). Series 2, 5 and 6 contain a fixed Sm^{+4}/Sm^{+3} ratio (0.07) and fixed Ce^{+4}/Ce^{+3} ratios (0, 0.07 and 0.50, respectively). Series 3 and 4 contain a decreasing ratio of Sm^{+4}/Sm^{+3}, without and with Ce^{+4}, respectively. The trend of series 4 appears to be the most consistent with the volume series, which suggests the presence of both Sm^{+4} and Ce^{+4}. The decreasing importance of Sm^{+4} as a function of total Ce dopant can be corroborated by XPS results (discussed in section 3.3.2). However the ratio of

Ce^{+4}/Ce^{+3} cannot be determined more accurately as ratios of 0.2 to 0.8 fit the volume change reasonably well, and this parameter can only be considered qualitative.

The thermal stability of all single phase perovskites ($Sm_{1-x}Ce_xFeO_{3-\delta}$, x = 0 - 0.05) was tested by calcination to high temperature (1350°C, 4h) in air. The XRD spectra obtained after calcination were virtually undistinguishable from those in Figure 3.1, demonstrating that the lattice structure does not decompose. Only a slight narrowing of the peaks was observed, consistent with increases in crystal size.

The chemical stability was also tested under reducing conditions (900°C in 5 % v/v H_2/N_2 for one hour). Figure 3.3 shows the resulting XRD spectra. The ceria substituted $Sm_{1-x}Ce_xFeO_{3-\delta}$ perovskites showed high stability, that is, no phase separation. Only the diffractogram of the non-substituted crystal (x = 0) showed the separation of non-perovskite phases. Sm_2O_3 can be clearly identified, and a second feature appears in the region of Fe/Fe_2O_3. These features are characterized by broad, weak peaks, which prevents the separation of the Fe/Fe_2O_3 feature ($2\theta_{Fe} = 44.673$ and $2\theta_{Fe_2O_3} = 44.703$ [22]). While metallic Fe may be expected as the decomposition product in reducing conditions, incomplete decomposition and exposure to air prior to the XRD measurements prevent the dismissal of Fe_2O_3 formation.

The introduction of cerium into the lattice up to the solubility limit has improved the stability of $SmFeO_3$ in reducing atmosphere. The partial substitution of Sm^{+3} (smaller cation) with Ce^{+3} (bigger cation) enhances the stability of the perovskite in reducing environments. This increase in stability with an increase in the concentration of Ce can also be discussed in terms of the tolerance factors of the resulting perovskites. The tolerance factor depends on the size of the cations present in the lattice of the crystalline material. Since all these perovskites have a Goldschmidt tolerance factor "t" within a range of 0.75 to 1.0, all fulfill the requirement of stability. However, an increase in tolerance factor is typically associated with an increase in the stability of the material. The values of tolerance factors for $Sm_{1-x}Ce_xFeO_{3-\delta}$ were calculated using available ionic radii, that is r[Sm^{+3} (XII)] =0.124 nm, r[Sm^{+4}] =0.104 nm, r[Ce^{+3} (XII)]=0.134 nm, r[Ce^{+4} (XII)]=0.114 nm, and r[Fe^{+3} (VI)]=0.0645nm [24]. The trend of tolerance factor for this series is not linear because these ceria substituted perovskites contain Sm^{+4} and Ce^{+4} in different ratios which are not known. However, the tolerance factor calculated by using the same composition which fits the

volume changes **(**see Fig. 2**)** are 0.91298, 0.90839, 0.90843 and 0.91163, for x=0, 0.01, 0.03 and 0.05, respectively. The tolerance factor first decreases from x=0 to x=0.01 and then increases from x=0.01 to x=0.05 due to different concentration trends of Sm^{+4} and Ce^{+4}.

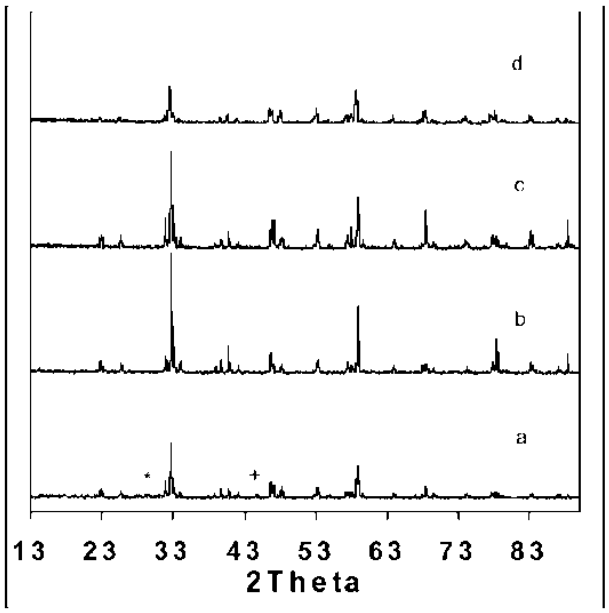

Figure 3.3. XRD spectra for $Sm_{1-x}Ce_xFeO_{3-\delta}$ sintered at 900 ^{0}C in 5%H_2/N_2 for one hour. a) x = 0; b) x = 0.01; c) x = 0.03; d) x = 0.05. ***** indicates peaks of Sm_2O_3; **+** indicates Fe/Fe_2O_3.

3.3.2. Surface structure

The surface morphology of all perovskite powders was observed directly by scanning electron microscopy. The microstructure was found to be similar for all ceria substituted $Sm_{1-x}Ce_xFeO_{3-\delta}$ perovskites. As an example, Figure 3.4 shows the surface morphology of $SmFeO_3$ and $Sm_{0.99}Ce_{0.01}FeO_{3-\delta}$ (representative of x = 0.01 – 0.05) powders calcined at 850^{o}C. The surface of each powder was porous, although $SmFeO_3$ appeared to be less porous than the substituted perovskites.

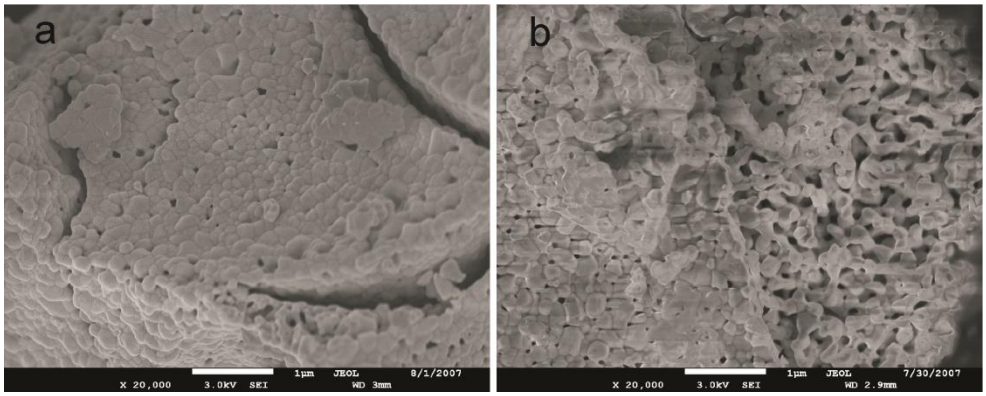

Figure 3.4. Surface morphology observed by SEM a) $SmFeO_3$; b) $Sm_{0.99}Ce_{0.01}FeO_{3-\delta}$.

The as-synthesized powders of $Sm_{1-x}Ce_xFeO_{3-\delta}$ (obtained after calcination in air for 24 hours at 850°C) were analyzed as to their surface area (SA). BET analysis of the nitrogen absorption experiments gave values of SA = 2.696, 8.665, 5.158 and 6.937 m^2/g for samples of x = 0, 0.01, 0.03, and 0.05, respectively. All the surface area values are of the same order of magnitude, but the lower value of the unsubstituted $SmFeO_3$ is consistent with the observed SEM images.

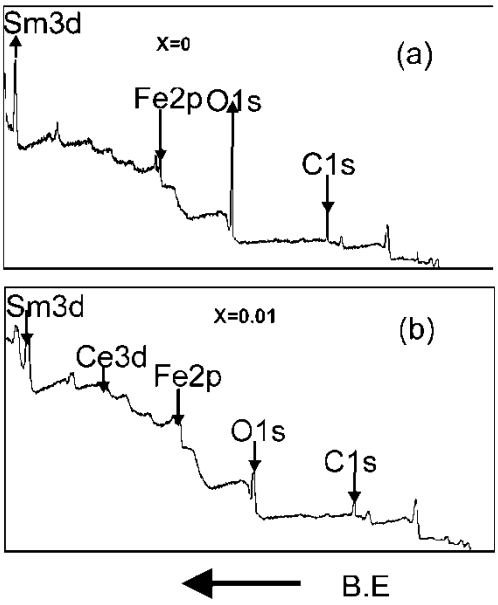

Figure 3.5. Full range XPS spectrum of (a) $SmFeO_3$ and (b) $Sm_{0.99}Ce_{0.01}FeO_{3-\delta}$.

The chemical state and relative abundance of the elements in the surface of $Sm_{1-x}Ce_xFeO_{3-\delta}$ samples were revealed by X-ray photoelectron spectroscopy. Figure 3.5 shows the XPS spectra of $SmFeO_3$, and $Sm_{1-x}Ce_xFeO_{3-\delta}$ (x = 0.01, representative of all cerium doped compounds). The peaks for $Sm3d_{5/2}$, $Ce3d_{5/2}$, $Fe2p_{3/2}$ and O1s core levels were used for identification of oxidation states and for quantification. The XPS spectra were analyzed and quantified using CasaXPS software [25]. All spectra were energy calibrated by using the B.E. of carbon set at 284.8 eV. The surface atomic ratios were calculated from R.S.F values of each metal and are presented in Table 3.3.

The different thermodynamic models that allow practical determination of surface composition for solid solutions are well established [26]. The surface tension of the components, which is ultimately dependent on the Gibbs free energy of formation (Δ_fG) for each component, is important to determine surface composition. More negative values of Δ_fG correlate with a smaller surface tension and a more likely segregation of the component of a solid solution to the surface. This approach has been demonstrated with a related perovskite ($La_{1-x}Ce_xCoO_3$) in which Co_3O_4 and La_2O_3 segregate to the surface [16]**.** The Gibbs' free energy of formation for Sm_2O_3, CeO_2 and Fe_2O_3 are -1744.2 kJ mol^{-1}, -1025.8 kJ mol^{-1} and -87.5 kJ mol^{-1}, respectively [27]. Since the Δ_fG of Sm_2O_3 is very large (negative), it is expected to segregate to the surface. The experimental atomic ratios obtained by XPS support this analysis by showing that the surface is enriched with Sm.

The O1s peaks in all cases can be divided into two components The first component, at lower B.E, is ascribed to oxygen in the lattice ($O^{-2}_{lattice}$) of the perovskite-type structure [28] and the second, at higher B.E, is ascribed to surface- adsorbed oxygen (O^{-2}_{ad}) [29].

Table 3.3. B.E. in (eV) and surface atomic ratio of $Sm_{1-x}Ce_{x}FeO_{3-\delta}$.

	Binding Energy (eV)[a]				Metal atomic ratios		
sample	$Sm3d_{5/2}$	$Ce3d_{5/2}$	$Fe2p_{3/2}$	O1s	$\frac{Sm}{Sm+Ce+Fe}$	$\frac{Ce}{Sm+Ce+Fe}$	$\frac{Fe}{Sm+Ce+Fe}$
					(Sm:Ce:Fe[b])		
x=0	1082.16	-	710.66	529.50 531.68	0.670	-	0.330
					(2.03:0.00:1.00)		
x=0.01	1081.90	884.43	710.40	529.77 532.44 533.07	0.705	0.002	0.293
					(2.41:0.009:1.00)		
x=0.03	1082.12	884.75	710.62	529.19 530.12	0.634	0.007	0.359
					(1.8:0.02:1.00)		
x=0.05	1083.19	883.72	712.69	529.42 530.86	0.590	0.004	0.406
					(1.45:0.011:1.00)		

[a]Binding energies are calibrated by the C 1s peak, set at 284.8.eV.
[b]Stoichiometric ratios are normalized to the iron content.

The oxidation states of both Sm and Fe in $SmFeO_3$ (i.e. x = 0) were reported to be +3 by Aono *et al*. [30, 31]. The peak position and peak shape of Sm3d and Fe2p in $Sm_{1-x}Ce_xFeO_{3-\delta}$ were the same as those of $SmFeO_3$. However, initial (fast) XPS measurements showed an additional feature in the spectrum, as shown in Figure 3.6. The $Sm_{0.99}Ce_{0.01}FeO_{3-\delta}$ sample showed a splitting of the Sm3d peaks with a high binding energy shoulder (Figure 3.6a). The shoulder was found to decrease in size as a function of time, finally disappearing after ~ 26 minutes of continuous XPS measurements (Figure 3.6b). This splitting suggests that for this low concentration of ceria (x = 0.01), there are two oxidation states of samarium initially present at the surface, i.e. Sm^{+3} and Sm^{+4}. This splitting of the Sm3d peak is also associated with an additional peak in the O1s region. The O1s peak, which normally consists of two components, shows three components at 529.77 eV, 530.12eV and 533.07 eV, as shown in Figure 3.6c. The third component, at 533.07eV, can be ascribed to oxygen in the vicinity Sm^{+4} on the surface. This third component disappears as the Sm^{+4} is reduced to Sm^{+3} (Figure 3.6d). The process of reduction under the beam occurs faster (less than 6 minutes) for x=0.03 and Sm^{+4} is not visible for x = 0.05.

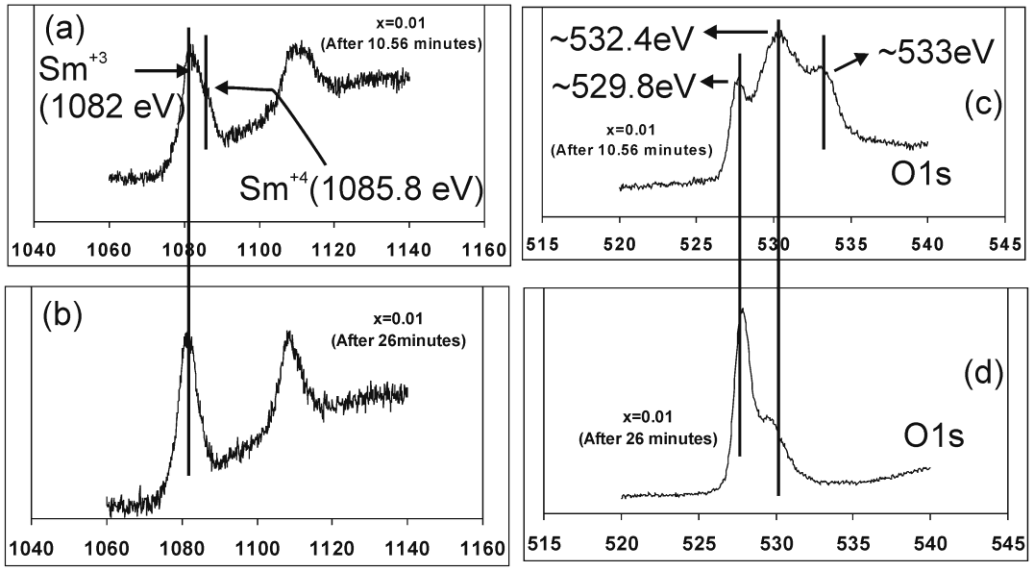

Figure 3.6. XPS spectrum x=0.01 at different times showing splitting of $Sm3d_{5/2}$ and O1s peaks.(a) and (b) showing $Sm3d_{5/2}$ peaks after 10.56 and 26 minutes respectively while (c) and (d) showing O1s peaks after 10.56 and 26 minutes respectively.

Since no splitting of the samarium peaks has been observed or reported in the literature, we can infer that the presence of a high oxidation state Sm^{+4} is due to the ceria substitution. The mechanism by which Sm^{+4} is produced remains unclear. The XPS spectra do not show a splitting of the Ce 3d peak which would indicate the presence of a redox couple ($Ce^{+4} \leftrightarrow Ce^{+3}$). However, the low intensity of the Ce 3d peak makes this result inconclusive. The dependence of the reduction kinetics of Sm^{+4} on cerium concentration suggests that cerium ions are acting as redox agents.

The presence of Sm^{+4}, together with the possible presence of Ce^{+4}, may also account for the observed changes in volume of the substituted $Sm_{1-x}Ce_xFeO_{3-\delta}$ perovskite series (see Table 2 and Figure 2). Upon substitution with ceria (increasing x), an increase in unit cell volume was expected since the ionic radius of Ce^{+3} is larger than that of Sm^{+3}. This was indeed observed, except for the initial substitution, where the data shows a decrease in volume between $SmFeO_3$ and $Sm_{0.99}Ce_{0.01}FeO_{3-\delta}$. The decrease in volume from x=0 to x=0.01 can be explained by the presence of the Sm^{+4} ions, which have a much smaller ionic radius. The subsequent increase in ionic radii from x=0.01 to x=0.05 suggest that concentration of Sm^{+4} is decreasing while concentration of Ce^{+4} is increasing as shown in Figure 3.2.

The presence of Sm^{+4} and its reduction to Sm^{+3} during XPS measurements suggest an apparent conflict with the discussed XRD data, since such a redox process may involve a change in phase of the crystal and it is caused by the incident X-ray beam. The single crystal phase observed for $Sm_{0.99}Ce_{0.01}FeO_{3-\delta}$ can be explained in several ways: a) diffractograms require long time exposure and therefore the XRD observed is that of the final phase (containing only Sm^{+3}); b) Sm^{+4} is only a surface species and does not contribute to the diffractogram; c) the presence of Sm^{+4} ions does not alter the crystal structure of the Perovskite, only its lattice parameters. It is not possible to select a single explanation at this time.

3.3.3. Electrical Conductivity

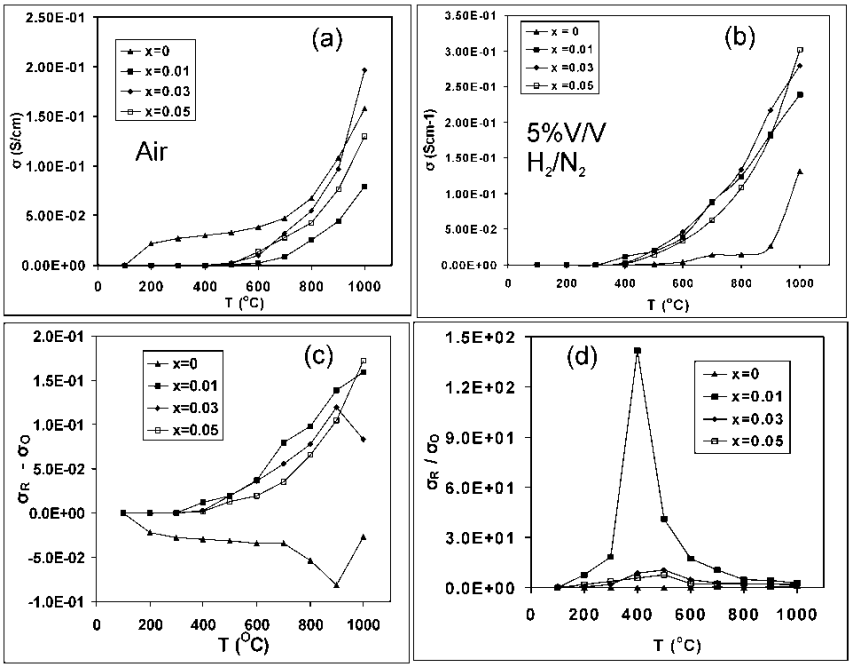

Figure 3.7. Conductivity of $Sm_{1-x}Ce_xFeO_{3-\delta}$ sintered at 1350°C as a function of temperature. (a) and (b) showing electrical conductivity measured in air and 5% v/v H_2/N_2 respectively while (c) and (d) showing ($\sigma_R - \sigma_O$) and σ_R / σ_O respectively as a function of temperature. Note that the solid lines joining the points are used only to guide the eye.

The total conductivity of $Sm_{1-x}Ce_xFeO_{3-\delta}$ was measured as a function of temperature from 25 to 1000 °C in both oxidizing and reducing environments (Figure 3.7a and 3.7b, respectively). The electrical conductivity of all these perovskites increases with temperature, as expected for non-metallic conductors. A closer look at the actual conductivity values indicates that $SmFeO_3$ has higher conductivity in oxidizing than in reducing atmospheres, while the ceria-substituted perovskites showed the opposite trend (Figure 3.7c). These behaviors are typical of p- and n- type semiconductors, respectively [8, 14, 32, 33]. In p-type semiconductors the charge carriers are electron holes. A reducing environment like 5%v/vH_2/N_2 favors the formation of oxygen vacancies[34], as represented by following equation [35]:

$$O_0^x \leftrightarrow \tfrac{1}{2}O_2 + V_0^{\cdot\cdot} + 2e^- \quad (3.3)$$

The oxygen vacancies decrease the number of electron holes by increasing the electron concentration, which causes the lower electrical conductivity of p-type semiconductors [36]. Additionally, the reduction in conductivity of $SmFeO_3$ in the reducing environment could be due to its chemical decomposition; i.e., phase separation of Sm_2O_3 and Fe/Fe_2O_3 under reducing conditions.

On the other hand the ceria doped $SmFeO_3$ perovskites showed higher electrical conductivities in reducing conditions as compared to oxidizing conditions, thereby showing n-type semiconducting behavior. In n-type semiconductors the charge carriers are electrons. The reducing environment increases the number of electrons by increasing oxygen vacancies as shown above in equation (3), thereby increasing their electrical conductivities. These observations indicate that doping $SmFeO_3$ with Ce has changed the behavior of the material from p-type to n-type.

Figure 3.7c and Figure 3.7d show $\Delta\sigma$ ($\sigma_R - \sigma_O$) and σ_R/σ_O as function of temperature. The quality of a good gas sensing material is given by its stability in different environments, a high electrical conductivity at different temperatures, and by a large change in electrical conductivity due to the change in concentration of the sensing gas. The difference and the ratio of conductivities provide measurable sensing quantities for operational devices. Indeed, the 1% ceria doped material has a very high σ_R/σ_O value as compared to all other ceria doped materials and its highest value of σ_R/σ_O corresponds to an operational temperature of 400°C. Thus we expect that these ceria doped $SmFeO_3$ perovskites will show good performance in sensing reducing gases.

These ceria doped perovskites could also be the candidates as mixed ion-electron conductors for anode materials of solid oxide fuel cells because they are stable in reducing conditions at high temperatures and their electrical conductivities are comparable to the titanates like YZT (~ 0.06 to 0.37 S/cm at 800°C to 930°C) [37] and Y/Pr-doped $BaCeO_3$and undoped $BaCeO_3$ (~0.01 to 0.30 S/cm at 800°C) [37, 38] which are being considered as anode materials for SOFC. Figure 3.8 shows the conductivity of $Sm_{1-x}Ce_xFeO_{3-\delta}$ as a function of cerium concentration at 800°C, 900°C and 1000°C. The conductivity values of ceria doped $SmFeO_3$ (0.124-0.30 S/cm at 800°C to 1000°C) fall well in the range of the conductivities of YZT and Y/Pr-doped $BaCeO_3$.

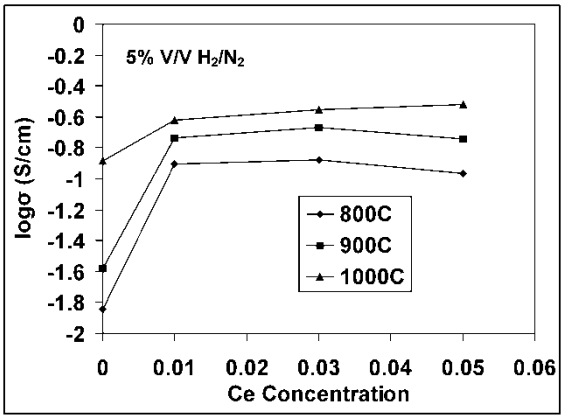

Figure 3.8. Conductivity of $Sm_{1-x}Ce_xFeO_{3-\delta}$ at 800-1000^{0}C as a function of cerium concentration. Note that the solid lines joining the points are used only to guide the eye.

3.4. Conclusions

The effect of ceria doping on thermal stability and conductivity in $SmFeO_3$ was investigated. The solubility limit of Ce is between 5 to 7 atom% on the A-site. The doping of ceria at the A-site in $SmFeO_3$ improves its thermal stability, preventing the phase separation observed in $SmFeO_3$ reduced at 900°C for one hour. The higher conductivity of undoped $SmFeO_3$ in air is due to its p-type semiconducting behavior while higher conductivity of ceria doped $SmFeO_3$ in reducing condition indicates n-type semiconducting behavior. The 3% ceria substituted $SmFeO_3$ has better conductivities than 1% and 5% in both air and reducing conditions. $Sm_{1-x}Ce_xFeO_{3-\delta}$ perovskites show substantial improvement in stability and conductivity making these materials promising as suitable sensors . Since these ceria doped $SmFeO_3$ are stable in reducing environments and have conductivity values which are comparable to most of the titanates that are amongst the most promising anode materials of SOFC, so ceria doped $SmFeO_3$ perovskites have potential of being used as catalyst for oxidation processes, and as anode material for intermediate temperature SOFC.

3.5. References

[1] H. Ulmann, N. Trofimenko, F. Tietz, D. Stover, A. Ahmad-Khanlou, Solid State Ionics. 138 (2000) 79-90.

[2] J. Canales-Vazquez, J.C. Ruiz-Morales, D. Marrero-Lopez, J. Pena-Martinez, P. Gomez-Romero, J. Power Sources. 171 (2007) 552-557.

[3] J.-j. Choi, J.-H. Lee, D.-S. Park, B.-D. Hahn, W.-H. Yoon, J. Am. Ceram. Soc. 90 (2007) 1926-1929.

[4] M.-J. Lee, J.-H. Jun, Jin-Seung, Y.-R. Kim, S.-H. Lee, Bull. Korean Chem. Soc. 26 (2005) 1591-1596.

[5] P. Ciambelli, S. Cimino, S.D. Rossi, L. Lisi, G. Minelli, P. Porta, G. Russo, Appl. Catal. B. 29 (2001) 239-250.

[6] M. Ikeguchi, T. Mimura, Y. Sekine, E. Kikuchi, M. Matsukata, Appl. Catal., A. 290 (2005) 212-220.

[7] Y. Itagaki, M. Mori, Y. Hosoya, H. Aono, Y. Sadaoka, Sens. Actuators, B. 122 (2007) 315-320.

[8] M.C. Carotta, G. Martinelli, Y. Sadaoka, P. Nunziante, E. Traversa, Sens. Actuators B. 48 (1998) 270-276.

[9] X. Niu, W. Du, W. Du, Sens. Actuators B. 99 (2004) 399-404.

[10] M.A. Pena, J.L.G. Fierro, Chem. Rev. 101 (2001) 1981-2017.

[11] Q.T. Wei, R.S. Guo, F.H. Wang, H.L. Li, J. Mater. Sci. 40 (2005) 1317-1319.

[12] M.L. Keith, R. Roy, Am. Mineral. 39 (1954) 1-23.

[13] V.M. Goldschmidt, Oslo, Naturwissenschaften. 14 (1926) 477.

[14] Y. Hosoya, Y. Itagaki, H. Aono, Y. Sadaoka, Sens. Actuators, B. 108 (2005) 198-201.

[15] A. Qi, S. Wang, G. Fu, C. Ni, D. Wu, Appl. Catal. A. 281 (2005) 233-246.

[16] K. Tabata, I. Matsumoto, S. Kohiki, M. Misono, J Mater Sci. 22 (1987) 4031-4035.

[17] H.I. S. Hashmito, J. Electroceram. 4 (2000) 225-231.

[18] S.-i. Hashimoto, H. Iwahara, Mater. Res. Bull. 35 (2000) 2253-2262.

[19] V.V. Vashook, M.V. Zinkevich, Y.G. Zonov, Solid State Ionics. 116 (1999) 129-138.

[20] A.E. Giannakas, A.A. Leontiou, A.K. Ladavos, P.J. Pomonis, Appl. Catal., A. 309 (2006) 254-262.

[21] G. Cairong, F. Guoliang, H. Yanfeng, S. Chonglin, H. Qifei, Z. Zhongrong, Front. Chem. Eng. Chin. 1 (2007) 6-10.

[22] I. MDI Jade 6.1 Software Materials Data. Serial#MDI-R97738 (2002).

[23] E.N. Maslen, V.A. Streltsov, N. Ishizawa, Acta Cryst. B52 (1996) 406-413.

[24] R.D. Shanon, Acta cryst. A32 (1976) 751-767.

[25] N. Fairley, CasaXPS Version 2.3.13 Dev73 ed., Casa Sotware Ltd, 2007.

[26] S.H. Overbury, P.A. Bertrand, G.A. Somorjai, Chem. Rev. 75 (1975) 547.

[27] W.F. Gale, C.J. Smithels, T.C. Totemeier (Eds.), Smithels Metals Refernce Book, 8 ed., Elsvier.

[28] L. Xi, L. Xiaoxun, X. Baokun, Z. Muyu, J. Alloys Compd. 186 (1992) 315-319.

[29] J.L.G. Fierro, L.G. Tejuca, Appl. Surf. Sci. 27 (1987) 453-457.

[30] H. Aono, M. Sato, E. Traversa, M. Sakamoto, Y. Sadaoka, J. Am. Ceram. Soc. 84 (2001) 341-347.

[31] H. Aono, E. Traversa, M. Sakamoto, Y. Sadaoka, Sens. Actuators B. 94 (2003) 132-139.
[32] G. Martinelli, M.C. Carotta, M. Ferroni, Y. Sadaoka, E. Traversa, Sens. Actuators B. 55 (1999) 99-110.
[33] M. Zhao, H. Peng, J. Hu, Z. Han, Sens. Actuators B. 129 (2008) 953-957.
[34] J.N. Kuhn, U.S. Ozkan, Catal. Lett. 121 (2008) 179-188.
[35] J.W. Fergus, Sens. Actuators, B. 123 (2007) 1169-1179.
[36] S.P. Jiang, L. Liu, K.P. Ong, P. Wu, J. Li, J. Pu, J. Power Sources. 176 (2008) 82-89.
[37] J.W. Fergus, Solid State Ionics. 177 (2006) 1529-1541.
[38] T. Hibino, A. Hashimoto, M. Suzuki, M. Sano, J. Electrochem. Soc. 149 (2002) A1503.

4. Performance of Ce doped $SmFeO_3$ perovskite materials as SOFC anodes for direct oxidation of methane and hydrogen

The contents of this chapter have been submitted as: Syed M. Bukhari and Javier B. Giorgi, J. Power Sources (2011)

Abstract

$Sm_{1-x}Ce_xFeO_{3-\delta}$ (x=0-0.05) perovskite materials were investigated as anodes for low-temperature Solid Oxide Fuel Cells (LT-SOFC) using dry hydrogen and dry methane fuels. Ce doping changes the electrical behaviour of $SmFeO_3$ from p-type to n-type and improves the reduction stability under the strong reducing atmosphere required at the anode. The resulting Ce doped materials presented good and stable performances as anodes under hydrogen and methane fuels. The $Sm_{0.95}Ce_{0.05}FeO_{3-\delta}$ anode showed the lowest charge transfer resistances in the series at 700^{o}C, 0.05Ωcm^2 and 1.4Ωcm^2 under dry hydrogen and methane respectively. At 450^{o}C, the $Sm_{0.95}Ce_{0.01}FeO_{3-\delta}$ anode demonstrated performance with an OCV of 0.690V and lowest R_{CT} of 1.5KΩcm^2 under dry methane fuel. More importantly no visible coking was found on the surface of these anodes after the performance under dry methane for ~23h at all temperatures.

4.1. Introduction

Solid oxide fuel cells (SOFC) technology converts chemical energy directly into electrical energy with high efficiency. Hydrogen has been explored as a fuel in SOFCs in the context of zero emission technologies [1-4]. However, SOFC technology may be used with readily available hydrocarbons (such as methane) making it an ideal bridging technology with high efficiency and low pollution. In this line, the deactivation of anodes due to coking has been pointed out as one of the main stumbling blocks [5-8]. To prevent coking on the anode while operating under hydrocarbon fuels, internal steam reforming has been suggested as a viable solution. Nonetheless, this has a detrimental effect on both the fuel efficiency and the power density of the cell, and it requires a heat recovery system for heating steam in the feed gas. A more efficient solution involves the preparation of efficient anode materials for the direct use of hydrocarbons as fuel (without internal steam reforming) to improve fuel efficiency and performance of the SOFC.

Conventional high temperature SOFCs operate with Ni/YSZ cermets as the anode material. The Ni/YSZ anode works well with hydrogen as fuel, but shows long term instability and poisoning from coke and sulphur under hydrocarbon fuels [9-11]. Additionally, the high operational temperature of YSZ-based SOFCs results in high cost for the technology. A recent direction of research has involved the use of ceria-based SOFCs, which can operate at lower temperatures because of the higher ionic conductivity of ceria [12]. Ceria and doped-ceria materials are also useful as anode components because of their mixed oxide ion and electronic conductivity under reducing conditions; an ability for continuous carbon cleaning due to oxygen storage/release; and good electrocatalytic activity for oxidation of methane [8, 13, 14]. However, although doped ceria has been predicted to have the ability to oxidize hydrogen and methane, a more reactive anode with higher electronic conductivity is required [5, 14-16]. It is therefore highly desirable to find anode materials which should enable SOFCs to run at lower temperature, while being resistant towards coke and sulphur under hydrocarbon fuels. The achievement of this target is a milestone in the commercialization of SOFC technology towards cleaner energy production with lower cost and high efficiency.

Perovskite type oxides (ABO_3) have attracted considerable interest as alternative SOFC anodes due to: (i) Mixed electronic and oxide ion conducting nature (ii) Chemical and reduction stability (iii) Catalytic performance (iv) Tuneability i.e., multiple substitutions can be done at A-site, B-site and/or both A-site and B-site to obtain desirable properties [17-23]. Perovskite materials are suitable candidates as anodes for hydrocarbon fuels because their lattice oxygen provides a potential carbon cleaning mechanism depending on the chemical composition of the perovskite[24]. Despite such potential, most of the perovskite materials used to date require mixing of steam (internal steam reforming) with the hydrocarbon fuel to prevent poisoning of the anode due to coking [25-27].

Ce substituted perovskites have been tested as anode and interesting results have been reported. However limited solubility of Ce at the A-site always made a challenge to obtain the perovskite with single phase composition [28]. Marina et al. reported that cerium doped lanthanum strontium titanates have good performance as SOFC anodes but these cerium doped anodes are not single phase perovskites. In fact these materials are combination of ceria and a perovskite phase [29]. Recently our group has reported a new series of

perovskites with composition $Sm_{1-x}Ce_xFeO_{3-\delta}$ (x=0-0.05) [30]. These Ce doped perovskites are single phase with n-type electrical behaviour and their perovskite phase does not decompose under reducing conditions up to 900^{o}C. Their electrical conductivity values are comparable to most of the perovskite anodes under investigation, including YZT (yttrium zirconium titanate) and Y/Pr doped $BaCeO_3$ [31, 32] which indicates their potentials as SOFC anodes. However, these materials are more suitable catalysts for SOFC anodes because they are resistant to coking when exposed to pure methane [33].

In this report, the new Ce doped perovskite materials with composition $Sm_{1-x}Ce_xFeO_{3-\delta}$ (x=0-0.05) have been investigated as SOFC anodes under both dry hydrogen and dry methane fuels. These materials present excellent performance under hydrogen and are resistant to coking under dry methane fuel in the temperature range of 450^{o}C and 700^{o}C.

4.2. Experimental

4.2.1. Powder synthesis

Trimetallic perovskites with formula $Sm_{1-x}Ce_xFeO_{3-\delta}$ (x=0-0.05) were prepared by a sol-gel method using citric acid as a complexing agent [30]. Chemicals used in this sol gel method were iron nitrate [$Fe(NO_3)_3 \cdot 9H_2O$, AlfaAesar, >98%], Cerium nitrate [$Ce(NO_3)_3 \cdot 6H_2O$, AlfaAesar, 99.5%], Samarium nitrate ($Sm(NO_3)_3 \cdot 6H_2O$, AlfaAesar, 99.9%),), and citric acid monohydrate [AlfaAesar, minimum 99.0%]. The three metal nitrates were weighed separately according to the desired stoichiometry keeping A-site and B-site metal ratio 1:1 ($Sm_{(1-x)} + Ce_x$: Fe = 1:1) and solutions were prepared by dissolving in de-ionized water. Citric acid monohydrate was weighed such that the ratio between citric acid and total metal content was 1:1. After dissolving citric acid into de-ionized water, the metal nitrate and citric acid solutions were mixed. This resulting solution was evaporated at 100 °C to form a gel and then dry amorphous citrate precursors. These amorphous citrate precursors were then manually ground and finally calcined at 850 °C for 24 hours to form the perovskite phase. A single phase of the perovskite in each case was confirmed by powder X-ray diffraction.

4.2.2. Button cell fabrication

To test the performance Ce doped perovskite anodes, electrolyte supported button cells were fabricated with a three-electrode geometry. The three-electrode geometry was adopted because it facilitates the separation of the performance of an electrode from the performance of the whole cell. Thus enables the evaluation and comparison of the performance of each perovskite material independently in the series as anodes. In a typical three electrode geometry both counter electrode (CE) and reference electrode (RE) are mounted on one side of electrolyte disc at a reasonable distance while the working electrode (WE) is mounted on the other side. However, one must take into account the alignment of counter and working electrodes while building this geometry because cross talk between electrodes can result in large errors in the measurements [34, 35]. Although this geometry has been largely used by our group and others, we have recently switched to a more symmetrical configuration, as shown in Figure 4.1 [36].

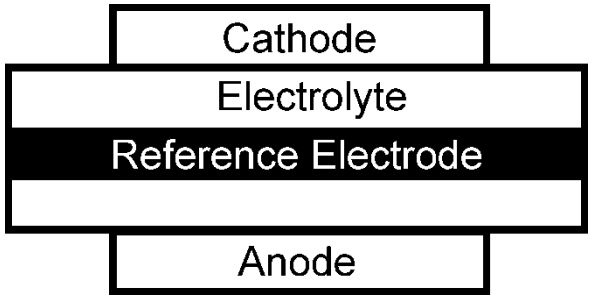

Figure 4.1. Configuration of electrolyte supported button cells with three electrode geometry.

This configuration allows to: (i) Minimize the cross talk between electrodes (ii) Reduce the misalignment problem of CE and WE (iii) Maximize the electrode effective area. However, the increase in thickness of the electrolyte disc results in lower measured values of the cell current and power.

In this three electrode geometry, the electrolyte is a sintered samarium doped ceria pellet of ~2 mm thickness and ~20mm diameter, pure $Sm_{1-x}Ce_xFeO_{3-\delta}$ (x=0-0.05) perovskite materials were used as the anode, and a mixture of LSCF and SDC (50%w/w) was used as the cathode. The reference electrode was a Pt wire wrapped around the electrolyte disc. To

build the multi-electrode assembly, slurries of both anode and cathode materials were prepared in an emulsion (Triton-X100). First the anode slurry was painted and sintered at 1400^{o}C for 4h. A Pt mesh together with a second coating of anode slurry was applied as the current collector and sintered again at 1400^{o}C for 4h. The cathode (LSCF + SDC, 50%w/w) slurry along with a Pt mesh was painted in the same fashion on the other side of electrolyte disc. The effective electrode area was 1.5 cm^{2}. The reference electrode, Pt wire, was wrapped around the electrolyte disc. Pt paste was painted around the Pt wire and dried at 800^{o}C for 1h. It is important to note that the contribution of Pt mesh towards performance of anodes is expected to be negligible due to the very low surface area of the Pt mesh [37].

4.2.3. Fuel Cell Setup

The detail description of the fuel cell setup used for the measurements has been already described elsewhere in the literature (Chapter 7, Chapter 11) [36, 38]. Briefly, the setup includes: one inch customized stainless steel ultratorr and three alumina tubes, one large diameter and other two with small diameter. The bottom part of the large diameter alumina tube is sealed into an ultratorr fitting with the help of a Viton O-ring while its top part supports the button cell. The button cell is sealed on the top of the alumina tube by a Pyrex ring. A small piece of alumina tube is placed at the top of button cell to build a pressure which facilitates a good sealing. A small diameter alumina tube is introduced from bottom of the ultratorr acting as the fuel inlet. This whole set up is suspended vertically with the help of clamps in such a way that the whole fuel cell assembly fits inside a vertically suspended tube furnace. To reduce the background electronic noise which can be introduced by the furnace, a Chromel-shielded quartz tube was placed around the fuel cell and connected to ground. The tube furnace was connected to an Omron E5CN temperature controller and a K-type thermocouple was placed outside of the shielded quartz tube to measure the temperature. Sealing of the button cell on the alumina tube was done by partially melting of the Pyrex ring at 950^{o}C for 1h. Three Pt wires were used as leads and served to connect the three electrodes i.e., CE, WE & RE to a PARSTAT 2273 potentiostat for data collection.

4.2.4. Electrochemical tests

The electrochemical measurements for $Sm_{1-x}Ce_xFeO_{3-\delta}$ (x=0-0.05) perovskite anodes were performed under two fuels: pure hydrogen and pure methane. The flow rate of fuel gas was maintained at 50 sccm with Alicat mass flow controllers. Fuel cells were operated in the

temperature range of 450 to 700 ^{o}C and tested at temperature increments of 50 ^{o}C. A PARSTAT 2273 instrument was used to perform both AC (electrochemical impedance, EIS) and DC (chronoamperometry, CA) measurements. In all measurements a sequence of experiments was used with a total time period of ~23h. The experiments ran in a sequence include: open circuit potential (OCP) measurement, electrochemical impedance measurement at OCP (100 kHz to 100 mHz with an AC amplitude of 10mA), CA experiment for 15h at an overpotential of 0.450V, and a series of CA experiments at different overpotentials from 0V to 1.0V with an increment of 50mV.

The analysis of electrochemical impedance spectra was done by using an equivalent circuit model ($L_1R_S[R_{CT}CPE_1]$) This equivalent circuit provides a serial resistance (R_s) and a charge transfer resistance (R_{CT}) for the anode which can be converted into the exchange current density (i_o) for the processes at the anode by using: $i_o=RT/nFR_{CT}$ where R is universal gas constant, T is temperature, n is number of electron involved in the charge transfer process, F is Faraday constant and R_{CT} is charge transfer resistance. The values of cell current were obtained from CA experiments which were then used to calculate cell powers.

4.3. Results and discussions

4.3.1. Performance under dry hydrogen

In trying to qualify the performance of the $Sm_{1-x}Ce_xFeO_{3-\delta}$ (x=0-0.05) anodes, a comparison with the undoped material is necessary. Previous work has shown that undoped $SmFeO_3$ is a semiconductor with p-type electrical behaviour [39-41] and that it decomposes when exposed to reducing gases at high temperature [30]. These properties make $SmFeO_3$ unsuitable for usage as an SOFC anode and therefore testing was limited to creating a baseline for comparison of the doped perovskites. These results also show that the contribution of the Pt current collectors to the cell performance in negligible. Figure 4.2a shows the results of chronoamperometry measurements in which the cell current was measured as a function of time at an overpotential of 450mV at 700^{o}C under dry hydrogen. The anode performance is observed to decrease rapidly and finally the cell current dropped to zero after ~9h. Similarly the values of the serial and charge transfer resistances after 1h were 33.74 Ωcm^2 and 3.25Ωcm^2, respectively, and increased to 894 Ωcm^2 and 12580 Ωcm^2 after 15h (Figure 4.2b and 4.2c). The low performance of the undoped $SmFeO_3$ anode under

dry hydrogen at the operational temperature can be linked to its very low electrical conductivity under reducing conditions due to its p-type electrical behaviour [30] and the drastic drop in performance as a function of time can be ascribed to its structure degradation [30].

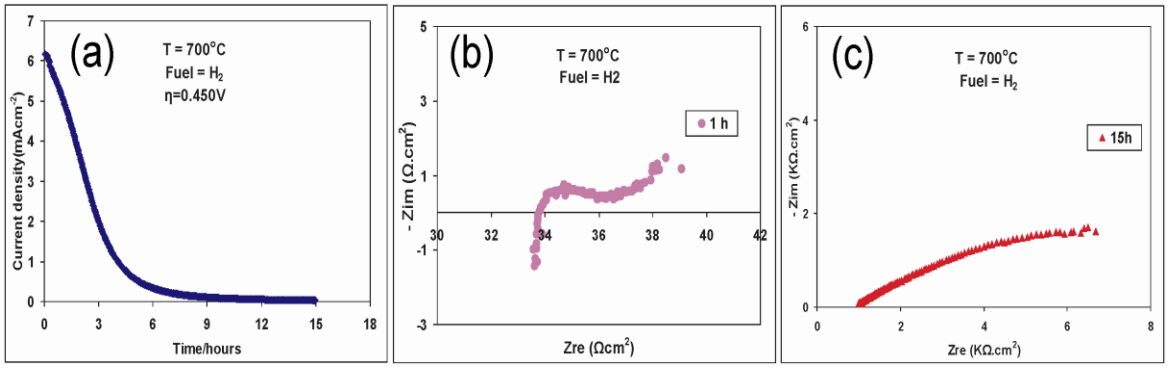

Figure.4.2. Performance of undoped $SmFeO_3$ anode under dry hydrogen fuel (x=0) (a) Current density obtained at an overpotental of 0.450V as a function of time. (b) & (c) Impedance spectra at different times during cell operation.

To evaluate and compare the performance of Ce doped $SmFeO_3$ based anodes, the fuel cells were operated between 450^{o}C and 700^{o}C under dry hydrogen. Experimentally measured open circuit potential values for Ce doped $SmFeO_3$ anodes as a function of temperature are summarized in Table 4.1. The low values of OCP are typical for SOFCs utilizing an SDC electrolyte. This effect has been attributed to a partial permeability of SDC toward oxygen which permit some gas leakage across the electrolyte pellet [42], and a partial reduction of SDC near the surface of the anode under fuel conditions which causes current leakage. The OCP increases with a decrease in temperature as expected according to the Nernst's equation.

Figure 4.3 shows the impedance spectra of $Sm_{1-x}Ce_xFeO_{3-\delta}$ (x=0.01-0.05) anodes at 450^{o}C and 550^{o}C under dry hydrogen as examples (at higher temperatures the arcs are smaller). The impedance plots show the characteristic semicircle for charge transfer, and a Warburg element characteristic of diffusion. The intercept of the semicircle at low frequency is the charge transfer resistance (R_{CT}) or polarization resistance (R_p). The values of charge transfer resistance were determined from fittings of an equivalent circuit model which was

done by using ZSimpWin software version 3.21. The equivalent circuit considers the serial resistance of the circuit (R_s), inductance (L) due to electrical wires, inhomogeneity of the anode surface (constant phase element, Q) and a single anode polarization process which is also called as charge transfer resistance. The overall circuit can be written as $LR_s(R_{ct}Q)$. Results of the fitting showed that the charge transfer resistance decreases not only with increase in temperature but also with increase in Ce content for dry oxidation of hydrogen fuel. The activation energies calculated from Arrhenius plots revealed the same trend i.e., the activation energy decreases with increase in Ce concentration along the series. The activation energy for x=0.01, 0.03 & 0.05 are 104, 92 & 79 kJ/mol, respectively. These Ce doped $SmFeO_3$ anode materials are very good candidates for oxidation of pure hydrogen because they exhibited R_{ct} values less than $1\Omega cm^2$ in the temperature range of 550-700^oC which matches well with the R_{ct} values obtained with other materials operated at higher temperature under wet hydrogen (hydrogen with 3% water contents) [1, 2, 4, 5, 27, 43].

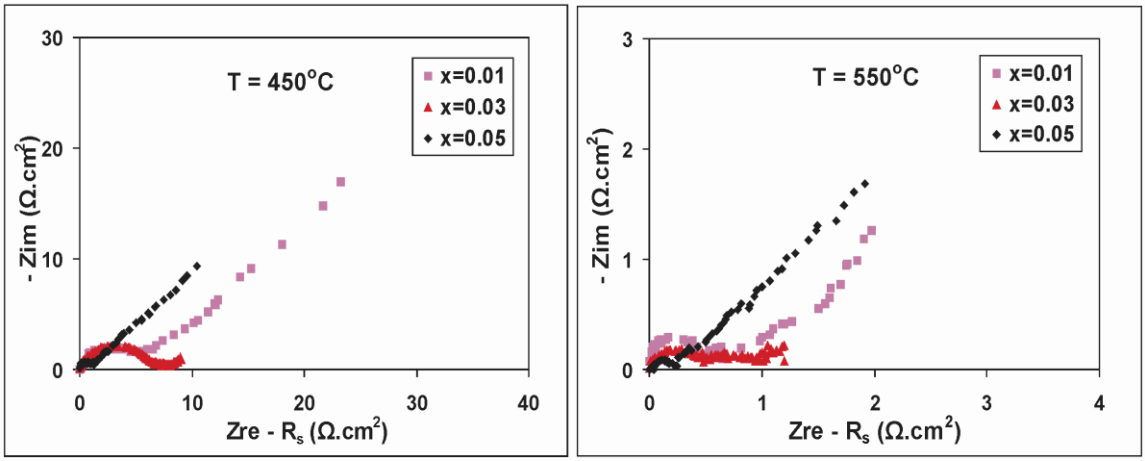

Figure 4.3. Impedance spectra for $Sm_{1-x}Ce_xFeO_{3-\delta}$ (x=0.01-0.05) anodes obtained at 450^oC and 550^oC in dry hydrogen fuel conditions.

The exchange current densities calculated from charge transfer resistances for each anode are presented in Table 4.1. Generally, a lower charge transfer resistance (higher exchange current density) indicates a better performance of the anode. All these Ce doped $SmFeO_3$ based anodes exhibited high values of exchange current densities indicating that these materials are good candidates for SOFC anodes. Indeed, x=0.05 has the best

performance as anode in the series under dry hydrogen fuel. The increase in exchange current densities as a function of Ce content indicates that the introduction of Ce into the lattice of $SmFeO_3$ has actually improved its catalytic performance towards dry hydrogen oxidation.

Table 4.1: Open circuit potentials (OCP), charge transfer resistances (R_{CT}) and exchange current densities (i_o) of $Sm_{1-x}Ce_xFeO_{3-\delta}$ (x=0.01-0.05) anodes obtained from impedance analysis under dry hydrogen fuel.

T°C	**x=0.01**		**x=0.03**		**x=0.05**	
	OCP (V)	**R_{CT} (Ω.cm^2)**	**OCP (V)**	**R_{CT} (Ω.cm^2)**	**OCP (V)**	**R_{CT} (Ω.cm^2)**
450	0.977	12.9 ± 2 (5 ± 1)[a]	0.957	7.9 ± 1 (8 ± 1)[a]	0.986	1.77 ± 0.3 (35 ± 5)[a]
500	0.973	4.42 ± 0.7 (15 ± 2)[a]	0.980	2.6 ± 0.4 (25 ± 2)[a]	0.974	0.64 ± 0.1 (103 ± 15)[a]
550	0.956	1.47 ± 0.2 (48 ± 7)[a]	0.974	0.87 ± 0.13 (82 ± 12)[a]	0.960	0.29 ± 0.04 (248 ± 37 [a]
600	0.927	0.35 ± 0.05 (215 ± 32)[a]	0.948	0.30 ± 0.04 (248 ± 37)[a]	0.924	0.15 ± 0.02 (497 ± 74)[a]
700	0.863	0.20 ± 0.03 (430 ± 64)[a]	0.869	0.14 ± 0.02 (595 ± 89)[a]	0.844	0.05 ± 0.01 (1663 ±249)[a]

[a] exchange current densities in $mAcm^{-2}$ calculated from the charge transfer resistances

In order to determine the reduction stability of these Ce doped $SmFeO_3$ based anodes, the cell current was measured at an overpotential of 0.450V under dry hydrogen fuel for 15h in each case. Figure 4.4 shows the cell powers calculated from cell currents at different temperatures. Careful analysis shows that the values of cell powers in each case remained stable for 15h. From this we inferred that, unlike $SmFeO_3$, these Ce doped perovskite anodes did not suffer from perovskite phase decomposition while working under the strongly reducing atmosphere of the anode chamber. This fact was further confirmed by XRD analysis of the anodes after performance, where the single perovskite phase was observed. This reduction stability of Ce doped $SmFeO_3$ perovskite materials has been described in terms of the bigger size of the Ce cation as compared to Sm [30]. In general, the bigger the

size of the A-site cation in the perovskite structure, the greater the reduction stability of the perovskite.

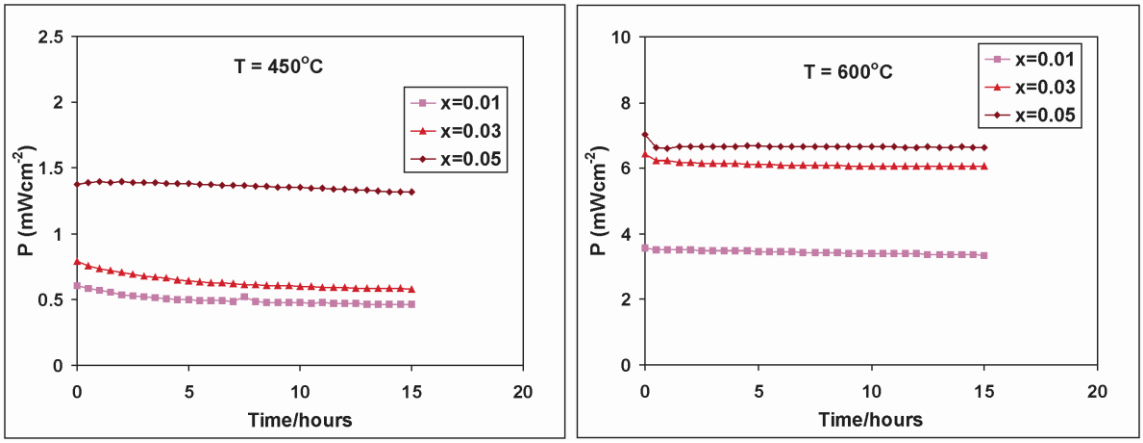

Figure 4.4. Performance of $Sm_{1-x}Ce_xFeO_{3-\delta}$ (x=0.01-0.05) anodes under dry hydrogen fuel. Cell powers calculated from current density obtained at an overpotential of 0.450V as a function of time

In Figure 4.5, I-V and P-I curves for $Sm_{1-x}Ce_xFeO_{3-\delta}$ (x=0.01-0.05) anodes are shown at different temperatures. The P_{max} and I_{max} follow the same performance trends as shown by electrochemical impedance data. The values of both P_{max} and I_{max} have increasing trends as a function of both the temperature and Ce concentration. In the series, x=0.05 has highest values of both P_{max} and I_{max}. It is important to remember that the values of P_{max} and I_{max} obtained in this work are low due to our cell design (use of very thick electrolyte) but comparison between materials is pertinent and allows selection of the best anode candidate.

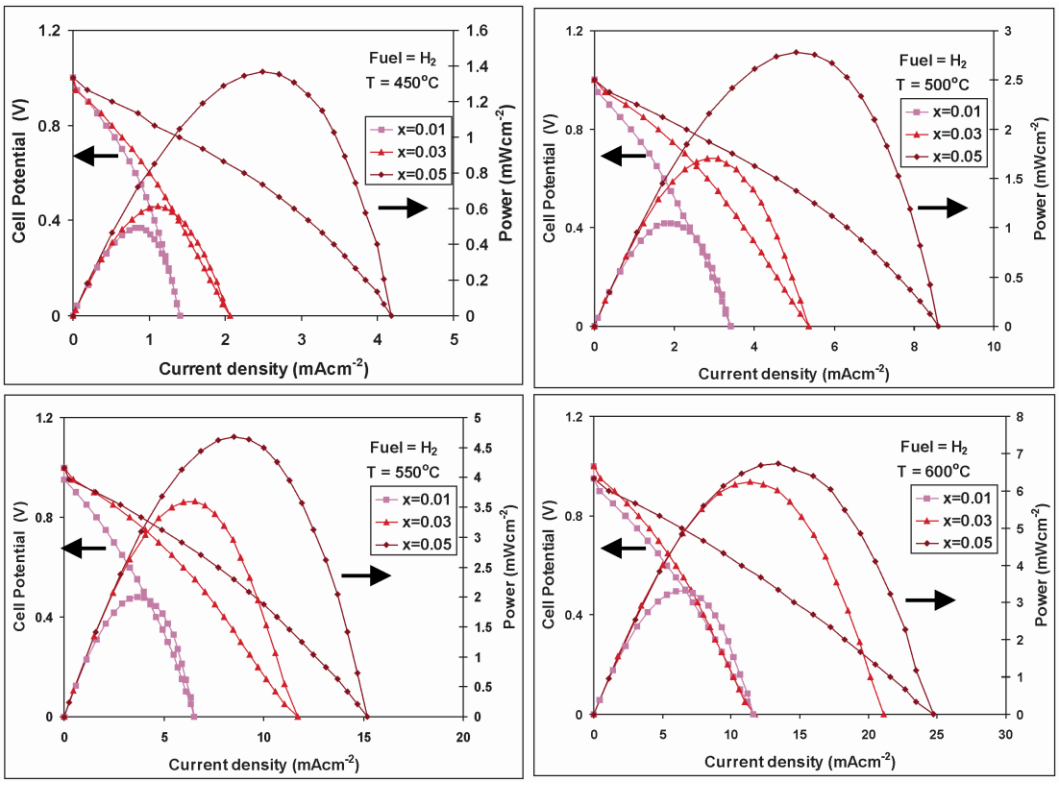

Figure 4.5. I-V and I-P curves of the $Sm_xCe_{1-x}FeO_{3-\delta}$ (x=0.01, 0.03 and 0.05) anodes under dry hydrogen fuel at different temperatures.

4.3.2. Performance under dry methane.

Experimentally measured OCP values of fuel cells based on $Sm_xCe_{1-x}FeO_{3-\delta}$ (x=0.01, 0.03 and 0.05) anodes under dry methane fuel are given in Figure 4.6a. As expected, the OCP values are considerably lower than those measured under hydrogen due to relatively less reactive nature of methane as compared to hydrogen. Interestingly, the experimentally measured OCP values are also lower than the theoretically expected OCP values. This observation has been attributed to lower densification and internal shorting due to the mixed conductor behaviour of the SDC electrolyte in anodic conditions [42, 44-46]. The observation of low OCP values at all operational temperatures as compared to theoretical Nernst's potentials suggested that it is the intrinsic property of the system and not due to the experimental set up. The open circuit potentials presented a non linear trend as a function of both temperature and cerium content which can be attributed to multiple step oxidation of hydrocarbons (methane in this case) on the surface and establishment of an equilibrium

between the hydrocarbons and partial oxidation products [47]. This also suggests different mechanisms of methane oxidation on each anode at different temperatures.

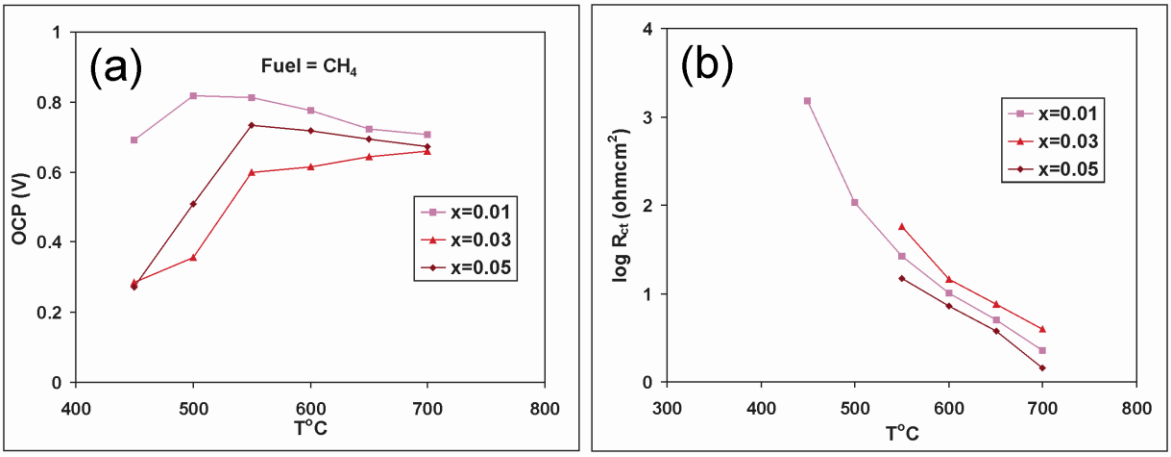

Figure 4.6. (a) OCP of fuel cells (b) Charge transfer resistances of $Sm_xCe_{1-x}FeO_{3-\delta}$ (x=0.01, 0.03 and 0.05) anodes under dry methane fuel as a function of temperature.

Under dry methane fuel conditions, it is expected that methane directly oxidizes on the anode consuming oxide ions (equation 4.1).

$$CH_4 + 4O^{2-} \rightleftharpoons CO_2 + 2H_2O + 8e^- \qquad (4.1)$$

This reaction may occur in multiple steps following a Bagotzky type mechanism (Figure 4.7) where the removal of H and the addition of O to the methane may occur in a variety of mechanistic sequences [48].

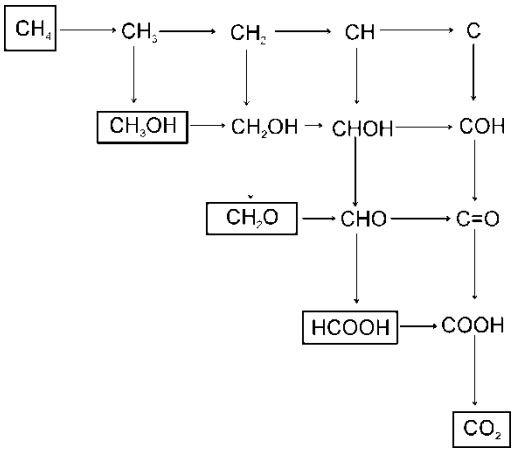

Figure 4.7. Bagotzky type mechanism, showing various pathways and intermediate products that can be formed during oxidation of methane.

Along the way, the mechanism may yield reactions that produce secondary (undesired) products including methanol (CH_3O), methanal (CH_2O), formic acid (HCOOH) etc. One of most likely reactions involves the partial oxidation of methane to form CO along with water (equation 4.2). Additionally, methane can also undergo thermal decomposition to form carbon and hydrogen (equation 4.3).

$$CH_4 + 3O^{2-} \rightleftharpoons CO + 2H_2O + 6e^- \quad (4.2)$$

$$CH_4 \rightleftharpoons C + 2H_2 \quad (4.3)$$

However these by-products may be prevented from accumulating if they undergo electrochemical oxidation (equations 4.4 and 4.5).

$$C + O^{2-} \rightleftharpoons CO + 2e^- \quad (4.4)$$

$$CO + O^{2-} \rightleftharpoons CO_2 + 2e^- \quad (4.5)$$

From the above reactions, it is possible that the different OCPs that were observed are due to the contribution of each reaction in different proportions. Furthermore, the extent of contribution of each reaction depends solely on the catalytic properties of the anode materials which in turn are temperature dependent.

Electrochemical impedance plots for Ce doped $SmFeO_3$ based anodes obtained under dry methane fuel are shown in Figure 4.8 while the values of charge transfer resistance obtained after electrochemical impedance analysis of these plots are presented as a function of temperature in Figure 4.6b. The values of charge transfer resistance for dry methane oxidation are higher than the charge transfer resistances of these anode materials for dry hydrogen oxidation. This can be attributed to the lower reactivity of methane as compared to hydrogen in heterogeneous oxidation [49]. Furthermore, relatively high activation values for methane oxidation revealed that these anode materials are less reactive towards methane oxidation. The values of activation energy calculated from the Arrhenius plots for x=0.01, 0.03 and 0.05 are 108, 117 & 102 kJ/mol, respectively.

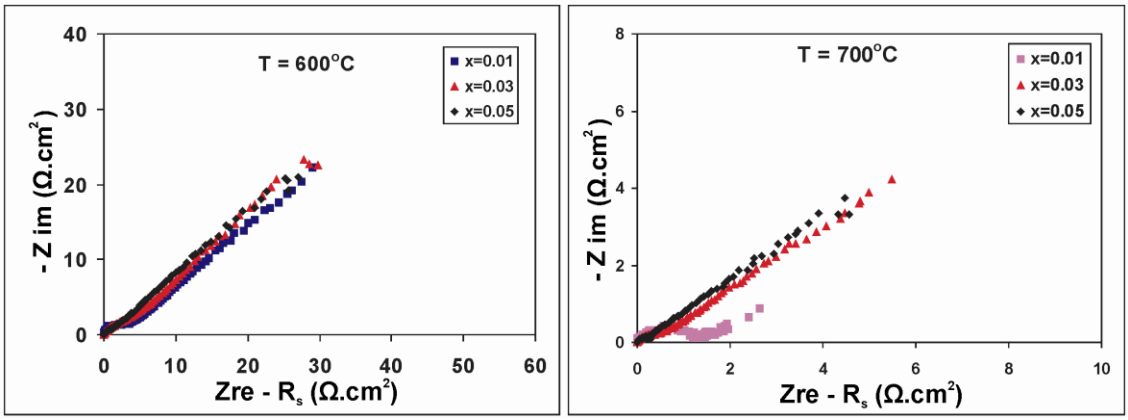

Figure 4.8. Impedance spectra for $Sm_{1-x}Ce_xFeO_{3-\delta}$ (x=0.01-0.05) anodes obtained at 600°C and 700°C under dry methane fuel condition.

The values of charge transfer resistances have a linear trend with respect to the temperature, however, as a function of Ce contents, the trend was found to be non-linear. Indeed, the anode with 5%Ce has the lowest charge transfer resistance in the series suggesting that this anode material has the best performance as anode under dry methane fuel. The charge transfer resistance values of these anodes for dry methane oxidation (1-7 Ω cm^2 at 650-700°C) are comparable with previously tested anodes under wet methane at higher temperatures [5, 25, 50-52]. So these Ce doped $SmFeO_3$ anode materials have the potential to oxidize methane fuel in SOFC at lower temperatures.

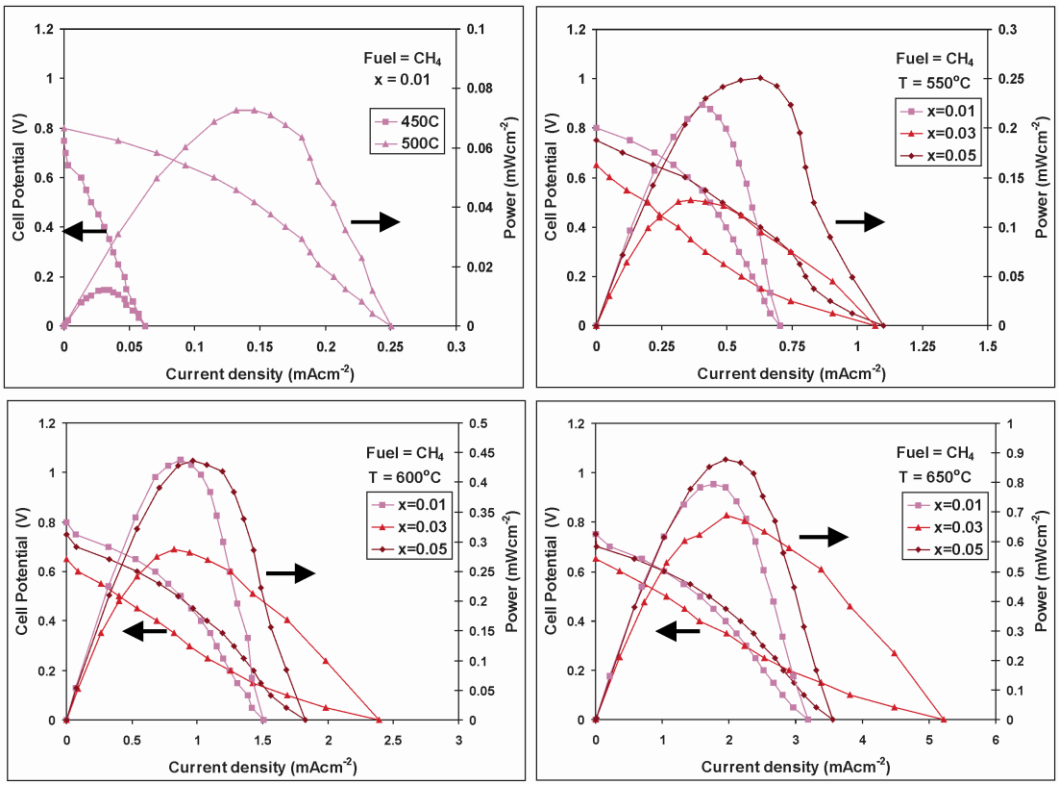

Figure 4.9. I-V and I-P curves of the $Sm_xCe_{1-x}FeO_{3-\delta}$ (x=0.01, 0.03 and 0.05) anodes under dry methane fuel at different temperatures.

The relationships of cell powers and currents with cell voltage for SOFC using $Sm_xCe_{1-x}FeO_{3-\delta}$ (x=0.01, 0.03 and.05) anodes under dry methane at different temperatures are given in Figure 4.9. At lower temperatures (450 and 500°C), only fuel cell operating with the x=0.01 anode offered a reasonably high OCP. However, the values of cell power and current were low and the cells had high values of impedance resistances. At higher temperatures (550-700°C) the cell powers and currents presented the same trend as a function of Ce contents as previously shown by charge transfer resistances. On the other hand, the cell powers and currents of the SOFC based on these Ce doped anodes gradually increase with increase in temperature.

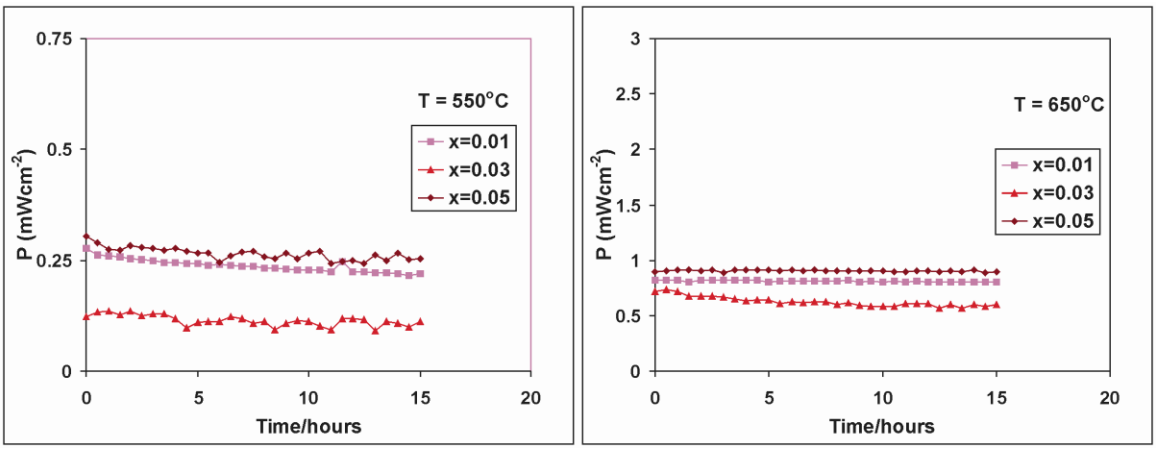

Figure 4.10. Performance of $Sm_{1-x}Ce_xFeO_{3-\delta}$ (x=0.01-0.05) anodes under dry methane fuel for 15h. Cell powers calculated from current density obtained at an overpotential of 0.450V as a function of run time.

Figure 4.10 presents the performance of the fuel cells for 15h under dry methane. The cell currents were measured against an overpotential of 0.450V yielding the power shown. The values of cell power remained stable during the course of the test showing no significant degradation or coke poisoning. The low values of cell currents and powers can be ascribed to the design of the button cell (i.e. a three electrode geometry with a very thick electrolyte). Most importantly, values of cell power showed an increasing trend with temperature, while they varied non-linearly as a function of Ce contents.

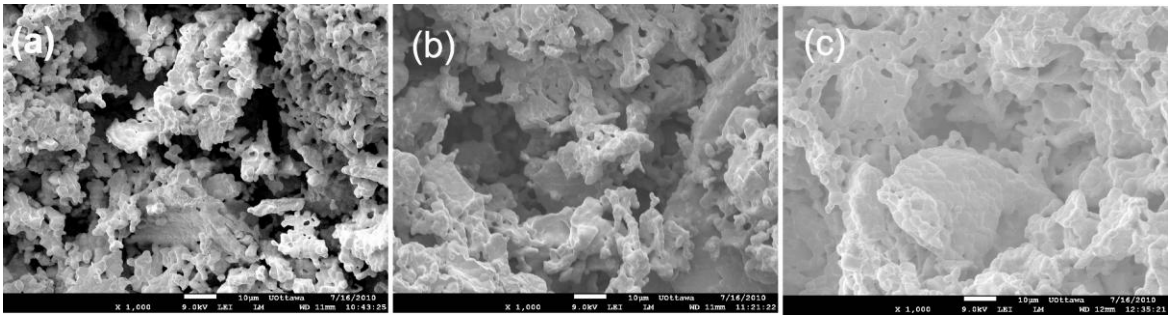

Figure 4.11. SEM micrographs of $Sm_{1-x}C\ e_xFeO_{3-\delta}$ (x=0.01-0.05) anodes after performance of 23h under dry methane.

The potential for coke poisoning was also checked by the direct observation of the anode post-mortem (after operation under dry methane fuel for 23 h). Figure 4.11 shows the SEM micrographs of used anodes. The images show that the anodes remained clear; no typical formation of carbon tubes or deposits was observable. This observation strongly suggests that these materials are resistant to coke formation and will aid to developing technology for the formation of coke resistant anodes for SOFC.

4.4. Conclusions

Ce doped $SmFeO_3$ perovskite materials have been synthesized by a sol gel combustion method using citric acid as a complexing agent. The resulting $Sm_{1-x}Ce_xFeO_{3-\delta}$ materials were examined as anodes for SOFCs under both dry hydrogen and dry methane separately. Undoped $SmFeO_3$ material is an unviable candidate as an SOFC anode due to its p-type electrical behaviour and reduction instability under fuel atmospheres. Ce doping not only provided reduction stability but it also changed the electrical behaviour of the resulting perovskites to n-type. The new $Sm_{1-x}Ce_xFeO_{3-\delta}$ (x=0.01-0.05) materials have good performance as anodes under both dry hydrogen and dry methane fuels. Indeed, the x=0.05 material presented the best performance in the series under both dry hydrogen and dry methane fuels. The x=0.05 anode material was able to operate under dry hydrogen at temperatures as low as 450^oC with reasonably good performance. Furthermore under dry methane fuel, x=0.05 exhibited significantly lower charge transfer resistances (7-1.5$\Omega.cm^2$) at intermediate temperatures (600-700^oC). In light of these results, $Sm_{1-x}Ce_xFeO_{3-\delta}$, and the x=0.05 anode material in particular, provide an important step forward toward reduction of fabrication costs of SOFCs by lowering their operational temperature under both dry hydrogen and dry methane fuels.

4.5. References

[1] J.C. Ruiz-Morales, J. Canales-Vazquez, B. Ballesteros-Perez, J. Pena-Martinez, D. Marrero-Lopez, J.T.S. Irvine, P. Nunez, J. Eur. Ceram. Soc., 27 (2007) 4223.

[2] L. Deleebeeck, J.L. Fournier, V. Birss, Solid State Ionics, 181 (2010) 1229.

[3] B.H. Smith, M.D. Gross, Electrochem. Solid-State Lett., 14 (2011) B1.

[4] A. Babaei, L. Zhang, S.L. Tan, S.P. Jiang, Solid State Ionics, 181 (2010) 1221.

[5] A. Fuerte, R.X. Valenzuela, M.J. Escudero, L. Daza, J. Power Sources, 196 (2011) 4324.

[6] B. Huang, X.F. Ye, S.R. Wang, H.W. Nie, J. Shi, Q. Hu, J.Q. Qian, X.F. Sun, T.L. Wen, J. Power Sources, 162 (2006) 1172.

[7] J. Sfeir, P.A. Buffat, P. Möckli, N. Xanthopoulos, R. Vasquez, H.J. Mathieu, J.V. herle, K.R. Thampi, J Catalysis, 202 (2001) 229.

[8] A. Atkinson, S. Barnett, R.J. Gorte, J.T.S. Irvine, A.J. McEvoy, M. Mogensen, S.C. Singhal, J. Vohs, Nature Materials, 3 (2004) 17.

[9] J. Liu, V. Birss, J. Hill, AlChE Journal, 56 (2010) 1651.

[10] Y. Lin, Z. Zhan, J. Liu, S.A. Barnett, Solid State Ionics, 176 (2005) 1827.

[11] L. Yang, Z. Cheng, M. Liu, L. Wilson, Energy Environ. Sci., 3 (210) 1804.

[12] C. Xia, F. Chen, M. Liu, Electrochem. Solid-State Lett., 4 (2001) A52.

[13] J.B. Wang, J.-C. Jang, T.-J. Huang, J Power Sources, 122 (2003) 122.

[14] A.A. Yaremchenko, V.V. Kharton, A.A. Valente, E.V. Frolova, M.I. Ivanovskaya, A.V. Kovalevsky, F.M.B. Marques, J. Rocha, Catal. Lett., 112 (2006) 19.

[15] D. Knapp, T. Ziegler, J Phys. Chem. C, 112 (2008) 17311.

[16] N.M. Galea, D. Knapp, T. Ziegler, J Catalysis, 247 (2007) 20.

[17] D.P. Fagg, V.V. Kharton, A.V. Kovalevsky, A.P. Viskup, J. Eur. Ceram. Soc., 21 (2001) 1831.

[18] A.E. Giannakas, A.A. Leontiou, A.K. Ladavos, P.J. Pomonis, Appl. Catal., A, 309 (2006) 254.

[19] T. Ishihara, H. Furutani, M. Honda, T. Yamada, T. Shibayama, T. Akbay, N. Sakai, H. Yokokawa, Y. Takita, Chem. Mater., 11 (1999) 2081.

[20] T. Ishihara, T. Yamada, H. Arikawa, H. Nishiguchi, Y. Takita, Solid State Ionics, 135 (2000) 631.

[21] V.V. Kharton, A.P. Viskup, E.N. Naumovich, N.M. Lapchuk, Solid State Ionics, 104 (1997) 67.

[22] C. Li, K. Chi, K. Soh, P. Wu, J. Alloys Compd., 372 (2004) 40.

[23] M.A. Pena, J.L.G. Fierro, Chem. Rev., 101 (2001) 1981.

[24] K. Urasaki, Y. Sekine, S. kawabe, E. Kikuchi, M. Matsukata, Appl. Catal. A, 286 (2005) 23.

[25] E. Lay, G. Gauthier, S. Rosini, C. Savaniu, J.T.S. Irvine, Solid State Ionics, 179 (2008) 1562.

[26] P. Vernoux, M. Guillodo, J. Fouletier, A. Hammou, Solid State Ionics, 135 (2000) 425.

[27] S. Tao, J.T.S. Irvine, J. Electrochem. Soc., 151 (2004) A252.

[28] A. Qi, S. Wang, G. Fu, C. Ni, D. Wu, Appl. Catal. A, 281 (2005) 233.

[29] O.A. Marina, L.R. Pederson, in Proceeding of the 5th European Solid Oxide Fuel Cell Forum,J. Huijsmans, Editor, pp. 481-489, European SOFC Forum, Switzerland (2002).

[30] S.M. Bukhari, J.B. Giorgi, Solid State Ionics, 180 (2009) 198.

[31] J.W. Fergus, Solid State Ionics, 177 (2006) 1529.

[32] T. Hibino, A. Hashimoto, M. Suzuki, M. Sano, J. Electrochem. Soc., 149 (2002) A1503.

[33] S.M. Bukhari, J.B. Giorgi, ECS Trans., 28 (2010) 19.

[34] J. Winkler, P.V. Hendriksen, N. Bonanos, M. Mogensen, J. Electrochem. Soc., 145 (1998) 1184.

[35] S. McIntosh, J.M. Vohs, R.J. Gorte, J. Electrochem. Soc., 150 (2003) A1305.

[36] S.M. Bukhari, J.B. Giorgi, ECS Trans., 33 (2010) 81.

[37] C.M. Grgicak, J.B. Giorgi, J. Phys. Chem. C, 111 (2007) 15446.

[38] S.M. Bukhari, J.B. Giorgi, ECS Trans., 35 (2011) 1539.

[39] Y. Itagaki, M. Mori, Y. Hosoya, H. Aono, Y. Sadaoka, Sens. Actuators, B, 122 (2007) 315.

[40] M.C. Carotta, G. Martinelli, Y. Sadaoka, P. Nunziante, E. Traversa, Sens. Actuators B, 48 (1998) 270.

[41] Y. Hosoya, Y. Itagaki, H. Aono, Y. Sadaoka, Sens. Actuators, B, 108 (2005) 198.

[42] H. Shi, W. Zhou, R. Ran, Z. Shao, J. Power Sources, 195 (2010) 393.

[43] N.E. Kiratzis, P. Connor, J.T.S. Irvine, J. Electroceram., 24 (2010) 270.

[44] T. Miyashita, J. Mater. Sci., 40 (2005) 6027.

[45] T. Miyashita, The Open Materials Science Journal, 3 (2009) 33.

[46] X. Zhang, M. Robertson, C. Deces-Petit, W. Qu, O. Kesler, R. Maric, D. Ghosh, J. Power Sources, 164 (2007) 668.

[47] O.A. Marina, M. Mogensen, Appl. Catal. A, 189 (1999) 117.

[48] V.S. Bagotzky, Y.B. Vassiliev, O.A. Khazova, J. Electroanal. Chem., 81 (1977) 229.

[49] R.J. Farrauto, M.C. Hobson, T. Kennelly, E.M. Waterman, Appl. Catal. A, 81 (1992) 227.

[50] B.H. Smith, M.D. Gross, Electrochem. Solid-State Lett., 14 (2011) B1.

[51] J. Qiao, N. Zhang, Z. Wang, Y. Mao, K. Sun, Y. Yuan, Fuel Cells, 09 (2009) 729.

[52] D.N. Miller, J.T.S. Irvine, ECS Trans., 7 (2007) 1447.

5. Synthesis and characterization of $Sm_{0.95}Ce_{0.05}Fe_{1-x}Co_xO_{3-\delta}$ (x=0-0.10) perovskite oxides

The contents of this chapter have been published as: Syed M. Bukhari and Javier B. Giorgi, Solid State Ionics, 181 (2010) 392-401

Abstract

A series of cobalt doped $Sm_{0.95}Ce_{0.05}FeO_{3-\delta}$ perovskites with formula $Sm_{0.95}Ce_{0.05}Fe_{1-x}Co_xO_{3-\delta}$ (x=0 - 0.10) were prepared by thermal decomposition of amorphous citrate precursors followed by calcination at 850°C in air for 24 hours. These materials are stable in air even at 1350°C and under reducing conditions (5% v/v H_2/N_2) up to ~800 °C, when phase separation ensues. Their conductivities were measured both in air and H_2/N_2 by the four point probe method from 25°C to 1000°C. The electrical conductivities increased from x=0 to x=0.10 in air with an increase in both temperature and cobalt concentration but in H_2/N_2 the trend is nonlinear. The higher conductivity in air is due to oxygen vacancies created as a result of cobalt doping. Improved conductivity of $Sm_{0.95}Ce_{0.05}Fe_{1-x}Co_xO_{3-\delta}$ in 5%v/v H_2/N_2 as compared to air is as high as two orders of magnitude. The specific species responsible for the sensing behaviour (conductivity changes) is unclear, but the surface analysis by XPS showed that all these materials have a samarium rich surface. The potential sensing ability of these materials toward reducing atmospheres was probed with variable concentrations of H_2/N_2 gas. A linear and reversible response was observed with high sensitivity at room temperature.

5.1. Introduction

Perovskites of the type ABO_3, have shown great technological versatility due to their variable physical properties. Substituted perovskites have shown properties that can be tailor-made to the needs of the application. The nature and amount of cations A and B play a key role in imparting specific properties to these compounds. The partial substitution of A and B cations allows the fine tuning of properties such as ionic and electronic conductivity, thermal expansion, chemical stability and reactivity. For this reason, these materials are being extensively used in a large number of technologies including gas sensors[1-9], solid oxide fuel cells [10-19], and catalytic partial oxidation reactions [20].

$SmFeO_3$ is one of the rare earth orthoferrites that is being used as a sensor for oxidizing gases like O_3 and NO_2 due to its p-type semiconductivity [21-24]. However, the reducibility and lower electrical conductivity of $SmFeO_3$ in reducing environments has limited its use to only oxidizing gas sensor applications. In previous work [25] we have reported that the partial substitution of Sm by Ce within the solubility limit not only improves electrical conductivity of the perovskite, but also prevents it from decomposing under reducing conditions, thus creating the possibility of using ceria doped $SmFeO_3$ as a gas sensor for reducing gases like CO.

Partial substitution at the B-site is also expected to affect the thermal stability and the electrical conductivity. A stronger B-O bond is expected to provide greater stability to the perovskite structure under reducing conditions [26]. The electrical conductivity of perovskite type oxides is greatly influenced by the B-site dopant due to its ability to form oxygen vacancies. In general the formation of oxygen vacancies increases with increasing temperature, with reducing nature of the environment, by doping the trivalent A-site with divalent cations, and by doping the B-site cation with more reducible cations [27]. Cobalt has been found to be a reducible element that easily induces vacancy formation by substitution at the B-site in ferrite substituted perovskites. The effect of cobalt substitution on $SmFeO_3$ has been recently explored for its electrical conductivity [28, 29], particularly as applied to ozone (O_3) and NO_2 sensing [8]. Cobalt doping improves the conductivity of $SmFeO_3$ under oxidizing conditions but reduces its chemical stability under reducing conditions. This reducibility issue is due to the fact that the bond between cobalt and oxygen is weaker than the bond between iron and oxygen [26]. The presence of Co makes the resulting perovskite more susceptible to phase separation due to formation of Fe^0, Co^0 and Fe-Co alloys, often with the complete destruction of the perovskite [27, 30-32].

In this current work, we took advantage of the increased stability of the perovskite induced by the introduction of Ce at the A-site [25], to manipulate the electrical conductivity by doping with Co at the B-site of $Sm_{0.95}Ce_{0.05}FeO_3$. We prepared perovskites with formula $Sm_{0.95}Ce_{0.05}Fe_{1-x}Co_xO_{3-\delta}$ ($0 \leq x \leq 0.10$, δ may be positive or negative [33-35]) by partial substitution of Co at Fe in $Sm_{0.95}Ce_{0.05}FeO_{3\pm\lambda}$ and studied the resulting perovskites in terms of their thermal stability and electrical conductivity under both oxidizing and reducing conditions. Phase purity, structural stability both under oxidizing and reducing conditions and surface properties were determined by

using X-ray diffraction (XRD), X-ray photoelectron spectroscopy (XPS) and X-ray flourescence. The total conductivity was determined by the four probe method and trends are discussed as a function of cobalt content. The potential of $Sm_{0.95}Ce_{0.05}Fe_{1-x}Co_xO_{3-\delta}$ as a gas sensor is also explored.

5.2. Experimental

5.2.1. Synthesis

Cobalt doped $Sm_{0.95}Ce_{0.05}$ Fe $O_{3-\delta}$ powders were prepared using the sol gel method, which involves the thermal decomposition of amorphous citrate precursors. The chemicals used in the synthesis include samarium nitrate ($Sm(NO_3)_3.6H_2O$, Alfa Aesar, 99.9%), cerium nitrate ($Ce(NO_3)_3 \cdot 6H_2O$, Alfa Aesar, 99.5%), iron nitrate ($Fe(NO_3)_3 \cdot 9H_2O$, Alfa Aesar, minimum 98%), cobalt nitrate ($Co(NO_3)_2 \cdot 6H_2O$, Alfa Aesar, 99%) and citric acid monohydrate (minimum 99.0%). Separate solutions of samarium nitrate, cerium nitrate, iron nitrate and cobalt nitrate were prepared according to the desired stoichiometry in de-ionized water. In the whole synthesis process the sum of the moles of Sm and Ce was set to unity. The same is true for Fe and Co. The solution of citric acid was prepared by keeping the ratio of citric acid to total metal ion at unity. The solutions of metal nitrates and citric acid were mixed. Amorphous citrate precursors were obtained on drying the solution at 100°C. The resulting amorphous citrates were then ground and finally calcined at 850°C for 24 hour to form the perovskite structures.

5.2.2. Characterization

X-ray diffraction (XRD, Phillips PW 1830) analyses were carried out to determine the phase composition and the crystallite sizes using CuK_α radiation with a wavelength of 1.54 Å. The scans were measured in the range of $2\theta = 13°$ to 90° at a scan rate of 0.02°/sec. The crystalline phase was assigned using the Powder Diffraction File database (ICDD/JCPDS, 2001, Dataset 1-99). Lattice parameters were measured after theta calibration with SrO as the internal standard. Peak refinements were performed using Jade 6.1 software.

The nominal stoichiometry of each perovskite was verified by determining the exact composition using X-ray fluorescence (Philips PW2400/00). Quantities of Sm, Ce Co and Fe in each sample were determined using a calibration curve consisting of a concentration gradient of Sm_2O_3, CeO_2 Co_3O_4 and Fe_2O_3. The BET surface areas of all samples were determined by using

a Quantachrome Autosorb 1-C instrument using nitrogen as the vector gas. The surface composition of the materials was characterized by X-ray photoelectron spectroscopy (XPS; Kratos AXIS Ultra^{DLD} 39-3061) using a monochromatic Al source with pass energy of 80 eV and a dwell time of 200 ms.

The four-probe DC method was used to determine the total conductivities of each perovskite in air and in 5% v/v H_2/N_2, in the temperature range of 25-1000°C. For these measurements, the materials were pelleted by uniaxially pressing 2 g of powder of each perovskite to 22.3 MPa (15000 lbs) and sintering the pellet in air at 1350°C for four hours with a ramp of 2°C/min during heating and cooling. The final density of the pellets was measured as 1.95±0.15 g/cm^3, as measured by the Archimedes method. Current measurements were often performed for multiple heating and cooling cycles. During initial heating, current measurements were not considered reliable due to desorption processes and degassing of the furnace itself. For that reason, subsequent current measurements were taken at least during subsequent cooling (1000°C to 25°C) and heating (25°C to 1000°C) to ensure overlapping curves, which indicates that, the material is at equilibrium throughout the measurement process.

The sensing behavior of the most promising perovskite (x = 0.03) was tested by measuring the total conductivity of the material by the four-probe method at 400°C and at room temperature under conditions of flowing air, flowing N_2 and flowing 1- 5% H_2/N_2 (v/v), flow rate = 50 SCCM.

5.3. Results and discussions

5.3.1. Bulk structure

The quantitative elemental composition of the cobalt doped perovskites was experimentally confirmed by using X-ray florescence. Table 5.1 shows the quantification of $Sm_{0.95}Ce_{0.05}Fe_{1-x}Co_xO_{3-\delta}$ obtained from X-ray florescence spectroscopy. The calibration curve was obtained by using Co_3O_4, CeO_2, Sm_2O_3 and Fe_2O_3, which were obtained by thermal decomposition of $Co(NO_3)_3 \cdot 6H_2O$, $Ce(NO_3)_3 \cdot 6H_2O$, $Sm(NO_3)_3 \cdot 6H_2O$ and $Fe(NO_3)_3 \cdot 9H_2O$ respectively. The stoichiometric ratios between metal atoms obtained experimentally are in good agreement with the expected composition based on the synthesis quantities. The oxygen composition is obtained

from the balance of the sample mass and the percent composition of all the metals. The discrepancy to the expected composition is 1-2%, within the error of the measurement.

Table 5.1. Elemental quantification of $Sm_{0.95}Ce_{0.05}Fe_{1-x}Co_xO_{3-\delta}$ obtained from XRF.

$Sm_{0.95}Ce_{0.05}Fe_{1-x}Co_xO_{3-\delta}$	% w/w Sm[a]	% w/w Ce[a]	% w/w Fe[a]	% w/w Co[a]	Experimental Stoichiometric ratio Sm : Ce : Fe : Co :O[b]
x=0	56.226	2.776	21.676	0	0.949 : 0.050 : 0.985 : 0: 3.064
x=0.01	56.122	2.78	21.365	0.213	0.947 : 0.050 : 0.971 : 0.009: 3.096
x=0.03	56.258	2.78	21.005	0.698	0.950 : 0.050 : 0.954 : 0.030: 3.055
x=0.05	56.46	2.786	20.562	1.184	0.953 : 0.050 : 0.935 : 0.051: 3.016
x=0.07	56.598	2.779	20.199	1.662	0.956 : 0.050 : 0.918 : 0.072: 2.977
x=0.10	56.389	2.777	19.508	2.401	0.952 : 0.050 : 0.887 : 0.104: 3.005

[a]Measured by XRF using a calibrations curves of the corresponding oxides. Values are given as % w/w of the overall sample.
[b]Oxygen cannot be measured directly. The oxygen content is calculated from the balance of the sample weight.

Powder X-ray diffraction was used to determine the perovskite structure. Figure 5.1 shows the XRD pattern of $Sm_{0.95}Ce_{0.05}Fe_{1-x}Co_xO_{3-\delta}$ with x =0, 0.01, 0.03, 0.05, 0.07 and 0.10. The comparison with standard JCPDS card # 39-1490 indicates an orthorhombic symmetry from the Pnma (62) space group. No additional peaks were observed that would indicate a separate phase. From this data we conclude that a single perovskite phase is obtained for each material. Peak positions and full-width-half-maxima were used to determine cell parameters and crystallite sizes for all the perovskites. Table 5.2 shows the unit cell lengths, crystallite sizes and densities.

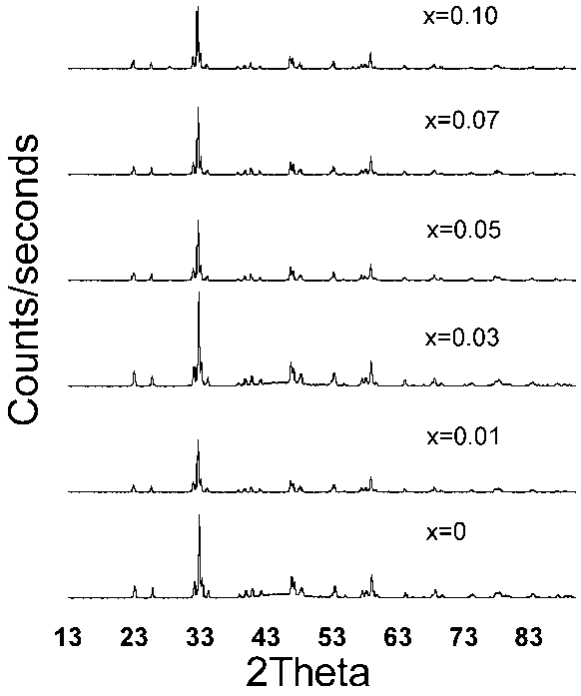

Figure 5.1. XRD pattern of $Sm_{0.95}Ce_{0.05}Fe_{1-x}Co_xO_{3-\delta}$ (x =0-0.10) obtained after calcination of amorphous citrates at 850°C for 24 hours.

Comparing the relative ionic radii of Fe^{+3} and Co^{+2} (Fe^{+3} (0.645Å) and Co^{+2} (0.745Å) [36]), one would expect that substituting Co into the Fe positions would increase the unit cell volume (from x = 0 to x = 0.10). However, the experimental trend shows an initial decrease in unit cell volume (from x = 0 to x = 0.01), followed by an increase from x = 0.01 to x = 0.10. It was also noticed that the unit cell volumes of all cobalt doped perovskites, $Sm_{0.95}Ce_{0.05}Fe_{1-x}Co_xO_{3-\delta}$, were smaller than the undoped $Sm_{0.95}Ce_{0.05}FeO_{3-\delta}$ material. These observations suggest the presence of additional oxidation states of the metals that change as a function of dopant concentration at the B-site (Fe^{+4} (0.585Å) & Co^{+3} (0.61Å) [36]).

Table 5.2. Calculated cell parameters, theoretical densities, cell volumes and crystallite sizes from XRD

$Sm_{(1-x)}Ce_xFe_{1-x}Co_xO_{3-\delta}$	Crystallite Size (Å)	a (Å)	b (Å)	c (Å)	Volume (Å^3)	Density[a] (g/cm^3)
x=0	627	5.610	7.718	5.413	233.927	7.203
x=0.01	480	5.586	7.720	5.392	232.522	7.248
x=0.03	306	5.593	7.704	5.401	232.701	7.244
x=0.05	334	5.589	7.711	5.400	232.721	7.245
x=0.07	700	5.592	7.716	5.406	233.277	7.230
x=0.10	635	5.599	7.699	5.419	233.597	7.222

[a] Densities calculated as $D = \frac{W \times Z}{V \times 0.6022169}$ where W is the formula mass, Z is the number of formula units per unit cell (4) and V is volume calculated from unit cell constants [37].

In order to explain this trend of unit cell volume quantitatively, we calculated the weighted average radii of B-site cations, r_B, by using different concentrations and concentration trends of Fe^{+3}, Fe^{+4}, Co^{+2} and Co^{+3}. These results were compared with volume (as $V^{1/3}$) to provide qualitative guidance regarding the ions present and in which ratios. Of the multiple combinations attempted, Figure 5.2 shows a representative set of series:

(1) $Sm_{0.95}Ce_{0.05}Fe^{+3}_{1-y-x'}Fe^{+4}_{y}Co^{+2}_{x'}O_{3-\delta}\,(y = 50\%Fe^{+3}, x' = 0-0.10)$

(2) $Sm_{0.95}Ce_{0.05}Fe^{+3}_{1-y-x'-x''}Fe^{+4}_{y}Co^{+2}_{x'}Co^{+3}_{x''}O_{3-\delta}\,(y = 50-15\%Fe^{+3}, x'+x'' = 0-0.10, x'' = 50\%Co^{+2})$

(3) $Sm_{0.95}Ce_{0.05}Fe^{+3}_{1-y-x'-x''}Fe^{+4}_{y}Co^{+2}_{x'}Co^{+3}_{x''}O_{3-\delta}\,(y = 50\%Fe^{+3}, x'+x'' = 0-0.10, x'' = 50\%Co^{+2})$

(4) $Sm_{0.95}Ce_{0.05}Fe^{+3}_{1-x'}Co^{+2}_{x'}O_{3-\delta}\,(x'=0-0.10)$

(5) $Sm_{0.95}Ce_{0.05}Fe^{+3}_{1-x''}Co^{+3}_{x''}O_{3-\delta}\,(x''=0-0.10)$

(6) $Sm_{0.95}Ce_{0.05}Fe^{+3}_{1-y-x'-x''}Fe^{+4}_{y}Co^{+2}_{x'}Co^{+3}_{x''}O_{3-\delta}\,(y=50-15\%Fe^{+3},\, x'+x''=0-0.10,\, x''=50-15\%Co^{+2})$

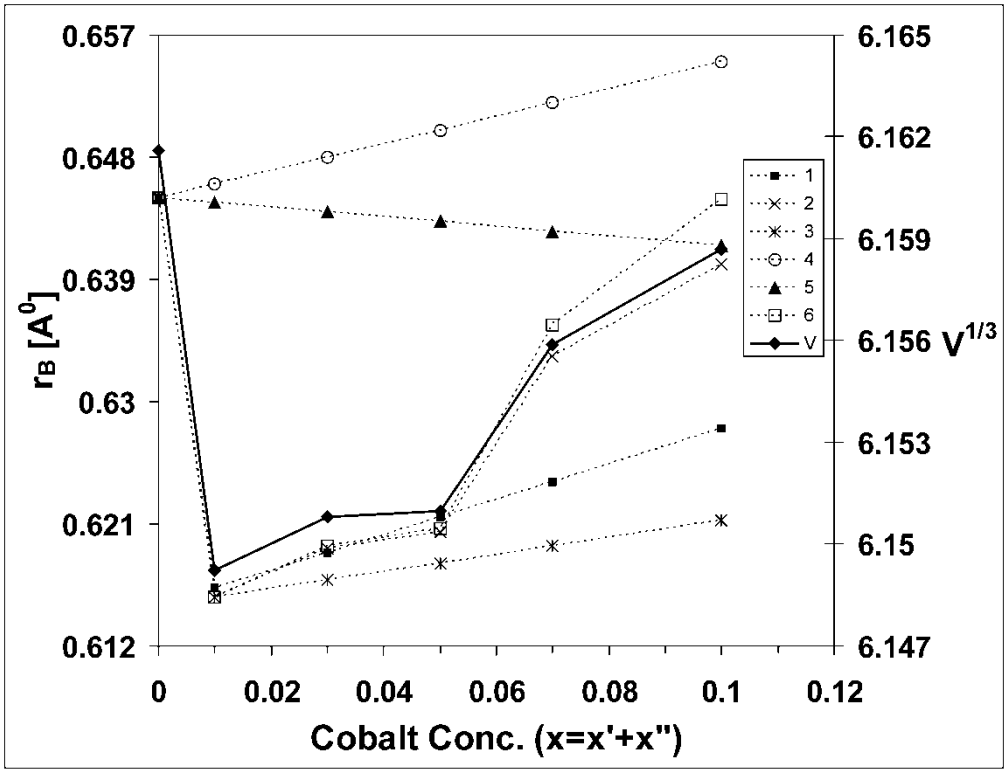

Figure 5.2. The weighted average ionic radii of B-cation (r_B) and normalized experimental cell volume ($V^{1/3}$) as a function of total concentration of Co (x=x′+x″).The solid line represents $V^{1/3}$ and broken lines show the weighted average ionic radii (r_B) for series 1 through 6, as described in the text.

Figure 5.2 shows the comparison of calculated weighted average radii with the cube root of unit cell volumes as a function of total concentration of cobalt [x=x′(Co^{+2})+x″(Co^{+3})]. The best

manual fit of these series to the experimental behaviour of the volume change is provided by series 2. Although one cannot conclude that this series trend is indeed accurate, the comparison allows the direct conclusion that both iron and cobalt must be present in mixed oxidation states. That is, the perovskites formed must contain Fe^{+3}, Fe^{+4}, Co^{+2} and Co^{+3}. This analysis also suggests that since redox couples are present, one cannot dismiss the formation of oxygen vacancies in the bulk material [9].

The thermal stability of these perovskites ($Sm_{0.95}Ce_{0.05}Fe_{1-x}Co_xO_{3-\delta}$ x=0-0.10) was tested by calcining them in air at 1350°C for four hours. The XRD spectra of these calcined perovskite materials remain identical to those shown in Figure 5.1, revealing that the lattice structure does not decompose at this temperature.

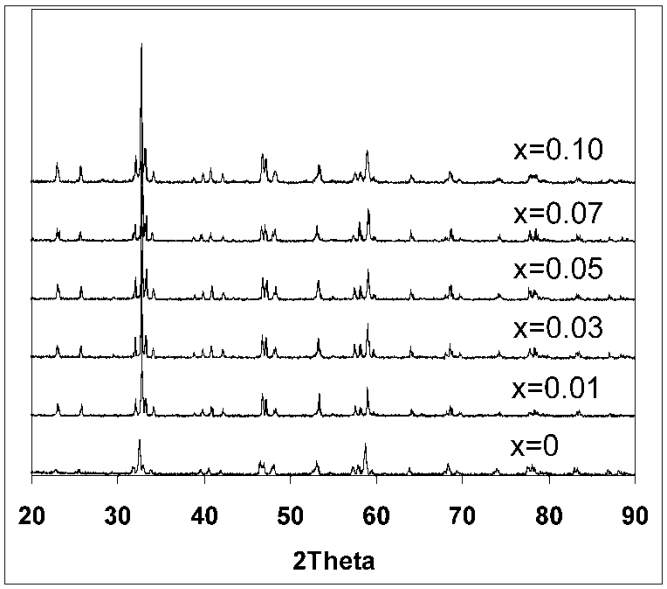

Figure 5.3. XRD pattern of $Sm_{0.95}Ce_{0.05}Fe_{1-x}Co_xO_{3-\delta}$ (x =0-0.10) heated in 5%v/v H_2/N_2 at 700°C for 1 hour.

The thermal stability of these perovskite materials was also examined as a function of temperature under 5%v/v H_2/N_2 for 1 hour. Figure 5.3 and Figure 5.4 show the XRD patterns after heating in 5 %v/v H_2/N_2 at 700°C and 800°C, respectively, for 1 hour. These cobalt doped perovskites do not show phase separation after treatment at 700°C which means that they are stable under reducing conditions at this temperature. But the onset of phase separation can be

seen after treatment under reducing conditions at 800°C, as indicated by the appearance of two additional peaks in the diffractogram. The peak at 2θ=28.25 corresponds to Sm_2O_3 [Figure 5.4(b**)]**, while the second peak at 2θ ~44.8 [Figure 5.4(d)] is broad and weak, preventing identification of the corresponding phase which could be Fe^0, Co_3O_4 and/or a Fe-Co alloy [$2\theta_{Fe} = 44.673$, $2\theta_{Co_3O_4} = 44.808$, $2\theta_{Co_3Fe_7} = 44.750$, $2\theta_{CoFe} = 44.865$].

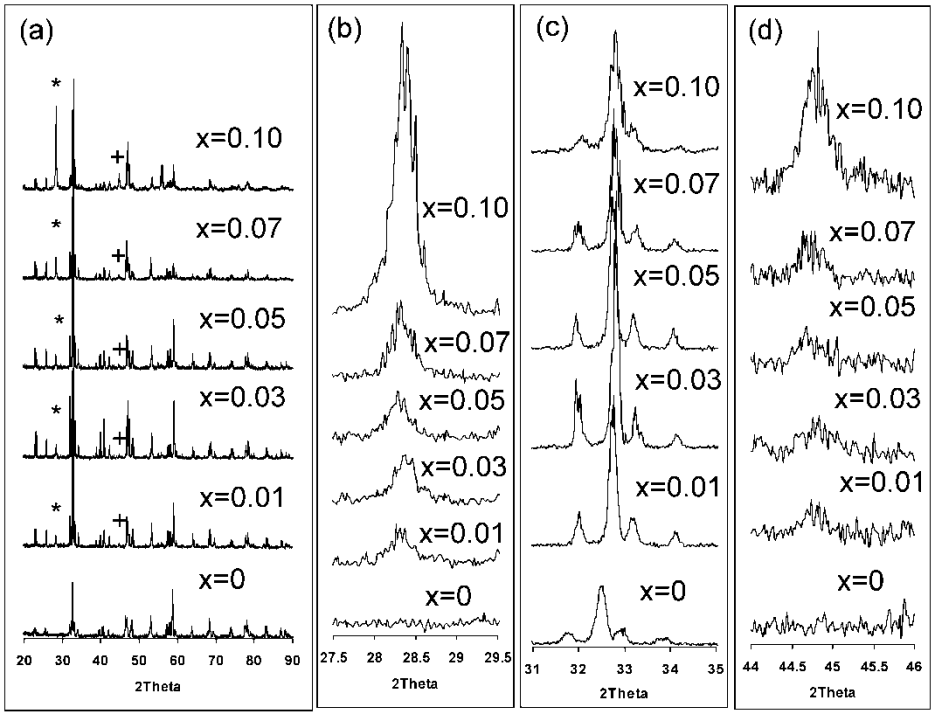

Figure 5.4. XRD pattern of $Sm_{0.95}Ce_{0.05}Fe_{1-x}Co_xO_{3-\delta}$ heated in 5 %v/v H_2/N_2 at 800°C for 1 hour. (a) full range XRD pattern, ***** indicates Sm_2O_3 phase and **+** indicates Fe^0, Co_3O_4 and/or Fe-Co alloy phases. (b), (c) and (d) are highlighted regions of (a). (b) shows phase separation of Sm_2O_3, (c) shows the destruction of perovskite phase and (d) shows formation of Fe^0, $Co_3O_4$and/or Fe-Co alloy phases.

Interestingly, Figure 5.4(c) shows that despite the phase separation observed, the characteristic perovskite peak remains substantially unchanged for all samples except x=0.10. That is, the remaining perovskite phase appears to conserve its structure after 1 hr at 800°C in the reducing atmosphere. Upon treatment under reducing atmosphere at 900°C [Figure 5.5], phase separation occurred more readily in all samples and the destruction of the perovskite phase, as

indicated by the distortion/broadening of the characteristic peak, is observed for samples of x > 0.05. It is worth noting that a brownmillerite phase that is often observed in partially reduced perovskite materials [38, 39]of formula ABO_{3-d} was not observed for any of the samples. It is conceivable that such a phase may be present under reducing conditions and that the equilibrium shifts back to a perovskite phase during transfer to the XRD instrument.

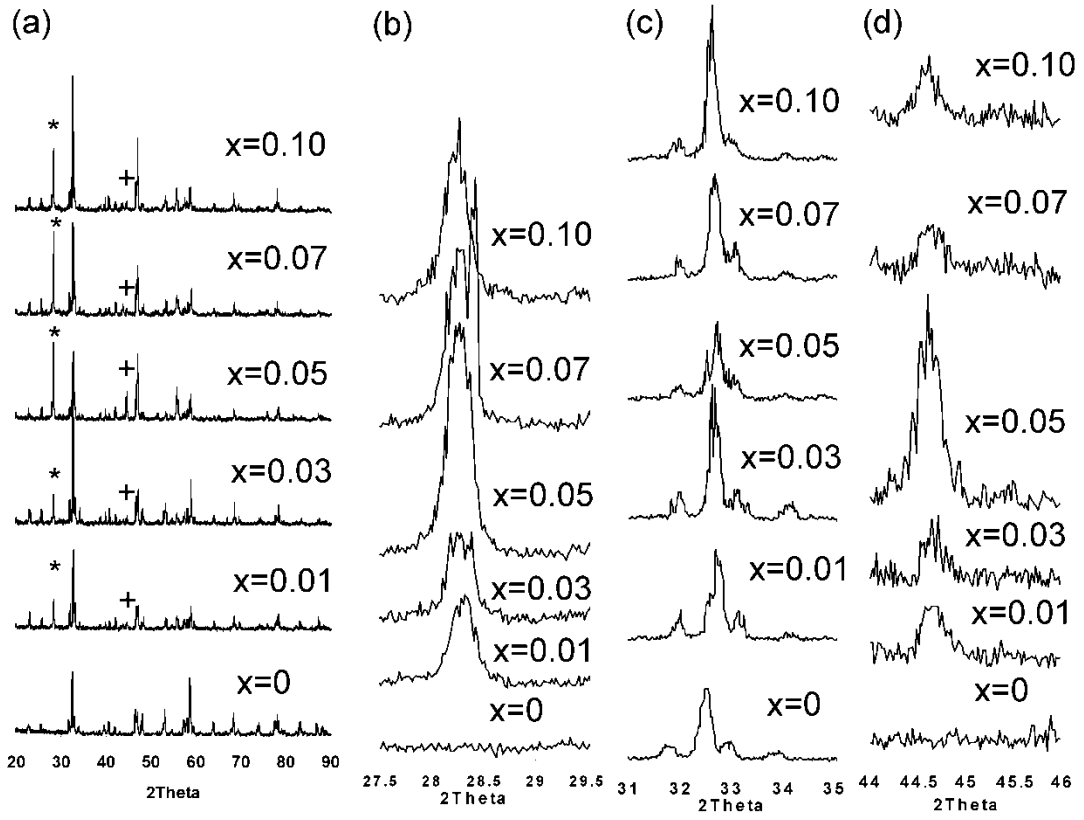

Figure 5.5. XRD pattern of $Sm_{0.95}Ce_{0.05}Fe_{1-x}Co_xO_{3-\delta}$ heated in 5 %v/v H_2/N_2 at 900°C for 1 hour. (a) full range XRD pattern, ***** indicates Sm_2O_3 phase and **+** indicates Fe^0, $Co_3O_4$and/or Fe-Co alloy phases. (b), (c) and (d) are highlighted regions of (a). (b) shows phase separation of Sm_2O_3, (c) shows the destruction of perovskite phase and (d) shows formation of Fe^0, $Co_3O_4$and/or Fe-Co alloy phases.

The phase separation and perovskite structure deterioration in reducing atmosphere can be rationalized by the nature of the cobalt substitution. Cobalt is more reducible than Fe [40] due to the relatively weak bond between cobalt and oxygen as compared to the bond between iron and oxygen [26]. For that reason, cobalt substitution at the Fe position decreases the stability of the

perovskite in reducing conditions, which results in the phase separation of Fe^0, Co^0 and/or Fe/Co-alloy [27, 30, 41]. In contrast, the presence of Ce at the A-site position enhances the thermal stability of the perovskite under reducing conditions due to its bigger size [2, 25, 40, 42]. In previous work we reported that $SmFeO_3$, which shows phase separation under reducing conditions, becomes stable on partial substitution of Ce at Sm within the solubility limit ($0 < x < 0.7$) [25]. In $Sm_{0.95}Ce_{0.05}Fe_{1-x}Co_xO_{3-\delta}$, the presence of Ce at A-site provides stability to the perovskite structure under reducing conditions, while the presence of Co at the B-site increases its reducibility. The combined effect is that for low Co concentrations (x=0.01-0.03), the decomposition is only partial and the perovskite phase remains undecomposed. This observation is in agreement with results reported by F.J. Berry and X. Ren regarding the reduction properties of $LaFe_{1-x}Co_xO_3$[30]. According to the authors, at low concentration of Co a phase separation is observed, but with preservation of the perovskite structure, while higher concentration of Co causes the phase separation accompanied by complete destruction of the perovskite structure. The present work also shows the temperature dependence of the stability toward reduction, with an onset of phase separation between 700^{o}C and 800^{o}C. As temperature increases to 800^{o}C all samples show phase separation without deterioration of the perovskite structure except x=0.10 which also shows decomposition of perovskite structure. Upon a further increase in temperature to 900^{o}C, phase separation without decomposition of perovskite structure is limited to x=0-0.03.

5.3.2. Surface Structure

The surface areas of as synthesized $Sm_{0.95}Ce_{0.05}Fe_{1-x}Co_xO_{3-\delta}$ perovskites were measured by the BET method using nitrogen adsorption experiments. The measured BET surface area values are given in Table 5.3.

Table 5.3. BET surface area of as synthesized $Sm_{0.95}Ce_{0.05}Fe_{1-x}Co_xO_{3-\delta}$ perovskites

Cobalt Conc.	x=0	x=0.01	x=0.03	x=0.05	x=0.07	x=0.10
SA (m^2/g)	6.94	3.05	5.56	3.31	4.47	4.0

X-ray photoelectron spectroscopy was used to reveal the chemical state and relative abundance of the elements at the surface of $Sm_{0.95}Ce_{0.05}Fe_{1-x}Co_xO_{3-\delta}$. Figure 5.6 shows the XPS spectrum of x=0.01, which is representative of all these cobalt doped perovskites. The peaks for $Sm3d_{5/2}$, $Ce3d_{5/2}$, $Fe2p_{3/2}$, $Co2p_{3/2}$ and O1s core levels were used for identification of oxidation states and quantification. The XPS spectra were analyzed and quantified by using CasaXPS software [43]. All spectra were calibrated by using the binding energy (B.E.) of carbon set at 284.8 eV. The surface atomic ratio of each metal cation was calculated from their relative sensitivity factors (R.S.F.). The results are given in Table 5.4. The experimental atomic ratios obtained by XPS show that the surface is enriched with samarium while cerium, cobalt and iron ions show a reduced concentration as compared to the bulk.

The O1s signal consists of two peaks, the low B.E. component has been ascribed to lattice oxygen [44] while the high B.E. component has been ascribed to surface adsorbed oxygen [45]. The peak positions of Sm3d and Fe2p are the same as those observed for $SmFeO_3$ and all Ce doped $SmFeO_3$, consistent with the nominal oxidation state of Sm^{+3} and Fe^{+3}. The peaks for Ce and Co were small and broad, making the determination of their oxidation states not possible.

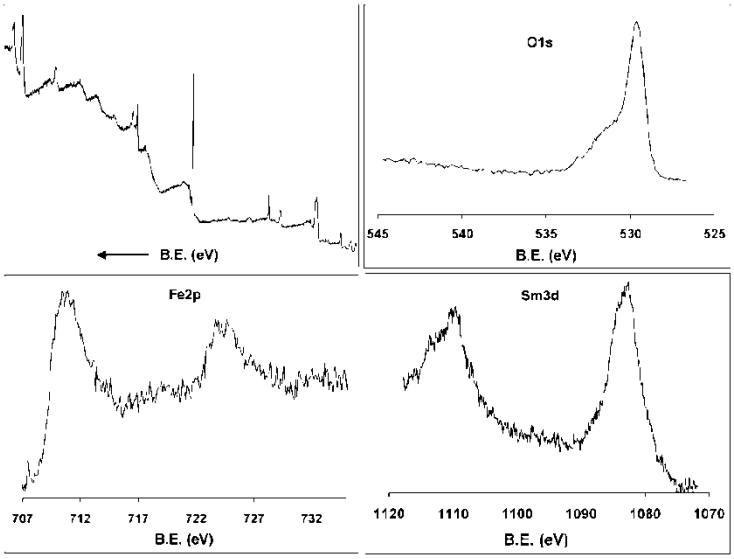

Figure 5.6. XPS spectrum of x=0.01 showing full range spectrum, and peaks of O1s, Sm3d, Fe2p.

Table 5.4. B.E. in (eV) and surface atomic ratio of $Sm_{0.95}Ce_{0.05}Fe_{1-x}Co_xO_{3-\delta}$

Sample	Binding Energy[a] (eV)					Metal atomic ratio[b] (bulk ratio)			
	$Sm3d_{5/2}$	$Ce3d_{5/2}$	$Fe2p_{3/2}$	$Co2p_{3/2}$	O1s	$\frac{Sm}{Sm+Ce+Fe+Co}$	$\frac{Ce}{Sm+Ce+Fe+Co}$	$\frac{Fe}{Sm+Ce+Fe+Co}$	$\frac{Co}{Sm+Ce+Fe+Co}$
x=0	1082.12	884.745	710.62	-	529.19	0.59 (0.475)	0.004(0.025)	0.406(0.500)	0(0)
x=0.01	1083.02	883.003	710.528	778.427	529.528	0.58(0.475)	0.005(0.025)	0.382(0.495)	0.033(0.005)
x=0.03	1082.1	882.922	710.931	778.413	529.842	0.622(0.475)	0.003(0.025)	0.367(0.485)	0.008(0.015)
x=0.05	1082.43	883.7	710.727	778.914	529.807	0.711(0.475)	0.003(0.025)	0.278(0.475)	0.009(0.025)
x=0.07	1082.35	882.96	710.987	780.045	529.731	0.705(0.475)	0.005(0.025)	0.271(0.465)	0.019(0.035)
x=0.10	1082.29	883.266	710.868	780.244	529.80	0.693(0.475)	0.003(0.025)	0.247(0.450)	0.057(0.050)

[a]Binding energies are calibrated by the C 1s peak, set at 284.8.eV.
[b]Stoichiometric ratios are normalized to the iron content.

5.3.3. Electrical Conductivity

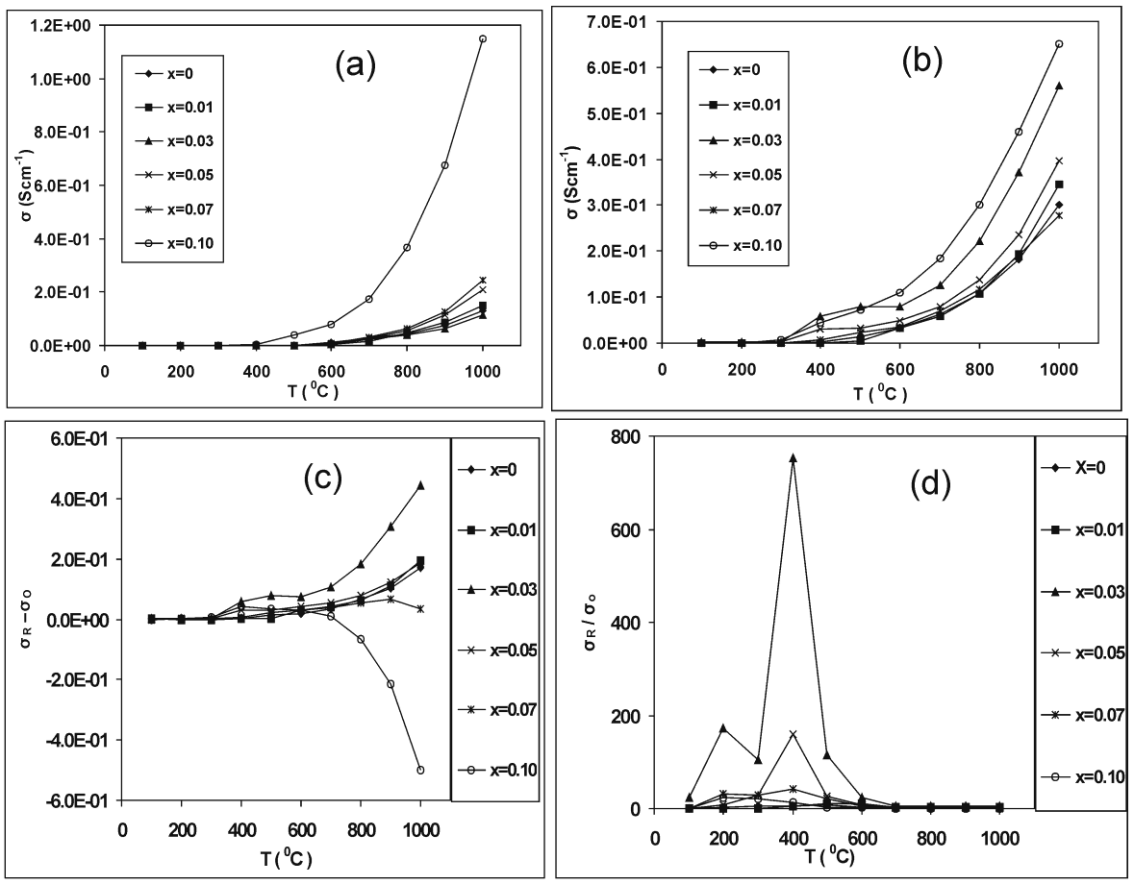

Figure 5.7. Electrical Conductivity of $Sm_{0.95}Ce_{0.05}Fe_{1-x}Co_xO_{3-\delta}$ sintered at 1350°C as a function of temperature. (a) and (b) shows electrical conductivity measured in air and 5% v/v H_2/N_2 respectively while 7(c) and 7(d) shows ($\sigma_R - \sigma_O$) and $\frac{\sigma_R}{\sigma_O}$ respectively as a function of temperature.

The total conductivities of $Sm_{0.95}Ce_{0.05}Fe_{1-x}Co_xO_{3-\delta}$ were measured as a function of temperature from 25-1000°C by the four probe DC method under both oxidizing and reducing conditions. The electrical conductivities measured under air are shown in Figure 5.7(a) as a function of temperature while Figure 5.8(a) shows the electrical conductivities as a function of cobalt concentration from 700 to 1000°C. The electrical conductivity of these cobalt doped materials increase with increase in temperature which reflects their semiconducting nature.

Furthermore the electrical conductivity under air increases as a function of cobalt concentration and the 10% cobalt doped has highest conductivity among all members of the series (Figure 5.7 and 5.8).

Figure 5.7(b) shows electrical conductivities measured under reducing conditions (5% v/v H_2 /N_2). All perovskites of this cobalt doped series have relatively high conductivities under reducing conditions as compared to air except x=0.10 whose conductivity starts dropping at ~800°C. This is most probably due to the destruction of perovskite structure (XRD pattern Figure 5.4). However, like the conductivity under air, the conductivity of x=0.10 under reducing conditions is highest amongst the series. Importantly the trend of increase in electrical conductivity as a function of cobalt concentration under reducing conditions is non-linear (Figure 5.8(b)), which is associated with the different extent of phase separation and destruction of perovskite structure. Thus we infer that the electrical conductivities of the cobalt doped perovskites under reducing conditions greatly depend on their thermal stability at different temperatures.

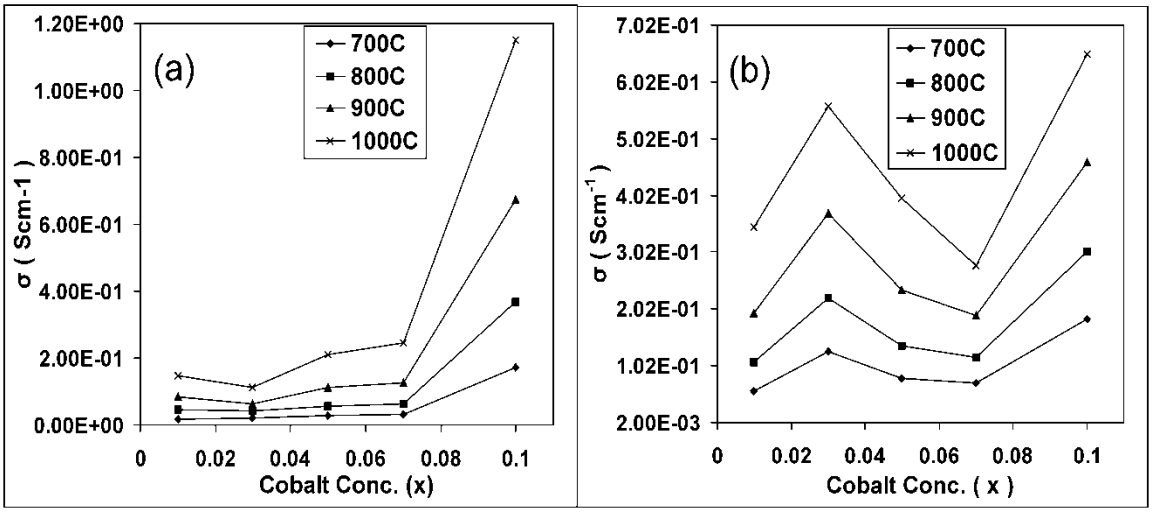

Figure 5.8. Electrical conductivities of $Sm_{0.95}Ce_{0.05}Fe_{1-x}Co_xO_{3-\delta}$. (a) Electrical conductivities as a function of cobalt concentration at 700°C, 800°C, 900°C and 1000°C under air. (b) Electrical conductivities as a function of cobalt concentration at 700°C, 800°C, 900°C and 1000°C under reducing conditions (5% v/v H_2/N_2).

The electrical conductivity improvement due to cobalt doping is associated with the number of oxygen vacancies. The oxygen vacancies increase with increase in Co content due to the variable oxidation state of both Fe and Co. Since oxygen vacancies act as electron donors [46], an increase in oxygen vacancies will increase the number of electrons [28, 47] which eventually cause an increase in the electrical conductivity. The numbers of oxygen vacancies formed under reducing condition are higher than under oxidizing conditions (air in the present situation) due to the fact that Co is more reducible than Fe. Consequently, all these cobalt doped perovskites have higher conductivities under reducing conditions than in air.

The comparison of electrical conductivities reveals the following:

(i) The cobalt doped materials have higher conductivity under both oxidizing and reducing conditions than undoped $Sm_{0.95}Ce_{0.05}FeO_{3-\delta}$

(ii) The conductivities of cobalt doped materials are lower under oxidizing conditions than under reducing condition.

(iii) The resulting cobalt doped materials have n-type behavior like that of $Sm_{0.95}Ce_{0.05}FeO_{3-\delta}$ which means that cobalt doping has improved the electrical conductivity of $Sm_{0.95}Ce_{0.05}FeO_{3-\delta}$ with the preservation of n-type behavior under both oxidizing and reducing conditions.

The cobalt containing perovskite type oxides exhibit very high oxygen permeability and therefore these are prominent amongst those materials which are very attractive for the use as oxygen permeable membranes in either membrane reactors or solid oxide fuel cells (SOFCs). However, their poor stability under reducing conditions has reduced their usage for constructing membrane reactors for the partial oxidation of natural gas to syngas [26, 31]. Since these cobalt doped perovskites, $Sm_{0.95}Ce_{0.05}Fe_{1-x}Co_xO_{3-\delta}$ ($0 < x \leq 0.03$) are relatively stable in reducing environments, they are good candidates for making membrane reactors for partial oxidation of natural gas to syngas with operating temperatures below 800°C. Above this temperature, and despite the phase separations, these materials can be considered for SOFC anodes since their conductivities (~0.1-0.5 S/cm at 800°C to 900°C) match well with some recently reported titanates as anode materials like $La_{0.4}Sr_{0.6}Ti_{1-x}Mn_xO_{3-\delta}$ (~ 0.08-1.5S/cm at 810°C to 910°C) [48], YZT (~0.06-0.37 S/cm at 800°C to 930°C) [49] and un-doped $BaCeO_3$ and Yr/Pr-doped $BaCeO_3$ (~ 0.01-0.30 S/cm at 800°C) [49, 50].

Figure 5.7(c) and 5.7(d) show Δσ, ($\sigma_R - \sigma_O$) and σ_R / σ_O as a function of temperature. These quantities are potential "measurable" which can be used in the fabrication of sensors. Indeed the 3% cobalt doped material has the highest value of both ($\sigma_R - \sigma_O$) and σ_R / σ_O as compared to the remaining cobalt doped materials. The highest value of σ_R / σ_O for 3% cobalt doped material corresponds to an operational temperature of 400°C. Since the quality of a good gas sensor depends on the change in electrical conductivity due to a change in concentration of the sensing gas and these materials have reasonably high values of ($\sigma_R - \sigma_O$) and σ_R / σ_O thus one could expect that these cobalt doped materials will show good performance in sensing reducing gases.

The working temperature of sensors is one of the very important factors that affect the stability of sensors. Generally, a high working temperature is not advantageous for a sensor [8] due to the fact that exposure to high temperature for a long time can change the chemical composition and most of the physical properties of the material (grain size, grain boundaries etc). For this reason, there is a need to find materials that can perform effectively (that can do sensing) at lower temperature.

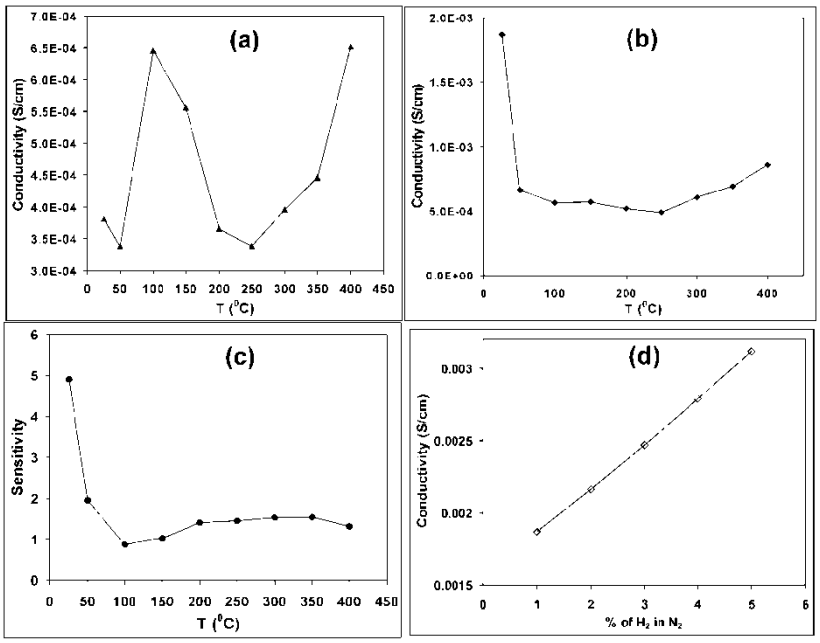

Figure 5.9. (a) Conductivity of x=0.03 as a function of temperature in N_2 atmosphere (b) Conductivity of x=0.03 as a function of temperature in 1% v/v H_2 /N_2 (c) Sensitivity $\left[\frac{\sigma_{1\%H_2/N_2}}{\sigma_{N_2}}\right]$ of x=0.03 (d) Conductivity of x=0.03 as a function of %v/v of H_2 in N_2 at 25^0C.

The conductivity of x=0.03 is measurable at room temperature under both N_2 and 1%v/v H_2/N_2. Figure 5.9(a) and Figure 5.9(b) show the conductivity of x=0.03 measured at room temperature under N_2 and 1%v/v H_2/N_2, respectively. The sensitivity of x=0.03 is maximum at 25°C [Figure 5.9(c)]. Dynamic changes in electrical conductivity at 25°C resulting from change in hydrogen concentration are presented in Figure 5.10. It is clear from Fig. 5.10 that introduction of hydrogen in flowing nitrogen leads to an increase in electrical conductivity. The conductivity increases linearly with an increase in concentration of H_2 [Figure 5.9(d)]. Furthermore when hydrogen flow is shut off and pure nitrogen as reference gas is let in, the conductivity drops to its original value. As a conclusion, at 25°C the adsorption process of H_2 gas is reversible. In the light of these results, 3% cobalt doped $Sm_{0.95}Ce_{0.05}FeO_3$ could be a good candidate for detecting reducing gases at room temperature.

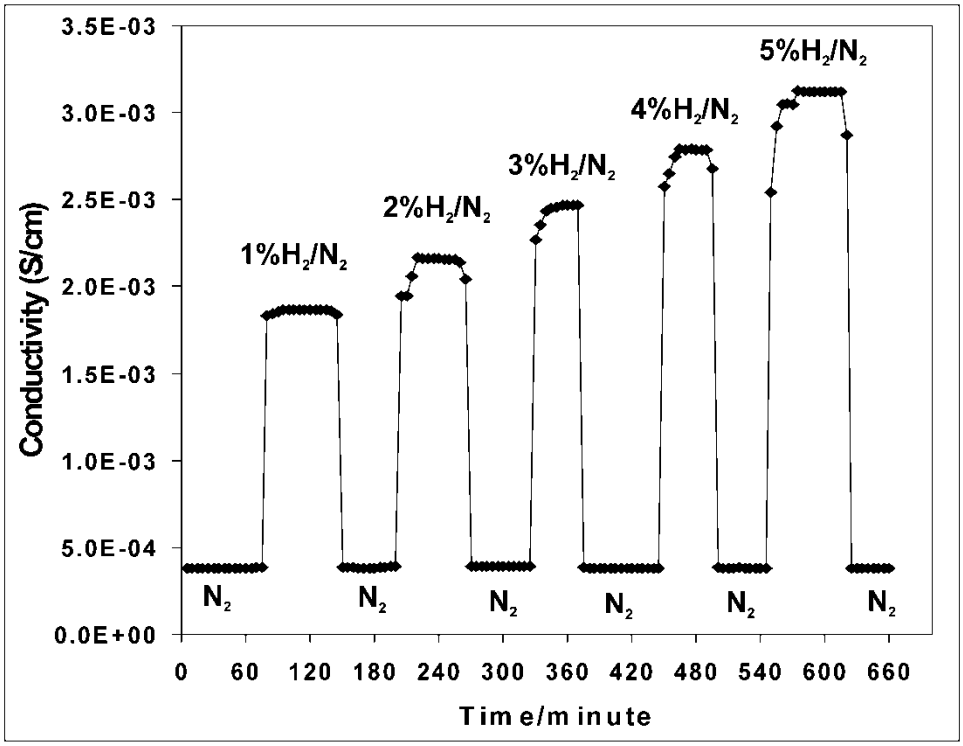

Figure 5.10. Dynamic changes in electrical conductivity at 25°C caused by H_2 adsorption for x=0.03.

5.4. Conclusions

$Sm_{0.95}Ce_{0.05}Fe_{1-x}Co_xO_{3-\delta}$ ($0 \leq x \geq 0.10$) materials were prepared by calcination of citrate precursors at 850°C for 24 hours. The effect of cobalt doping on their thermal stability and electrical conductivity in both air and 5%v/v H_2/N_2 was determined. The cobalt doped materials showed improved electrical conductivities in both air and 5%v/v H_2/N_2. Indeed the conductivity of x=0.10 is highest in both oxidizing and reducing conditions while x=0.03 has highest sensitivity [$\frac{\sigma_R}{\sigma_O}$] value at 400°C as compared to all other members of the series. Since the sensitivity of x=0.03 is reasonably high even at room temperature, it can be considered as a candidate material for sensors of reducing gases in atmosphere at room temperature. The improvement in electrical conductivities is thought to occur via oxygen vacancies produced by Co doping. The relatively high conductivities in reducing condition as compared to air strongly suggest that $Sm_{0.95}Ce_{0.05}Fe_{1-x}Co_xO_{3-\delta}$ materials are n-type semiconductors like $Sm_{0.95}Ce_{0.05}FeO_{3-\delta}$.

The doping of Co improves the electrical conductivities of $Sm_{0.95}Ce_{0.05}FeO_{3-\delta}$ but destabilizes the crystal lattice under reducing conditions at higher temperatures. The decomposition of the Co substituted perovskites under reducing conditions starts at ~ 800°C, however these materials remain as a single perovskite phase below that temperature, so their potential for applications as sensors and as anode materials for low temperature SOFCs should be considered. In particular, $Sm_{0.95}Ce_{0.05}Fe_{1-0.03}Co_{0.03}O_{3-\delta}$ has been shown to be sensitive to reducing atmospheres at room temperature.

5.5. References

[1] P.T. Moseley, Sens. Actuators B. 6 (1992) 149-156.
[2] D.E. Williams, P.T. Moseley, J. Mater.Chem. 1 (1991) 809-814.
[3] P.T. Moseley, Sens. Actuators B. 3 (1991) 167-174.
[4] Z. Szklarski, K. Zakrzewska, Thin Solid Films. 174 (1989) 269-275.
[5] N. Barsan, R. Grigorovici, R. Ionescu, M. Motronea, A. Vancu, Thin Solid Films. 171 (1989) 53-63.
[6] N. Mullera, A. Jess, R. Moos, Sens. Actuators B. doi:10.1016/j.snb.2009.03.008 (2009).
[7] X. Jia, H. Fan, X. Lou, J. Xu, Appl Phys A. 94 (2009) 837-841.
[8] M. Zhao, H. Peng, J. Hu, Z. Han, Sens. Actuators B. 129 (2008) 953-957.
[9] X. Liu, J. Hu, B. Cheng, H. Qin, M. Jiang, Sens. Actuators B. 134 (2008) 483-487.
[10] A. Martinez-Juarez, L. Sanchez, E. Chinarro, P. Recio, C. Pascual, J.R. Jurado, Solid State Ionics. 135 (2000) 525-528.
[11] J. Molenda, K. Swierczek, W. Zajac, J. Power Sources. 173 (2007) 657-670.
[12] M. Gonzelez-Cuenca, W.Zipprich, B.A. Boukamp, G. Pudmich, F.Tietz, Fuel Cells. 1 (2001) 256-264.
[13] H.L. Tuller, A.S. Nowick, J. Electrochem. Soc. 122 (1975) 255-259.
[14] A. Atkinson, Solid State Ionics. 95 (1997) 249-258.
[15] J.H. White, A.F. Sammells, J. Eletrochem. Soc. 140 (1993) 2167-2177.
[16] T. Ishihara, M. Honda, T. Shibayama, H. Minami, H. Nishiguchi, Y. Takita, J. Eletrochem. Soc. 145 (1998) 3177-3183.
[17] H.Y. Tu, Y.Takeda, N. Imanishi, O. Yamamoto, Solid State Ionics. 100 (1997) 283-288.
[18] V. Vashook, L. Vasylechko, J. Zosel, R. Muller, E. Ahlborn, U. Guth, Solid State Ionics. 175 (2004) 151-155.
[19] G. Pudmich, B.A. Boukamp, M. Gonzalez-Cuenca, W. Jungen, W. Zipprich, F. Tietz, Solid State Ionics. 135 (2000) 433-438.
[20] M. Ikeguchi, T. Mimura, Y. Sekine, E. Kikuchi, M. Matsukata, Appl. Catal., A. 290 (2005) 212-220.
[21] H. Aono, M. Sato, E. Traversa, M. Sakamoto, Y. Sadaoka, J. Am. Ceram. Soc. 84 (2001) 341-347.

[22] M.C. Carotta, G. Martinelli, Y. Sadaoka, P. Nunziante, E. Traversa, Sens. Actuators B. 48 (1998) 270-276.
[23] Y. Hosoya, Y. Itagaki, H. Aono, Y. Sadaoka, Sens. Actuators, B. 108 (2005) 198-201.
[24] H. Aono, E. Traversa, M. Sakamoto, Y. Sadaoka, Sens. Actuators B. 94 (2003) 132-139.
[25] S.M. Bukhari, J.B. Giorgi, Solid State Ionics. 180 (2009) 198-204.
[26] X. Zhu, H. Wang, W. Yang, Solid State Ionics. 177 (2006) 2917-2921.
[27] J.N. Kuhn, U.S. Ozkan, Catal. Lett. 121 (2008) 179-188.
[28] R. Yinzhe, L. Erbao, W. Jianying, W. Yuxiang, Rare Metals. 21 (2002) 190-192.
[29] Y. Itagaki, M. Mori, Y. Hosoya, H. Aono, Y. Sadaoka, Sens. Actuators, B. 122 (2007) 315-320.
[30] F.J. Berry, X. Ren, Czech. J. Phys. 55 (2005) 771-780.
[31] Y. Teraoka, H. Shimokawa, C.Y. Kang, H. Kusaba, K. Kasaki, Solid State Ionics. 177 (2006) 2245-2248.
[32] M.R. Goldwasser, M.E. Rivas, M.L. Lugo, E. Pietri, J. Perez-Zurita, M.L. Cubeiro, A. Gibroval-Constant, G. Lecrlercq, Catal. Today. 107-108 (2005) 106-113.
[33] S. McIntosha, J.F. Vente, W.G. Haije, D.H.A. Blank, H.J.M. Bouwmeester, Solid State Ionics. 177 (2006) 833-842.
[34] N.A. Merino, B.P. Barbero, P. Eloy, L.E. Cadús, Appl. Surf. Sci. 253 (2006) 1489-1493.
[35] V.V. Kharton, I.P. Marozau, N.P. Vyshatko, A.L. Shaula, A.P. Viskup, E.N. Naumovich, F.M.B. Marques, Mater. Res. Bull. 38 (2003) 773-782.
[36] R.D. Shanon, Acta cryst. A32 (1976) 751-767.
[37] E.N. Maslen, V.A. Streltsov, N. Ishizawa, Acta Cryst. B52 (1996) 406-413.
[38] C.d.l. Calle, J.A. Alonso, A. Aguadero, M.T. Fernandez-Diaz, Dalton Trans. (2009) 4104-4114.
[39] S. Mclntosh, J.F. Vente, W.G. Haije, D.H.A. Blank, H.J.M. Bouwmeester, Solid State Ionics. 177 (2006) 833-842.
[40] M.A. Pena, J.L.G. Fierro, Chem. Rev. 101 (2001) 1981-2017.
[41] J. Ovenstone, J. Jung, J.S. White, D.D. Edwards, S.T. Misture, J. Solid State Chem. 181 (2008) 576-586.
[42] A. Qi, S. Wang, G. Fu, C. Ni, D. Wu, Appl. Catal. A. 281 (2005) 233-246.
[43] N. Fairley, CasaXPS Version 2.3.13 Dev73 ed., Casa Sotware Ltd, 2007.
[44] L. Xi, L. Xiaoxun, X. Baokun, Z. Muyu, J. Alloys Compd. 186 (1992) 315-319.
[45] J.L.G. Fierro, L.G. Tejuca, Appl. Surf. Sci. 27 (1987) 453-457.
[46] S.P. Jiang, L. Liu, K.P. Ong, P. Wu, J. Li, J. Pu, J. Power Sources. 176 (2008) 82-89.
[47] R. Yinzhe, W. Jianying, L. Erbao, J. Rare Earths. 20 (2002) 471-474.
[48] Q.X. Fu, F. Tietz, D. Stöver, J Electrochem. Soc. 153 (2006) D74-D83.
[49] J.W. Fergus, Solid State Ionics. 177 (2006) 1529-1541.
[50] T. Hibino, A. Hashimoto, M. Suzuki, M. Sano, J. Electrochem. Soc. 149 (2002) A1503.

6. Performance of Cobalt doped $Sm_{0.95}Ce_{0.05}FeO_{3-\delta}$ as sensors for the detection of reducing gases

The contents of this chapter have been published as: Syed M. Bukhari and Javier B. Giorgi, J. Electrochemical Society, 158(6) (2011) J159-J164 ; Syed M. Bukhari and Javier B. Giorgi, Electrochemical Society Trans. 28(20)(2010) 19-29

Abstract

The newly developed $Sm_{0.95}Ce_{0.05}Fe_{1-x}Co_xO_{3-\delta}$ perovskites were assessed as sensors for reducing gases. The solid state sensors were prepared in the form of pellets. Sensors with larger particle size and reduced grain boundaries are obtained as the concentration of cobalt is increased. The sensor's surface is enriched with Sm and Co, but the Sm concentration decreases with an increase in cobalt content. The introduction of cobalt in the perovskite lattice results in an increase in lattice oxygen and a decrease in surface adsorbed oxygen. The electrical conductivity responses toward H_2, CO and CH_4 (1-5%v/v) were measured in air and at different temperatures. The cobalt doping has improved the response to such an extent that H_2, CO and CH_4 can be detected at room temperature. Response and recovery time of these sensors are associated with surface chemical composition and surface morphology.

6.1. Introduction

ABO_3 type perovskite oxides have great tuneability in their properties by substitutions at the A-site, the B-site or both [1-5]. Generally the size of the A-site cation determines the thermal and reduction stability while the nature of the B-site cation plays an important role in the catalytic properties of the resulting perovskite structure [6]. $SmFeO_3$ is a p-type semiconductor and has been used as a sensor for detecting oxidizing gases like ozone and NO_2 [7, 8]. However, these sensors need improvement due to their low electrical conductivity and reduction instability [9]. Ce doping at the A-site in $SmFeO_3$ has not only improved reduction stability and electrical conductivity but also changed its electrical behavior from p-type to n-type [9], thus making this perovskite promising for sensing reducing gases like H_2, CO and CH_4. However, sensors for carbon containing compounds should also be coke resistant to prevent poisoning of the sensor.

Perovskites with formula $Sm_{0.95}Ce_{0.05}Fe_{1-x}Co_xO_{3-\delta}$ ($0 \leq x \leq 0.10$) have been recently reported by our group [10]. The cobalt doped materials (x=0-0.03) are n-type with unusually

high electrical conductivity under both oxidizing (air) and reducing conditions (5%H_2/N_2), while the x=0.05-0.10 materials are p-type. $Sm_{0.95}Ce_{0.05}Fe_{0.97}Co_{0.03}O_{3-\delta}$ materials have the capability of reproducibly sensing hydrogen from 1-5% v/v H_2 in N_2 at room temperature [10]. X-ray diffraction of the as-synthesized powders showed these materials to have a single phase with orthorhombic symmetry. These materials are stable in air up to 1350^oC and phase separation does not occur until 800^oC upon treatment with 5 %v/v H_2/N_2 for one hour.

This work will demonstrate the potential of n-type $Sm_{0.95}Ce_{0.05}Fe_{1-x}Co_xO_{3-\delta}$ (x=0-0.03) as sensors for the detection of H_2, CO and CH_4 at different temperatures i.e., 25^oC, 200^oC and 300^oC.

6.2. Experimental

Powders of $Sm_{0.95}Ce_{0.05}Fe_{1-x}Co_xO_{3-\delta}$ (x=0-0.03) were prepared by thermal decomposition of the amorphous citrate precursors as described elsewhere [10]. Briefly, samarium nitrate ($Sm(NO_3)_3 \cdot 6H_2O$, AlfaAesar, 99.9%), cerium nitrate ($Ce(NO_3)_3 \cdot 6H_2O$, AlfaAesar, 99.5%), iron nitrate ($Fe(NO_3)_3 \cdot 9H_2O$, AlfaAesar, >98%) , cobalt nitrate ($Co(NO_3)_2.6H_2O$, AlfaAesar, 99%) and citric acid monohydrate (minimum 99.0%) were used as precursors. The nitrates were weighed separately according to the desired stoichiometric ratio of the four metals ($Sm_{0.95}$ + $Ce_{0.05}$: $Fe_{(1-x)}$ + Co_x = 1:1) and were then dissolved in de-ionized water to prepare their solutions. Solutions were mixed and the resulting mixture was added to aqueous citric acid such that the metal to citric acid ratio was 1:1. Water was evaporated at 100°C until the amorphous citrate precursors were dried and the material was then ground and finally calcined at 850 °C for 24 hours to form the perovskite phase. The resulting powders were then uniaxially compressed to form pellets which were then sintered at 1350^oC for four hours. The surface morphology of each sensor pellet was determined by scanning electron microscopy (SEM, JEOL JSM-7500F) while the surface chemical states and composition were measured by X-ray photoelectron spectroscopy (XPS; Kratos AXIS Ultra^{DLD} 39-306l), using a monochromatic Al anode.

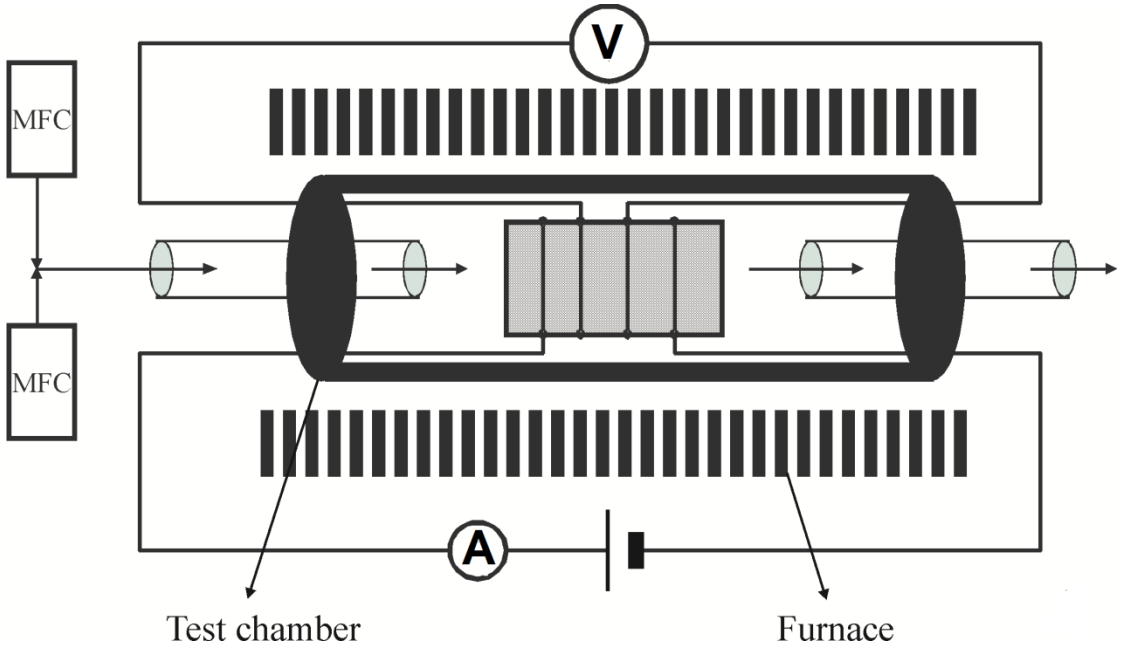

Figure 6.1. Schematic of the sensor setup. The sensor fits inside a gas chamber located inside a furnace. The gas manifold can be modified to access different concentration ranges of each gas.

The sintered pellets were chopped into rectangular shape sensors. The average size of the sensor was 13mm x 7mm x 0.80mm. Four contact points were made by wrapping four platinum wires. The two outer wires were connected to a DC power supply as a source of current (50mA) while the inner two wires were connected to digital multimeters to measure voltage. A schematic of the sensing experiment is shown in Figure 6.1. The sensing experiment was done in a testing chamber consisting of a hollow quartz tube, the openings of which were sealed with rubber septa. The electrical conductivity of each sensor was measured in mixtures of different gases (H_2, CO and CH_4) in air 1-5% v⁄v at temperatures of 25^{o}C, 200^{o}C and 300^{o}C. The sensitivity of the sensor to different gases was monitored according to equation 6.1, as it is often done in the literature (e.g. [11-13]). Strictly speaking, equation 1 is a modified resistance ratio (conductance ratio in this case), but this form of the equation has the advantage of allowing direct comparison of different sensors under similar conditions, and of a single sensor with different gases. For the remainder of the manuscript, we shall refer to this quantity as the “sensor signal”, S (equation 6.1), which can have any value larger than zero [14, 15].

$$S(\%) = 100 \times \left(\frac{\sigma_{gas} - \sigma_{Air}}{\sigma_{Air}} \right) \quad (6.1)$$

The conductivities of all sensors were measured as a function of time and concentration for different gases and at different temperatures. The sensor signal was calculated in each case. The variations between different experiments allowed the estimation of the error in the sensor signal as 7 to 15%, with the larger errors at the lowest gas concentration values.

6.3. Results and Discussions

6.3.1. Microstructural properties

The surface morphology of each sensor was explored by scanning electron microscopy (SEM, JEOL JSM-7500F). Figure 6.2 shows the microstructure of each sensor. The particle size of the perovskite in the pellets grows as a function of cobalt concentration and particles on the surface have well defined grain boundaries.

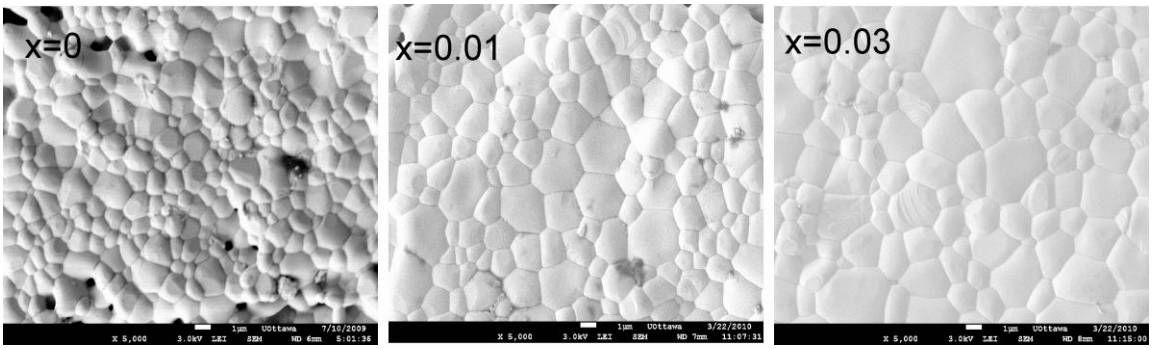

Figure 6.2. SEM images of $Sm_{0.95}Ce_{0.05}Fe_{1-x}Co_xO_{3-\delta}$ (x=0, 0.01 and 0.03) sensors showing surface morphology.

The chemical state and relative abundance of the elements in the surface of each sensor was revealed by X-ray photoelectron spectroscopy. The peaks for $Sm3d_{5/2}$, $Ce3d_{5/2}$, $Fe2p_{3/2}$, $Co2p_{3/2}$ and O1s core levels were used for identification of oxidation states and for quantification. The XPS spectra were analyzed and quantified using the CasaXPS software [16]. The binding energy of the $Sm3d_{5/2}$ peak is found to be ~1082eV, which is in good agreement with reported values for Sm^{+3} [17]. The determination of accurate oxidation state

for Ce and Co was not possible due to low intensity in the $Ce3d_{5/2}$ and $Co2p_{3/2}$ peaks. $Fe2p_{3/2}$ peaks for all three sensors appeared as broad envelopes consisting of several peaks. Figures 6.3a, 6.3b and 6.3c show the result of peak fitting for $Fe2p_{3/2}$ peaks for the three sensors. Three distinct peaks were identified in all cases. The peak in the range of 709.6-709.9eV can be ascribed to Fe^{+2} [B.E.=709.3eV [18]]; the peak in the range of 710.5-711eV corresponds to Fe^{+3} [B.E.=710.5eV [18]]; and the peak at 712-714eV is due to Fe^{+4}. The percentages of the three iron species are shown in Table 6.1. Upon introduction of cobalt, the concentration of the Fe^{+4} species decreases, suggesting a redox reaction between cobalt and iron species in the lattice.

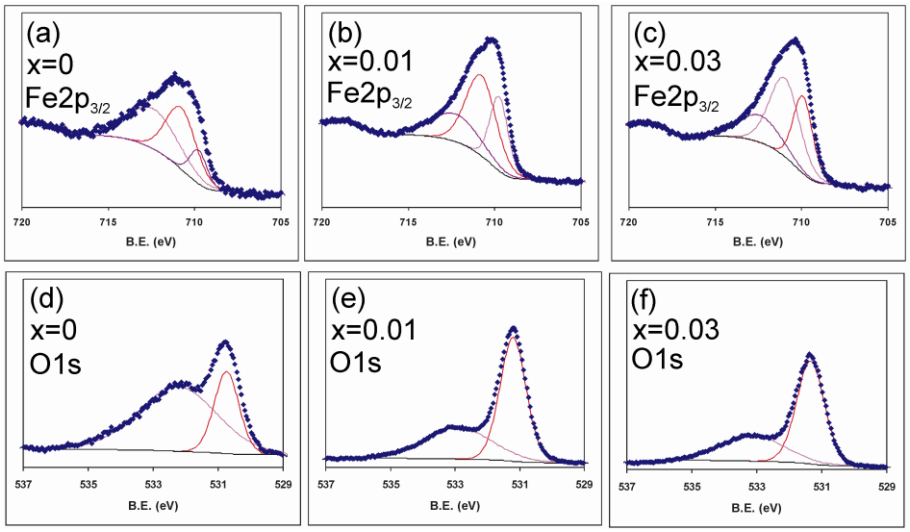

Figure 6.3. XPS results for $Sm_{0.95}Ce_{0.05}Fe_{1-x}Co_xO_{3-\delta}$ (x=0-0.03). Peak fitting of $Fe2p_{3/2}$ (a, b, c) and O1s (d, e, f) peaks are shown.

Figure 6.3d, 6.3e and 6.3f show the peak fitting results for the O1s peaks. The O1s peak has two components, a low binding energy component ascribed to lattice oxygen (O_{latt}) and a high binding energy component due to surface adsorbed oxygen (O_{ads}) [17]. The percentages of lattice and adsorbed oxygen, and their relative ratios as a function of cobalt concentration are shown in Table 6.1. The comparison shows that upon introduction of cobalt in the perovskite structure, the concentration of lattice oxygen increased while that of surface adsorbed oxygen decreased. The decrease in surface adsorbed oxygen can be explained in terms of Sm surface concentration. Since the coordination number of Sm is higher than Fe

and Co (i.e. 12), more sites are available for oxygen adsorption as the concentration of surface-Sm increases. In the present case, the concentration of surface Sm decreases as a function of cobalt concentration, and therefore the concentration of adsorbed oxygen also decreases. On the other hand, the increase in lattice oxygen can be ascribed to a decrease in concentration of Fe^{+4} species in the lattice as a function of cobalt concentration.

Table 6.1. Quantification results obtained from peak fittings of O1s and $Fe2p_{3/2}$ peaks

Cobalt conc.(x)	Iron (Fe)			Oxygen		
	Fe^{+2}	Fe^{+3}	Fe^{+4}	O_{latt}	O_{ads}	$\frac{O_{latt}}{O_{ads}}$
0	20.73	45.86	33.41	29.63	70.37	0.42
0.01	26.25	47.63	26.12	61.65	38.35	1.61
0.03	32.69	50.77	16.54	63.06	36.06	1.75

Figure 6.4 shows the metal quantification (relative surface atomic ratios) of Sm, Ce, Fe and Co, calculated by peak fittings of $Sm3d_{5/2}$, $Ce3d_{5/2}$, $Fe2p_{3/2}$ and $Co2p_{3/2}$ core levels. The sensors' surfaces were enriched with Sm and Co due to surface segregation. As the concentration of Co increases in the composition of sensors, the Sm surface segregation decreases while that of Co increases. This decrease in surface atomic ratio of Sm has a strong impact on surface adsorbed oxygen, as discussed above.

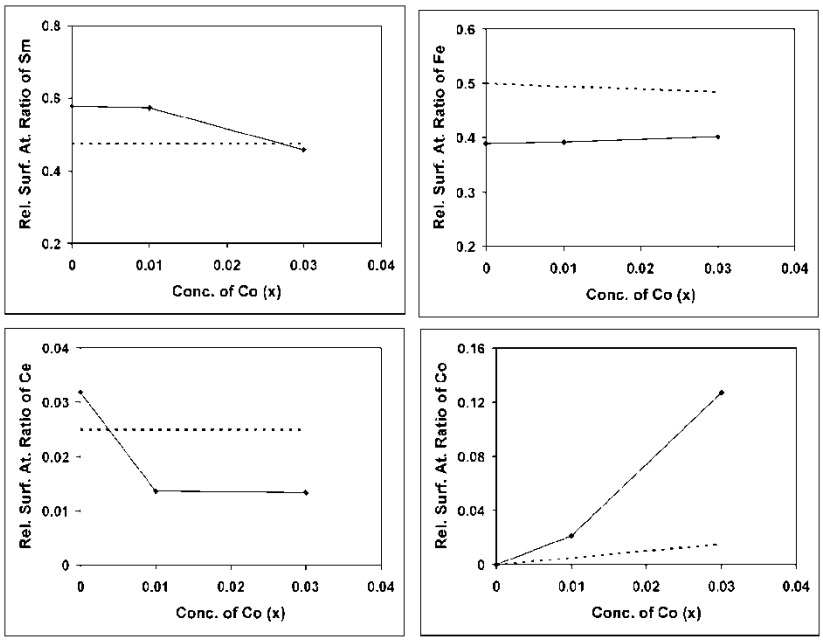

Figure 6.4. Surface atomic ratios of metal atoms in $Sm_{0.95}Ce_{0.05}Fe_{1-x}Co_xO_{3-\delta}$ sensors as calculated from peak fitting of XPS spectra of the $Sm3d_{5/2}$, $Ce3d_{5/2}$, $Fe2p_{3/2}$ and $Co2p_{3/2}$ core levels. The dotted lines represent the expected bulk atomic ratios.

6.3.2. Sensor behaviour

The sensitivity of $Sm_{0.95}Ce_{0.05}Fe_{1-x}Co_xO_{3-\delta}$ (x=0-0.03) sensors were tested at low temperatures. Of particular interest is the behavior at room temperature, which would allow cheaper and simpler construction of sensors. Pellet-design sensors were tested in air toward three industrially relevant reducing gases (H_2, CO, and CH_4), simulating the conditions under which the sensor could be used.

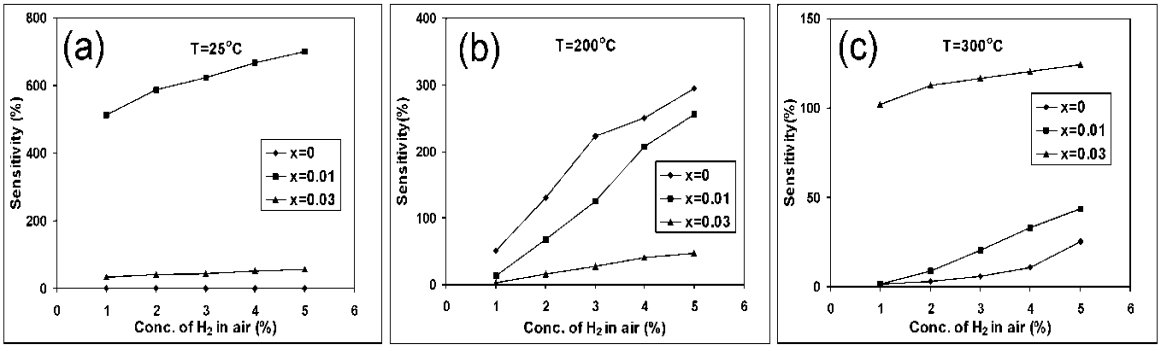

Figure 6.5. Hydrogen concentration dependence of the sensor signal for $Sm_{0.95}Ce_{0.05}Fe_{1-x}Co_xO_{3-\delta}$ (x=0-0.03) sensor in air at 25, 200 and 300°C.

The sensor signal toward hydrogen was tested at three different temperatures (i.e., 25°C, 200°C and 300°C) for a range of concentrations (1-5%v/v H_2) in air (Figure 6.5). At all the temperatures tested, the sensors showed linear and reversible responses as a function of hydrogen concentration in air. The cobalt doped material based sensors were able to detect hydrogen at room temperature (Figure 6.5a), where the x=0.01 material showed the highest signal in the series. At 200°C, the best sensor signal was observed for x=0 while at 300°C the largest response was observed for x=0.03.

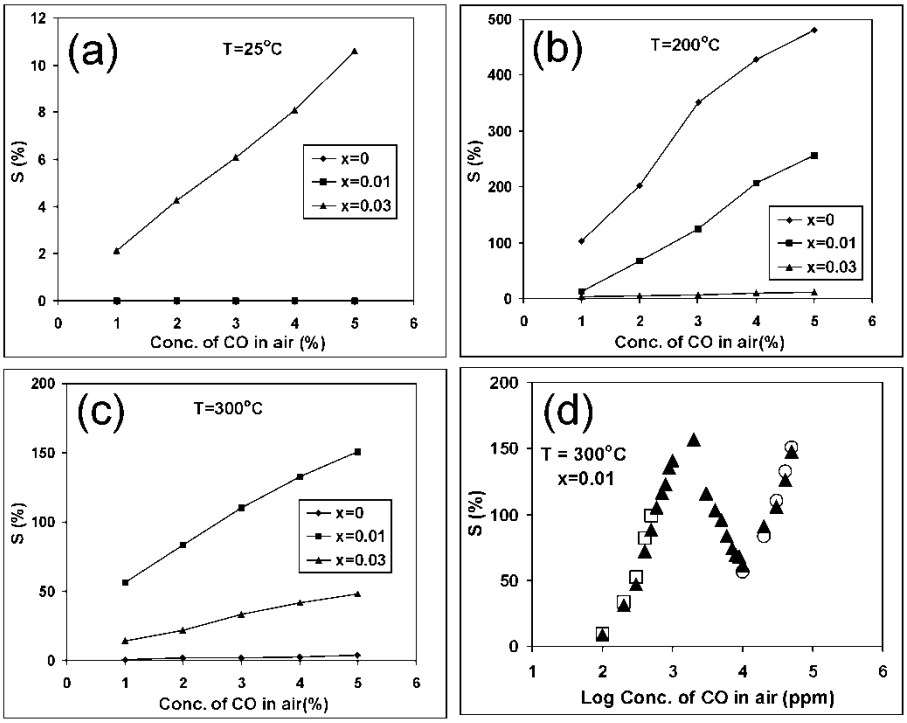

Figure 6.6. CO Concentration dependence of the sensor signal for $Sm_{0.95}Ce_{0.05}Fe_{1-x}Co_xO_{3-\delta}$ (x=0-0.03) sensors at (a) 25°C, (b) 200°C, and (c) 300°C. (d) Sensor signal for the x=0.01 sensor at 300°C in the low and high concentration regimes. Open symbols represent narrow concentration range experiments while the full symbols are representative of experiments that cover the full concentration range.

Figure 6.6 displays the results for detection of CO in air at different temperatures as a function of test gas concentration. The figure shows that best response temperatures for x=0,

0.01 and 0.03 are 200^{o}C, 300^{o}C and 300^{o}C, respectively. Nevertheless, detection of CO at room temperature is possible using the x=0.03 perovskite. Additionally, the small concentration regime was explored, and the x=0.01 sample shows a detectable response at 300^{o}C. The response of x=0.01 towards CO in air was linear and reversible in the concentration range of 100ppm to 500ppm (Figure 6.6d).

Separate experiments showed linear behavior in the 100-500ppm range and in the 1-5% range (open symbols in Figure 6.6d). However, a drop in the sensor signal was observed between the two ranges. To assess this apparent inconsistency, the experimental setup was modified to allow a full range of concentrations to be explored in a single run. The result indicates that there is a continuous curve with expected responses in the low and high concentration regimes (full symbols in Figure 6d). The sensor signal increases linearly up to 1,000 ppm (0.1%), then decreases up to 10,000 ppm (1%), and increases linearly again from 10,000 ppm (1%) to 50,000 (5%). The overlap between measurements, particularly considering the modifications of the experimental setup, emphasizes the reproducibility of the sensor signal for these materials. This type of behavior, non-linear for an extended concentration range, is not uncommon in solid sensors [11, 12, 19, 20]. The behavior may be explained by different sensing mechanisms in the low and high concentration regimes, or by a reversible modification of the material. These possibilities will be discussed further in the next subsections.

The reproducibility of the sensors was addressed by multiple measurements for certain runs and by the observation of baseline and conductivity changes over time in various atmospheres. Figure 6.7 shows a typical experiment of conductivity versus time for increasing concentrations of CO in air (in this case for the x=0.01 sample at 300 ^{o}C). As can be seen from the figure, the conductivity values are stable for each concentration and the conductivity in air does not drift after each exposure indicating that the sensing mechanism is fully reversible. Response and recovery times can also be obtained from this type of figure, as discussed below.

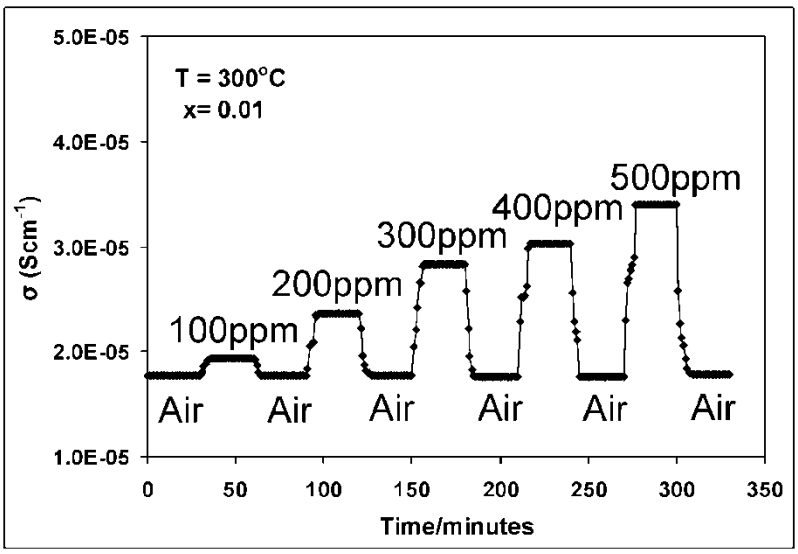

Figure 6.7. Sample experiment of conductivity vs. time for a sensor exposed to increasing concentrations of CO (x=0.01 material at 300°C).

A common occurrence in solid state sensors is the formation of coke upon exposure to carbon containing gases, and in particular hydrocarbons. In view of the success of the $Sm_{0.95}Ce_{0.05}Fe_{1-x}Co_xO_{3-\delta}$ (x=0-0.03) perovskites toward CO detection, the sensors were used for the detection of methane. In preliminary tests, undoped $Sm_{0.95}Ce_{0.05}FeO_{3-\delta}$ showed promise for the detection of methane at high temperature (Figure 6.8a). The figure shows changes in electrical conductivity upon exposure to pure hydrogen and methane at 500°C. Not only are the conductivity measurements stable for 24h under each gas, but the air baseline is recovered when the test gas is removed. These results indicate that the sensor response is reversible, it is not degraded during use and that no coke was formed in the process.

Figures 6.8b, 6.8c and 6.8d show the response of the cobalt doped sensors to different concentrations of methane in air. The x=0 material has sensitivity towards methane only at 300°C (and above), while the sensitivity of x=0.01 is almost the same at 200°C and 300°C. As a comparison, x=0.03 has highest sensitivity at 300°C but there is also a detectable response for methane at room temperature.

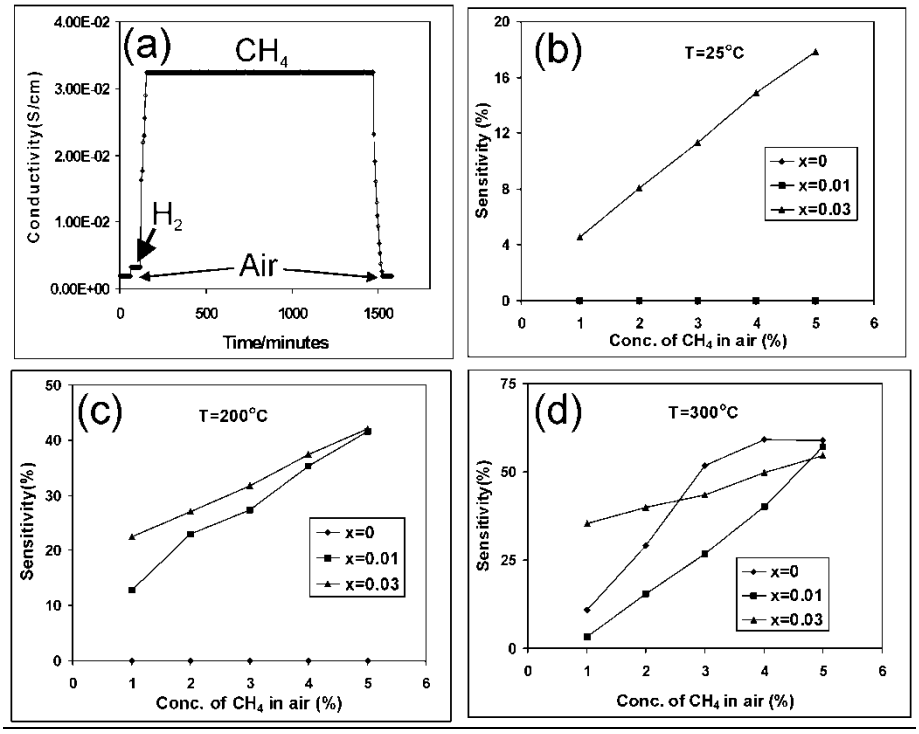

Figure 6.8. (a) Conductivity response of $Sm_{0.95}Ce_{0.05}FeO_{3-\delta}$ under air, pure hydrogen and pure methane at 500°C. (b, c and d) Methane concentration dependence of the sensor signal for $Sm_{0.95}Ce_{0.05}Fe_{1-x}Co_xO_{3-\delta}$ (x=0-0.03) sensors at 25°C, 200°C, and 300°C, respectively.

Generally, sensors can have different magnitudes of response at different temperatures for different gases. In this particular set, the performance of the sensors improves as the Co content increases; the sensor shows higher sensitivity at lower temperatures. This improvement could be interpreted as a combination of the increase in a more reactive species on the surface (Co) and the lowering of activation energies involved in the combined sensing process. The differential behavior of each sensor with respect to gases and temperature implies that a family of sensors can be used together and the multiple responses combined for identification of target gases.

6.3.3. Sensing mechanism

The injection of test gas in the testing chamber containing carrier gas (air) causes a change in electrical conductivity due to interactions of the gas with the surface of the sensors. In this work, the sensors under examination are n-type semiconductors while the testing gases are reducing agents (hydrogen, methane and carbon monoxide). In n-type sensors, the charge carrier species are electrons. As a general rule, oxidizing gases promote

the formation of electrons holes by taking away electrons from the conduction band, thereby decreasing the electrical conductivity of the n-type material; conversely, reducing gases increase the number of electrons by releasing electrons to the conduction band.

Such general behavior can in fact arise from a variety of possible mechanisms. For dense sensor designs, such as is the case here, one could describe a general surface reaction mechanism as in equation 6.2, where the reducing gas R (which may be pre-adsorbed) reacts with a surface oxygen species (O_2, O_2^-, or O^-) and releases electrons to the conduction band of the material [13, 19-21].

$$R + xO_{ads}^{y} \rightarrow RO_x + |xy|e^- \tag{6.2}$$

Alternatively, a bulk type mechanism may be considered. In this context, the perovskite sites can be described as oxide ions and electron-holes. The net result is the formation of oxygen vacancies and electrons which are released into the conduction band for increased conductivity. Using the Kröger-Vink notation [22], the reaction can be written as equation 6.3. There is a clear relationship between both mechanisms, since the removal of a surface oxygen species may be considered to generate a surface vacancy.

$$R + O_O^x + 2h^{\bullet} \rightarrow RO + V_O^{\bullet\bullet} + 2e^- \tag{6.3}$$

The concentration of adsorbed oxygen varies between the different materials as shown in Table 6.1. Additionally, for this type of perovskite the ratio of adsorbed to lattice oxygen changes for oxidizing and reducing atmospheres [23], suggesting a surface mechanism. However, a differentiation between both mechanisms was not possible in these experiments. The observations discussed in relation to Figure 6d may indicate that different mechanisms are in fact operational at different concentration ranges of the target gas, and the multiple oxidation states of metals measured at the surface may result in a transition at intermediate concentrations.

6.3.4. Response and efficiency of the sensors

The sensitivity of the sensors towards a particular gas (in the 1 to 5% range of concentration, figures 6.5, 6.6 and 6.8) can be further analyzed according to a power law behavior with respect to gas concentration as discussed by Windischmann et al. [24]. This relation can be expressed as (equation 6.4)

$$S_g = KC_g^{-\alpha} \qquad (6.4)$$

where S_g and C_g are the sensitivity (sensor signal) and concentration of a gas while K and α are fitting constants. The value of α is typically obtained from the slope of a plot between $\ln S_g$ and $\ln C_g$. In this type of analysis, the value of α gives a measure of the response of the sensor such that a larger value of α is desired.

Table 6.2. The values of α $Sm_{0.95}Ce_{0.05}Fe_{1-x}Co_xO_{3-\delta}$ (x=0-0.03) based sensors

Temperature(^{o}C)	**Co Conc. (x)**	α_{H_2}	α_{CO}	α_{CH_4}
25^{o}C	0	--[a]	--[a]	--[a]
	0.01	0.3737	--[a]	--[a]
	0.03	0.1916	0.9772	0.8429
200^{o}C	0	1.0997	1.0019	--[a]
	0.01	1.8736	0.6424	0.7127
	0.03	1.9245	0.7328	0.388
300^{o}C	0	1.759	0.9714	1.1007
	0.01	2.0935	0.6197	1.7408
	0.03	0.1195	0.7802	0.2654

[a] The conductivity of the sensors under these conditions was below the detection limit, and therefore values of sensitivity were not obtainable.

The values of α were calculated for each gas at 25^{o}C, 200^{o}C and 300^{o}C and the results are presented in Table 6.2. In general, the higher the value of alpha, the stronger is the dependence of sensitivity on concentration, and therefore the sensor is considered of higher quality. The value of α is also useful in the comparison with traditional sensors such as those based on tin oxide. The value of α for SnO_2 base sensors, for hydrogen detection, ranges between 1/6 (0.17) and 1/2 (0.5) [15, 25]. The $Sm_{0.95}Ce_{0.05}Fe_{1-x}Co_xO_{3-\delta}$ (x=0-0.03) based

sensors have significantly higher values of α for hydrogen, carbon monoxide and methane suggesting that these are strongly concentration dependant sensors.

The time required for the sensor to achieve 99% of the stable response values (response time) and for it to recover its original conductivity upon removal of the target gas (recovery time) is an important measure in the design of sensors. These values are summarized in Table 6.3. The data shows that: (1) recovery times are typically shorter than response times, which suggests that the oxidation process is faster than the reduction process for these materials; (2) the response and recovery times decrease as a function of temperature as one would expect for activated processes; and (3) the response time increases as a function of cobalt concentration, which can be ascribed to a decrease in grain boundaries due to increased particle sizes, a decrease in the number of active sites due to a decrease in the surface atomic ratio of Sm (high coordination number, more active sites for adsorption) and a decrease in surface adsorbed oxygen (available for interaction of target gas molecules) as a function of cobalt concentration.

Table 6.3. Response and recovery times for $Sm_{0.95}Ce_{0.05}Fe_{1-x}Co_xO_{3-\delta}$ (x=0-0.03) sensors

T°C	**Co conc. (x)**	**Response time (minutes)**			**Recovery time (minutes)**		
		1%H_2/air	1%CO/air	1%CH_4/air	1%H_2/air	1%CO/air	1%CH_4/air
25	0	--[a]	--[a]	--[a]	--[a]	--[a]	--[a]
	0.01	15	18	--[a]	12	15	--[a]
	0.03	18	14	22	14	11	18
200	0	3	4	--[a]	2	2	--[a]
	0.01	5	7	8	3	5	6
	0.03	8	6	10	4	5	9
300	0	2	2	4	1	2	3
	0.01	3	4	3	3	2	4
	0.03	4	5	6	3	4	5

[a] The conductivity of the sensors under these conditions was below the detection limit, and therefore values of sensitivity were not obtainable.

6.4. Conclusions

Sensors based on n-type semiconductors composed of $Sm_{0.95}Ce_{0.05}Fe_{1-x}Co_xO_{3-\delta}$ (x=0-0.03) were prepared. XPS shows that their surfaces were enriched with Sm and Co due to surface segregation, but cobalt doping decreases the level of Sm segregation. Furthermore surface adsorbed oxygen species decrease in concentration while lattice oxygen increases as

a function of cobalt content. All sensors showed a linear and reversible response towards H_2, CO and CH_4 at different temperatures. Higher values of constant "α ", suggested that these sensors are strongly concentration dependent. The performance of cobalt doped $Sm_{0.95}Ce_{0.05}FeO_{3-\delta}$ is highlighted its ability to detect H_2, CO and CH_4 even at room temperature in the concentration range of 1-5% in air. Additionally, the x=0.01 material was shown to perform in the detection of CO at the ppm range at 300^{o}C. The response time has strong dependence on the surface chemical composition and surface morphology of sensors.

6.5. References

[1] J.H. White, A.F. Sammells, J. Eletrochem. Soc. 140 (1993) 2167-2177.
[2] N. Bonanos, K. Knight, B. Ellis, Solid State Ionics. 79 (1995) 161-170.
[3] H.Y. Tu, Y.Takeda, N. Imanishi, O. Yamamoto, Solid State Ionics. 100 (1997) 283-288.
[4] T. Ishihara, M. Honda, T. Shibayama, H. Minami, H. Nishiguchi, Y. Takita, J. Eletrochem. Soc. 145 (1998) 3177-3183.
[5] V.V. Kharton, A.P. Viskup, E.N. Naumovich, V.N. Tikhonovich, Mater. Res. Bull. 34 (1999) 1311-1317.
[6] M.A. Pena, J.L.G. Fierro, Chem. Rev. 101 (2001) 1981-2017.
[7] H. Aono, E. Traversa, M. Sakamoto, Y. Sadaoka, Sens. Actuators B. 94 (2003) 132-139.
[8] M.C. Carotta, G. Martinelli, Y. Sadaoka, P. Nunziante, E. Traversa, Sens. Actuators B. 48 (1998) 270-276.
[9] S.M. Bukhari, J.B. Giorgi, Solid State Ionics. 180 (2009) 198-204.
[10] S.M. Bukhari, J.B. Giorgi, Solid State Ionics. 181 (2010) 392-401.
[11] Y.C. Chen, Y.H. Chang, G.J. Chen, Y.L. Chai, D.T. Ray, Sens. Actuators B. 96 (2003) 82-87.
[12] H. Tang, K. Prasad, R. Sanjines, F. Levy, Sens. Actuators B. 26-27 (1995) 71-75.
[13] O. Lupan, G. Chai, L. Chow, Microelec. Eng. 85 (2008) 2220-2225.
[14] J. Watson, Sens. Actuators B. 8 (1992) 173-177.
[15] J. Watson, K. Ihokura, G.S.V. Coles, Meas. Sci. Technol. 4 (1993) 711-719.
[16] N. Fairley, Casa XPS version 2.3.13 Dev73 (2007).
[17] H. Aono, M. Sato, E. Traversa, M. Sakamoto, Y. Sadaoka, J. Am. Ceram. Soc. 84 (2001) 341-347.
[18] W. Cheng, X. Ma, J. Phys.: Conference Series. 152 (2009) 012039.
[19] S. Nakata, M. Nakasuji, N. Ojima, M. Kitora, Appl. Surf. Sci. 135 (1998) 285-292.
[20] S. Nakata, K. Takemura, K. Neya, Sens. Actuators B. 76 (2001).
[21] R.K. Srivastava, P. Lal, R. Dwivedi, S.K. Srivastava, Sens. Actuators B. 21 (1994) 213-218.
[22] F.A. Kroger, H.J. Vink, Solid State Physics. 3 (1956) 307-435.
[23] S.M. Bukhari, J.B. Giorgi, Sens. Actuators B. 155 (2010) 524-537.
[24] H. Windischmann, P. Mark, J. Electrochem. Soc. 126 (1979) 627-633.
[25] P.K. Clifford, D.T. Tuma, Sens. Actuators B. 3 (1982) 233-254.

7. Performance of Co doped $Sm_{0.95}Ce_{0.05}FeO_{3-\delta}$ as SOFC anode under dry hydrogen and dry methane fuels

The contents of this chapter have been published as: Syed M. Bukhari and Javier B. Giorgi, Electrochemical Society Trans., 33(39) (2011) 81-91

Abstract

A newly developed perovskite series was investigated for performance as SOFC anodes. $Sm_{0.95}Ce_{0.05}Fe_{1-x}Co_xO_{3-\delta}$ (x=0-0.05) single phase perovskite oxides were synthesized through a sol gel method. AC and DC measurements were carried out on three-electrode button cells in order to investigate the effect of Co doping on reduction stability, coke resistance and electrochemical performance as SOFC anodes. The electrical conductivity under both air and $5\%H_2/N_2$ decreases while catalytic activity towards methane oxidation increases as a function of cobalt concentration. Under dry hydrogen fuel, all x=0-0.03 materials showed good performance with R_{CT} values lower than $1\Omega cm^2$. The fuel cell tests under methane revealed that the x=0.03 perovskite is the most catalytically active while being resistant to coking at low operating temperatures (500^oC).

7.1. Introduction

Solid oxide fuel cells (SOFC) are electrochemical devices which provide a realistic alternative toward clean energy by converting the chemical energy produced by oxidation of fuels directly into electricity with high conversion efficiency and low pollution emission [1, 2]. SOFCs have the ability to use hydrocarbons as fuel without external reforming [3], thereby improving efficiencies with existing fuels. The conventional SOFC uses yttria-stabilized-zirconia (YSZ) as the electrolyte and operates at high temperatures (800-1000^oC) to get sufficiently high ionic conductivity. High operational temperatures cause many problems, including material deterioration, sealing issues, long term stability and high cost. Recently low-temperature SOFCs (LT-SOFC) have received much attention; however at low operational temperatures polarization losses at the electrodes are usually high. The anode of LT-SOFCs should fulfill several requirements including good electrocatalytic activity, thermal and chemical stability in the anode compartment, thermal expansion matching with the electrolyte, and sufficiently high electronic and ionic conductivities.

The traditional SOFC anode, a Ni-YSZ cermet, has excellent catalytic properties and high electronic conductivity at high temperature, but it is not suitable for LT-SOFCs as it is

prone to coke and sulphur poisoning, and it has high mechanical stress with respect to appropriate low-temperature electrolytes. In recent years, perovskite type oxides (ABO_3) have received great attention as anode materials [4, 5] due to their mixed electronic and ionic conduction which extends the triple phase boundary to the entire exposed surface of the anode. The properties of these perovskite materials can be tuned by introducing substitutions at A-, B-, or both A and B-sites, thereby providing an excellent way to develop new anodes. The nature of the dopant determines the properties of the resulting perovskite materials. For example, the substitution of a donor dopant at the A-site can improve both the electronic conductivity [6, 7] and the reduction stability of the perovskite anode material [8]. Recently developed $Sm_{1-x}Ce_xFeO_{3-\delta}$ (x=0-0.05) materials have shown high reduction stability and high electrical conductivity under reducing conditions [9]. Additionally, these Ce doped materials are resistant to coke formation [10-12], likely because the introduction of Ce at the A-site increases the oxide ion conductivity, which helps in carbon cleaning mechanisms [13]. The electrical conductivity of $Sm_{0.95}Ce_{0.05}FeO_{3-\delta}$ (SCF) under both oxidizing and reducing conditions can be further improved by cobalt doping at the Fe site [14] due to the acceptor nature of Co and the weaker Co-O bond. The more reducible nature of the Co-O bond is also expected to improve catalytic performance [15]. This set of properties suggests that $Sm_{0.95}Ce_{0.05}Fe_{1-x}Co_xO_{3-\delta}$ (x=0-0.05) materials will be successful candidates in LT-SOFCs.

This work explores the potential of newly developed Co doped $Sm_{0.95}Ce_{0.05}FeO_{3-\delta}$ (SCFC) materials as anodes for LT-SOFC using H_2 and CH_4 fuel in the temperature range of 450-700^oC.

7.2. Experimental

7.2.1. Synthesis of perovskite powders

Powders of $Sm_{0.95}Ce_{0.05}Fe_{1-x}Co_xO_{3-\delta}$ (x=0-0.05) were prepared by using a sol gel method via citrate precursors, as previously reported [14]. Briefly, separate solutions of iron nitrate [$(Fe(NO_3)_3 \cdot 9H_2O$, Alfa Aesar, minimum 98%], samarium nitrate [$(Sm(NO_3)_3.6H_2O$, Alfa Aesar, 99.9%)], cerium nitrate [$(Ce(NO_3)_3 \cdot 6H_2O$, Alfa Aesar, 99.5%)], and cobalt nitrate [$(Co(NO_3)_2. \cdot 6H_2O$, AlfaAesar, 99%] were prepared according to the desired stoichiometry in de-ionized water. These four metal nitrate solutions were mixed with a citric acid solution and the resulting mixture was dried at 100°C to obtain amorphous citrate precursors. These amorphous citrate precursors were ground manually and then calcined at 850°C for 24 hour

to form perovskite structures. Powder X-ray diffraction confirmed the single phase of the perovskite structures.

7.2.2. Preparation of button cells

Button cells were used to test the performance of these cobalt doped $Sm_{0.95}Ce_{0.05}FeO_{3-\delta}$ perovskite materials as anodes. An electrolyte supported cell design with a three-electrode geometry was chosen. The three electrode geometry allows the separation of performance for each electrode, thereby allowing the independent assessment and comparison of each perovkite material in the series as anodes. The simplest design for an electrolyte-supported three-electrode cell is shown in Figure 7.1a, where the cathode and reference electrodes are placed on the same side of electrolyte at a reasonable distance while ensuring the alignment of cathode and anode. Although we have successfully used this geometry in the past, care must be taken to minimize potential problems such as cross talk between electrodes and misalignment of cathode and anode [16, 17]. These issues can result in very large errors in the measurements. Additionally, the distance requirement in this geometry forces the area of anode and cathode to be small.

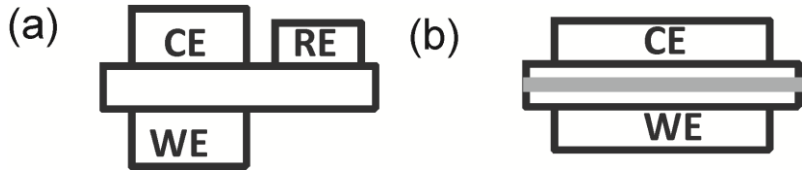

Figure 7.1. Configuration of electrolyte supported button cells. (a) Conventional configuration with both the reference electrode (RE) and the counter electrode (CE) on the same side of the electrolyte; (b) Modified configuration in which the reference electrode (grey color) is wrapped around the electrolyte disc.

In order to maximize the electrode area and minimize errors in the electrochemical measurements, a symmetric geometry was chosen in which the reference electrode was wrapped around the electrolyte disc (Figure 7.1b). The main drawback of this geometry is that the large electrolyte thickness required results in low values of current and power measured.

To make each button cell, an anode disc was made from samarium doped ceria (SDC, fuelcellmaterials.com). The 6.0g of SDC powder was uniaxially pressed to make a disc. The SDC disc was sintered in air at 1400^{o}C for 4h. The sintered disc was ~2mm thick with a

diameter of ~20mm. An anode slurry consisting of the perovskite material and Triton-X100 (Avocado Research Chemicals Ltd.) was painted on one side of the SDC disc and sintered in the furnace for 4h at 1400^{o}C. A current collector (Pt gauze, AlfaAesar) was attached by embedding it in additional anode slurry and sintered again at 1400^{o}C for 4h. Similarly, a cathode slurry consisting of a mixture of LSCF and SDC (50%w/w) in Triton-X100 emulsion was painted along with a current collector opposite to the anode. Finally, a Pt wire reference electrode was wrapped around the electrolyte disc and Pt paste was used to optimize the contact. The disc was then sintered at 800^{o}C for 1h to finalize the attachment of the reference electrode. The surface morphology of the electrodes was analyzed before and after fuel cell operation by scanning electron microscopy (SEM, JEOL JSM-7500F).

7.2.3. Fuel cell setup

Figure 7.2 shows the detailed schematic of the fuel cell setup used for the measurements. A customized stainless steel ultratorr fitting was used to provide gas inlet and outlet distribution. The button cell is supported on a large diameter alumina tube. A small diameter alumina tube serves as the fuel inlet. A Pyrex ring is used to seal the button cell at the top of the big alumina tube. To ensure a good sealing, a small piece of alumina tube is placed on top of the button cell to provide pressure. The whole setup fits within a tube furnace connected to temperature controller. Sealing at the anode side was achieved by partially melting the Pyrex ring at 950^{o}C for 1h. The three electrodes were connected to a PARSTAT 2273 potentiostat for data collection.

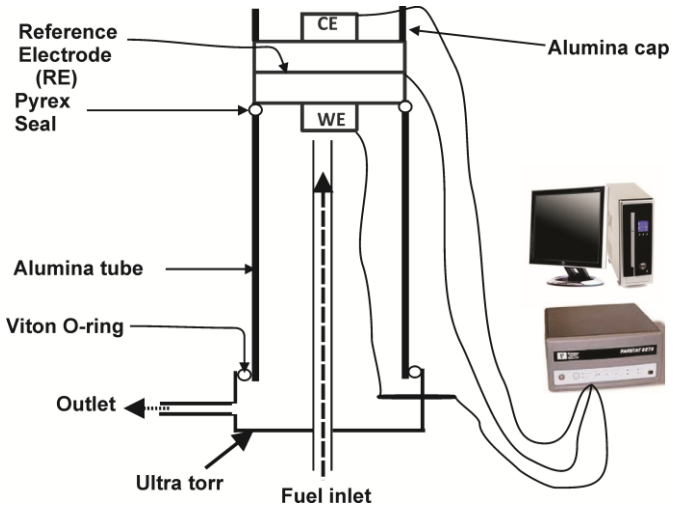

Figure 7.2. Schematic of the fuel cell setup.

Electrochemical measurements were performed in the temperature interval of 450 to 700^{o}C in 50^{o}C steps under dry hydrogen and dry methane, separately. Choronoamperometry experiments were carried out at different overpotentials (0V to 1.0V) to measure cell potentials and currents. To determine anode polarization resistance, R_P (charge transfer resistance, R_{CT}), electrochemical impedance (EI) measurements were obtained at OCV from 100 kHz to 100 mHz with an AC amplitude of 10mV. The impedance spectra were fitted by using a simple equivalent circuit model: $L_1R_S[R_{CT}CPE_1]$. In this equivalent circuit, R_S and R_{CT} are the serial and charge transfer resistances respectively. L_1 is an inductor having a value in the order of 10^{-6}. CPE_1 is a constant phase element which accounts for inhomogenity of the anode surface and its value is less than 1. The exchange current density values were calculated by using the general formula: $i_o=RT/nFR_{CT}$ where R is the universal gas constant, T is temperature, n is the number of electrons involved in the charge transfer process, F is Faraday constant and R_{CT} is the charge transfer resistance.

7.3. Results and Discussions

7.3.1. Hydrogen fuel cell performance

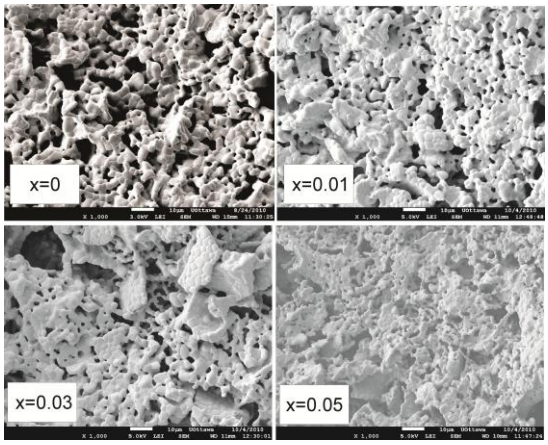

Figure 7.3. SEM micrographs of four perovskite anodes, $Sm_{0.95}Ce_{0.05}Fe_{1-x}Co_xO_{3-\delta}$ (x=0-0.05).

Prior to installation of the button fuel cell for performance testing, the surface morphology of the perovskite anodes was observed by electron microscopy. Figure 7.3 shows typical images for the four Co concentrations discussed in this manuscript. All

samples show porous surfaces with similar porosities and particle sizes. The cross sectional view of these samples also revealed that both cathode and anode layers were well adhered to the electrolyte with an average electrode thickness of 450 microns.

Previous work had shown that these perovskites are stable in a reducing atmosphere at temperatures below 800^{o}C. The electrode morphology does not change significantly upon operation with pure hydrogen. However, the conductivity of the material does depend on the surrounding environment. Figure 7.4 shows a comparison of the conductivities measured in air and 5%v/v H_2/N_2 for materials in this perovskite series. The x=0-0.03 materials show higher electrical conductivity under reducing conditions than in air (i.e., positive value of σ_R-σ_o). In contrast, the x=0.05 sample shows higher electrical conductivity under air (i.e., negative value of σ_R-σ_o). This indicates a change in electrical behaviour from x=0.03 to x=0.05 from n-type to p-type.

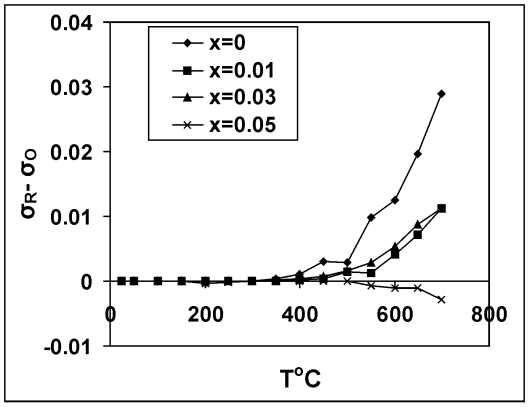

Figure 7.4. Comparison of electrical conductivities measured under air (σ_o) and 5%v/vH_2/N_2 (σ_R).

The fuel cells were operated under dry hydrogen fuel in the temperature range of 450 to 700^{o}C. At 700^{o}C, the theoretical OCV is 1.03V, but the measured values were always significantly lower (~ 0.860V). Usually, a lower OCV value suggests the presence of gas or current leakage across the electrolyte. However, SDC has consistently shown OCV values lower than expected. This observation has been explained in the literature in terms of SDC's low densification [18] and its partial reduction near the surface of the anode [19, 20] under fuel conditions. Additionally, the difference between the theoretical and experimental OCV values is consistently temperature dependent, suggesting that it is an intrinsic property of the

system and not a function of the setup. At 450^{o}C the theoretical value of OCV is -1.089V while the experimentally determined value was -1.026V.

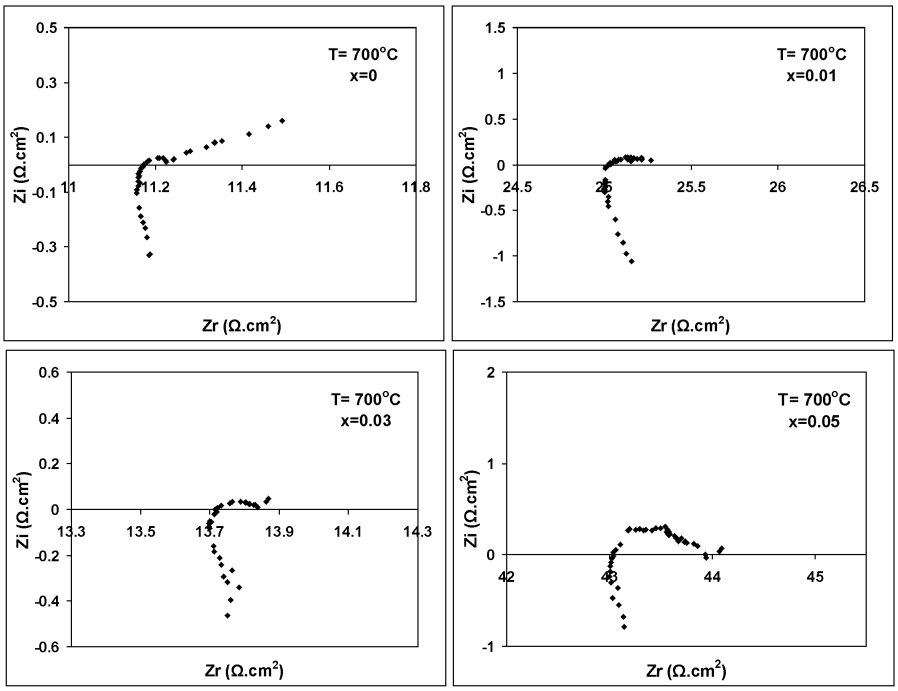

Figure 7.5. AC impedance spectra of $Sm_{0.95}Ce_{0.05}Fe_{1-x}Co_xO_{3-\delta}$ (x=0-0.05) anodes collected at OCV at 700^{o}C under dry hydrogen.

Fuel cells with OCVs above 0.8V were considered viable and run for a full collection of electrochemical data. Figure 7.5 shows the AC impedance spectra for x=0, 0.01, 0.03 and 0.05 at 700^{o}C while results of EIS analysis are summarized in Table 7.1. The charge transfer resistance values decrease as a function of temperature for each anode material. This is expected, as the kinetics are temperature dependent and one would expect that the higher the temperature, the easier the transfer of electrons (higher exchange current density and lower resistance). In contrast, the charge transfer resistance varies in an irregular manner as a function of cobalt concentration. Importantly, the undoped cobalt anode (SCF) shows the lowest values of R_{CT} (highest i_o, 1662 mAcm^{-2} at 700^{o}C) in the series while among the cobalt doped materials, x=0.03 shows the highest i_o of 522 mAcm^{-2} (lowest R_{CT},0.16 Ωcm^2 at 700^{o}C)

Table 7.1. The charge transference resistances (R_{CT}) ans current densities (i_o) $Sm_{0.95}Ce_{0.05}Fe_{1-x}Co_xO_{3-\delta}$ (x=0-0.05) anodes at different temperatures under dry hydrogen.

T°C	x=0	x=0.01	x=0.03	x=0.05
	R_{CT} (Ωcm^2)	R_{CT} (Ωcm^2)	R_{CT} (Ωcm^2)	R_{CT} (Ωcm^2)
450	1.8±0.27 (35±5) [a]	16.1± 2 (4±0.6)[a]	4.09± 0.6 (15±2)[a]	8.25± 1.2 (8±1)[a]
500	0.64± 0.09 (103±15)[a]	5.5± 0.8 (12±2)[a]	0.97± 0.14 (69±10)[a]	7.02± 10 (10±2)[a]
550	0.29± 0.04 (248±37)[a]	1.4± 0.2 (50±8)[a]	0.56± 0.08 (127±19)[a]	2.69± 0.40 (26±4)[a]
600	0.15± 0.02 (496±74)[a]	1.1± 0.2 (72±11)[a]	0.39± 0.06 (194±29)[a]	2.22± 0.33 (34±5)[a]
650	0.08± 0.01 (1060±159)[a]	0.56± 0.08 (143±21)[a]	0.30± 0.04 (265±40)[a]	1.82± 0.27 (44±7)[a]
700	0.05± 0.01 (1662±249)[a]	0.25± 0.03 (329±49)[a]	0.16± 0.02 (522±78)[a]	1.00± 0.15 (84±13)[a]

[a] exchange current densities in $mAcm^{-2}$ calculated from the charge transfer resistances

The values of charge transfer resistances of these cobalt-doped perovskite materials are lower than the more traditional Cu-CeO_2/YSZ cermets as well as some other perovskite type oxides like $LaMn_{0.50}Cr_{0.50}O_{3\pm\delta}$ (LMC), $La_{0.75}Sr_{0.25}Cr_{0.5}Mn_{0.5}O_3$ (LSCM) and $La_{0.65}Ce_{0.1}Sr0_{.25}Cr_{0.5}Mn_{0.5}O_3$ (Ce-LSCM) at relatively low operational temperatures. Table 7.2 summarized the anode polarization resistances of some reported anode materials. The values of R_{CT} for LSCM and Ce-LSCM perovskites were reported as 0.26 and 0.20 Ωcm^2 at 900°C for hydrogen oxidation in humidified condition. The Cu-CeO_2/YSZ anode has shown 0.8 Ωcm^2 charge transfer resistance at 710°C. As shown in Table 7.1, the R_{CT} value for perovskites with cobalt content up to x=0.03 is less than 1 Ωcm^2 in the temperature range of 500-700°C. Such low R_{CT} values suggest a facile electron transfer process and emphasize the potential of these materials as SOFC anodes.

The variation of the exchange current density with Co content was unexpected, but it can be rationalized by considering the general effects of Co doping on the properties of the perovskite. Qualitatively, after an initial disruption in the perovskite properties by the addition of a small amount of cobalt, the addition of cobalt is expected to increase reactivity toward oxidation reactions because of the more reducible nature of the Co-O bond [26]. However, as discussed above (Figure 7.4), addition of Co also changes the conductivity of

the perovskite from n-type to p-type thereby increasing the resistance in a reducing atmosphere. The net result is an increase in i_0 at low Co content, and an eventual decrease.

Table 7.2. Reported charge transference resistances (R_{CT}) of different anodes at different temperatures under wet hydrogen.

Anodes	**T (^oC)**	**R_{CT} (Ωcm^2)**	**Reference**
$La_{0.75}Sr_{0.25}Cr_{0.5}Mn_{0.5}O_3$(LSCM)	900	0.26	[21]
$La_2Sr_4Ti_6O_{19-\delta}$	900	2.97	[22]
$La_{0.65}Ce_{0.1}Sr0_{.25}Cr_{0.5}Mn_{0.5}O_3$ (Ce-LSCM)	900	0.2	[23]
3%CeO_2-27%Ni-70%YSZ	800	1.32	[24]
MCuCo40	750	1.70	[25]
Cu/CeO_2/YSZ	710	0.8	[17]
SCFC (x=0.03)	450	4.09	This work
SCFC (x=0.03)	700	0.16	This work

Polarization curves and power curves were obtained for all the fuel cells. The general trend in performance follows the kinetic trends observed by EIS, namely the maximum cell power of the cobalt doped perovskites was found for the x=0.03 Co content. Figure 7.6 shows the power curves for all cells at the different operating temperatures. In analyzing the figure, it is important to remember that the low values of cell power are due to the very thick electrolyte in our design.

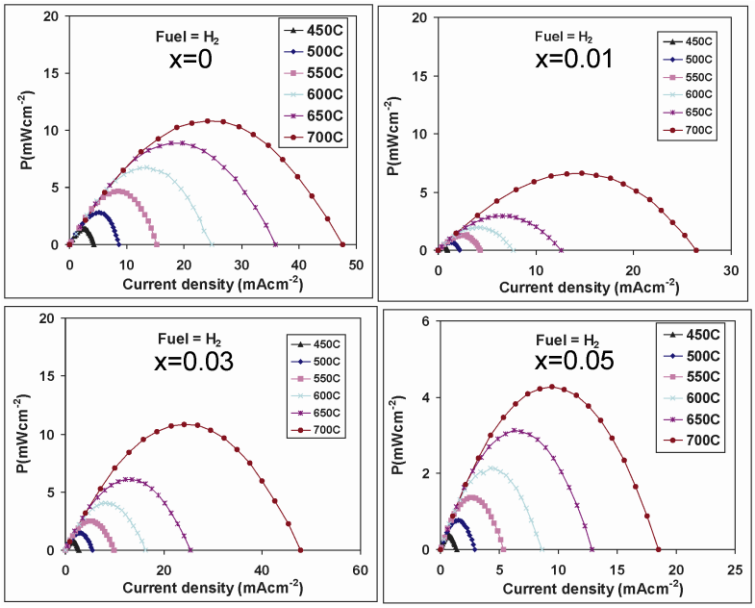

Figure 7.6. Power curves of $Sm_{0.95}Ce_{0.05}Fe_{1-x}Co_xO_{3-\delta}$ (x=0-0.05) anodes at different temperatures under hydrogen fuel.

In order to test the performance of these newly developed $Sm_{0.95}Ce_{0.05}Fe_{1-x}Co_xO_{3-\delta}$ (x=0-0.05) perovskite anodes in terms of their reduction stability, choronoamperometry experiments were performed under dry hydrogen fuel in each case. In these experiments, cell current was measured against an overpotential of 0.450V under dry hydrogen for 15h. These cell currents were then used to calculate cell powers in each case. Some of the results of these experiments are presented in Figure 7.7. Analysis of the results revealed; (i) Cell power values increase with increase in temperature; (ii) As a function of Co concentration the trend of cell powers is the same as presented by EIS analysis i.e., cell power is maximum for the x=0.03 sample; (iii) Performances of these anodes are stable, the cell powers did not change significantly over time.

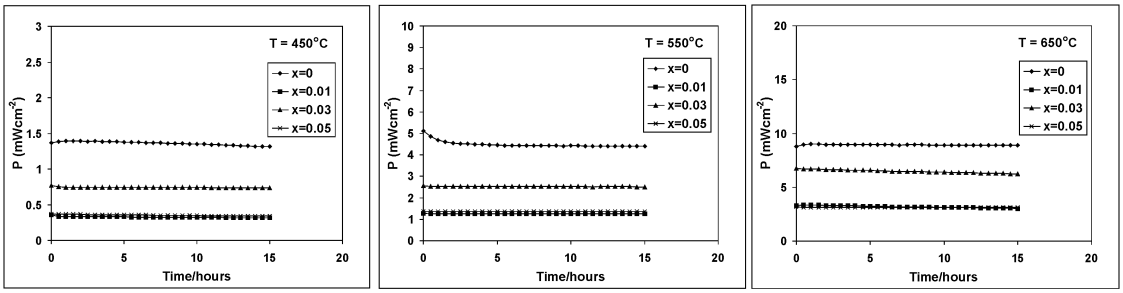

Figure 7.7. Performance of $Sm_{0.95}Ce_{0.05}Fe_{1-x}Co_xO_{3-\delta}$ (x=0-0.05) anodes under dry hydrogen for 15h at 450°C, 550°C and 650°C. Cell powers calculated from current density obtained at an overpotential of 0.450V as a function of time.

7.3.2. Methane fuel cell performance

The performance of the fuel cell with hydrogen fuel showed the potential of the perovskite anodes, but the effect of Co doping was expected to be particularly notable for oxidation of methane. The different anodes were therefore run with pure methane fuel and their resistance toward coking was evaluated. At the start of each measurement, OCV was measured. The OCV values for these fuel cells under dry methane were lower as compared to hydrogen. The x=0.03 material showed the highest value of OCV at all temperatures in the series. At 700°C, the OCV for x=0, 0.01, 0.03 and 0.05 anode based fuel cells were 0.647V, 0.602V, 0.710V and 0.640V respectively.

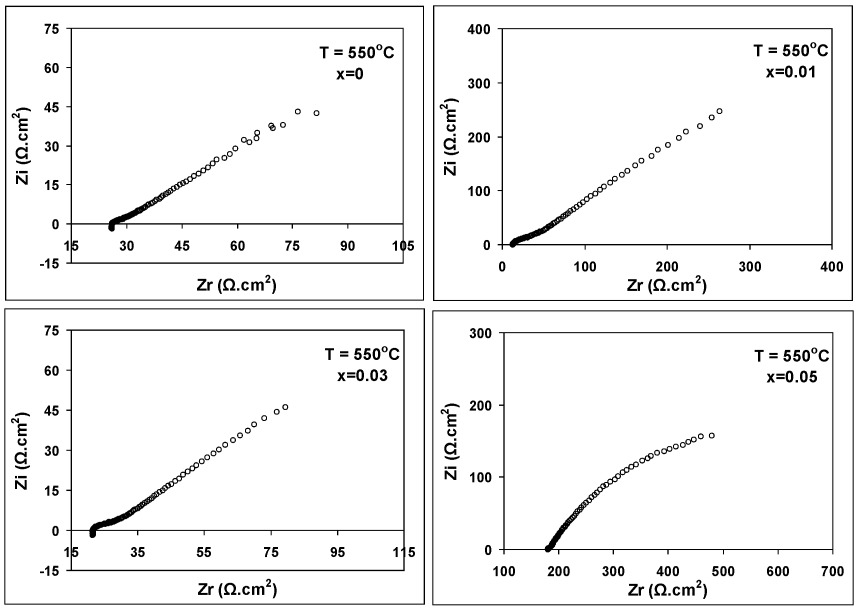

Figure 7.8. AC impedance spectra of $Sm_{0.95}Ce_{0.05}Fe_{1-x}Co_xO_{3-\delta}$ (x=0, 0.03 and 0.05) anodes collected at OCV at 550°C under dry methane.

Table 7.3. The charge transference resistances (R_{CT}) and exchange current densities of $Sm_{0.95}Ce_{0.05}Fe_{1-x}Co_xO_{3-\delta}$ (x=0-0.05) anodes at different temperatures under dry methane.

T°C	x=0	x=0.01	x=0.03	x=0.05
	R_{CT} (Ωcm^2)	R_{CT} (Ωcm^2)	R_{CT} (Ωcm^2)	R_{CT} (Ωcm^2)
450	2643±396[a]	3800±570	285±43	3882±582[a]
500	214±32[a]	881±130	53.49±8	2244±300[a]
550	21.48±3	42.82±6	14.01±2	687±100
600	8.85±1	16.26±2	8.78±1	419±60
650	3.79±0.6	12±2	2.4±0.4	10.5±2
700	1.8±0.3	7.5±1	1.35±0.2	6±1

[a] These values were obtained at the beginning of the measuring sequence, but the cells were unstable and further performance measurements were not possible.

From EIS experiments with all $Sm_{0.95}Ce_{0.05}Fe_{1-x}Co_xO_{3-\delta}$ (x=0-0.05) anodes, the charge transfer resistances were obtained at different temperatures (Table 7.3). Figure 7.8 shows the Nyquist plots collected at 550°C of these cobalt doped anodes. The performance follows the same trend observed with hydrogen fuel, namely that there is an increase in charge transfer resistance upon introduction of Co in the perovskite lattice, and a minimum R_{CT} is observed at x=0.03 cobalt content. The R_{CT} values obtained for the x=0 and x=0.05 samples at low temperature reflect the initial conditions. These anodes are not stable and their performance changes quickly with time. Table 7.4 summarizes the reported charge transfer resistances for

some novel anode materials. It is noteworthy that the operational temperature of these anode materials is in the range of 800-900^{o}C. Although the value of R_{CT} is less than one in some cases, the operational temperature is high. Therefore, there is still need of developing new materials which can operate at lower temperature with the comparable performance to the existing anode materials. In this cobalt doped perovskite series, the values of the charge transfer resistances for x=0.03 is in the range of 1-9 Ωcm^2 at operational temperatures of 600-700^{o}C which is as good as existing novel anode materials. This suggests that fuel cells can be run with better performance at lower temperature under dry methane with an x=0.03 anode.

Table 7.4. Reported charge transference resistances (R_{CT}) of different anodes under wet methane.

Anodes	T (^{o}C)	R_{CT} (Ωcm^2)	Reference
$La_{0.75}Sr_{0.25}Cr_{0.5}Mn_{0.5}O_3$	900	0.87	[21]
3%CeO_2-27%Ni-70%YSZ	800	2.54	[24]
LSCM/GDC(33:67)	800	0.65	[27]
$La_2Sr_4Ti_6O_{19-\delta}$	850	8.93	[22]
$Sm_{0.95}Ce_{0.05}Fe_{0.97}Co_{0.03}$	500	53.49	This work
	700	1.35	

The fuel cell power data is presented in Figure 7.9. The cell power trends are the same as those found by observation of the exchange current density from EI analysis. Indeed, the x=0.03 perovskite has the highest value of cell power in the series. However, it is important to note that only the perovskites with moderate cobalt content operate in the full temperature range. The undoped perovskite is not reactive enough toward methane oxidation, and therefore its operation at temperatures below 550^{o}C is not stable and even the OCV values are not reliable. In the case of x=0.05 at low temperature, the lack of stability may be linked to a different phenomenon, such as limiting kinetics due to low conductivity of the p-type material.

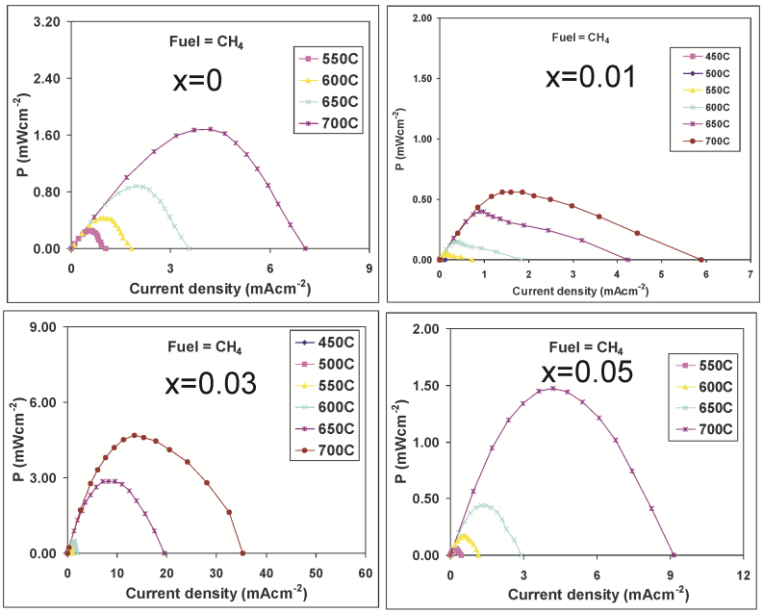

Figure 7.9. Power curves of $Sm_{0.95}Ce_{0.05}Fe_{1-x}Co_xO_{3-\delta}$ (x=0-0.05) anodes at different temperatures under dry methane as fuel.

Qualitatively, one can expect an increase in catalytic activity towards methane oxidation (due to the weaker Co-O bond) and a decrease in n-type conductivity (due to the p-type nature of cobalt oxide) as a function of cobalt concentration in this series. As a result of the combined effect the R_{CT} value of x=0.03 is minimum in the series. However, with the use of methane as fuel, an additional effect must be taken into consideration, namely the formation of coke at the anode surface. Figure 7.10 shows the surface morphology of anodes after operation under dry methane at 700^{o}C for 22h. The images show that the x=0.01 perovskite is progressively poisoned due to high levels of coking as indicated by the carbon wires observed. The x=0.03 sample shows light coking, and there was no coking at all in the case of x=0 and x=0.05 samples.

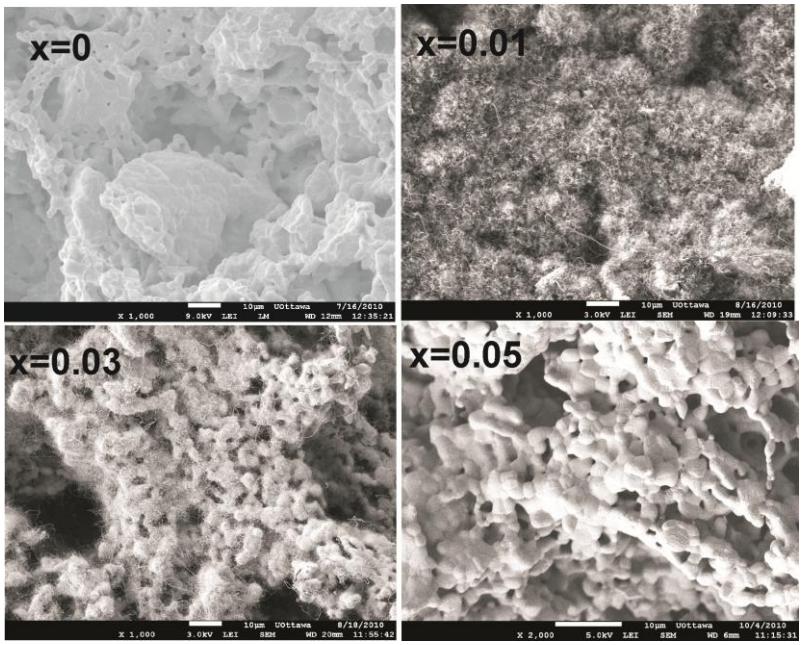

Figure 7.10. SEM micrographs of $Sm_{0.95}Ce_{0.05}Fe_{1-x}Co_xO_{3-\delta}$ (x=0-0.05) anodes after operation under dry methane at 700^{o}C.

Coking seemed to be more pronounced at high temperature. In order to test this and other degradation processes, the best performing perovskite (x=0.03) was selected for a long term performance experiment under dry methane at 500^{o}C. Figure 7.11 shows all aspects of this test for nine days with electrochemical data collected in cycles over that time period. Figure 7.11a shows an initial decrease in the OCV value which stabilizes after approximately 48h of continuous operation. Similarly, the polarization curves and power curves converge after two days (Figure 7.11b and Figure 7.11c). All performance parameters remain stable after the initial two days, suggesting a conditioning or microstructural change of the anode during the initial stages. SEM analysis of the anode surface after operation for nine days revealed a densification of the anode but no coke formation (Figure 7.11d). This observation suggests that by improving microstructural characteristics we will have obtained an active anode resistant to carbon poisoning for operation at low temperature.

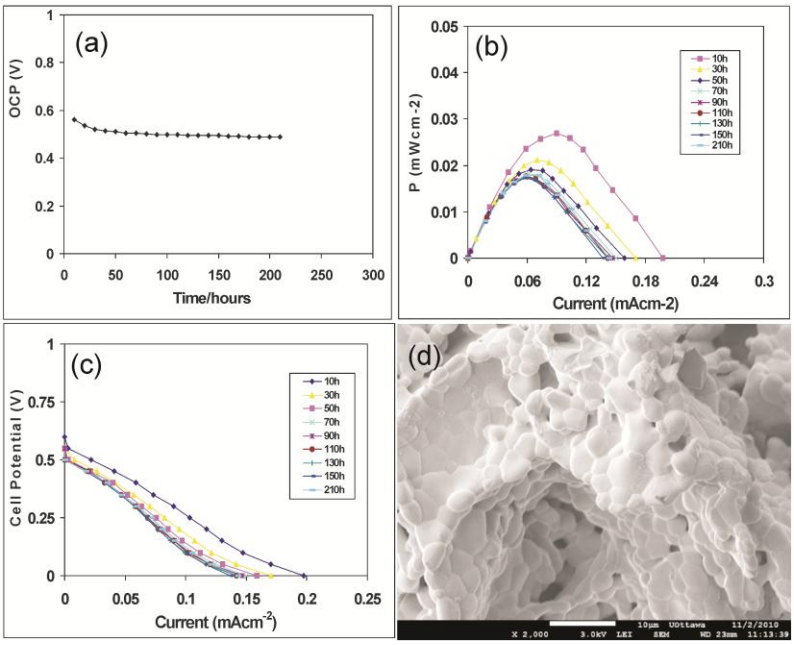

Figure 7.11. Long term performance of $Sm_{0.95}Ce_{0.05}Fe_{0.97}Co_{0.03}O_{3-\delta}$ at 500°C under dry methane. (a) OCV (b) Cell power (c) Polarization curves (d) surface morphology after performance.

7.4. Conclusions

A new family of perovskite oxides with formula $Sm_{0.95}Ce_{0.05}Fe_{1-x}Co_xO_{3-\delta}$ (x=0-0.05) has been investigated as SOFC anodes for direct oxidation of dry hydrogen and dry methane. These materials are stable under reducing conditions below 800°C. Electrical conductivity measurements under air and 5%v/v H_2/N_2 reveal a change in conductivity from n-type to p-type above x=0.03. The fuel cell tests performed under dry hydrogen revealed that the x=0.03 material exhibited the highest exchange current density among cobalt doped materials. Under dry methane, the performance of the x=0.03 perovskite was highest in the series with the lowest charge transfer resistance. Importantly, while coking is observed at high temperatures, the x=0.03 material is resistant to coking at low temperature (500°C). These results suggest that these cobalt doped perovskite materials are good candidates for SOFC anodes.

7.5. References

[1] N.Q. Minh, J. Am. Ceram. Soc. 76 (1993) 563-588.
[2] S.P.S. Badwal, K. Foger, Ceram. Int. 22 (1996) 257-265.
[3] D. Sanchez, R. Chacartegui, A. Munoz, T. Sanchez, International Journal of Hydrogen Energy. 33 (2008) 1834-1844.
[4] A. Ovalle, J.C. Ruiz-Morales, J. Canales-Vázquez, D. Marrero-López, J.T.S. Irvine, Solid State Ionics. 177 (2006) 1997-2003.
[5] G. Pudmich, B.A. Boukamp, M. Gonzalez-Cuenca, W. Jungen, W. Zipprich, F. Tietz, Solid State Ionics. 135 (2000) 433-438.
[6] S. Hui, A. Petric, J. Eur. Ceram. Soc. 22 (2002) 1673-1681.
[7] K.T. Lee, A. Manthiram, Solid State Ionics. 178 (2007) 995-1000.
[8] M.A. Pena, J.L.G. Fierro, Chem. Rev. 101 (2001) 1981-2017.
[9] S.M. Bukhari, J.B. Giorgi, Solid State Ionics. 180 (2009) 198-204.
[10] S.M. Bukhari, J.B. Giorgi, ECS Trans. 28 (2010) 19-29.
[11] S.M. Bukhari, J.B. Giorgi, J. Electrochem. Soc. 158 (2011) J159-J164.
[12] S.M. Bukhari, J.B. Giorgi, J Power Sources. submitted May (2011).
[13] K. Urasaki, Y. Sekine, S. kawabe, E. Kikuchi, M. Matsukata, Appl. Catal. A. 286 (2005) 23-29.
[14] S.M. Bukhari, J.B. Giorgi, Solid State Ionics. 181 (2010) 392-401.
[15] J.R. Mawdsley, T.R. Krause, Appl. Catal. A. 334 (2008) 311-320.
[16] J. Winkler, P.V. Hendriksen, N. Bonanos, M. Mogensen, J. Electrochem. Soc. 145 (1998) 1184-1192.
[17] S. McIntosh, J.M. Vohs, R.J. Gorte, J. Electrochem. Soc. 150 (2003) A1305-A1312.
[18] H. Shi, W. Zhou, R. Ran, Z. Shao, J. Power Sources. 195 (2010) 393-401.
[19] T. Miyashita, J. Mater. Sci. 40 (2005) 6027.
[20] T. Miyashita, The Open Materials Science Journal. 3 (2009) 33-39.
[21] S. Tao, J.T.S. Irvine, Nature Materials. 2 (2003) 320-323.
[22] J. Canales-Vazquez, S.W. Tao, J.T.S. Irvine, Solid State Ionics. 159 (2003) 159-165.
[23] E. Lay, G. Gauthier, S. Rosini, C. Savaniu, J.T.S. Irvine, Solid State Ionics. 179 (2008) 1562-1566.
[24] J. Qiao, N. Zhang, Z. Wang, Y. Mao, K. Sun, Y. Yuan, Fuel Cells. 09 (2009) 729-739.
[25] A. Fuerte, R.X. Valenzuela, M.J. Escudero, L. Daza, J. Power Sources. 196 (2011) 4324-4331.
[26] I.-H. Park, H.-P. Lee, Bull. Korean Chem. Soc. 9 (1988) 283-288.
[27] X.J. Chen, Q.L. Liu, K.A. Khor, S.H. Chan, J. Power Sources. 165 (2007) 34-40.

8. Synthesize and characterization of $Sm_{0.95}Ce_{0.05}Fe_{1-x}Ni_xO_{3-\delta}$ (x=0-0.10) perovskite materials

The contents of this chapter have been published as: Syed M. Bukhari and Javier B. Giorgi, Solid State Ionics, 194 (2011) 33-40

Abstract

A new series of perovskite materials with formula $Sm_{0.95}Ce_{0.05}Fe_{1-x}Ni_xO_{3-\delta}$ ($0 \leq x \leq 0.10$) has been prepared by sol-gel combustion via a citrate precursor route. X-ray diffraction data showed that materials prepared by this method had a single orthorhombic phase belonging to the Pnma (62) space group. The study of powders sintered in air and in reducing atmospheres reveals that these materials do not show phase separation in air (up to 1350^{o}C) nor under 5%v/v H_2/N_2 (up to 700^{o}C), but a phase separation of Sm_2O_3 does occur at and above 800^{o}C under 5%v/v H_2/N_2 without deterioration of the perovskite phase. The surfaces of all the powders (fresh, in-situ reduced and ex-situ reduced) were Sm rich, and multiple oxidation states for Fe were observed. XP analysis of in-situ reduced samples (800^{o}C and above) shows that metallic Fe forms in all nickel doped materials except x=0.07. The surface oxygen vacancies and percentages of lattice and adsorbed oxygen for this series of Ni doped materials were determined and the oxygen recapturing ability is explained in terms of the multiple oxidation states of Fe.

8.1. Introduction

Perovskites with the ABO_3 structure have demonstrated great promise in a variety of applications, including sensors[1-8], solid oxide fuel cells[9-17], and catalysis[18-21]. In the traditional formulation of ABO_3 perovskites, the A site is usually occupied by lanthanides, alkali metals or alkaline earth metals while the B-site elements are typically first row transition metals[4, 22, 23]. However, partial substitution can be done at the A-site, at the B-site, or both at the A- and the B-sites simultaneously. The purpose of substitution is to enhance the commercial utility of the perovskite devices by improving or fine tuning physical properties such as thermal stability, chemical stability, electrical conductivity, magnetic effects, catalytic activity and electrode-electrolyte compatibility.

The traditional ABO_3 perovskite $SmFeO_3$ is an orthoferrite semiconductor material. It has been reported to have utility for sensing oxidizing gases like ozone, oxygen and NO_2 [1,

24], as well as limited utility toward reducing gases like CO [2, 25, 26]. However, these sensors suffer from a lack of response at lower temperatures due to the very low electrical conductivity of the material. There is a need to improve the electrical conductivity of the perovskite to obtain a better response at lower temperature.

The nature of the A-site cation in ABO_3 perovskites can play an important role in electrical conductivity and chemical stability. In previous work, we have reported that doping Ce (a bigger cation) at the Sm site in $SmFeO_3$ addressed the stability (phase separation) and poor electrical conductivity issues of undoped $SmFeO_3$ under reducing conditions [25]. This Ce doping transformed $SmFeO_3$ from a p-type into a n-type material. This modification opened new opportunities for research in sensing reducing gases by using modified $SmFeO_3$ ($Sm_{1-x}Ce_xFeO_3$, x=0-0.05).

The nature of the B-site cation in ABO_3 perovskites can also play an important role in electrical conductivity and chemical stability. Typically, a weaker B-O bond results in a more easily reducible perovskite, which increases the likelihood of possible phase separations and limits the utility of the device [27]. However, a dopant at the B site may also increase the electrical conductivity of the perovskite. A balance between greater stability and better electrical conductivity may help to achieve an optimally performing material.

B-site substitution by Co, Ni and Mg in $SmFeO_3$ has been previously studied [28-31]. This substitution has improved conductivity and sensitivity towards different gases like O_3, NO_2, ethanol and acetone. These $SmFeO_3$ based materials have not been effectively used for detection of reducing gases like H_2, CO and CH_4. The most probable reason is the relative bond strength of M-O (M= Co, Ni and Mg) under reducing conditions. The Co-O, Ni-O and Mg-O bonds are weaker than the Fe-O bond under reducing conditions [27, 32], therefore one would expect that the reducibility of $SmFeO_3$ would increase on doping Co, Ni and Mg at the Fe site of $SmFeO_3$. In recent work [33], the electrical conductivity of $Sm_{0.95}Ce_{0.05}FeO_{3-\delta}$ was tuned by doping Co at the Fe-site. The results showed an improvement in the electrical conductivity at the expense of reduction stability. The resulting cobalt doped materials were stable in reducing environments (5%v/v H_2/N_2) up to 700^{o}C, but suffered from phase separation and perovskite structure deterioration issues at 800^{o}C and above. Subsequent exploration of Co doped $Sm_{0.95}Ce_{0.05}FeO_{3-\delta}$ toward sensing of reducing gases like H_2, CO, and CH_4 in air suggested that the chemical composition and redox stability of both bulk and

surface play a key role in explaining the sensing mechanism and performance of these sensors [34].

In this work, we synthesized a new series of perovskite materials with formula $Sm_{0.95}Ce_{0.05}Fe_{1-x}Ni_xO_{3-\delta}$ ($0 \leq x \leq 0.10$) and studied the effect of Ni substitution on the redox stability of both bulk and surface to evaluate their material properties in view of future applications (including sensors and anodes of solid oxide fuel cells). The objective of the substitution is an improvement in the electrical conductivity with a minimal decrease in reduction stability. The manuscript focuses on the material properties of the new perovskite series and discuses the origin of the observations in terms of crystal structure, elemental chemical composition, surface structure and redox characteristics.

8.2. Experimental

8.2.1. Synthesis

A sol-gel citrate method was used to synthesize the Ni doped $Sm_{0.95}Ce_{0.05}FeO_{3-\delta}$ with formula $Sm_{0.95}Ce_{0.05}Fe_{1-x}Ni_xO_{3-\delta}$ ($0 \leq x \leq 0.10$). Precursor materials include iron nitrate [$Fe(NO_3)_3 \cdot 9H_2O$, Alfa Aesar, minimum 98%], cerium nitrate [$Ce(NO_3)_3 \cdot 6H_2O$, Alfa Aesar, 99.5%], nickel nitrate [$Ni(NO_3)_2 \cdot 6H_2O$, Alfa Aesar, 99%], samarium nitrate [$Sm(NO_3)_3 \cdot 6H_2O$, Alfa Aesar, 99.9%] and citric acid monohydrate [Alfa Aesar, minimum 99.0%]. Solutions of Sm, Ce, Fe and Ni nitrates were prepared separately in de-ionized water. The solution of citric acid was prepared by keeping the ratio of citric acid to total metal ion at unity. The solutions of metal nitrates and citric acid were mixed according to the desired stoichiometry. The mixtures were dried at 100°C to obtain amorphous citrate precursors, which were further ground, and then calcined at 850°C for 24 hours to form the perovskite structures.

8.2.2. Characterization

X-ray fluorescence (Philips PW2400/00) was used to determine the stoichiometry of the nickel doped materials. Using a calibration curve consisting of a concentration gradient of Sm_2O_3, CeO_2, NiO and Fe_2O_3, the quantities of the four metals i.e., Sm, Ce, Ni and Fe, were obtained. Phase composition and crystallite sizes were determined by X-ray diffraction (XRD, Phillips PW 1830) analysis using CuK_α radiation. The scans were measured in the range of $2\theta = 13°$ to 90° at a scan rate of 0.02°/sec. The powder diffraction file database (ICDD/JCPDS, 2001, Dataset 1-99) was used to assign the crystalline phase. Theta

calibration was performed with SrO as the internal standard and the Jade 6.1 software was used to perform peak refinements.

The BET surface areas of all as synthesized powdered samples were determined by using a Quantachrome Autosorb 1-C instrument using nitrogen as the vector gas. The surface morphology of all samples in the form of powders was observed by scanning electron microscopy (SEM, JEOL JSM-7500F). The surface chemical states and compositions of fresh samples, ex-situ reduced samples (reduced but exposed to air during the transfer to the XPS chamber), and in-situ reduced samples (reduced and tranfered without exposure to air) were determined by X-ray photoelectron spectroscopy (XPS; Kratos AXIS Ultra^{DLD} 39-306l), using a monochromatic Al anode. For the purpose of quantification and identification of oxidation states, peaks of $Sm3d_{5/2}$, $Ce3d_{5/2}$, $Fe2p_{3/2}$, $Ni2p_{3/2}$ and O1s core levels were used. The Casa Software [35] was used for the analysis and quantification of XP spectra. For a complete survey, a pass energy of 80eV was used, while a 20eV pass energy was used for individual regions. The B.E. scale of all spectra was calibrated with the B.E. of the C1s level set at 284.8eV. A nonlinear background subtraction (Shirley) was used to fit peaks.

8.3. Results and discussion

8.3.1. Bulk structure

The quantitative elemental composition of all synthesized nickel doped materials, $Sm_{0.95}Ce_{0.05}Fe_{1-x}Ni_xO_{3-\delta}$ ($0 \leq x \leq 0.10$), was confirmed by X-ray fluorescence (Table 8.1). Since oxygen cannot be measured directly, its quantity was calculated from the balance of the sample mass. The comparison showed that the measured and expected elemental stoichiometric ratios of all compositions match well.

Table 8.1. Elemental quantification of $Sm_{0.95}Ce_{0.05}Fe_{1-x}Ni_xO_{3-\delta}$ obtained from XRF.

$Sm_{0.95}Ce_{0.05}Fe_{1-x}Ni_xO_{3-\delta}$	% w/w Sm[a]	% w/w Ce[a]	% w/w Fe[a]	% w/w Ni[a]	Experimental Stoichiometric ratio Sm : Ce : Fe : Ni : O[b]
x=0	56.13	2.78	21.68	0.00	0.95 : 0.05 : 1.00 : 0.00 : 3.00
x=0.01	56.15	2.79	21.70	0.25	0.95 : 0.05 : 0.99 : 0.01 : 3.00
x=0.03	56.14	2.79	21.16	0.68	0.95 : 0.05 : 0.97 : 0.03 : 3.00
x=0.05	56.12	2.79	20.89	1.16	0.95 : 0.05 : 0.95 : 0.05 : 3.00
x=0.07	56.16	2.79	20.44	1.57	0.95 : 0.05 : 0.93 : 0.07 : 3.00
x=0.10	56.10	2.79	19.81	2.29	0.95 : 0.05 : 0.90 : 0.10 : 3.00

[a]Measured by XRF using a calibrations curves of the corresponding oxides. Values are given as % w/w of the overall sample.
[b]Oxygen cannot be measured directly. The oxygen content is calculated from the balance of the sample mass.

The crystal structure and lattice parameters were determined by pXRD (Powder X-ray diffraction). Figure 8.1 shows the XRD pattern of as synthesized $Sm_{0.95}Ce_{0.05}Fe_{1-x}Ni_xO_{3-\delta}$ perovskite materials with x=0, 0.01, 0.03, 0.05, 0.07 and 0.10. These patterns match well the standard JCPDS card number 39-1490 ($SmFeO_3$), suggesting that all these nickel doped materials have orthorhombic symmetry and belong to the Pnma (62) space group. Importantly, a single phase is observed for all the prepared perovskites. Cell parameters and crystallite sizes were calculated from peak positions and full-width-half-maxima using the Scherrer equation [36].

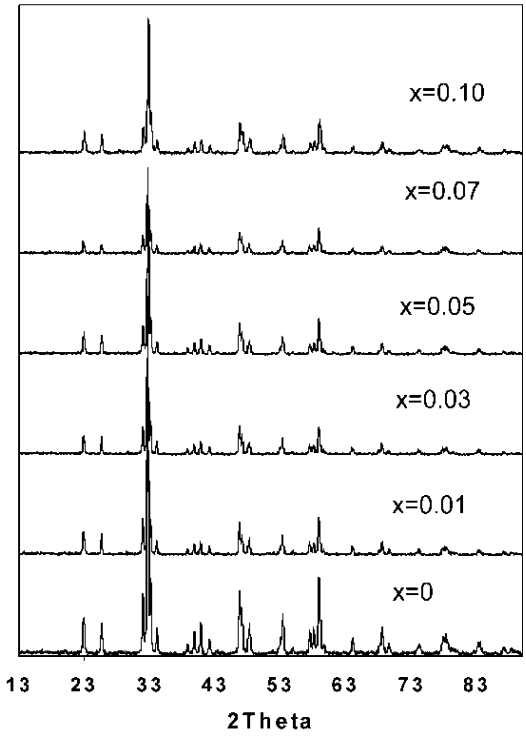

Figure 8.1. XRD pattern of $Sm_{0.95}Ce_{0.05}Fe_{1-x}Ni_xO_{3-\delta}$ (x =0-0.10) obtained after calcination of amorphous citrates at 850°C for 24 hours.

Table 8.2 shows the cell parameters and crystallite sizes which were measured directly, as well as the calculated cell volumes and tolerance factors "t". The tolerance factor is derived from a cubic geometry according to Goldschmidt, with t=1 for a perfect cube [37]

V. M. Goldschmidt and Oslo, Naturwissenschaften 14 (1926) 477 : $t = \frac{r_A + r_O}{\sqrt{2}(r_B + r_O)}$ where

r_A, r_B and r_O are ionic radii of the A-cation, the B-cation and the oxygen anion present in the lattice. The shifts in diffraction angles due to Ni doping result in a trend of the lattice volumes. This trend provides insight into the ions present in the structure. If Fe^{+3} in the lattice is substituted by Ni^{+2}, one would expect a shift in the XRD peaks towards smaller 2θ values and a correspondingly larger crystal volume, since Ni^{+2} (0.69Å [38]) is a larger cation than Fe^{+3} (0.645Å [38]). However, the analysis of the XRD profiles showed larger 2θ values and a decrease in crystal volumes as the nickel content increased. This suggests that Fe^{+3} (0.645Å [38]) is been substituted by the slightly smaller Ni^{+3} cation (0.60Å [38],[39]) in this Ni doped series.

Table 8.2. Cell parameters, cell volumes, crystallite sizes and Goldschmidt tolerance factors of $Sm_{0.95}Ce_{0.05}Fe_{1-x}Ni_xO_{3-\delta}$ (x =0-0.10)

$Sm_{0.95}Ce_{0.05}Fe_{1-x}Ni_xO_{3-\delta}$	Crystallite Size (Å)	a (Å)	b (Å)	c (Å)	Volume ($Å^3$)	Tolerance factor (t)
x=0	627	5.600	7.718	5.413	233.95	0.858
x=0.01	860	5.604	7.724	5.404	233.91	0.859
x=0.03	749	5.600	7.734	5.399	233.83	0.859
x=0.05	542	5.598	7.710	5.390	232.64	0.859
x=0.07	555	5.601	7.651	5.423	232.39	0.860
x=0.10	371	5.584	7.683	5.409	232.06	0.860

The tolerance factors for this series were calculated by using available ionic radii: Sm^{+3}=0.964Å, Ce^{+3}=1.143Å, Fe^{+3}=0.645Å, Ni^{+3}=0.60Å and O=0.964Å [38]. The tolerance factors ranged from 0.8584 to 0.8603 in a continuously increasing trend, well within the range of 0.75 - 1.00 which characterizes stable perovskite structures.

The thermal and chemical stability of the $Sm_{0.95}Ce_{0.05}Fe_{1-x}Ni_xO_{3-\delta}$ (x =0-0.10) perovskites was tested in air as the reference oxidizing medium and under 5% v/v H_2/N_2 as the reducing atmosphere. In air, all the materials in the series were stable within the temperature range tested (up to 1350°C for four hours). XRD patterns obtained after heat treatment showed no indication of phase separation or decomposition of the perovskite structure.

In order to test the thermal and phase stability under reducing conditions, the nickel doped materials were heated at different temperatures for 1 hour under 5% v/v H_2/N_2 flow. Figures 8.2a and 8.2b show the XRD patterns observed after treatment at 700°C and at 800°C, respectively. All the perovskites were stable after treatment at 700°C, i.e. no phase separation occurred. However, upon treatment at higher temperature (800°C and above), the

onset of a separate Sm_2O_3 phase was observed. Despite the appearance of the samaria phase, the remaining material preserved the perovskite structure unaltered.

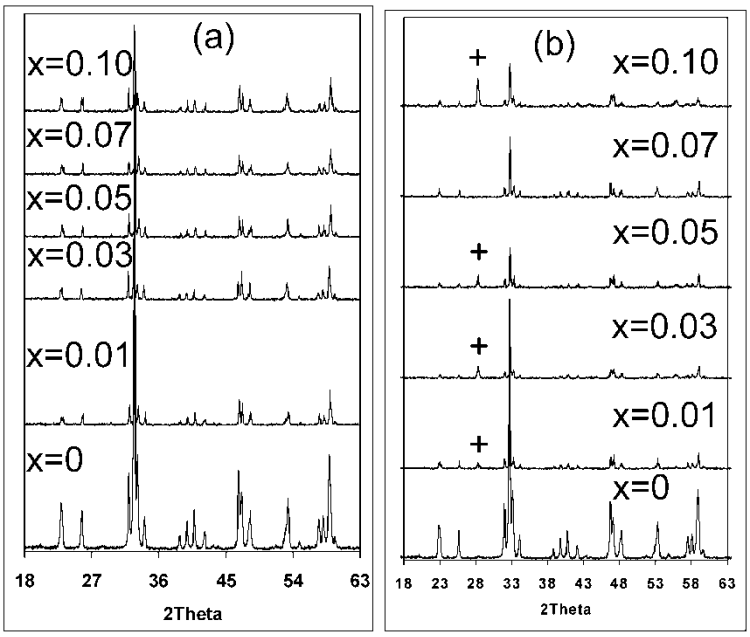

Figure 8.2. (a) XRD pattern of $Sm_{0.95}Ce_{0.05}Fe_{1-x}Ni_xO_{3-\delta}$ (x =0-0.10) heated in 5% v/v H_2/N_2 at 700°C for 1 hour. (b) XRD pattern of $Sm_{0.95}Ce_{0.05}Fe_{1-x}Ni_xO_{3-\delta}$ (x =0-0.10) heated in 5 %v/v H_2/N_2 at 800°C for 1 hour. + indicates Sm_2O_3 phase.

The preservation of the perovskite phase under reducing conditions (5%H_2/N_2 v/v) at temperatures at and above 800^{o}C indicates that Ni doping of $Sm_{0.95}Ce_{0.05}FeO_{3-\delta}$ does not impair the lattice's stability to reduction. The relatively weaker bond nature of Ni-O as compared to Fe-O [27, 32] would suggest that the stability of the lattice under reducing conditions should be impaired. It is speculated that the observed unusual stability of the Ni doped $Sm_{0.95}Ce_{0.05}FeO_{3-\delta}$ materials may be associated with the electronegativity of the Ni cation. The electronegativity values for Ni^{+2} and Ni^{+3} are 1.57 and 1.79 respectively [40]. As a consequence, the Ni^{+3}– O bond is more ionic and stronger than the Ni^{+2}– O bond. As the Ni^{+3} species is believed to predominate in the Ni doped $Sm_{0.95}Ce_{0.05}FeO_{3-\delta}$ perovskites, this may account for the unusual stability of the lattice.

The x=0.07 sample appears to be an exception. At this concentration, the material is more resistant and the onset of Sm_2O_3 phase separation occurs at higher temperature. The phase separation of Sm_2O_3 can be explained as the mechanism to compensate for the instability produced in the lattice when oxygen is removed and reduction of some metal

cations occurs. We can in fact correlate the propensity toward samaria separation to the reducibility of iron in the structure. “In-situ” XP measurements discussed below show that the x=0.07 sample is the only one where there is a negligible change in the oxidation state of Fe, and therefore no phase separation is required (no phase separation occurs).

8.3.2. Microstructure

The surface morphologies of the as-synthesized powders were examined by scanning electron microscopy (SEM). Figure 8.3 shows the SEM images of the as- synthesized powders obtained after calcination of their citrate precursors at 850°C for 24h. Figure 8.3 presents the microstructures of the x=0-0.10 samples, which clearly show that x=0 has a relatively more porous surface, while x=0.05 has the least porous surface. The average diameter of the grains gradually decreases as a function of Ni concentration (Table 8.3) which implies that Ni may have prevented the growth of grains.

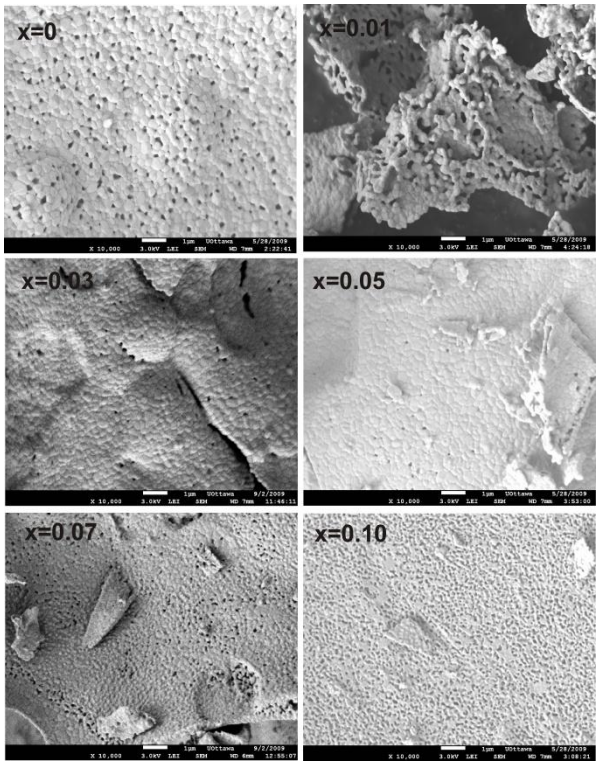

Figure 8.3. Surface morphology of as synthesized powders of $Sm_{0.95}Ce_{0.05}Fe_{1-x}Ni_xO_{3-\delta}$ (x=0-0.10) observed by SEM

The surface areas of the materials follow the qualitative picture shown by the SEM images (BET surface areas are presented in Table 8.3). All nickel doped materials have relatively low surface areas as compared to undoped $Sm_{0.95}Ce_{0.05}FeO_{3-\delta}$, and indeed x=0.10 has the highest surface area amongst the nickel doped materials as predicted by its smaller crystallite sizes. The undoped material has well organized grains with well distributed pores as compared to the other perovskites while the x=0.05 material appears to have sintered more efficiently during preparation.

Table 8.3. Surface area of as synthesized $Sm_{0.95}Ce_{0.05}Fe_{1-x}Ni_xO_{3-\delta}$ perovskites[a].

Nickel Conc.	x=0	x=0.01	x=0.03	x=0.05	x=0.07	x=0.10
SA (m^2/g)	6.94	2.98	2.476	2.174	2.522	4.349
Average Particle diameter from SEM(nm)	512±5[b]	504±6[b]	470±10[b]	466±7[b]	298±6[b]	289±5[b]

[a] Surface area obtained using the BET multipoint analysis method
[b] Average standard deviation.

8.3.3. Surface Structure

The oxidation states and the relative surface atomic ratios of the elements in $Sm_{0.95}Ce_{0.05}Fe_{1-x}Ni_xO_{3-\delta}$ (x=0-0.10) were determined by X-ray photoelectron spectroscopy (XPS) for fresh, in-situ reduced, and ex-situ reduced samples (the reduction was performed at 800^{o}C in 5%v/v H_2/N_2 for one hour). The $Sm3d_{5/2}$, $Ce3d_{5/2}$, $Fe2p_{3/2}$, $Ni2p_{3/2}$ and O1s core level peaks were used to quantify the elemental composition, and to identify the oxidation states. The comparison of $Sm3d_{5/2}$, $Ni2p_{3/2}$ and O1s core level peaks for all the Ni doped materials before and after reduction treatment is shown in Figure 8.4.

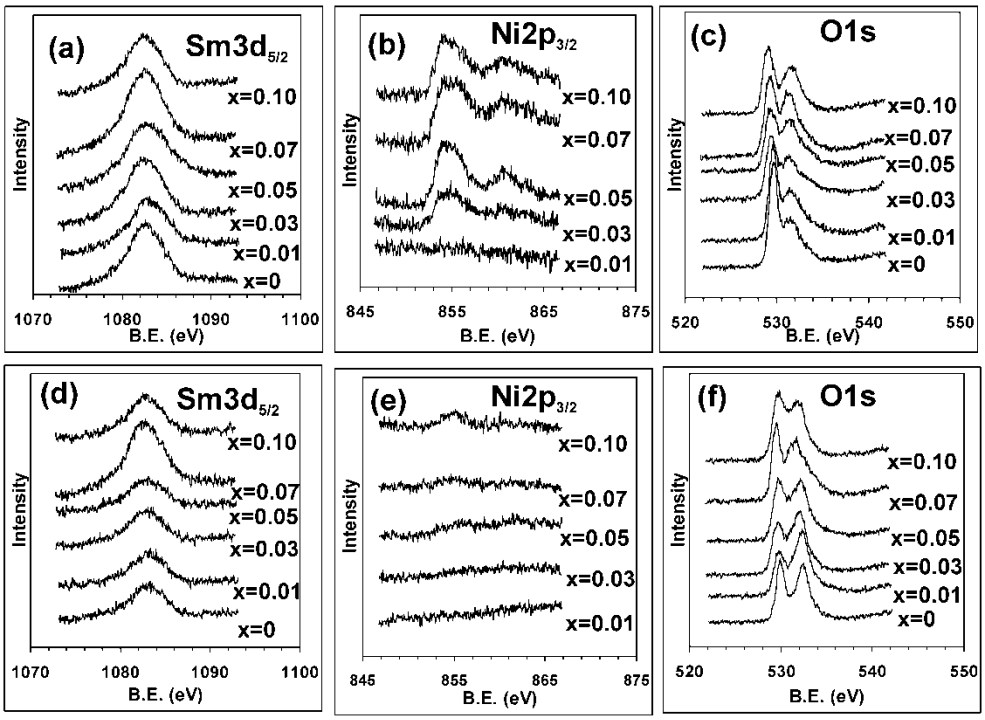

Figure 8.4. $Sm3d_{5/2}$, $Ni2p_{3/2}$ and O1s peaks of as synthesized $Sm_{0.95}Ce_{0.05}Fe_{1-x}Ni_xO_{3-\delta}$ (x=0-0.10). a, b and c: before reduction; d, e and f: after reduction under 5%H_2/N_2 v/v at 800^oC for one hour (ex-situ).

The position of $Sm3d_{5/2}$ in fresh, in-situ reduced, and ex-situ reduced samples, is ~1082.9eV which is in good agreement to reported values for Sm^{+3} [41]. This suggests that Sm remains in the +3 state even after reduction of the perovskite. $Fe2p_{3/2}$ peaks for all fresh, in-situ reduced, and ex-situ reduced samples were broad envelopes consisting of several peaks.

Figure 8.5 and 8.6 show the result of peak fittings for $Fe2p_{3/2}$ peaks of fresh and ex-situ reduced samples, respectively. Three distinct features were observed. The peak in the range of 709.6-709.9eV can be ascribed to Fe^{+2}; (B.E.=709.3eV [42]) the peak in the range of 710.5-711eV can be ascribed to Fe^{+3} (B.E.=710.5eV [42]), while the peak at 712-714eV can be ascribed to Fe^{+4}. Peak fitting results show that all samples before and after ex-situ reduction have multiple oxidation states of Fe suggesting that the introduction of the Ni dopant has produced some disproportionation in the oxidation state of iron.

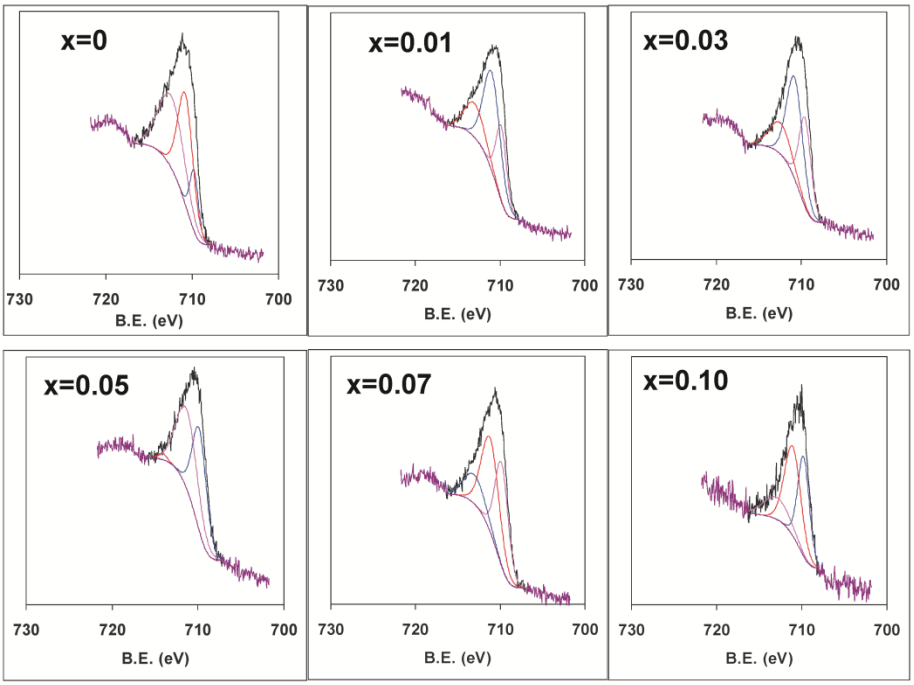

Figure 8.5. Fitting results of $Fe2p_{3/2}$ peaks of $Sm_{0.95}Ce_{0.05}Fe_{1-x}Ni_xO_{3-\delta}$ (x=0-0.10) before reduction treatment.

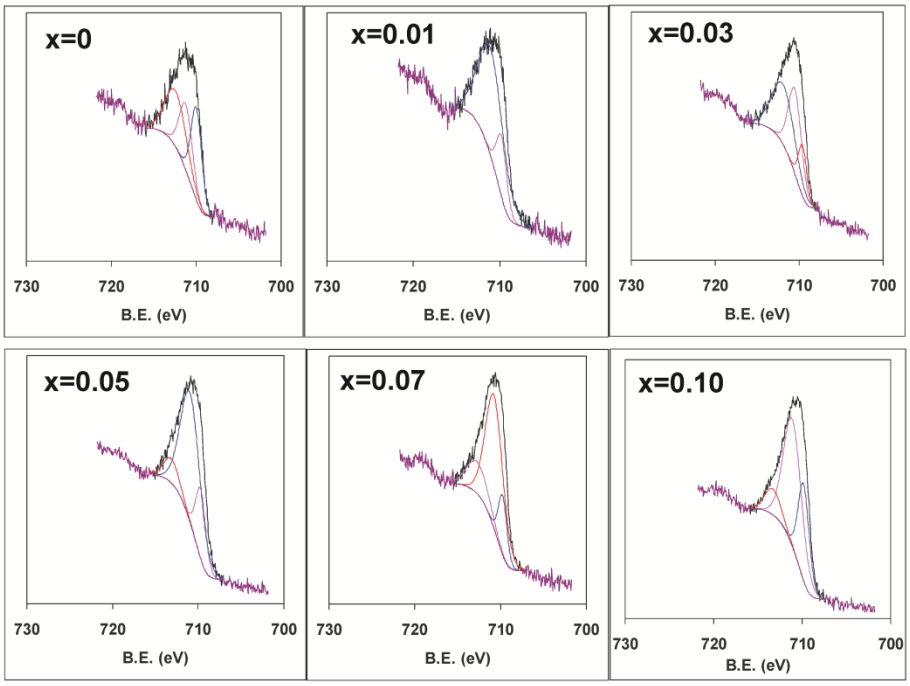

Figure 8.6. Fitting results of $Fe2p_{3/2}$ peaks of $Sm_{0.95}Ce_{0.05}Fe_{1-x}Ni_xO_{3-\delta}$ (x=0-0.10) after reduction treatment at 800°C in 5%v/v H_2/N_2 for one hour (ex-situ).

Figure 8.7 shows the comparison of $Fe2p_{3/2}$ peaks for in-situ reduced samples. Peaks are very broad and of low intensity preventing an accurate quantitative analysis. However, a shoulder in the spectra around 707 eV is clear evidence for the formation of metallic iron in all samples except x=0 and 0.07. Since the ex-situ reduced samples did not show metallic iron, one can conclude that a metallic iron phase is formed during reduction but it is reoxidized upon exposure to air.

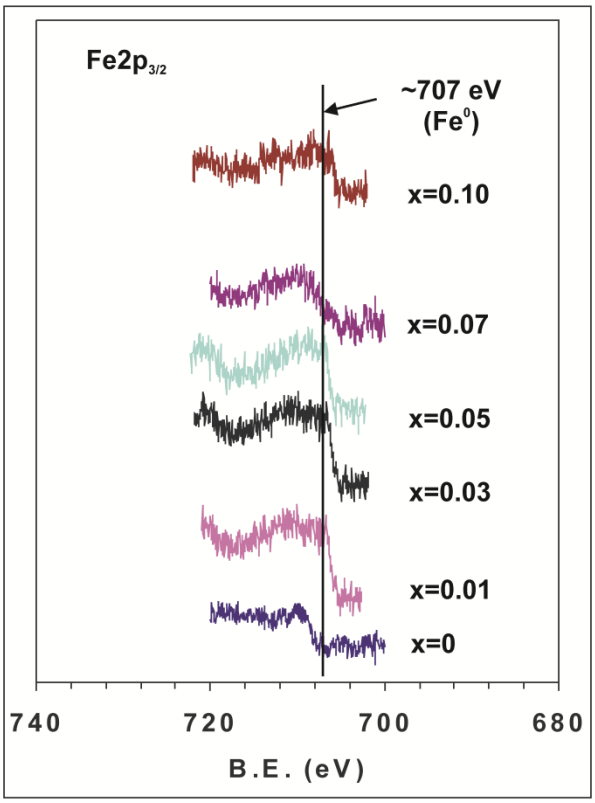

Figure 8.7: $Fe2p_{3/2}$ peaks of $Sm_{0.95}Ce_{0.05}Fe_{1-x}Ni_xO_{3-\delta}$ (x=0-0.10) obtained after in-situ reduction treatment at 800°C in 5%v/v H_2/N_2 for one hour.

As discussed above from XRD data, the oxidation state of nickel was inferred to be Ni^{+3} due to the gradual decrease in lattice volumes. An attempt was made to confirm the oxidation state using XPS data. The presence of both Ni^{+2} and Ni^{+3} is suggested since two peaks can be fitted to the data (reported B.E. for Ni^{+2} and Ni^{+3} are 854.3eV and 855.8eV [43]), but the $Ni2p_{3/2}$ core level peaks are very broad and of low intensity making quantification suspect. Similarly, for $Ce3d_{5/2}$ peaks (not shown) in fresh and reduced (in-situ and ex-situ) samples, prediction of Ce oxidation states was not possible because of very low signal intensity.

Despite fitting difficulties of low intensity peaks, the overall area of each peak was used to obtain the relative surface atomic ratios of Sm, Ce, Fe, Ni and O in fresh, in-situ reduced, and ex-situ reduced samples. Table 8.4 shows the relative surface atomic ratios of the metal species using the $Sm3d_{5/2}$, $Ce3d_{5/2}$, $Fe2p_{3/2}$, $Ni2p_{3/2}$ peaks. The comparison reveals several interesting features: (i) All fresh samples have Sm rich surfaces due to surface segregation; (ii) The in-situ reduction tends to segregate more Sm on the surface (all in-situ reduced samples have almost two times more Sm on the surface than the fresh samples); (iii) The Sm richness on the surface of all ex-situ reduced samples is similar to that of fresh samples. From these observations one can speculate that upon exposure to air, the surface of reduced samples tends to re-oxidize in a more or less reversible way. This feature will need to be further explored for sensor applications because reversibility is one of the key factors for a practicable sensor. Additionally, Sm rich surfaces for this type of material suggest enhancement in sensor behavior because the high coordination of Sm (12) should provide more chances of adsorption for target molecules on surface during sensing process than the other lower coordination atoms in the perovskite [34].Both fresh and reduced samples have Sm rich surfaces due to surface segregation. However, upon reduction the surface concentration of iron increases at the expense of samarium.

For the O1s core level, two peaks were observed for all samples, fresh as well as reduced at $800^{o}C$ in 5%v/v H_2/N_2 for one hour. The observation of two peaks is consistent with observations in other perovskites [41]. The low binding energy peak represents oxygen which is present in the lattice and bound to several metal atoms (O^{-2}). It is typically identified to be a bulk species (within the depth of view of the XPS experiment). On the other hand, surface adsorbed oxygen (O_{ads}) results in the high binding energy peak. At the surface, some of the oxygen is bonded to the perovskite phase while some may be bonded to the surface segregated species (like Sm_2O_3 or Fe_2O_3) and therefore the high binding energy peak of O1s, represents all surface adsorbed oxygen. Careful comparison shows that both peaks of O1s core levels in both fresh and reduced samples showed a gradual shift towards low binding energy indicating a decrease in oxidation state of some metal species present in the lattice as well on surface. The relative percentage of lattice and adsorbed oxygen was determined from the relative intensity (integrated area) of these two peaks.

Table 8.4: The relative surface atomic ratios of Sm, Ce, Fe, Ni in both fresh samples and reduced samples of $Sm_{0.95}Ce_{0.05}Fe_{1-x}Ni_xO_{3-\delta}$ (x=0-0.10).

		Sm	Ce	Fe	Ni
x=0	Nominal	0.475	0.025	0.500	0
	Fresh	0.583	0.009	0.409	0
	Ex-situ Reduction	0.525	0.006	0.469	0
	In-situ Reduction	0.845	0.013	0.142	0
x=0.01	Nominal	0.475	0.025	0.495	0.005
	Fresh	0.594	0.015	0.364	0.027
	Ex-situ Reduction	0.527	0.003	0.456	0.014
	In-situ Reduction	0.847	0.018	0.120	0.015
x=0.03	Nominal	0.475	0.025	0.485	0.015
	Fresh	0.589	0.015	0.345	0.051
	Ex-situ Reduction	0.601	0.004	0.400	0.006
	In-situ Reduction	0.721	0.026	0.228	0.026
x=0.05	Nominal	0.475	0.025	0.475	0.025
	Fresh	0.728	0.020	0.207	0.045
	Ex-situ Reduction	0.559	0.002	0.433	0.006
	In-situ Reduction	0.831	0.014	0.136	0.018
x=0.07	Nominal	0.475	0.025	0.465	0.035
	Fresh	0.688	0.007	0.241	0.063
	Ex-situ Reduction	0.659	0.006	0.297	0.038
	In-situ Reduction	0.798	0.011	0.160	0.031
x=0.10	Nominal	0.475	0.025	0.450	0.050
	Fresh	0.674	0.017	0.213	0.097
	Ex-situ Reduction	0.594	0.005	0.366	0.038
	In-situ Reduction	0.810	0.054	0.112	0.024

The comparison shows several interesting characteristics of the perovskite reduction behavior. The expected stoichiometry of lattice oxygen is 1.5 (oxygen/metal in ABO_3) before reduction, but slightly smaller values are observed. This is indicative of vacancies in the near surface region of the powders (as probed by XPS), and of the presence of adsorbed oxygen that "terminates" the surface. The deviation from stoichiometric amounts of oxygen allows the calculation of the oxygen loss parameter δ. The loss of bulk oxygen vacancies near the surface was calculated by using the formula: $\delta = 3 - 2[O^{-2} / Sm + Ce + Fe + Ni]$ [44]. Table 8.5 shows the bulk oxygen stoichiometry, the number of oxygen vacancies as given by the loss parameter, and the relative concentration of lattice and adsorbed oxygen as a function of Ni concentration for fresh and reduced powders.

All fresh Ni doped materials have higher concentration of oxygen vacancies than undoped $Sm_{0.95}Ce_{0.5}FeO_{3-\delta}$, which indicates that introduction of Ni has created a charge imbalance in the lattice. The ratio of lattice to adsorbed oxygen varies in a non-linear way as a function of nickel content. Samples measured after ex-situ reduction showed unexpectedly high concentration of lattice oxygen as compared to fresh samples. That is, there is more oxygen than expected from the ABO_3 stoichiometry, as indicted also by negative values of δ. In fact, even the ratio of lattice to adsorbed oxygen does not vary significantly. These observations suggest that the samples may be recapturing oxygen at room temperature due to exposure to air during the transfer between the reduction furnace and the XPS chamber. This oxygen recapturing could be for stabilizing the lattice after removal of some lattice oxygen upon reduction and/or by surface segregated species. To test this hypothesis, we performed XPS spectra immediately after reduction, without exposing the sample to air (labeled as "in-situ" in Table 8.5). In this case, the data revealed that bulk oxide ion concentration decreases upon reduction and the value of δ increases substantially during reduction, consistent with the formation of oxygen vacancies. Reduction "in-situ" also shows an increase in the lattice/adsorbed oxygen ratio as one would expect since the surface should be affected to a larger extent than the bulk.

Table 8.5. Oxygen composition of $Sm_{0.95}Ce_{0.05}Fe_{1-x}Ni_xO_{3-\delta}$ (x=0-0.10) powders.

	Experimental Bulk Stoichiometry $\frac{O^{-2}}{Sm+Ce+Fe+Ni}$			Bulk Oxygen Vacancy (δ)			$\frac{O^{-2}}{O_{ads}}$		
	Fresh	Ex-situ Reduction	In-situ Reduction	Fresh	Ex-situ Reduction	In-situ Reduction	Fresch	Ex-situ Reduction	In-situ Reduction
x=0	1.47	2.26	0.06	0.06	-1.52	2.88	0.63	0.61	1.61
x=0.01	1.45	1.62	0.75	0.10	-0.25	1.49	0.46	0.44	0.86
x=0.03	1.44	2.15	0.90	0.12	-1.3	1.21	0.63	0.51	2.19
x=0.05	1.22	1.86	0.99	0.56	-0.72	1.02	0.42	0.42	0.73
x=0.07	1.14	1.42	0.89	0.73	0.16	1.23	0.40	0.35	0.67
x=0.10	1.14	1.91	0.64	0.73	-0.83	1.72	0.69	0.44	0.76

The large decrease in oxide ion concentration is expected to affect the oxidation state of the metal species during the reduction process. However, Sm, Ni and Ce XP spectra are similar to those of the ex-situ and in-situ reduced samples; no discernible change in oxidation state is observed. The only sensitive species appears to be iron (Figure 8.7). All "in-situ" reduced $Sm_{0.95}Ce_{0.5}Fe_{1-x}Ni_xO_{3-\delta}$ (x=0.01-0.10) samples clearly show metallic iron (shoulder at ~707 eV) except x=0.07. Metallic Fe appears to be formed upon reduction treatment but it is re-oxidized on exposure to air while transferring to the XPS instrument.

While all the perovskites in the series lose a substantial concentration of oxygen during reduction, the formation of metallic iron seems to have an impact upon the stability of the perovskite structure. As seen in the XRD data (Figure 8.2), the x=0.07 sample is the only one that does not decompose during the reduction process at 800°C.

As these materials have good reduction stability at reasonably high temperatures and reversible surface reduction properties, they could be considered as potential candidates for detection of reducing gases like H_2, CO and CH_4, for anode materials in solid oxide fuel cells, and for oxygen membranes for catalytic applications like the partial oxidation of methane.

8.4. Conclusions

We have prepared Ni doped $Sm_{0.95}Ce_{0.5}FeO_{3-\delta}$ with x=0-0.10 through a sol-gel method. XRD of as synthesized materials showed that all the materials were produced with a single phase of orthorhombic structure. These materials are stable up to 1350^oC under air, and up to 700^oC under 5%v/v H_2/N_2. A phase separation of Sm_2O_3 does occur with the preservation of the perovskite phase when these materials are heated under 5%v/v H_2/N_2 at 800^oC and above. Sinterablity increases as a function of nickel content in the series as revealed by SEM. All the perovskites have Sm rich surfaces due to surface segregation. Bulk stoichiometry analysis shows that introduction of Ni into the lattice of $Sm_{0.95}Ce_{0.05}FeO_{3-\delta}$ increased oxygen vacancies. In situ reduction treatment and XPS measurements reveal that these materials have the ability to recapture oxygen at room temperature when exposed to air after reduction. The redox stability under reducing condition and oxygen recapturing ability upon exposure to air (reversible redox process)

suggests their candidacy for some important applications including as sensors and anode for SOFC.

8.5. References

[1] H. Aono, E. Traversa, M. Sakamoto and Y. Sadaoka, Sens. Actuators B 94 (2003) 132
[2] G. Martinelli, M. C. Carotta, M. Ferroni, Y. Sadaoka and E. Traversa, Sens. Actuators B 55 (1999) 99
[3] X. Liu, J. Hu, B. Cheng, H. Qin and M. Jiang, Current Applied Physics 9 (2009) 613
[4] J. cerda, J. Arbiol and G. Dezanneau, Sens. Actuators B 84 (2002) 21
[5] L. Zhang, J. Hu, P. Song, H. Qin, K. An, X. Wang and M. Jiang, Sens. Actuators B 119 (2006) 315
[6] J. Zosel, D. Franke, K. Ahlborn, F. Gerlach, V. Vashook and U. Guth, Solid State Ionics 179 (2008) 1628
[7] X. Jia, H. Fan, X. Lou and J. Xu, Appl Phys A 94 (2009) 837
[8] C. R. Michel, E. Delgado, G. Santillan, A. H. Martynez and A. Chavez-Chavez, Mat. Res. Bull. 42 (2007) 84
[9] G. Pudmich, B. A. Boukamp, M. Gonzalez-Cuenca, W. Jungen, W. Zipprich and F. Tietz, Solid State Ionics 135 (2000) 433
[10] Z. Cheng, S. Zha and M. Liu, J. Electrochem. Soc. 153 (2006) A1302
[11] S. Tao and J. T. S. Irvine, Solid State Ionics 179 (2008) 725
[12] M. D. Gross, K. M. Carver, M. A. Deighan, A. Schenkel, B. M. Smith and A. Z. Yee, J Electrochem. Soc. 156 (2009) B540
[13] A. El-Himri, D. Marrero-Lopez, J. C. Ruiz-Morales, J. Pena-Martínez and P. Nunez, J. Power Sources 188 (2009) 230
[14] J. Molenda and J. Marzec, Electrochemistry 11 (2005) 355
[15] V. V. Kharton, F. M. Figueiredo, L. Navarro, E. N. Naumovich, A. V. Kovalevsky, A. A. Yaremchenko, A. P. Viskup, A. Carneiro, F. M. B. Marques and J. R. Frade, J. Mater. Sci. 36 (2001) 1105
[16] D. P. Fagg, V. V. Kharton, A. V. Kovalevsky and A. P. Viskup, J. Eur. Ceram. Soc. 21 (2001) 1831
[17] T. Kolodiazhnyi and A. Petric, J Electroceram. 15 (2005) 5
[18] F. Martinez-Ortega, C. Batiot-Dupeyrant, G. Valderrama and J.-M. Tatibouet, C. R. Acad. Sci. Paris, Serie llc, Chimie / Chemistry 4 (2001) 49
[19] V. N. Staphopoulos, V. C. Blessi and A. K. Ladavos, React.Kinet.Catal.Lett. 72 (2001) 49
[20] J. R. Mawdsley and T. R. Krause, Appl. Catal., A 334 (2008) 311
[21] P. Ciambelli, S. Cimino, S. D. Rossi, L. Lisi, G. Minelli, P. Porta and G. Russo, Appl. Catal. B 29 (2001) 239
[22] D. D. Boulay, E. N. Maslen and V. A. Streltsov, Acta Cryst. B51 (1995) 921
[23] N. G. Eror and D. M. Smyth, J.Eletrochemical. Soc. 128 (1981) 1762
[24] M. C. Carotta, G. Martinelli, Y. Sadaoka, P. Nunziante and E. Traversa, Sens. Actuators B 48 (1998) 270
[25] S. M. Bukhari and J. B. Giorgi, Solid State Ionics 180 (2009) 198

[26] E. Traversa, Y. Sadaoka, M. C. Carotta and G. Martinelli, Sens. Actuators B 65 (2000) 181
[27] X. Zhu, H. Wang and W. Yang, Solid State Ionics 177 (2006) 2917
[28] L. Chen, J. Hu, S. Fang, Z. Han, M. Zhao, ZhanleiWu, X. Liu and H. Qin, Sens. Actuators B 139 (2009) 407
[29] M. Zhao, H. Peng, J. Hu and Z. Han, Sens. Actuators B 129 (2008) 953
[30] X. Liu, J. Hu, B. Cheng, H. Qin and M. Jiang, Sens. Actuators B 134 (2008) 483
[31] Y. Itagaki, M. Mori, Y. Hosoya, H. Aono and Y. Sadaoka, Sens. Actuators, B 122 (2007) 315
[32] D. Klissurski and R. Dimtrova, Bull. Chem. Soc. Jpn. 63 (1990) 590
[33] S. M. Bukhari and J. B. Giorgi, Solid State Ionics 181 (2009) 392
[34] S. M. Bukhari and J. B. Giorgi, ECS Trans. accepted (2010)
[35] N. Fairley, Casa XPS version 2.3.13 Dev73 (2007)
[36] I. MDI Jade 6.1 Software Materials Data, Serial#MDI-R97738 (2002)
[37] V. M. Goldschmidt and Oslo, Naturwissenschaften 14 (1926) 477
[38] R. D. Shanon, Acta cryst. A32 (1976) 751
[39] G. Pecchi, P. Reyes, R. Zamora, L. E. Cadús and J. L. G. Fierro, J. Solid State Chem. 181 (2008) 905
[40] J. Portier, G. Campet, J. Etourneau and B. Tanguy, Journal of Alloys and Compounds 209 (1994) 285
[41] H. Aono, M. Sato, E. Traversa, M. Sakamoto and Y. Sadaoka, J. Am. Ceram. Soc. 84 (2001) 341
[42] W. Cheng and X. Ma, Journal of Physics: Conference Series 152 (2009) 012039
[43] T. Dickinson, A. F. Povey and P. M. A. Sherwood, J. Chem. Soc. Faraday Trans.I 73 (1977) 327
[44] N. A. Merino, B. P. Barbero, P. Eloy and L. E. Cadús, Appl. Surf. Sci. 253 (2006) 1489

9. Electrical conductivity dependence of Ni doped $Sm_{0.95}Ce_{0.05}FeO_{3-\delta}$ on surface morphology and composition

The contents of this chapter have been published as: Syed M. Bukhari and Javier B. Giorgi, Sensors and Actuators B, 155 (2010) 524-537

Abstract

$Sm_{0.95}Ce_{0.05}Fe_{1-x}Ni_xO_{3-\delta}$ materials are considered as candidates for sensing reducing gases. The total electrical conductivity of Ni doped $Sm_{0.95}Ce_{0.05}FeO_{3-\delta}$ perovskite materials is discussed in terms of Ni concentration, surface morphology and relative surface atomic ratios. Powders of formula $Sm_{0.95}Ce_{0.05}Fe_{1-x}Ni_xO_{3-\delta}$ (x=0-0.10) were prepared from citrate precursors by using a sol gel method and were then pressed uniaxially and sintered at 1350^oC for 4h to form pellets. In fresh pellets the relative surface atomic ratios of Sm and Ni increased while that of Fe and Ce decreased as a function of nickel concentration, showing the segregation of samarium species. In contrast, the chemically reduced pellets show Fe rich surfaces. The electrical conductivity of fresh, partially reduced (700^oC under 5% v/v H_2/N_2 for 1h) and fully reduced (1000^oC under 5% v/v H_2/N_2 for 1h) pellets were measured by the four probe DC method.

Under air, x=0.07 and x=0.10 showed the highest electrical conductivity in the series. Interestingly the x=0.01-0.05 materials were n-type conductors while x=0.07-0.10 exhibited p-type behaviour. The reduction treatment at 1000^oC enhanced electrical conductivities up to ~5000 fold due to changes associated with surface morphology and surface elemental composition. While phase separations are usually detrimental, in this case the reduced sensors are more sensitive without sacrificing reproducibility.

9.1. Introduction

Perovskites of type ABO_3 have shown great potential as chemical sensors due to the lability of their oxygen species [1-7]. The conductivity of these materials changes due to the interaction with oxidizing or reducing gases. In particular, the conductivity of $SmFeO_3$ (a p-type semiconductor material) increases with the adsorption of oxidizing gases like ozone, oxygen and NO_2 [8, 9]; and decreases with exposure to reducing gases like CO and H_2 [10-12]. In general, the electrical conductivity of p-type semiconductors depends on the electron-hole concentration ($\dot{h}$). Thus, the sensing behaviour is usually explained by the introduction

of hole charge carriers in the material upon oxidation (equation 9.1), and by the creation of oxygen vacancies due to reducing gases via removal of oxide anions and electron-holes from the lattice (equation 9.2). These two reactions can be written by using Kröger-Vink notation as:

$$\tfrac{1}{2}O_2 + 2e^- \rightarrow O^{-2} + 2\dot{h} \qquad (9.1)$$

$$H_2 + O^{-2} + 2\dot{h} \rightarrow H_2O + V_O^{\bullet\bullet} + 2e^- \qquad (9.2)$$

$SmFeO_3$ has been used to fabricate sensors for the detection of different gases like NO_2, ozone and propane [12-15]. However, these sensors suffer from a lack of response at lower temperature due to their very low electrical conductivity under both oxidizing and reducing conditions. In order to improve the response, there is a need to improve the electrical conductivity of the perovskite sensor. Furthermore, under reducing conditions $SmFeO_3$ shows phase separation of Sm_2O_3 and Fe_2O_3/Fe,[10] and therefore there is also a need to improve its chemical stability.

The conductivity and the reduction stability depend on the nature of both the A-site cation and the B-site cation [16]. In general, a bigger A-cation induces greater reduction stability. In previous work we have reported that doping of Ce at the Sm site in $SmFeO_3$: i) enhances the reduction stability i.e., no phase separation occurs even at 900°C under reducing conditions; ii) increases electrical conductivity under reducing conditions as compared to oxidizing conditions; and iii) results in new materials $Sm_{1-x}Ce_xFeO_{3\pm\lambda}$ ($0 \leq x \leq 0.05$) which are n-type semiconductors, unlike $SmFeO_3$ (which is p-type) [10]. These results indicate that cerium oxide is an electron dopant (and also an n-type conductor [17]) instead of a hole dopant [18].

B-site substitution by Co, Ni and Mg in $SmFeO_3$ has been attempted, resulting in better conductivity and sensitivity towards gases like O_3, NO_2, ethanol and acetone [1, 2, 5, 19]. Doping the Fe site with Co, Ni or Mg in $SmFeO_3$ does not affect the p-type nature of the doped perovskite, which suggests that Co, Ni and Mg are hole dopant impurities. This observation is consistent with the p-type nature of the corresponding single oxides CoO (and

Co_3O_4), NiO and MgO [17, 20]. However, when doping at the B-site, a weaker B-O bond results in a more easily reducible perovskite, increasing the likelihood of possible phase separations under reducing conditions [21]. The Co-O, Ni-O and Mg-O bonds are weaker than the Fe-O bond, therefore one would expect the doped $SmFeO_3$ material to be more reducible (as observed in [21, 22]).

In general, the electrical behaviour of the resulting perovskite upon addition of a dopant can be affected by many factors like the nature of the dopant, the amount of dopant incorporated and the surrounding environment. Dopants can be classified as either electron-dopants or hole-dopants. The addition of an electron-dopant in an n-type material or a hole-dopant into a p-type material does not change the nature of the resulting perovskite [1, 2, 19], but simply enhances the n-type or p-type conductivity, respectively. However, an electron-dopant can change a p-type perovskite into n-type [10], and a hole-dopant can change an n-type perovskite into p-type[23], depending on the concentration of the dopant [6, 10]. Furthermore, the nature of the dopant may change the redox behaviour of the perovskite producing a conductivity dependence as a function of oxygen pressure [23, 24].

Dopants change the electrical conductivity of the resulting perovskite materials not only by changing their chemical/electronic composition and creating structural defects, but also by changing its microstructure. The electrical conductivity of the materials (and devices built from them) greatly depends on grain size and grain boundaries [25]. The grain growth depends on many factors like the nature of the material itself, preparatory conditions of material powders, sintering conditions of the pellets, and the nature and amount of dopant. For example, Kuharuangrong [26] reported that in $La_{0.82}Sr_{0.16}Mn_{1-x}Ni_xO_3$ ($0 \leq x \leq 0.3$), an increase in Ni concentration decreases the electrical conductivity due to the fact that Ni inhibits the grain growth. In that material, smaller grain sizes, lowered the electrical conductivity. In contrast, Rout et al. found that an increase in Ni concentration in Ni doped $SrTiO_3$ increases the grain size while keeping the sintering conditions unchanged.

In this work, we evaluate the electrical conductivities of a recently developed new series of perovskite materials with formula $Sm_{0.95}Ce_{0.05}Fe_{1-x}Ni_xO_{3-\delta}$ ($0 \leq x \leq 0.10$). Substitution of Fe^{+3} by nickel in the n-type conductor ($Sm_{0.95}Ce_{0.05}FeO_{3-\delta}$) is expected to create more oxygen vacancies and should improve electrical conductivity under both oxidizing and reducing atmospheres. Furthermore, the addition of a weak Ni-O bond is expected to make the

perovskite more reducible with higher electrical conductivity under reducing conditions. High reducibility is generally considered as a disadvantage if it leads to phase separation because it may lead to irreversible responses of the sensor. In such cases, the materials may be used as one-time (alarm type) sensors. In this work we studied both surface compositions and electrical conductivities in air and under 5%v/v H_2/N_2 in order to asses these materials as potential sensors. We also demonstrate that phase separation in these Ni doped $Sm_{0.95}Ce_{0.05}FeO_{3-\delta}$ based sensors is an advantage because it helps to improve sensitivity while providing a new chemically stable and reproducible microstructure with reproducible performance.

9.2. Experimental

9.2.1. Synthesis

The powders of $Sm_{0.95}Ce_{0.05}Fe_{1-x}Ni_xO_{3-\delta}$ ($0 \leq x \leq 0.10$) were prepared via a sol gel method, through the decomposition of citric acid precursors. The materials used in the synthesis include samarium nitrate [$Sm(NO_3)_3 \cdot 6H_2O$, Alfa Aesar, 99.9%], cerium nitrate [$Ce(NO_3)_3 \cdot 6H_2O$, Alfa Aesar, 99.5%], iron nitrate [$Fe(NO_3)_3 \cdot 9H_2O$, Alfa Aesar, minimum 98%], nickel nitrate [$Ni(NO_3)_2 \cdot 6H_2O$, Alfa Aesar, 99%], and citric acid monohydrate [Alfa Aesar, minimum 99.0%]. The solutions of Sm, Ce, Fe and Ni nitrates were prepared separately in de-ionized water according to the desired stoichiometry. The citric acid solution was prepared by keeping the ratio of citric acid to total metal ion at unity. Finally all solutions of metal nitrates were mixed with the citric acid solution. The resulting mixture solution was dried at 100°C to obtain amorphous citrate precursors, which were further ground and then calcined at 850°C for 24 hours to form the perovskite structures.

9.2.2. Characterization

The BET surface areas of fresh pellets and reduced pellets were determined using a Quantachrome Autosorb 1-C instrument using nitrogen as the vector gas. The surface morphology of pellets (sintered at 1350°C for 4h) was observed by scanning electron microscopy (SEM, JEOL JSM-7500F). Imaging was also performed after reducing pellets at 1000°C under 5%v/v H_2/N_2. The surface chemical states and compositions of fresh pellets and reduced pellets were determined by X-ray photoelectron spectroscopy (XPS; Kratos AXIS Ultra^{DLD} 39-306l), using a monochromatic Al source. Peaks of $Sm3d_{5/2}$, $Ce3d_{5/2}$, $Fe2p_{3/2}$, $Ni2p_{3/2}$ and O1s core levels were used for quantification and identification of

oxidation states, and the Casa Software [27] was used for the analysis and quantification of the XPS spectra. The binding energy of the C1s level (284.8eV) was used to calibrate the energy scales of all spectra.

Electrical conductivities of all compositions were measured using a four-probe DC method under oxidizing conditions (air) and also under reducing conditions (5 %v/v H_2/N_2) in the temperature range of 25°C to 1000°C. Under reducing conditions two different types of samples were used in each case: i) partially reduced pellets; and ii) fully reduced pellets. Partially reduced samples were heated at 700°C under 5 %v/v H_2/N_2 for 1 hr prior to making conductivity measurements and did not show any phase separation when checked by XRD. Fully reduced samples were heated at 1000°C for 1hr before measurement. This treatment produces nanostructured surfaces with different composition, as will be discussed below. For conductivity measurements, the pellets of all compositions were made by uniaxially pressing 2g of powder to 15,000lbs ($6.67x10^4$N) and sintering the pellet in air to 1350°C for 4 hours with a ramp of 2°C/min during heating and cooling.

9.3. Results and discussions

The crystal structure of as synthesized $Sm_{0.95}Ce_{0.05}Fe_{1-x}Ni_xO_{3-\delta}$ perovskite materials with x=0-0.10 has been discussed recently [28]. The XRD patterns match well with the standard JCPDS card number 39-1490 of the traditional $SmFeO_3$ suggesting that all these nickel doped materials have a similar orthorhombic symmetry and belong to space group Pnma(62). Importantly, a single phase is observed for all the prepared perovskites. These materials are stable under air at 1350°C and do not show phase separation under 5%v/vH_2/N_2 up to at least 700^oC.

Pellets of $Sm_{0.95}Ce_{0.05}Fe_{1-x}Ni_xO_{3-\delta}$ ($0\leq x\leq 0.10$) sintered in air to 1350°C were prepared in order to test the perovskite series for sensing characteristics. The surface area of fresh, partially reduced, and fully reduced pellets was below our detection limit (the surface area of the sample is similar to that of the glassware that contains it during the measurement). The cross-sectional views of these pellets under the microscope confirm that the pellets were dense and can be considered as impenetrable by most gases.

9.3.1. Surface morphology and composition

The surface properties of the pellets were systematically studied to understand the sensing mechanism and the effect of different gases on the material itself. The microstructure of the sintered pellets before reduction is shown in Figure 9.1.

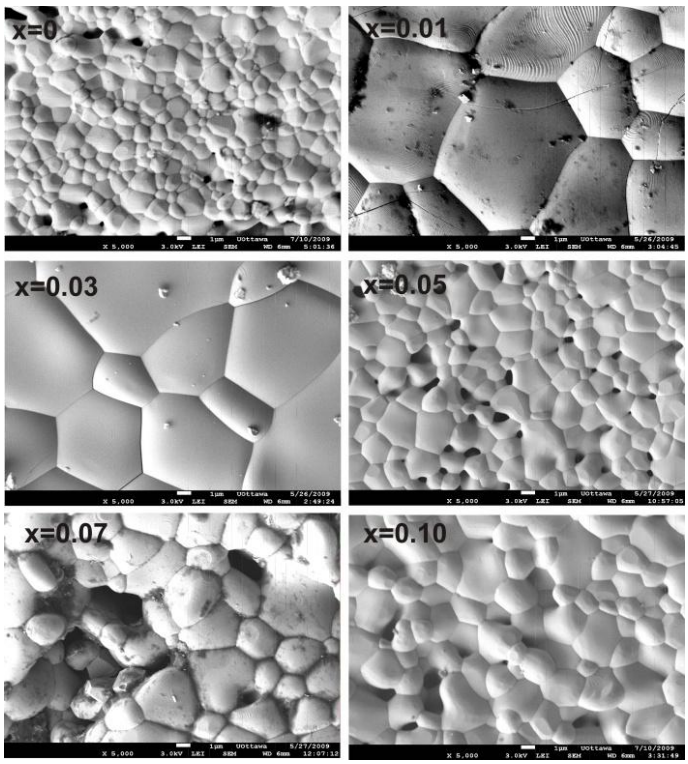

Figure 9.1. SEM images of pellets sintered at 1350°C for 4h of $Sm_{0.95}Ce_{0.05}Fe_{1-x}Ni_xO_{3-\delta}$ before reduction treatment. To improve comparison, all samples are shown in 5,000x magnification.

Grain sizes of each pellet sintered at 1350^{o}C for 4h under air were measured by averaging the diameter of the grains (Table 9.1) over at least two images of different areas per sample and at least two samples for each material (a total area of at least 800 μm^2). It was expected that the grain size should change monotonically as a function of Ni concentration. However, despite the fact that all samples were sintered under identical conditions, the grain size first increases up to x=0.03 and then decreases irregularly as a function of Ni concentration. This change in grain size as a function of Ni concentration can perhaps be related to the variability in powder preparation, although this variability is expected to be

random due to the intrinsic errors involved (grounding done manually or small variations in temperature ramp rates). Nevertheless, and despite this minor lack of control, it will be shown below that the observed changes in grain size cannot be correlated to the performance of these materials as sensors.

Table 9.1. Average diameter (D) of $Sm_{0.95}Ce_{0.05}Fe_{1-x}Ni_xO_{3-\delta}$ grains in pellets before and after reduction at 1000°C.

Ni Concentration	Fresh Pellets D (μm)[a]±SD[b]	Pellets After Reduction Treatment at 1000°C	
		Background Particles D (μm)[a]±SD[b]	Surface Nanoparticles D (μm)[a]±SD[b]
x=0	2.5±0.6	2.3±0.6	0.54±0.09
x=0.01	8.9±3.3	-[c]	0.83±0.14
x=0.03	9.5±4.4	9.3±3.2	0.22±0.09
x=0.05	2.4±0.6	8.5±3.0	0.66±0.41
x=0.07	4.6±1.6	9.8±3.4	0.40±0.06
x=0.10	3.7±1.3	1.8±0.8	0.076±0.003

[a] Values obtained by averaging particles diameters.
[b] Standard deviation.
[c] Not observable, background particles completely broke into nanoparticles.

The SEM images of fully reduced pellets (1000°C, 5%v/v H_2/N_2) show very different and interesting features (Figure 9.2). There is clear evidence of phase separation and surface segregation of small particles on the surface of all samples. The reduction treatment results in the formation of nanoparticles on the surface of the large background grains that formed the original pellets. After reduction treatment, the average size of background particles remains almost the same in the case of x=0, 0.03 and 0.10 while in the case of x=0.05 and 0.07 smaller grains have fused together to form bigger size grains (Table 9.1). For the x=0.01 sample, a different behaviour is observed in which surface grains break down into smaller particles (particle size goes from ~9 micron to ~800nm).

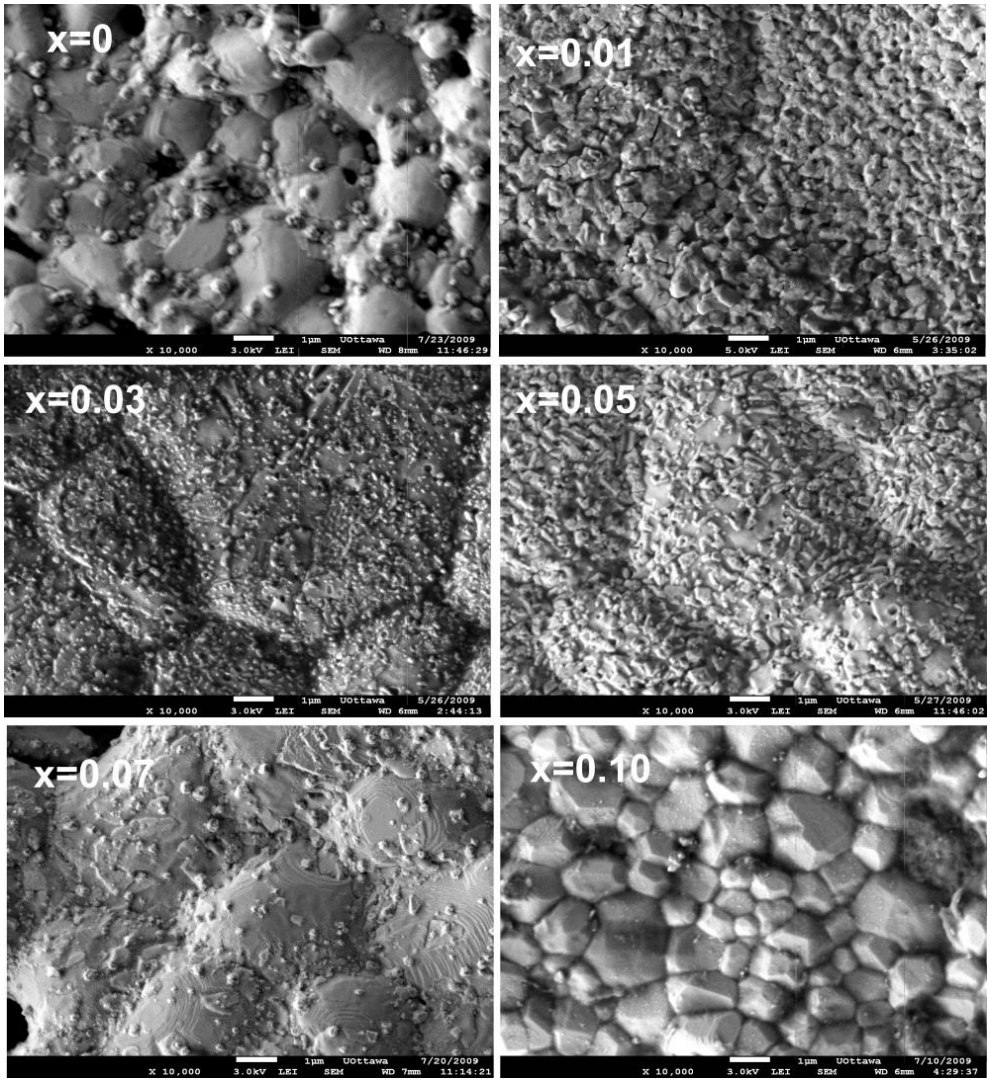

Figure 9.2. SEM image of sintered pellets of $Sm_{0.95}Ce_{0.05}Fe_{1-x}Ni_xO_{3-\delta}$ after reduction treatment. To improve comparison, all samples are shown in 10,000x magnification.

In order to identify the surface-segregated species, SEM imaging was done in two different modes, LEI-SEM and COMPO-SEM [29]. The LEI-SEM mode provides information about the surface topography while the COMPO-SEM mode provides an image with z-contrast. In the z-contrast image, the higher atomic number elements appear brighter than low atomic number elements. Figure 9.3 shows images of the same region taken in the two different modes for x=0, 0.03 and 0.07 samples after the reduction treatment. These images provide guidance in the identification of the surface segregated particles. The sample

containing x=0.03 has more iron (less bright spots) at the surface as compared to Sm (bright spots). The elemental identification was confirmed using point EDS measurements at multiple locations in the image (Figure 9.4).

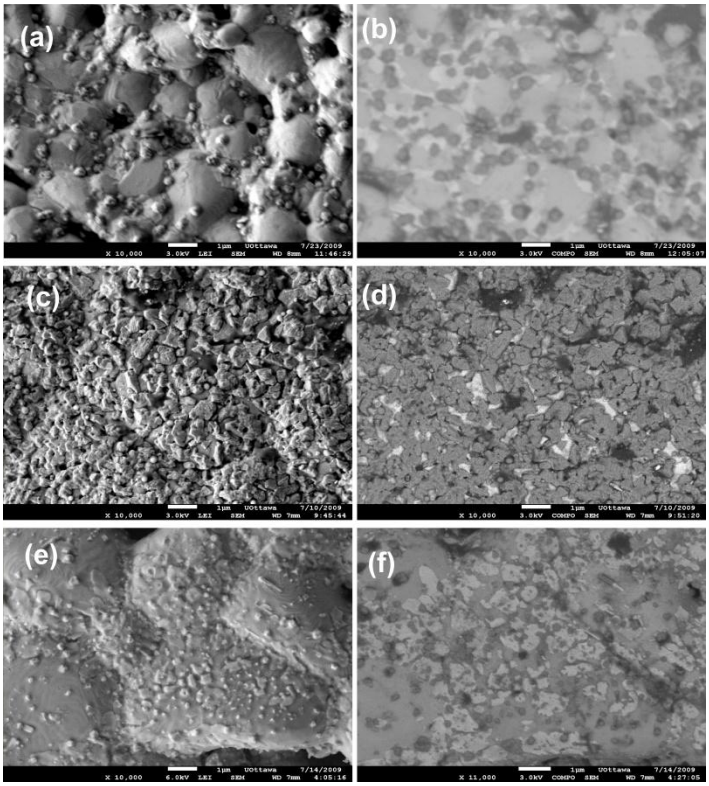

Figure 9.3. SEM image of reduced pellets of $Sm_{0.95}Ce_{0.05}Fe_{1-x}Ni_xO_{3-\delta}$ in two different modes. (a), (c) and (e) are images taken in LEI-SEM mode of x=0, 0.03 and 0.07 respectively while (b), (d) and (f) are images taken in COMPO-SEM mode of x=0, 0.03 and 0.07 respectively. Brighter areas are Sm rich, and darker areas are Fe rich.

Figure 9.4 shows the SEM images of x=0, 0.03 and 0.07. For each image, the right panel shows EDS point analysis of different regions. The regions where EDS analysis was performed are indicated as square boxes in the SEM image. The boxes represent the actual area sampled in each EDS spectrum. The spectra show the relative intensity of each component in the sample. In Figure 9.4a (x=0), a small difference in intensity is observed with the smaller particles containing a slightly higher ratio of iron (spectrum 2) than the large background particles (spectrum 1). The results of EDS point analysis of x=0.03 shown in Figure 9.4b are more clear. The nanoparticles formed upon reduction (spectrum 2) are Fe rich as compared with the larger background particles. Similarly, in Figure 9.4c the bright

region (spectrum 1) is the most Sm rich (larger Sm/Fe ratio) while the dark grey regions have more Fe.

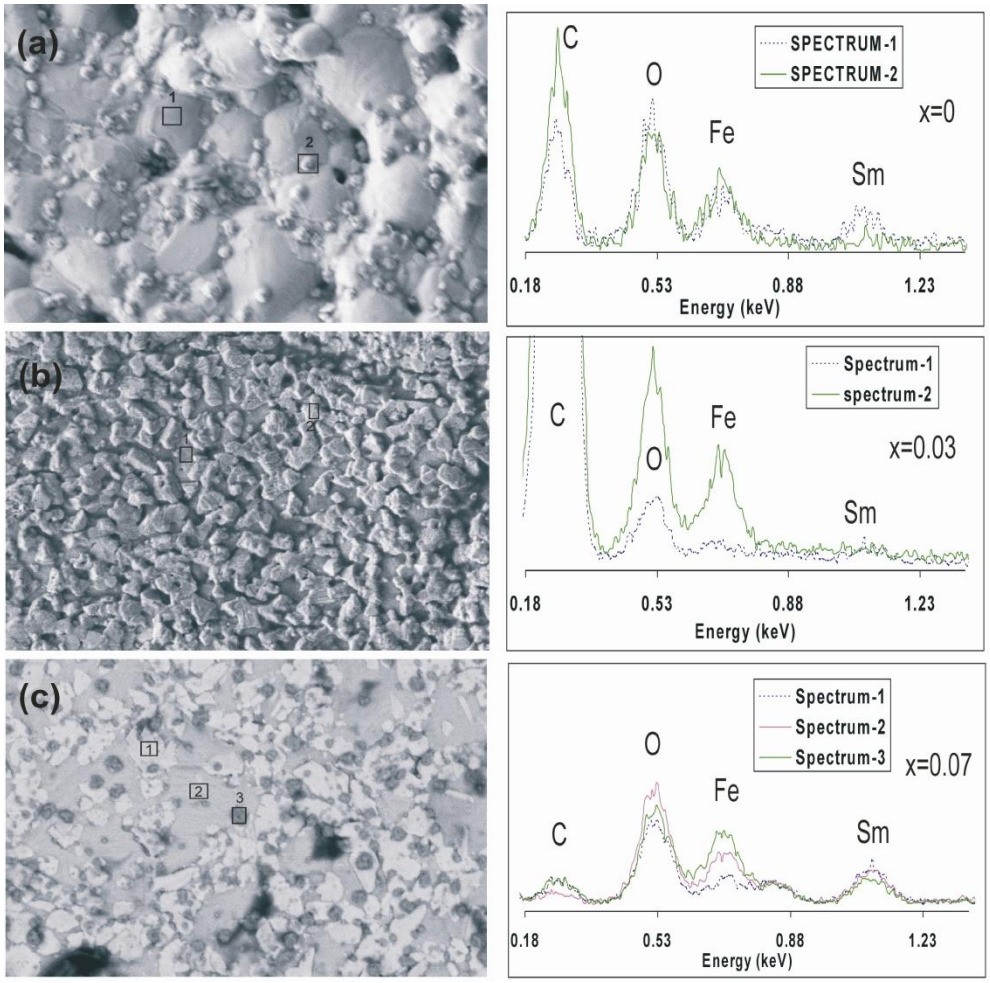

Figure 9.4. SEM image showing various regions taken for EDS point analysis. (a) x=0, (b) x=0.03 and (c) x=0.07. In front of each SEM image showing overlay of spectra taken at different regions of three samples

Figures 9.3 and 9.4 demonstrate that upon reduction, the surface of the pellets changes not only in morphology by the formation of nanoparticles, but also in composition, where the nanoparticles are formed with different chemical ratios than the microparticles of perovskite. The specific identification of chemical species, both for segregated surfaces and for non-segregated surfaces shows elemental enrichment but does not provide an identification of the chemical species (oxidation states) or phases present.

X-ray photoelectron spectroscopy (XPS) was used to determine the oxidation states and relative atomic ratios (at the surface) of the different elements in $Sm_{0.95}Ce_{0.05}Fe_{1-x}Ni_xO_{3-\delta}$ perovskites. For the purpose of quantification and identification of oxidation states, peaks of $Sm3d_{5/2}$, $Ce3d_{5/2}$, $Fe2p_{3/2}$, $Ni2p_{3/2}$ and O1s core levels were used. Figure 9.5 shows the spectra of $Sm3d_{5/2}$, $Fe2p_{3/2}$, $Ni2p_{3/2}$ and O1s core levels for all the Ni doped materials before reduction treatment. Identification of the oxidation states can be performed by comparison with the literature-reported photoelectron peak positions.

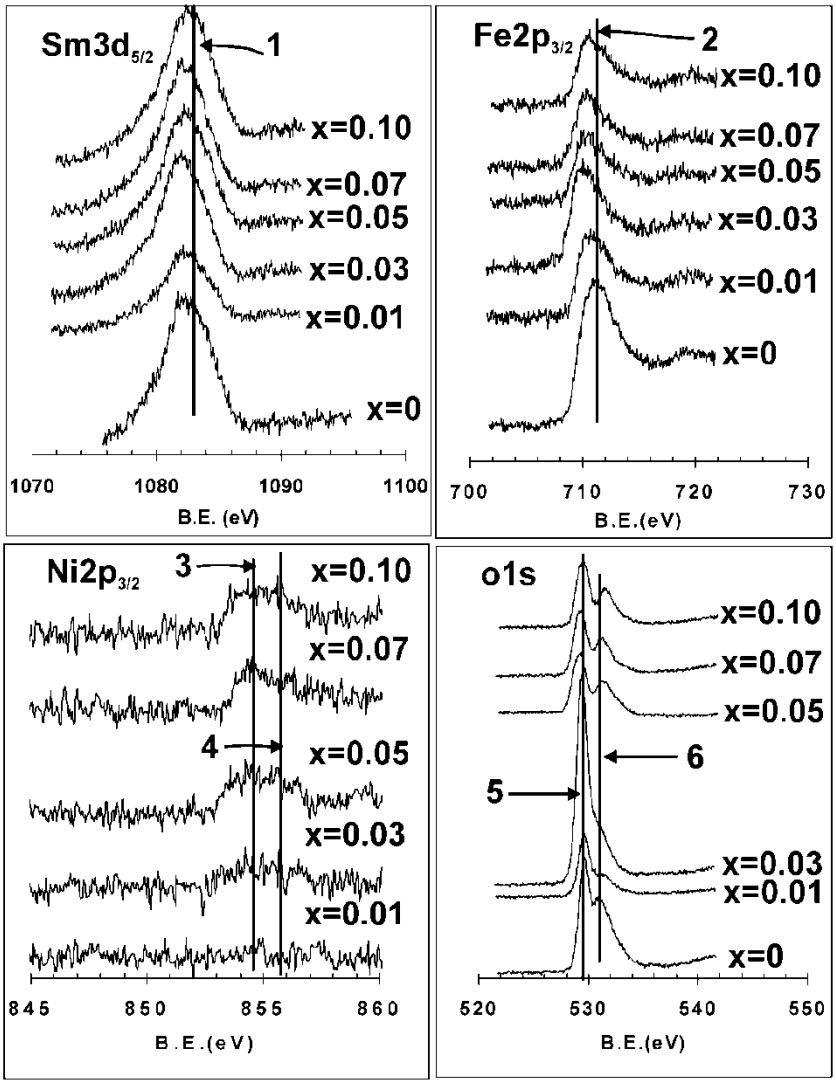

Figure 9.5. XPS spectra of $Sm3d_{5/2}$, $Fe2p_{3/2}$, $Ni2p_{3/2}$ and O1s core levels in $Sm_{0.95}Ce_{0.05}Fe_{1-x}Ni_xO_{3-\delta}$ before reduction treatment. Peaks labelled 1, 2, 3, 4, 5 and 6 are for Sm^{+3} at B.E. = 1082.9eV [14], Fe^{+3} at B.E. 710.62eV [10], Ni^{+2} at 854.3eV [30], Ni^{+3} at 855.8eV [30], $O^{-2}_{lattice}$ at 528.9eV [14] and O^{-}_{ads} at 530.9eV [14], respectively.

The position of the $Sm3d_{5/2}$ peak in all samples is only slightly shifted from the nominal Sm^{+3} position as measured for Sm_2O_3 (1082.9eV [14]). A small shift toward lower binding energy has been previously observed for $SmFeO_3$ (1082.4-1082.9eV [14]) and for $Sm_{1-x}Ce_xFeO_3$ (1081.9-1083.1eV [10]). As shown in Figure 9.5, the $Sm3d_{5/2}$ peak does not shift with Ni content, and its position is consistent with a single oxidation state for samarium, namely Sm^{+3}.

The oxidation state of Ni at low doping concentrations cannot be determined clearly from the XPS data. However, the peaks for Ni^{+2} and Ni^{+3} with B.E. 854.3eV and 855.8eV [30] can be easily observed within the broad peak at higher dopant levels. This suggests that Ni must be present in both +2 and +3 oxidation states. Since XRD data indicated the presence of Ni^{+3} in the bulk [28], the present observation suggests that the Ni^{+2} species must be concentrated at the surface.

The peak position and shape of $Fe2p_{3/2}$ indicates the presence of multiple oxidation states for iron. Figure 9.6 shows the peak fitting analysis for the x=0 and x=0.07 samples. The results for all samples are summarized in Table 9.2. In general, the $Fe2p_{3/2}$ peaks were broad and clear shoulders (peak separation) were not always visible. For this reason, the authors prefer not to use the fitting analysis in a quantitative manner; instead, a qualitative identification of oxidations states is most appropriate and reliable. As expected, all samples in the as prepared stage (before reduction) show high oxidation states for iron.

The $Ce3d_{5/2}$ peak (not shown) was extremely small and very broad for all samples, preventing identification of the Ce oxidation state. The O1s peaks for $Sm_{0.95}Ce_{0.05}Fe_{1-x}Ni_xO_{3-\delta}$ consist of two components, as previously observed for $SmFeO_3$ [14]. The low B.E. component has been assigned to lattice oxygen ($O^{-2}_{lattice}$) while the high B.E. component has been assigned to surface adsorbed oxygen (O^{-}_{ads}). The B.E. values of $O^{-2}_{lattice}$ and O^{-}_{ads} in this Ni doped series were 529±0.2eV and 530.7±0.4eV (Figure 5) which are in good agreement with the reported values for $SmFeO_3$[14].

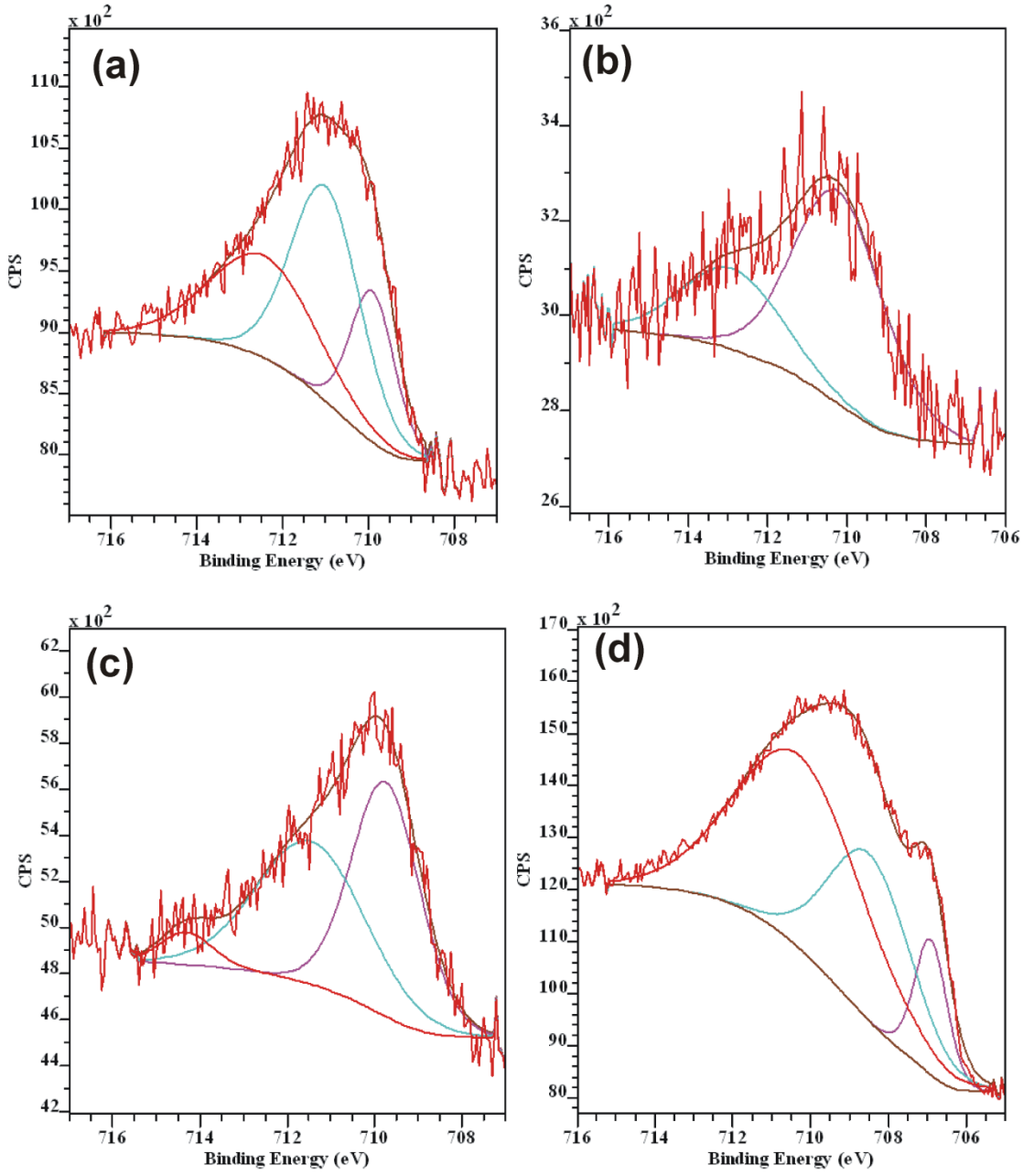

Figure 9.6. Fitting of $Fe2p_{3/2}$ XPS peaks for x=0 and x=0.07. (a) and (c) are peak fitting results of x=0.0 and x=0.07 respectively before reduction treatment while (b) and (d) are peak fittings of x=0.0 and x=0.07 respectively after reduction treatment at 1000^{o}C.

Table 9.2. Oxidation state assignment based on peak fittings for $Fe2p_{3/2}$ of pellets before reduction and after reduction at 1000°C.

		Binding energy (eV)			
		Fe^{0}	Fe^{+2}	Fe^{+3}	Fe^{+4}
x=0	Before Reduction	-	709.87	711.02	712.60
	After Reduction	-	-	710.20	712.97
x=0.01	Before Reduction	-	710.05	711.27	713.28
	After Reduction	707.28	708.63	710.43	-
x=0.03	Before Reduction	-	709.52	710.83	712.90
	After Reduction	707.12	708.69	710.35	-
x=0.05	Before Reduction	-	709.91	711.28	712.85
	After Reduction	706.69	708.20	710.01	-
x=0.07	Before Reduction	-	709.74	711.45	714.31
	After Reduction	706.91	708.47	710.26	-
x=0.10	Before Reduction	-	-	710.26	713.66
	After Reduction	706.53	708.63	-	-

XPS measurements were also performed after reducing the sintered pellets of the nickel doped perovskites under 5%v/v H_2/N_2 flowing at 1000°C for one hour. Figure 9.7 shows the XP spectra of $Sm3d_{5/2}$, $Fe2p_{3/2}$, $Ni2p_{3/2}$ and O1s core levels for this series. The B.E. of the $Sm3d_{5/2}$ core line does not change, which suggests that the reduced samples also have samarium as Sm^{+3}. The small shift observed for the x=0.10 sample is ascribed to a secondary effect due to the partial reduction of iron. The peak of $Fe2p_{3/2}$ core levels of all samples is broadened and there is the appearance of a shoulder towards low B.E. Peak fittings performed for these samples show the presence of multiple oxidation states of Fe (Figure 9.6 and Table 9.2). As expected, the reduced samples show, on average, a lower oxidation state for iron than the samples before reduction. However, the presence of Fe^{0} is surprising as it

suggests that there may be a metallic coating (or metallic particles) on the perovskite surface that would greatly increase electrical conductivity, with obvious consequences toward sensor performance.

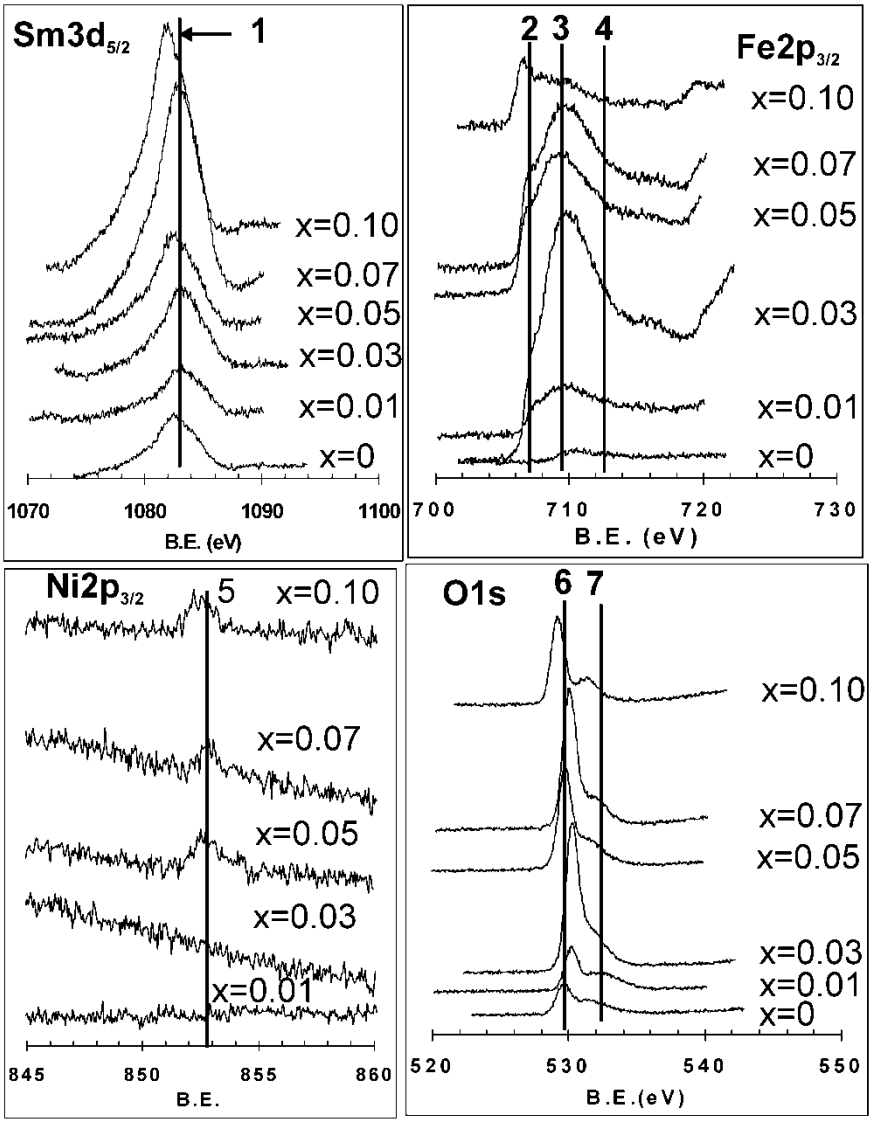

Figure 9.7. Comparison of peaks of $Sm3d_{5/2}$, $Fe2p_{3/2}$, $Ni2p_{3/2}$ and O1s core levels in $Sm_{0.95}Ce_{0.05}Fe_{1-x}Ni_xO_{3-\delta}$ after reduction treatment at 1000°C. Peaks labelled 1, 2, 3, 4, 5, 6 and 7 are for Sm^{+3} at B.E. = 1082.9 eV [14], Fe^0 at 706.5eV[31], Fe^{+2} at 709.3eV[31], Fe^{+3} at B.E. 710.62 eV[10], Ni^0 at 852.7eV[32], $O^{-2}_{lattice}$ at 528.9eV[14] and O^{-}_{ads} 530.9eV[14] respectively

The $Ni2p_{3/2}$ core level peaks of samples after reduction treatment are shown in Figure 9.7. In the case of the x=0.01 –0.03 samples, the Ni was not detectable on the surface as there were no signals from the $Ni2p_{3/2}$ core level. However, for the x=0.05-0.10 samples, the $Ni2p_{3/2}$ peak appears at ~852.6eV, which matches well with metallic Ni (852.7eV [32]). This observation suggests that some nickel dopant reduces to metallic nickel at the surface.

Table 9.3: Surface atomic ratio of lattice oxygen and ratios of lattice and adsorbed oxygen for $Sm_{0.95}Ce_{0.05}Fe_{1-x}Ni_xO_{3-\delta}$ (x=0-0.10) before and after reduction.

	Experimental Stoichiometry $\frac{O^{-2}}{Sm+Ce+Fe+Ni}$		$\frac{O^{-2}}{O^{-}_{ads}}$	
	Before Reduction	After Reduction	Before Reduction	After Reduction
x=0	1.17	0.83	0.42	0.84
x=0.01	1.97	0.94	1.63	3.09
x=0.03	1.89	0.29	1.18	1.30
x=0.05	0.42	0.29	1.04	1.55
x=0.07	0.42	0.35	1.08	2.98
x=0.10	1.30	0.24	0.84	1.93

The reduced samples also have two components for the O1s core level line, i.e. lattice oxygen $O^{-2}_{lattice}$ at 529.8±0.4eV and surface adsorbed oxygen O^{-}_{ads} at 531.8±0.4eV, as shown in Figure 9.7. These peaks are similar to those observed for fresh samples (i.e. before reduction treatment). Table 9.3 shows the surface oxygen composition of sintered pellets before and after reduction. As for the case of powder samples [28], these sintered materials have a lower value of oxygen stoichiometry than the expected O/M=1.5, which indicates the presence of oxygen vacancies. Upon reduction treatment, the ratio is further reduced, as

expected. However, the ratio of $O^{-2}_{lattice}$ to O^{-}_{ads} obtained by fitting O1s peaks indicates that reduced samples have a higher $O^{-2}_{lattice}/O^{-}_{ads}$ ratio, which indicates the preferential removal of surface adsorbed oxygen.

Quantification of the relative surface abundances of Sm, Ce, Fe and Ni in $Sm_{0.95}Ce_{0.05}Fe_{1-x}Ni_xO_{3-\delta}$ was performed using their respective core level lines by using the Casa XPS software. Concentrations before and after reduction treatment are presented in Figure 9.8. Before reduction treatment, all the perovskites show a Sm rich surface due to surface segregation within the perovskite structure (no phase separation or particle formation is observed by XRD or SEM). Upon reduction, there is a change in the average composition, the surface morphology and the phases present on the surface. In fact, in the case of x=0.03, the surface changes from Sm-rich before reduction to Fe-rich upon reduction. The changes in composition are in good agreement with SEM results shown in Figure 9.3 and EDS analysis shown in Figure 9.4. While the oxidized samples have a Sm enriched surface without disruption of the perovskite crystals, upon reduction small particles of material enriched in iron or samarium are segregated. Identification of the oxidation state of each component by XPS suggests that the surface segregated Sm species in all unreduced and reduced samples is Sm_2O_3 (samarium remains in the +3 state). In contrast, the surface segregated Fe species in all unreduced samples is Fe_2O_3 while in reduced samples Fe^0 and Fe_2O_3 are observable. The formation of Fe^0 and/or Fe_2O_3 on the surface is a combination of surface segregation and phase separation.

XRD failed to show Fe^0/Fe_2O_3 or Ni^0 as separated phases in the reduced samples, which were seen and confirmed by XPS and/or SEM. The apparent inconsistency between XRD and XPS/SEM is easily explained. The Fe^0/Fe_2O_3 and Ni^0 features are surface species and in very low concentration compared to bulk crystal structures observed in the XRD diffractogram.

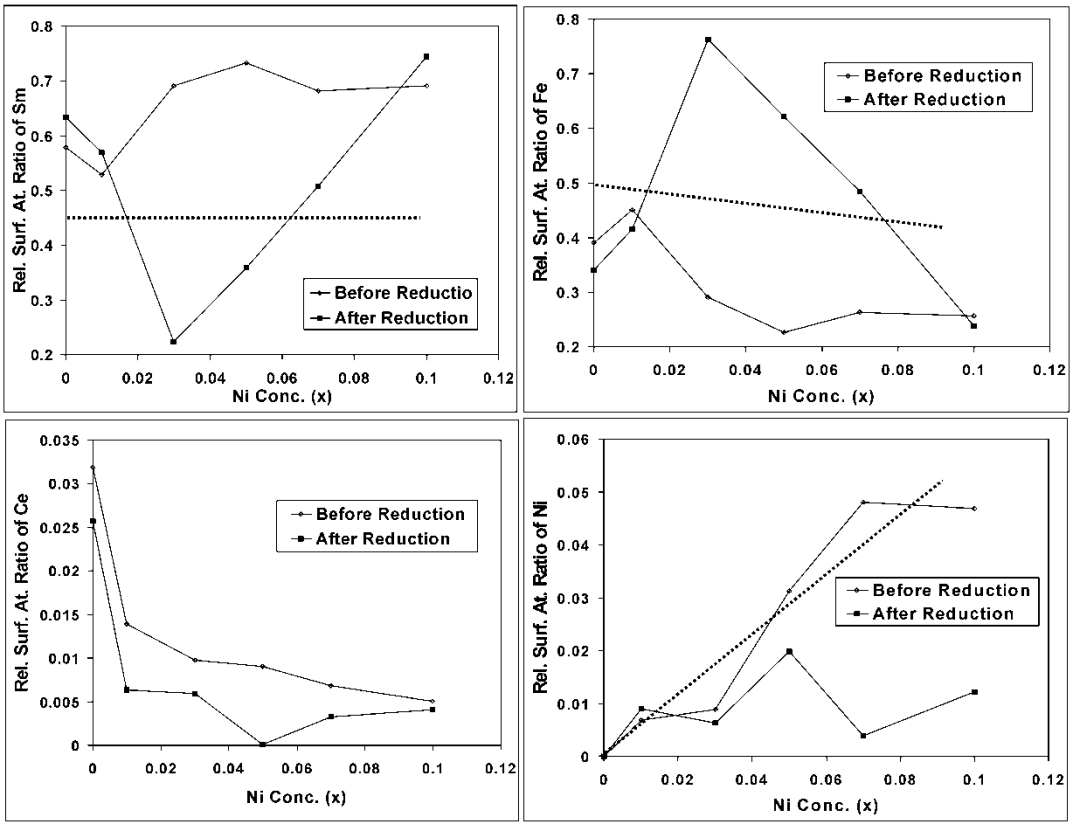

Figure 9.8. Relative Surface atomic ratios determined by XPS of Sm, Ce, Fe and Ni in $Sm_{0.95}Ce_{0.05}Fe_{1-x}Ni_xO_{3-\delta}$ as a function of nickel concentration. Dashed lines indicate nominal bulk concentration for Sm and Fe and Ni; the nominal value for Ce is off-scale (0.05).

9.3.2. Electrical conductivity

The electrical conductivity of $Sm_{0.95}Ce_{0.05}Fe_{1-x}Ni_xO_{3-\delta}$ was measured by the four probe DC method under air (25-1000°C) as well as under 5%v/v H_2/N_2 (25-700°C and 25-1000°C). Conductivity measurements were performed on sintered pellets, effectively a design for bulk solid state sensors.

Because a single perovskite structure is maintained for these materials up to 700°C under reducing conditions, a set of materials were studied for conductivity such that the temperature was never above 700°C (these samples shall be referred to as partially reduced). A second set (series) was treated to 1000°C (one hour under 5% v/v H_2/N_2) to allow full reduction and phase segregation. These two sets allow the study of the effect of change in surface morphology and composition discussed in the previous sections on the electrical conductivity of this nickel doped series.

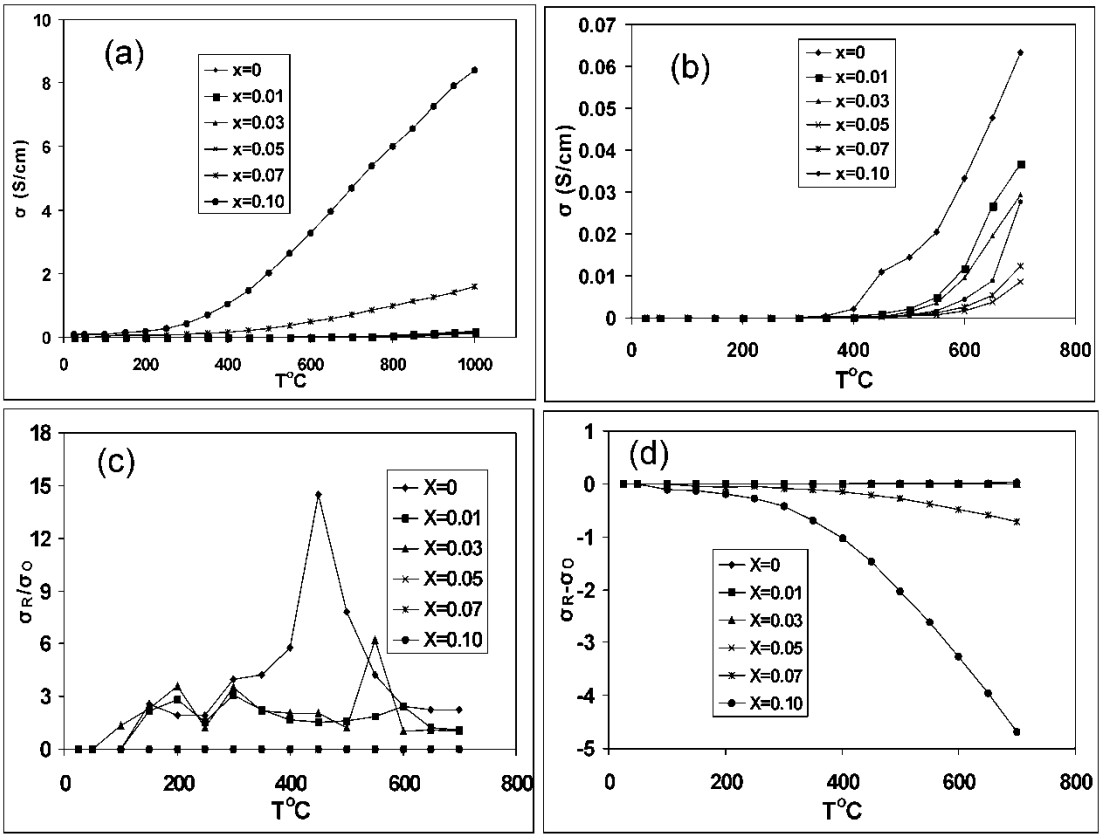

Figure 9.9. Electrical Conductivity of $Sm_{0.95}Ce_{0.05}Fe_{1-x}Ni_xO_{3-\delta}$ sintered at 1350°C as a function of temperature. (a) electrical conductivity measured in air from 25-1000°C (b) electrical conductivity of partially reduced $Sm_{0.95}Ce_{0.05}Fe_{1-x}Ni_xO_{3-\delta}$ at 700°C under 5%v/v H_2/N_2 from 25-700°C; (c) and (d) show potential sensing parameters ($\sigma_R - \sigma_O$) and $\frac{\sigma_R}{\sigma_O}$ respectively as a function of temperature

Figure 9.9a shows the electrical conductivity measured from 25-1000°C under air as a function of nickel concentration. In all measurements, the temperature was first maintained at 1000°C for 1h under air to obtain a stable electrical conductivity value and then the electrical conductivity was measured from 1000°C to 25°C in 50°C steps. It was expected that the electrical conductivity values of $Sm_{0.95}Ce_{0.05}FeO_{3-\delta}$ (n-type) under air would decrease as a function of Ni concentration due to the p-type (i.e., hole-dopant) nature of NiO/Ni_2O_3 [33]. However, the semiconducting nature of the materials indicates that the electrical conductivity should rise with temperature, as it is in fact observed. The change in electrical conductivity as a function of nickel concentration is not monotonic (Figure 10a). First, the electrical conductivity increases slightly from x=0 to x=0.01 then it decreases slightly from

x=0.01 to x=0.05 and finally a big rise in electrical conductivity is observed from x=0.05 to x=0.10.

The electrical conductivity dependence measured under 5%v/v H_2/N_2 after reducing at 700^{o}C is shown in Figure 9.9b. In these measurements, first all pellets were heated for 1h at 700^{o}C while flowing 5%v/v H_2/N_2 to obtain stable electrical conductivity values, which is an indication of equilibrium at this temperature. Second, the electrical conductivities were measured while decreasing temperature in 50^{o}C steps from 700^{o}C to 25^{o}C. Because the substituted perovskites remain as a single phase in this temperature range, these measurements should directly reflect the effect of Ni concentration on the electrical conductivity. The results show that the electrical conductivity increases as a function of temperature, indicating semiconducting behaviour but decreases slightly as a function of Ni concentration up to x=0.05 and then increases (Figure 9.10b). More importantly, all Ni doped materials have lower electrical conductivity under 5%v/v H_2/N_2 than undoped $Sm_{0.95}Ce_{0.05}FeO_{3-\delta}$.

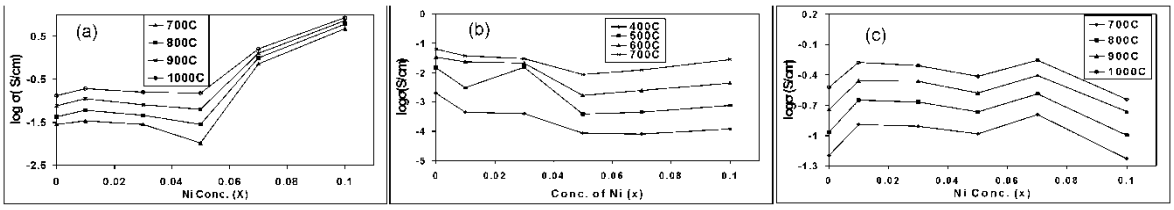

Figure 9.10. Electrical conductivities of $Sm_{0.95}Ce_{0.05}Fe_{1-x}Ni_xO_{3-\delta}$ as a function of nickel concentration at various temperatures. (a) Electrical conductivities of fresh pellets under air, (b) Electrical conductivities under 5%v/v H_2/N_2 after reduction treatment at 700^{o}C, (c) Electrical conductivities under 5%v/v H_2/N_2 after reduction treatment at 1000^{o}C.

The sensitivity of these materials is typically defined by equation 9.3, where σ_g is the conductivity in the presence of a test gas, in this case a reducing atmosphere (hence σ_R), and σ_{air} is the reference conductivity in air (σ_O). However, one can consider the response of the sensor material in terms of the improvement in conductivity (σ_R/σ_O) as in Figure 9.9c. The figure shows that the maximum sensitivity is exhibited by x=0 at 450^{o}C (σ_R/σ_O = ~15) while all nickel doped materials have almost identical but lower sensitivity values.

$$S = \left(\frac{\sigma_g - \sigma_{air}}{\sigma_{air}} \right) * 100\% \qquad (9.3)$$

Another way to consider the sensitivity is by simply measuring the difference in conductivity between the two environments. This parameter (σ_R - σ_O) is also used in order to characterize the electrical behaviour as n-type or p-type for these nickel doped materials. Generally, a positive value of σ_R - σ_O indicates n-type electrical behaviour while a negative value of σ_R - σ_O indicates a p-type electrical behaviour. This data is shown graphically in Figure 9.9d. The analysis of Figure 9.9d reveals that samples where x=0-0.05 have positive values of $\sigma_R - \sigma_O$, while samples where x=0.07-0.10 have negative values. This data points towards a change in conductivity behaviour from n-type to p-type at a nickel content between x=0.05 and x=0.07. This suggests that materials of different nickel concentration may be used for sensing different environments i.e., reducing and oxidizing.

The effect of Ni doping on the electrical conductivity of $Sm_{0.95}Ce_{0.05}FeO_{3-\delta}$ can be summarized as: (i) the electrical conductivity under air increases in a non-linear fashion as function of Ni concentration; (ii) all Ni doped materials have lower electrical conductivities as compared to the undoped perovskite ($Sm_{0.95}Ce_{0.05}FeO_{3-\delta}$) under reducing conditions (5%v/v H_2/N_2); (iii) the electrical behaviour changes from n-type to p-type as a function of Ni concentration. These observations can be explained in terms of: (i) formation of a very small number of oxygen vacancies due to the predominance of Ni^{+3} over Ni^{+2} in the lattice; (ii) predominance of the stronger Ni^{+3}-O bond over the more reducible Ni^{+2}-O bond even under reducing conditions; (iii) titration of the electron-doping effect of Ce by the hole-doping effect of Ni up to x=0.05, after which point the hole-doping effect becomes dominant (a transition from n-type to p-type).

From the discussion above, since the electrical conductivity under reducing conditions and the sensitivity towards 5%v/v H_2/N_2 of all Ni doped materials is lower than for undoped $Sm_{0.95}Ce_{0.05}FeO_{3-\delta}$, we decided to study the effect of phase separation and surface modification of these Ni doped materials. Previous results have indicated that a partial phase separation may be beneficial to sensor performance. All pellets were first reduced under 5%v/v H_2/N_2 for 1h at 1000^{o}C to allow the phase separation and formation of nanoparticles on the surface and then electrical conductivity values were measured from 1000^{o}C to 25^{o}C in

50^{o}C steps. It was noticed that after the 1h treatment, the electrical conductivity value was stable in for each sample. It can be inferred that the materials' surface chemical composition was stable after the reduction treatment.

Figure 9.10c shows the electrical conductivities of $Sm_{0.95}Ce_{0.05}Fe_{1-x}Ni_xO_{3-\delta}$ pellets measured after reduction treatment at 1000°C for 1h under 5%v/v H_2/N_2. The data shows that these fully reduced samples have higher electrical conductivity values as compared to partially reduced samples (reduced at 700^{o}C for 1h). This improvement in electrical conductivities is found to be associated with changes in surface morphology and surface chemical composition, as discussed above (SEM and XPS analysis). Summarizing, the enhancement in electrical conductivity can be attributed to: i) the formation of nanoparticles at the surface of the pellets; ii) the presence of highly reduced and even metallic species (Fe^0 and Ni^0) at the surface; iii) a decrease in surface adsorbed oxygen, which facilitates the formation of oxygen vacancies at the surface; and iv) decreasing the intensity of electron-hole production effect of Ni in the lattice by converting some Ni^{+2} and Ni^{+3} into metallic Ni. The electrical conductivity trend of these fully reduced samples was found to be non-linear as a function of Ni concentration. The behaviour can be considered as the combination of metallic Fe species and the presence of oxygen vacancies due to the Ni presence.

Figure 9.11 shows the full range of conductivity behaviour for the fully reduced perovskites. In analogy with Figure 9.9, Figure 9.11 shows the conductivity in air (panel a) and in reducing atmosphere (panel b). Similarly, sensitivity indicators are plotted in panels c and d. The electrical conductivity values change because of surface modification and phase separations, indicating perhaps a change in electrical behaviour of these materials. The calculated $\sigma_R - \sigma_O$ values displayed in Figure 9.11d show that the electrical behaviour of these perovskites did not change due to reduction treatment at 1000°C, that is the $\sigma_R - \sigma_O$ values for x=0-0.05 remain positive and for x=0.07-0.10 remained negative suggesting that these materials are still n-type and p-type, respectively. In other words after reduction at 1000°C, the electrical conductivity values of x=0-0.05 under reducing conditions remained higher as compared to air while the electrical conductivity values of x= 0.07-0.10 under reducing conditions remained lower as compared to air.

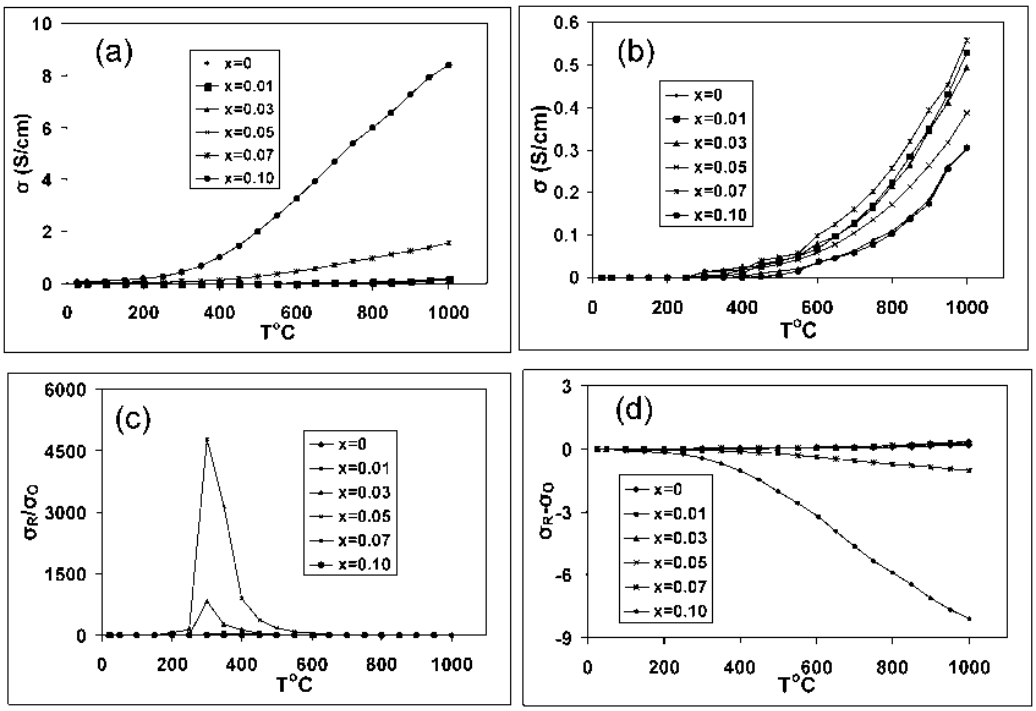

Figure 9.11. Electrical Conductivity of $Sm_{0.95}Ce_{0.05}Fe_{1-x}Ni_xO_{3-\delta}$ sintered at 1350°C as a function of temperature. (a) electrical conductivity measured in air from 25-1000°C; (b) electrical conductivity of fully reduced $Sm_{0.95}Ce_{0.05}Fe_{1-x}Ni_xO_{3-\delta}$ at 1000°C under 5%v/v H_2/N_2 from 25-1000°C; (c) and (d) show potential sensing parameters (σ_R-σ_O) and (σ_R/σ_O) respectively as a function of temperature.

The extent of improvement in electrical conductivities of fully reduced samples can be exemplified by considering the ratio (σ_R/σ_O) of the x=0.05 sample to hydrogen at 300°C (Figure 9.11c). The value of σ_R/σ_O is 4790 ($4.8x10^5$ %), more than three orders of magnitude improvement in conductivity which can be ascribed to presence of both metallic Fe and Ni species on the surface (Figure 9.2 and Figure 9.8). This value is much higher than for cobalt doped $Sm_{0.95}Ce_{0.05}FeO_{3-\delta}$ materials [34], and compares well with sensitivity published for other state of the art solid sensors at the same temperature. In fact, the x=0.01, 0.03 and 0.05 samples show a positive value of σ_R-σ_O for all temperatures (Figure 9.11d), with the highest sensitivity observed at 300°C after reduction treatment at 1000°C. However, it is important to note that the change in surface properties occurs the first time that the samples are treated under the reducing atmosphere which suggests that these can be used in alarm applications (single use) because a big rise in electrical conductivity occurred.

After the initial irreversible change in surface morphology, the sensors become reversible with moderate sensitivity (i.e. they can be cycled between oxidizing and reducing atmospheres and used as standard sensors). As an example of the reproducible sensor

behaviour of these materials, and hence their potential for applications, the x=0.05 sample ($Sm_{0.95}Ce_{0.05}Fe_{0.95}Ni_{0.05}O_{3-\delta}$) was cycled between oxidizing (air) and reducing (5%v/v H_2/N_2) atmospheres (Figure 9.12). The figure shows the material in its fresh, partially reduced and fully reduced state operating at 200°C. For each state of the perovskite, Figure 9.12 shows the reproducibility of the conductivity change where no significant drops in sensitivity were found. The difference in the baseline (air atmosphere) corresponds to the differences in conductivity shown in Figures 9.9 and 9.11. Upon exposure to the reducing atmosphere, each sample shows an increase in conductivity and upon return to an air atmosphere, the conductivity returns to the baseline reading. The sensitivity of the x=0.05 sample to hydrogen at 300°C is stable and reversible with a value of σ_R/σ_O=14.5 (or $1.4x10^3$ %). This suggests that upon surface modification at high temperature in the reducing gas, a new stable structure is formed that can be used for continuous monitoring.

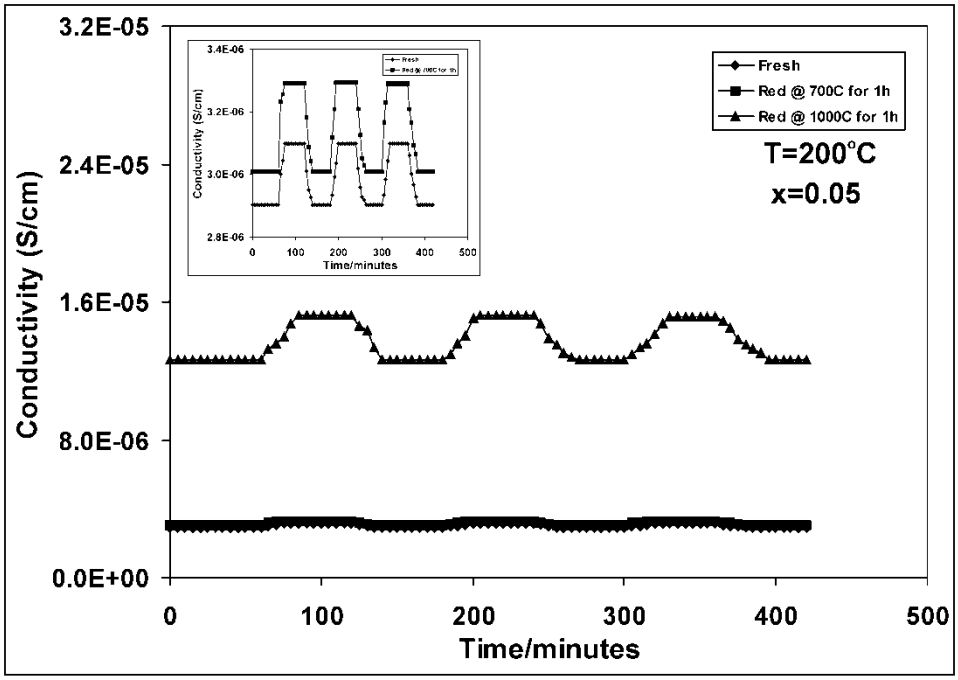

Figure 9.12. Reproducibility of the sensing response of $Sm_{0.95}Ce_{0.05}Fe_{0.95}Ni_{0.05}O_{3-\delta}$ at 200°C for samples prepared fresh, partially reduced, and fully reduced. Conductivity was measured while switching the atmosphere from air (baseline) to 5% v/v of H_2/N_2 and back. The insert shows an expanded scale of the two bottom curves (fresh material and partially reduced material).

In summary, the electrical conductivity of fully reduced samples depends on the Ni concentration present and the concentration of metallic Ni and Fe present on the surface. Clearly after reduction treatment at 1000^{o}C, the effect of Ni and Fe on the surface is more pronounced on the improvement of electrical conductivity values and thus on sensitivities of these Ni doped materials.

9.4. Conclusions

A new class of perovskite materials was prepared with formula $Sm_{0.95}Ce_{0.05}Fe_{1-x}Ni_xO_{3-\delta}$ ($0 \leq x \leq 0.10$) by using a citric acid sol gel combustion method. These materials were stable under air up to 1350°C and up to 700°C under 5%v/v H_2/N_2. A process of phase sepearation under 5%v/v H_2/N_2 is observed above that temperature, with the formation of small surface particles. Interstingly, x=0-0.05 samples are n-type while x=0.07-0.10 samples are p-type conductors. The reduction treatment at 1000^{o}C was very effective in increasing electrical conductivities. This improvement in electrical conductivities did not change the electrical behaviour of x=0-0.05 (n-type) and x=0.07-0.10 (p-type) samples, but rather it was found to be associated with changes in microstructure and surface chemical composition as revealed by XPS, SEM and EDS analysis. The improved electrical conductivities of these materials and in particular the ratios of σ_R/σ_O suggest that these materials should be considered as chemical sensors for the detection of oxidizing and reducing gases.

The response of these chemical sensors (x=0-0.10) depends on their electrical conductivity under a particular chemical environment. Generally sensors with higher electrical conductivity have a higher and more easily detectable response. If an n-type sensor has very low electrical conductivity under air, it will not be suitable for detection of an oxidizing gas because upon exposure its electrical conductivity can further decrease to such an extent that it could be out of the measurable range. The same fact is expected from a p-type sensor with very low electrical conductivity under air after exposure to a reducing gas. Since the reduction treatment of these Ni doped materials has resulted in reasonably high electrical conductivity under both oxidizing and reducing conditions due to formation metallic species i.e., Fe and Ni, these materials can now be consider as candidates for sensors to detect both oxidizing and reducing gases like O_3, NO_2, CO and H_2.

9.5. References

[1] L. Chen, J. Hu, S. Fang, Z. Han, M. Zhao, ZhanleiWu, X. Liu, H. Qin, Sens. Actuators B. 139 (2009) 407-410.
[2] X. Liu, J. Hu, B. Cheng, H. Qin, M. Jiang, Sens. Actuators B. 134 (2008) 483-487.
[3] X. Liu, B. Cheng, J. Hu, H. Qin, M. Jiang, Sens. Actuators B. 133 (2008) 340-344.
[4] A.B. Bodade, A.V. Kadu, G.N. Chaudhari, J Sol-Gel Sci Technol. 45 (2008) 27-33.
[5] M. Zhao, H. Peng, J. Hu, Z. Han, Sens. Actuators B. 129 (2008) 953-957.
[6] J. Zosel, D. Franke, K. Ahlborn, F. Gerlach, V. Vashook, U. Guth, Solid State Ionics. 179 (2008) 1628-1631.
[7] L. Zhang, J. Hu, P. Song, H. Qin, K. An, X. Wang, M. Jiang, Sens. Actuators B. 119 (2006) 315-318.
[8] H. Aono, E. Traversa, M. Sakamoto, Y. Sadaoka, Sens. Actuators B. 94 (2003) 132-139.
[9] M.C. Carotta, G. Martinelli, Y. Sadaoka, P. Nunziante, E. Traversa, Sens. Actuators B. 48 (1998) 270-276.
[10] S.M. Bukhari, J.B. Giorgi, Solid State Ionics. 180 (2009) 198-204.
[11] E. Traversa, Y. Sadaoka, M.C. Carotta, G. Martinelli, Sens. Actuators B. 65 (2000) 181-185.
[12] G. Martinelli, M.C. Carotta, M. Ferroni, Y. Sadaoka, E. Traversa, Sens. Actuators B. 55 (1999) 99-110.
[13] Y. Hosoya, Y. Itagaki, H. Aono, Y. Sadaoka, Sens. Actuators, B. 108 (2005) 198-201.
[14] H. Aono, M. Sato, E. Traversa, M. Sakamoto, Y. Sadaoka, J. Am. Ceram. Soc. 84 (2001) 341-347.
[15] Matsushima, Shigenori, Sano, Norihiko, Sadaoka, Yoshihiko, J. Ceram. Soc. Jpn. 108 (2000) 681-682.
[16] M.A. Pena, J.L.G. Fierro, Chem. Rev. 101 (2001) 1981-2017.
[17] N. Yamazoe, N. Miura, IEEE Transactions on Components, Packaging and Manufacturing Technolog-Part A. 18 (1995) 252-256.
[18] S. Das, P. Mandal, Zeitschrift Fur Physik B. 104 (1997) 7-9.
[19] Y. Itagaki, M. Mori, Y. Hosoya, H. Aono, Y. Sadaoka, Sens. Actuators, B. 122 (2007) 315-320.
[20] I. Balint, K.-i. Aika, Appl. Surf. Sci. 173 (2001) 296-306.
[21] X. Zhu, H. Wang, W. Yang, Solid State Ionics. 177 (2006) 2917-2921.
[22] D. Klissurski, R. Dimtrova, Bull. Chem. Soc. Jpn. 63 (1990) 590-591.
[23] I. Waernhus, P.E. Vullum, R. Holmestad, T. Grande, K. Wiik, Solid State Ionics. 176 (2005) 2783-2790.
[24] J. Mizusaki, T. Sasamoto, W.R. Cannon, H.K. Bowen, J. Am. Ceram. Soc. 66 (1983) 247-252.
[25] S.M. Bukhari, J.B. Giorgi, ECS Trans. 28 (2010) 19-29.
[26] S. Kuharuangrong, Ceram. Int. 30 (2004) 273-277.
[27] N. Fairley, Casa XPS version 2.3.13 Dev73 (2007).
[28] S.M. Bukhari, J.B. Giorgi, Solid State Ionics. submitted (2010).
[29] JEOL Trademark.

[30] T. Dickinson, A.F. Povey, P.M.A. Sherwood, J. Chem. Soc. Faraday Trans.I. 73 (1977) 327-343.
[31] W. Cheng, X. Ma, J. Phys.: Conference Series. 152 (2009) 012039.
[32] C.J. Powell, Appl. Surf. Sci. 89 (1995) 141-149.
[33] B.A. Reguig, M. Regragui, M. Morsli, A. Khelil, M. Addou, J.C. Bernede, Solar Energy Materials & Solar Cell. 90 (2006) 1381-1392.
[34] S.M. Bukhari, J.B. Giorgi, Solid State Ionics. 181 (2010) 392-401.

10. Hydrogen detection by reduced Ni doped $Sm_{0.95}Ce_{0.5}FeO_{3-\delta}$ perovskite based sensors

The contents of this chapter will be submitted to Sensors and Actuators B

Abstract

Recently we have reported a new series of perovskites with formula $Sm_{0.95}Ce_{0.5}Fe_{1-x}Ni_xO_{3-\delta}$ ($0 \leq x \geq 0.10$). In this series x=0-0.05 are n-type while x=0.07-0.10 are p-type semiconductors. In this work we tested the x=0-0.05 materials for hydrogen detection at 300°C. The bulk sensors were rectangular pellets which were reduced at 1000°C in 5% H_2/N_2 for 1h. This treatment has been shown to improve electrical conductivity due to formation of surface nanoparticles consisting of Sm_2O_3 and/or Fe. A four probe DC method was used to determine their electrical conductivities under air and mixtures of H_2 and N_2 containing H_2 from 1 to 5% v/v. The results showed that all these sensors have linear response as a function of H_2 concentration but the response was non linear as a function of Ni concentration. The sensitivity of x=0.01 was highest in the series but with very slow response (2h). The optimal electrical conductivity response towards 1 and 5% H_2/N_2 was shown by x=0.03 with shortest response time. Since all the materials showed complete response recovery, the sensing process appears to be reversible. The exponential plot between sensitivity and hydrogen concentration match well with the empirical relation $S = KC_{H_2}^{-\alpha}$ indicating that these sensors are strongly concentration dependent.

10.1. Introduction

The change in global climate caused by growing industries and vehicles has recently become a serious concern. As a result, the research interest in hydrogen as a near-future fuel has increased, since hydrogen is abundant, renewable and can be efficiently utilized. Unlike other commonly used fuels, hydrogen can provide zero emissions because the combustion product of hydrogen is water, which is environment friendly. The energy produced by hydrogen per weight of fuel is three and seven times greater than produced by equal amounts of gasoline and coal, respectively [1]. However, hydrogen is extremely flammable due to its small ignition energy (0.02mJ in air) [2], and it can easily leak from storage and transportation equipment due to its large diffusion coefficient (0.61cm^2/second) [2]. Therefore, hydrogen detection has become an important issue from a safety point of view.

Many hydrogen gas sensors have been developed and studied over the years. The conventional hydrogen sensors are mostly based on SnO_2 [1, 3-5] and TiO_2 [6]. Although the SnO_2 based sensors have high sensitivity for hydrogen, they often have poor reproducibility and low stability under reducing conditions. Additionally, there is a lack of information about the exact sensitivity mechanism and more detail research is needed. Similarly TiO_2 based sensing devices also have some issues like very low[7], even null [8] sensitivity at above 400^oC, restriction to an operating temperature lower than 300^oC due to oxidation of Ti metal and difficulty in miniaturization of devices. Overall, there is a demand for new types of hydrogen sensing materials.

It is evident from literature that perovskites have a great potential for use as gas sensors because they have high electrical conductivity and are capable of catalytic activity involving oxidation-reduction reactions. The ABO_3 type perovskite oxides have been extensively used as gas sensors. The beauty of this ABO_3 type structure is that substitution at the A-site and/or the B-site can be done to obtain desirable sensitivity and selectivity [9-15]. As a pre-requisite for hydrogen sensors, the perovskite material should be stable under reducing atmospheres and have reasonably high electrical conductivity. In previous work we have demonstrated that Ce substitution at the A-site in $SmFeO_3$ not only improves its reduction stability but also improves its electrical conductivity under reducing conditions by converting it from p-type into a n-type material [13], thus making it suitable for detection of reducing gases, including hydrogen. Substitution of Co at the B-site in $Sm_{0.95}Ce_{0.05}FeO_{3-\delta}$ further improves its electrical conductivity under reducing conditions to such extent that $Sm_{0.95}Ce_{0.05}Fe_{0.97}Co_{0.03}O_{3-\delta}$ shows good and reversible sensitivity for hydrogen at room temperature [12]. Recently we prepared a new series of perovskite materials by Ni substitution at the B-site in $Sm_{0.95}Ce_{0.05}FeO_{3-\delta}$ and characterization of these materials reveals that materials with x=0-0.05 are n-type while x=0.07-0.10 are p-type [16]. These Ni doped $Sm_{0.95}Ce_{0.05}FeO_{3-\delta}$ perovskites are stable up to 700^oC under 5%H_2/N_2 and a phase separation of Sm_2O_3 does occur with the preservation of the perovskite phase at a temperature of 800^oC and above. Interestingly, a little rise in electrical conductivity was found on Ni doping under reducing condition but a dramatic increase in electrical conductivity is observed upon reduction treatment (x=0-0.05) at 1000^oC in 5%H_2/N_2 for 1h. This enhancement in electrical conductivity upon reduction treatment was found to be associated with a change in surface morphology and composition. Despite

these changes, the electrical conductivity values were reproducible after reduction treatment indicating that the surface and bulk composition are stable. In this work we prepared bulk solid state sensors based on reduced perovskite materials, $Sm_{0.95}Ce_{0.05}Fe_{1-x}Ni_xO_{3-\delta}$ (x=0-0.05), and investigated them for hydrogen detection at 300^{o}C.

10.2. Experimental

10.2.1. Preparation of $Sm_{0.95}Ce_{0.05}Fe_{1-x}Ni_xO_{3-\delta}$ (x=0-0.05) powders

The $Sm_{0.95}Ce_{0.05}Fe_{1-x}Ni_xO_{3\pm\lambda}$ (x=0-0.05) powders were prepared by a sol-gel citrate method. In this method samarium nitrate [$Sm(NO_3)_3 \cdot 6H_2O$, AlfaAesar, 99.9%] , cerium nitrate [$Ce(NO_3)_3 \cdot 6H_2O$, AlfaAesar, 99.5%], iron nitrate [$Fe(NO_3)_3 \cdot 9H_2O$, AlfaAesar, >98%] and nickel nitrate [$Ni(NO_3)_2 \cdot 6H_2O$, Alfa Aesar, 99%] were weighed separately according to the desired stoichiometric ratio of the four metals ($Sm_{0.95}$ + $Ce_{0.05}$: $Fe_{(1-x)}$ + Ni_x = 1:1) and were then dissolved in de-ionized water to prepare their solutions. Solutions were mixed and the resulting solution was added to aqueous citric acid monohydrate [minimum 99.0%, AlfaAesar] such that the metal to citric acid ratio was 1:1. Water was evaporated at 100°C until the amorphous citrate precursors were dried and the material was then ground and finally calcined at 850°C for 24 hours to form the perovskite phase.

10.2.2. Fabrication and measurement of reduced $Sm_{0.95}Ce_{0.05}Fe_{1-x}Ni_xO_{3-\delta}$ (x=0-0.05) based sensors

The sensors can be fabricated in the form of thin films [7, 8, 17, 18], thick films[3, 4, 11, 19, 20] and pellets[12, 21-23]. Thick film sensors have some advantages over thin film e.g., shorter response time and faster recovery time. In thick sensors, deep penetration of analyte gas molecules into grain boundary areas is possible due to a well developed pore structure with three dimensionally interconnected fine grains. that shorter the potential barrier which ultimately improve the sensing quality of thick film sensors as compared to thin films [3] but using pellets as sensors is the easiest and more practicable way to test the preliminarily qualities of any material for sensing applications. Therefore, in this work, we used pellets for evaluating the hydrogen sensing qualities of these reduced Ni doped $Sm_{0.95}Ce_{0.05}FeO_{3-\delta}$ materials.

The detail description of sensor fabrication and measurement has been previously described (Chapter 6 and references [22, 24]). Briefly, the synthesized powders were uniaxially pressed with the help of a pellet press to prepared circular shaped pellets. These

pellets were sintered at 1350^{o}C for 4h with a ramp of 2^{o}/minute during heating and cooling. The resulting circular pellets were chopped to form rectangular pellets (sensors). In each case, four probes were mounted on each rectangular shaped sensor by raping four Pt wires. The two outer wires were connected to a power supply while the two inner wires were connected to a digital multimeter. These rectangular pellets (sensors) were set up in a quartz tube having rubber septa on both ends (testing chamber). Two mass flow controllers, one for controlling flow of air and the other for the mixture of H_2/N_2 were used. The total flow rate was set to 50 sccm.

Before testing, the sensors were reduced for 1h under 5%H_2/N_2 at 1000^{o}C. This treatment improves the electrical conductivity through the formation of surface nanoparticles [16]. The electrical conductivity of each sensor was measured under oxidizing conditions (air) and under reducing conditions (1%H_2/N_2v/v) to determine the activation energy of each process. Electrical conductivity responses of these sensors toward different mixtures of H_2/N_2 (1-5%v/v) were measured at 300^{o}C. The sensor response was defined as:

$$S(\%) = \frac{\sigma_g - \sigma_{air}}{\sigma_{air}} \times 100 \qquad (10.1)$$

where σ_g is electrical conductivity in H_2/N_2 mixture and σ_{air} is electrical conductivity in air.

10.3. Results and discussions

10.3.1. Phase structure of $Sm_{0.95}Ce_{0.05}Fe_{1-x}Ni_xO_{3-\delta}$ powders

The X-ray diffraction patterns of $Sm_{0.95}Ce_{0.05}Fe_{1-x}Ni_xO_{3-\delta}$ (x=0-0.05) are shown in Figure 10.1. The comparison of these X-ray diffraction patterns shows that all these perovskites were single phase with orthorhombic structure (space group Pnma). The detail information about their crystal structure, thermal and reduction stability has already reported in chapter 8 and 9 [16, 25].

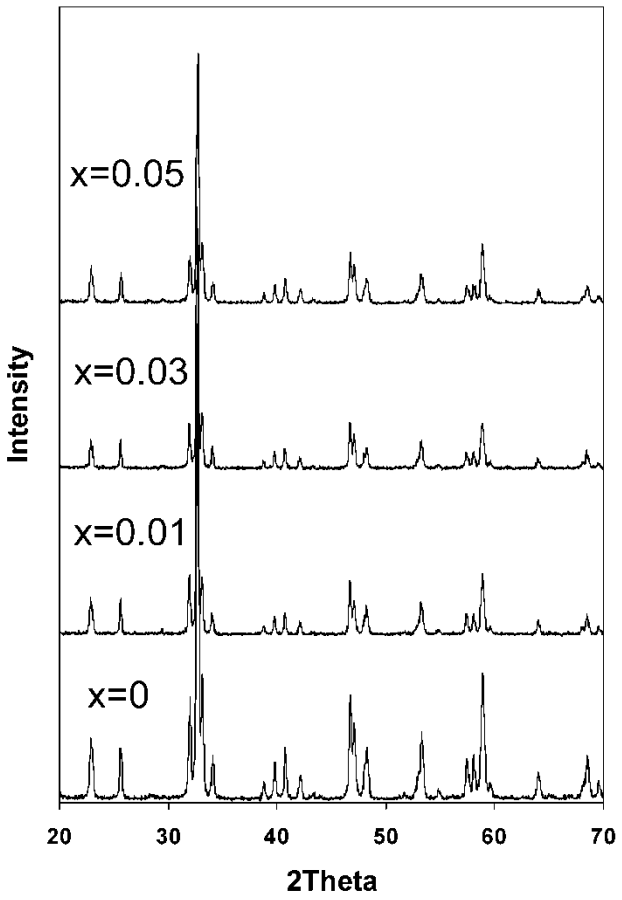

Figure 10.1. The XRD pattern of as synthesized $Sm_{0.95}Ce_{0.05}Fe_{1-x}Ni_xO_{3-\delta}$ powders.

10.3.2. Surface morphology of $Sm_{0.95}Ce_{0.05}Fe_{1-x}Ni_xO_{3-\delta}$ (x=0-0.05) based sensors

The electrical conductivity of these materials dramatically increases upon reduction treatment at 1000°C for 1h in 5%H_2/N_2 v/v due to the formation of nanoparticles of Fe and Sm_2O_3 on their surfaces[16]. Figure 10.2 shows the SEM images of a new series of $Sm_{0.95}Ce_{0.05}Fe_{1-x}Ni_xO_{3-\delta}$ (x=0-0.05) based sensors after reduction treatment. This figure shows identical surface morphology and composition to the images presented in Figure 9.2 (Chapter 9 and reference [16]).

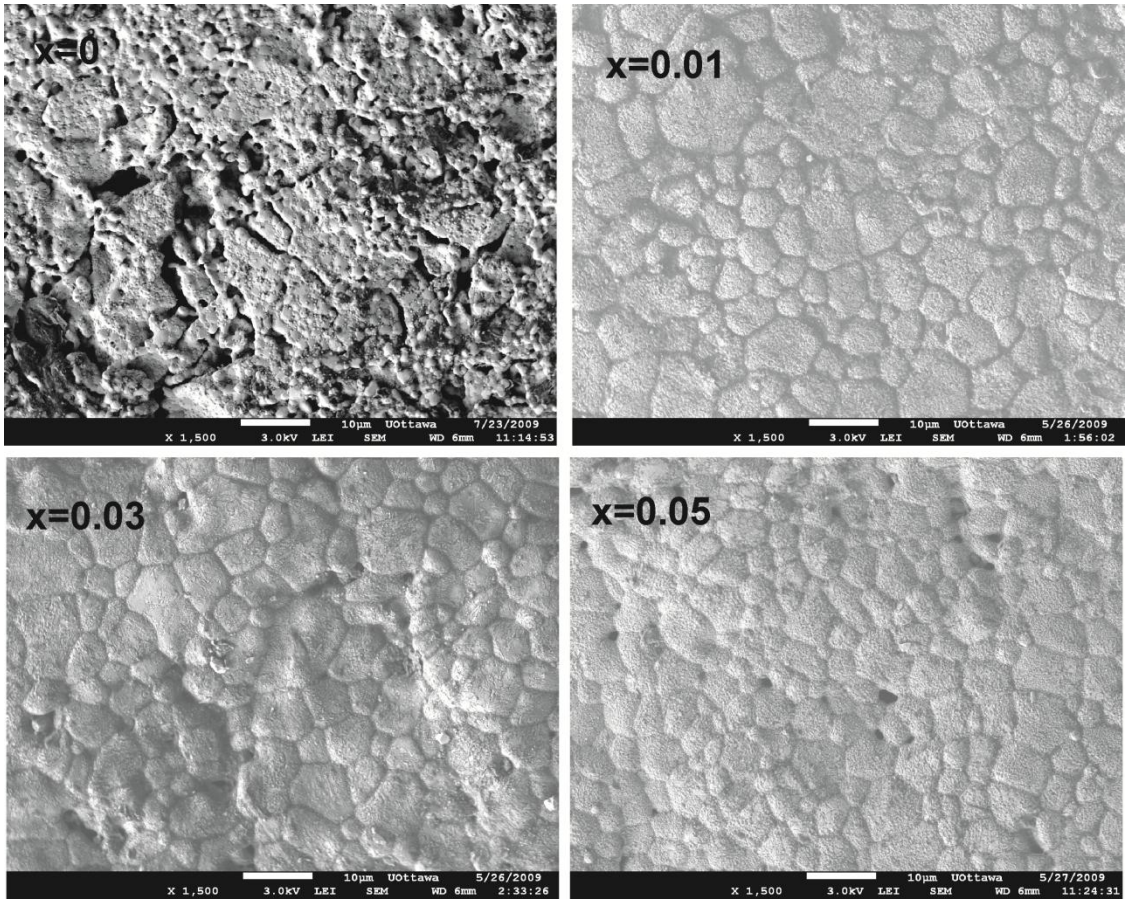

Figure 10.2. SEM images of $Sm_{0.95}Ce_{0.05}Fe_{1-x}Ni_xO_{3-\delta}$ (x=0-0.05) based sensors upon reduction in 5%H_2/N_2 v/v at 1000^{o}C for 1h.

10.3.3. Electrical properties

The electrical conductivities of all sensors (after reduction treatment) were measured under both air and 1%H_2/N_2 in the temperature range of 25-400^{o}C. Figure 10.3 shows the temperature dependence of electrical conductivities for $Sm_{0.95}Ce_{0.05}Fe_{1-x}Ni_xO_{3-\delta}$ based sensors in air and 1%H_2/N_2. The relationship between the electrical conductivity of a semiconductor and temperature T is:

$$\sigma = \sigma_o e^{-(E_a/kT)} \qquad (10.2)$$

where σ is electrical conductivity, e is pre-exponential factor, k is Boltzmann constant and E_a is activation energy. A linear relationship between $\ln\sigma$ and inverse temperature is shown by

these sensors under both air and 1%H_2/N_2. The activation energies calculated from the slopes of the Arrhenius plots are shown in Figure 10.4 as a function of Ni concentration. The higher activation energies explains the lower electrical conductivities under air. The higher electrical conductivities under 1%H_2/N_2 as compared to air indicates n-type behavior. It also confirms that the reduction treatment does not affect the n-type nature of Ni doped $Sm_{0.95}Ce_{0.05}FeO_{3-\delta}$ perovskite materials.

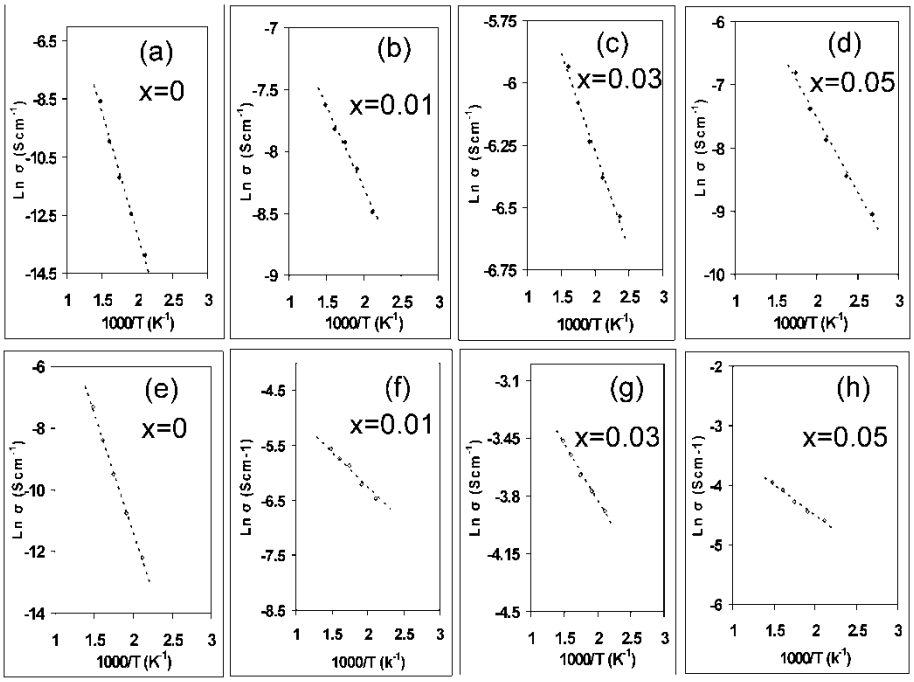

Figure 10.3: Variation of lnσ of Ni doped $Sm_{0.95}Ce_{0.05}FeO_{3-\delta}$ in air (a - d) and in 1%H_2/N_2 (e - f) with inverse of temperature.

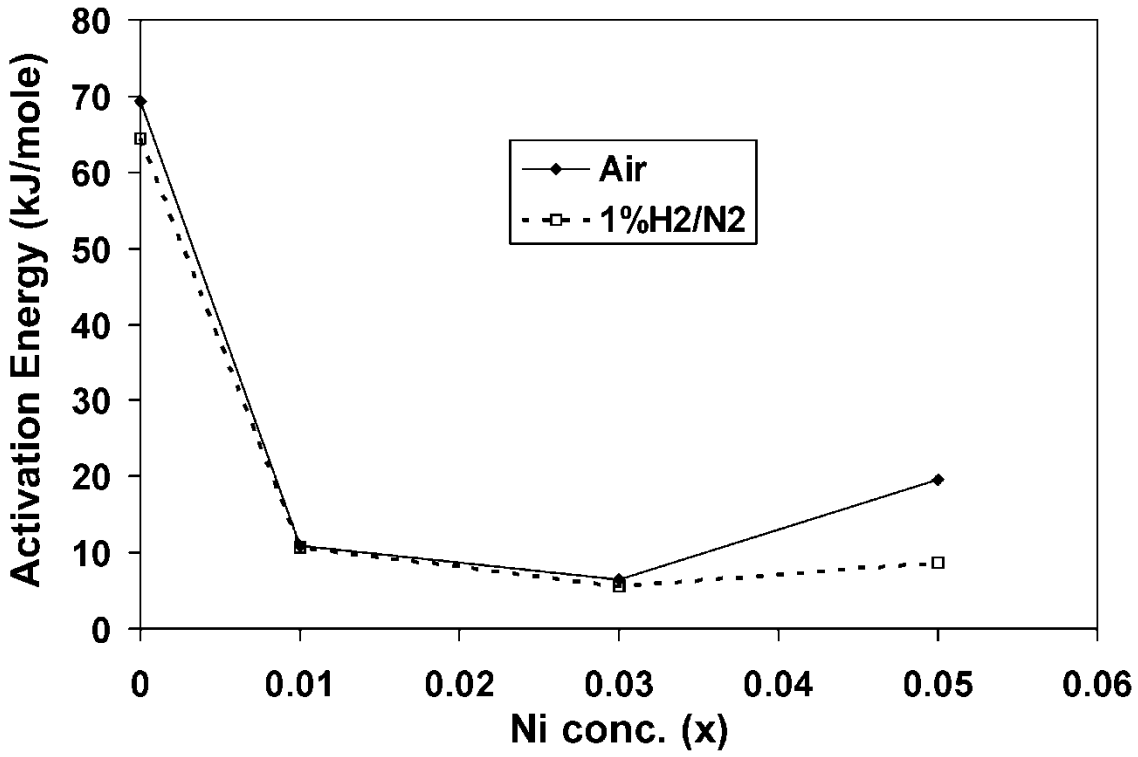

Figure 10.4. Activation energy of $Sm_{0.95}Ce_{0.05}Fe_{1-x}Ni_xO_{3-\delta}$ (x=0-0.05) calculated from Arrhenius plots for air and $1\%H_2/N_2$ as a function of Ni concentration.

10.3.4. Hydrogen sensing properties

The sensing response of all bulk sensors were measured at 300^{o}C. Initially sensors were kept for 3h at 300^{o}C in flowing air to obtain a stable electrical conductivity value and then a $1\%H_2/N_2$ mixture was introduced into the testing chamber while the flow of air was stopped. The electrical conductivity increased on introduction of the $1\%H_2/N_2$ mixture. The flow of the $1\%H_2/N_2$ mixture was continued until a stable electrical conductivity value was obtained. At that point, the $1\%H_2/N_2$ mixture was switched back to air and measurements continued until the sensors recovered their original conductivity value. This series of steps were repeated with 3 and 5% H_2/N_2; the results are shown in Figure 10.5.

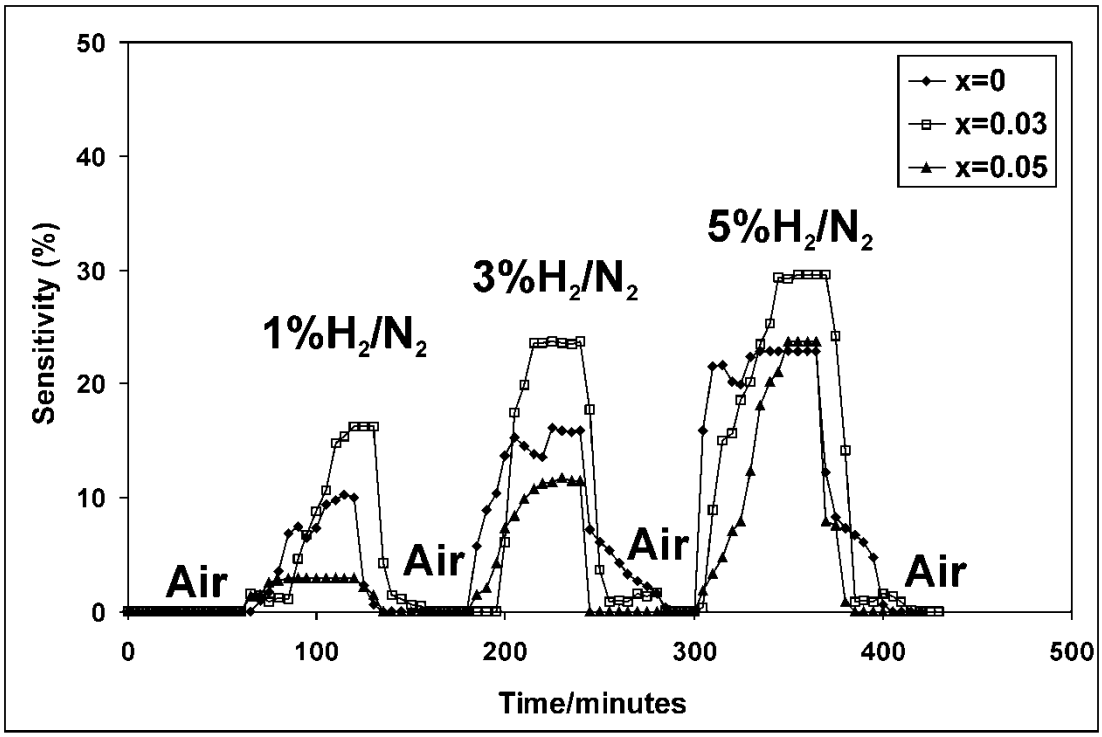

Figure 10.5. Time dependence sensing response of $Sm_{0.95}Ce_{0.05}Fe_{1-x}Ni_xO_{3-\delta}$ (x=0, 0.03 and 0.05) at 300°C as the air switched to mixtures of H_2/N_2 containing various concentrations of H_2 as time proceeds.

Figure 10.5 shows the electrical conductivity responses of x=0, 0.03 and 0.05 under 1-5% H_2/N_2 v/v as function of time at 300°C. The sensor response of the undoped Ni material (x=0) was 10, 16 and 23% with 1, 3 and 5%H_2/N_2 respectively and the response recovery time under 1%H_2 was short (i.e. 10min) as compared 3 and 5%H_2. Data for the x=0.01 material has been plotted separately in Figure 10.6 because it shows a more complex behaviour. The x=0.01 material showed a maximum sensitivity of ~700 under 3%H_2 in the series but the response stabilization was very slow (2h) and response recovery was not 100% (Figure 10.6, top panel). The sensitivity of x=0.01 was also measured at 250°C (Figure 10.6, bottom panel). At this temperature its sensitivity was lower but recoverable.

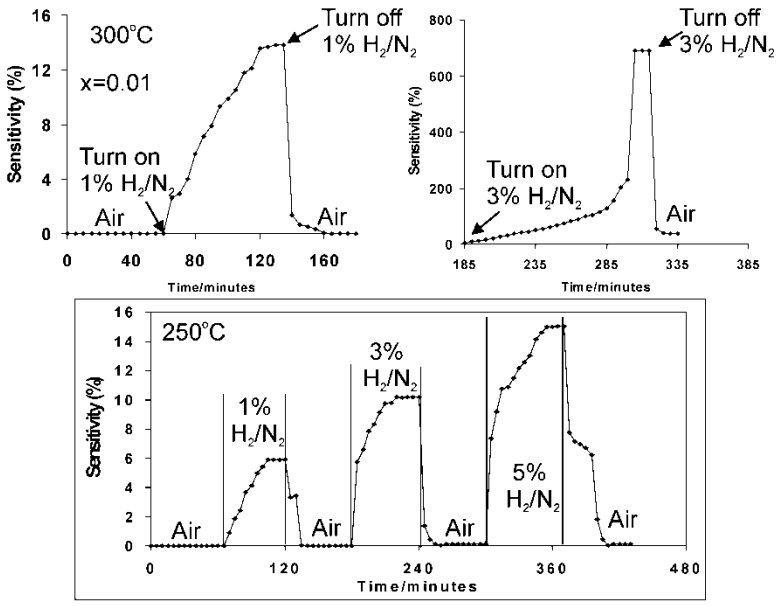

Figure 10.6. Time dependence sensing response of $Sm_{0.95}Ce_{0.05}Fe_{1-x}Ni_xO_{3-\delta}$ (x=0.01) as the air switched to mixtures of H_2/N_2 containing various concentrations of H_2 as time proceeds at 300°C (upper) and 250°C (lower)

The sensitivity of x=0.03 is highest as compared to x=0 and x=0.05 towards the 1 and 5% H_2/N_2 mixtures but lower than x=0.01 for the 3% H_2/N_2 mixture at 300°C. Overall, the performance of x=0.03 is optimal in the series due to better responses, shorter response and recovery times. The characteristic sensor behaviour can be explained in relation to surface morphology and composition of the sensors. In light of our previous work, the reduction at 1000°C results in the surface segregation of oxides along with formation of metallic iron on the surface [16] and x=0.03 has the highest concentration of metallic iron on the surface.

10.3.5. Sensing Mechanism

The sensing mechanism of these nickel doped materials in air and under hydrogen can be explained in terms of surface reaction of oxygen and hydrogen respectively. Since these perovskite materials are n-type, an increase in free electrons in the conduction band will increase the electrical conductivity. When a semiconductor perovskite (n-type or p-type) is exposed to air, the following general reactions are expected to occur:

$$O_2(gas) + e^- \rightarrow O_2^-(ads) \qquad (10.3)$$

$$O_2^-(ads) + e^- \rightarrow 2O^-(ads) \quad (10.4)$$

$$O^-(ads) + e^- \rightarrow O^{-2}(ads) \quad (10.5)$$

Oxygen will take electrons from the conduction band and create electron-holes. As these materials are n-type, the formation of electron-holes will lower their electrical conductivity. On the other hand when exposed to reducing molecules like H_2, the following general reactions occur on the surface:

$$H_2(gas) \rightarrow H_2(ads) \quad (10.6)$$

$$H_2(ads) \rightarrow 2H(ads) \quad (10.7)$$

$$2H(ads) + O^{-2}(ads) \rightarrow H_2O + 2e^- \quad (10.8)$$

The reaction of hydrogen with adsorbed oxide ions will increase the number of electrons in the conduction band. This increase in number of electrons increases the electrical conductivity of n-type semiconductors. This mechanism provides a clear explanation of decrease in electrical conductivity on exposure to air and increase in electrical conductivity when subjected to hydrogen atmosphere of these n-type sensors.

The other possible way of explaining the increase in electrical conductivity, is by considering a bulk type mechanism in which the hydrogen react with oxide ions and create oxygen vacancies (equation 10.9). This reaction leads to release electron in the conduction band which increases the electrical conductivity.

$$2H(ads) + O_O^x \rightarrow H_2O + V_O^{\bullet\bullet} + 2e^- \quad (10.9)$$

10.3.6. Concentration dependence and quality of sensors

The dependence of the response on the concentration of hydrogen at 300°C for x=0, 0.03 and 0.05 and at 250°C for x=0.01 sensors is shown in Figure 10.7. All materials have linear response as a function of hydrogen concentration. According to Windischmann [26], the gas sensitivity follows a power law behavior with respect to gas concentration which can be expressed as:

$$S = KC^{-\alpha} \tag{10.10}$$

where S is sensitivity, C is gas concentration, K and α are constants. The values of α calculated from the slopes of Figure 10.7 are 0.492, 0.568, 0.368 and 1.286 for x=0, 0.01, 0.03 and 0.05, respectively. The α values for the this Ni doped series are high as compared to SnO_2 based sensors (between 1/6 and 1/2 [27, 28]), with the x=0.05 material having the highest value of 1.286. This dependence indicates that the sensitivity of these reduced Ni doped based sensors is strongly affected by hydrogen concentration.

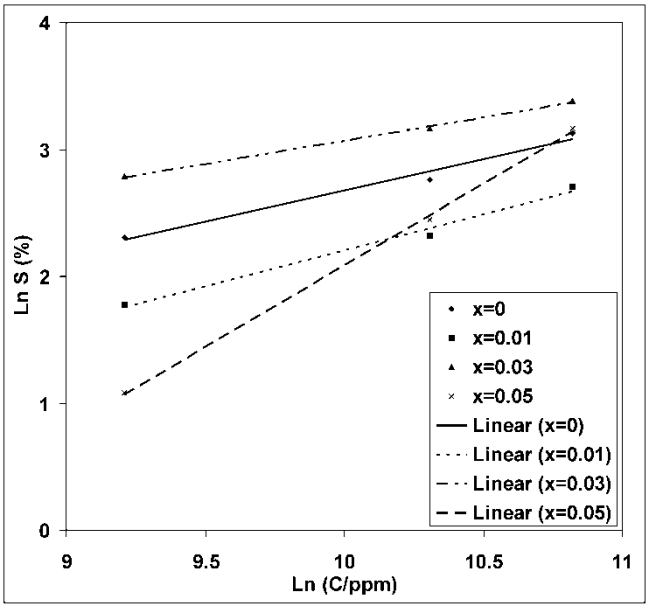

Figure 10.7. Hydrogen concentration dependence of the sensor response for $Sm_{0.95}Ce_{0.05}Fe_{1-x}Ni_xO_{3-\delta}$ at 300°C for x=0, 0.03 and 0.05 and at 250°C for x=0.01. Data points and linear fits are shown.

10.4. Conclusions

Hydrogen sensitivity of Ni doped perovskite material with formula $Sm_{0.95}Ce_{0.05}Fe_{1-x}Ni_xO_{3-\delta}$ (x=0-0.05) investigated at 300^oC by making bulk sensors in the form of rectangular pellets. The reduction treatment of these sensors at 1000^oC for 1h in 5%H_2/N_2 significantly improves the electrical conductivity and thus better sensitivity towards hydrogen by changing surface morphology and composition. These sensors exhibited high electrical conductivity under H_2/N_2 as compared to air confirming their n-type nature. 1% Ni doped material based sensor; indeed, showed highest sensitivity of ~700% for 3%H_2/N_2 but very long response time (2h) and also the response recovery was not 100%. Optimal response towards 1 and 5% H_2/N_2 mixture showed by x=0.03 with 100% response recovery. More importantly the response time was shortest and recovery was quickest in case of x=0.03 among all tested sensors. All these n-type sensors have linear response as a function of hydrogen concentration suggesting strong concentration dependence.

10.5. References

[1] S. Shukla, S. Seal, L. Ludwig, C. Parish, Sens. Actuators B. 97 (2004) 256-265.
[2] H. Nakagawa, N. Yamamoto, S. Okazaki, Sens. Actuators B. 93 (2003) 468-474.
[3] S.W. Lee, P.P. Tsai, H. Chen, Sens. Actuators B. 67 (2000) 122-127.
[4] V.V. Malyshev, A.V. Pislyakov, Sens. Actuators B. 134 (2008) 913-921.
[5] Y. Shen, T. Yamazaki, Z. Liu, C. Jin, T. Kikuta, N. Nakatani, Thin Solid Films. 516 (2008) 5111-5117.
[6] C. Lu, Z. Chen, Sens. Actuators B. 140 (2009) 109-115.
[7] H.-S. Kim, W.-T. Moon, Y.-K. Jun, S.-H. Hong, Sens. Actuators B. 120 (2006) 63-68.
[8] H. Tang, K. Prasad, R. Sanjines, F. Levy, Sens. Actuators B. 26-27 (1995) 71-75.
[9] X. Liu, J. Hu, B. Cheng, H. Qin, M. Jiang, Current Appl. Phys. 9 (2009) 613-617.
[10] L. Chen, J. Hu, S. Fang, Z. Han, M. Zhao, ZhanleiWu, X. Liu, H. Qin, Sens. Actuators B. 139 (2009) 407-410.
[11] G.N. Chaudharia, N.N. Gedam, S.V. Jagtap, S.V. Manorama, Talanta. 77 (2009) 1675-1679.
[12] S.M. Bukhari, J.B. Giorgi, Solid State Ionics. submitted in May (2009).
[13] S.M. Bukhari, J.B. Giorgi, Solid State Ionics. 180 (2009) 198-204.
[14] J. Zosel, D. Franke, K. Ahlborn, F. Gerlach, V. Vashook, U. Guth, Solid State Ionics. 179 (2008) 1628-1631.
[15] M. Zhao, H. Peng, J. Hu, Z. Han, Sens. Actuators B. 129 (2008) 953-957.
[16] S.M. Bukhari, J.B. Giorgi, Sens. Actuators B. 155 (2010) 524-537.
[17] Y.L. Chai, D.T. Ray, H.S. Liu, C.F. Dai, Y.H. Chang, Mater. Sci. Eng. A. 293 (2000) 39-45.

[18] I. Kosacki, T. Suzuki, V. Petrovsky, H.U. Anderson, Solid State Ionics. 136-137 (2000) 1225-1233.
[19] N.J. Dayan, S.R. Sainkar, R.N. Karekar, R.C. Aiyer, Thin Solid Films. 325 (1998) 254-258.
[20] S. Pokhrel, L. Huo, H. Zhao, S. Gao, Sens. Actuators B. 122 (2007) 321-327.
[21] M.Y. Faizah, A. Fakhru'l-Razi, R.M. Sidek, A.G.L. Abdullah, Inter. J. Eng. Tech. 4 (2007) 106-113.
[22] S.M. Bukhari, J.B. Giorgi, ECS Trans. 28 (2010) 19-29.
[23] S.M. Bukhari, J.B. Giorgi, ECS Trans. 33 (2010) 117-130.
[24] S.M. Bukhari, J.B. Giorgi, J. Electrochem. Soc. 158 (2011) J159-J164.
[25] S.M. Bukhari, J.B. Giorgi, Solid State Ionics. 194 (2011) 33-40.
[26] H. Windischmann, P. Mark, J. Electrochem. Soc. 126 (1979) 627-633.
[27] J. Watson, K. Ihokura, G.S.V. Coles, Meas. Sci. Technol. 4 (1993) 711-719.
[28] P.K. Clifford, D.T. Tuma, Sens. Actuators B. 3 (1982) 233-254.

11. Performance of $Sm_{0.95}Ce_{0.05}Fe_{1-x}Ni_xO_{3-\delta}$ perovskites as SOFC anode under dry methane fuel

The contents of this chapter have been published as: Syed M. Bukhari and Javier B. Giorgi, Electrochemical Society Trans., 35(1) (2011) 1539-1544

Abstract

$Sm_{0.95}Ce_{0.05}Fe_{1-x}Ni_xO_{3-\delta}$ (x=0-0.05) perovskite materials were investigated for their candidacy as anodes for Low temperature Solid Oxide Fuel Cell (LT-SOFC). Electrolyte supported button cells were made and tested with hydrogen and dry methane fuels. A three electrode geometry was used and electrochemical impedance measurements were carried out revealing that Ni doping does improve the performance of the resulting anodes as indicated by a decrease in charge transfer resistance values. The value of the charge transfer resistance is lowest for x=0.03 (1.65 Ωcm^2 at 600^oC) and only light coking was observed.

11.1. Introduction

Solid oxide fuel cells (SOFCs) have the capability to convert chemical energy of fuels into electrical energy with high efficiency and low pollution [1, 2]. However, to date, their high operating temperature and the expensive fabrication cost significantly limit the development of SOFCs towards practical applications. Extensive research is on the way to address these problems. The anode is one of the important components of SOFCs which faces intense conditions like a highly reducing environment. Under such conditions, many materials tend to decompose, and the performance is greatly affected by coke and/sulphur poisoning when exposed to hydrocarbon fuels such as natural gas. The conventional anode material for SOFCs is a Ni/YSZ cermet which works reasonably well at high temperature but has issues of long term stability and poisoning from coke and sulphur under hydrocarbon fuels. It is highly desirable to make anode materials able to run SOFCs at lower temperature, while being resistant towards coke and sulphur under hydrocarbon fuels.

Recently, perovskite type oxides (ABO_3) have opened a new door to solve the current issues of SOFCs [3, 4]. Perovskite type oxides (ABO_3) contain a rare-earth metal and transition metals at the A-site and B-site, respectively. The B-site metal typically provides an active site for catalysis while the A-site metal is responsible for thermodynamic stability and contributes in improving the catalytic performance via an interaction with the B-site metal

[5]. One of the great advantages of these perovskite materials is that their properties can be easily tailored according to the desired applications, by introducing substitutions at the A- and B- sites [5]. Additionally, lattice oxygen plays an important role in carbon cleaning mechanisms, where the oxygen is transported to the appropriate sites as required taking advantage of the mixed ion electron conductivity nature of the perovskite material [6, 7]. In previous work we have reported that Ce doping in $SmFeO_3$ solves not only the reduction instability issue under reducing conditions, but it also improves the electrical conductivity of the perovskite under reducing conditions by a transformation from p-type conductivity to n-type conductivity [8, 9]. Furthermore, Ce doping has made $SmFeO_3$ a coke resistant perovskite[9]. We also reported that Co doping in $Sm_{0.95}Ce_{0.05}FeO_{3-\delta}$ improves its catalytic properties towards methane oxidation and 3% Co doped has shown optimal performance while being coke resistant [10, 11]. In this work, we report on Ni doping in $Sm_{0.95}Ce_{0.05}FeO_3$ which shows improved electrical conductivity under reducing conditions. We study the performance of $Sm_{0.95}Ce_{0.05}Fe_{1-x}Ni_xO_{3-\delta}$ (x=0-0.05) as an anode material and explore its coke resistant qualities.

11.2. Experimental

A sol gel method was adopted to prepare powders of $Sm_{0.95}Ce_{0.05}Fe_{1-x}Ni_xO_{3-\delta}$ (x=0-0.05) perovskite materials because this method allows homogeneous mixing of precursor salts. The necessary quantities of metal nitrates i.e., $Fe(NO_3)_3 \cdot 9H_2O$, $Ce(NO_3)_3 \cdot 6H_2O$, $Ni(NO_3)_2 \cdot 6H_2O$ and $Sm(NO_3)_3 \cdot 6H_2O$ were weighed according to the aimed stoichiometry and dissolved in de-ionized water separately. The resulting solutions were mixed together followed by the introduction of a citric acid solution as a complexing agent. A gel was obtained after the evaporation of the resulting solution, which upon combustion produced amorphous citrate precursors. Powders with single perovskite phase were obtained after calcination of these amorphous citrate precursors at 850^{o}C for 24h. The single phase of these prepared Ni doped perovskites was confirmed by powder X-ray diffraction. To characterize anode materials before and after fuel cell tests, scanning electron microscopy (SEM) was performed on a JEOL JSM-7500F microscope, operated at an acceleration voltage of 9.0kV with an emission current of 20μA and a probe current 8.0μA.

Anode polarization measurements were carried out using a three-electrode arrangement and a thick SDC (samarium doped ceria) electrolyte. The electrolyte was a sintered samarium doped ceria pellet of ~2 mm thickness and ~20mm diameter. The anodes were pure Ni doped $Sm_{0.95}Ce_{0.05}FeO_{3-\delta}$ materials while a mixture of LSCF and SDC (50%w/w) was used as the cathode. The slurries of both anode and cathode materials were prepared in an emulsion (Triton-X100). First the anode slurry was painted and sintered at 1400^{o}C for 4h, followed by a second coating to hold a Pt mesh which acts as a current collector and sintered again at 1400^{o}C for 4h. The cathode was painted in the same fashion on the other side of the electrolyte disc. The reference electrode consisted of a Pt wire wrapped around the electrolyte disc and held in place by Pt paste.

Electrochemical measurements were performed under hydrogen and under dry methane in the temperature range of 450 to 600^{o}C with an increment of 50^{o}C. AC impedance of the electrochemical cells was carried out using PARSTAT 2273 potentiostat, at open circuit voltage (OCV), in the frequency range of 100 kHz to 100 mHz. A 10mV amplitude AC signal was used to obtain electrochemical impedance spectra. An equivalent circuit model ($L_1R_S[R_{CT}CPE_1]$) was used to analyze the electrochemical impedance spectra. In this equivalent circuit, R_S and R_{CT} are the serial and charge transfer resistances respectively. L_1 is an inductor having a value in the order of 10^{-6}, and CPE_1 is a constant phase element which accounts for the inhomogeneity of the anode surface and its value is less than 1.

11.3. Results and Discussions

The surface morphologies of fresh anodes were studied by scanning electron microscopy. Figure 11.1 shows SEM micrographs of fresh perovskite anodes. All exhibited very fine microstructures. The particle size in undoped Ni perovskite anodes is in the range of 6-8μ. All Ni doped perovskites have smaller particle size as compared to the undoped perovskite prepared in the same manner.

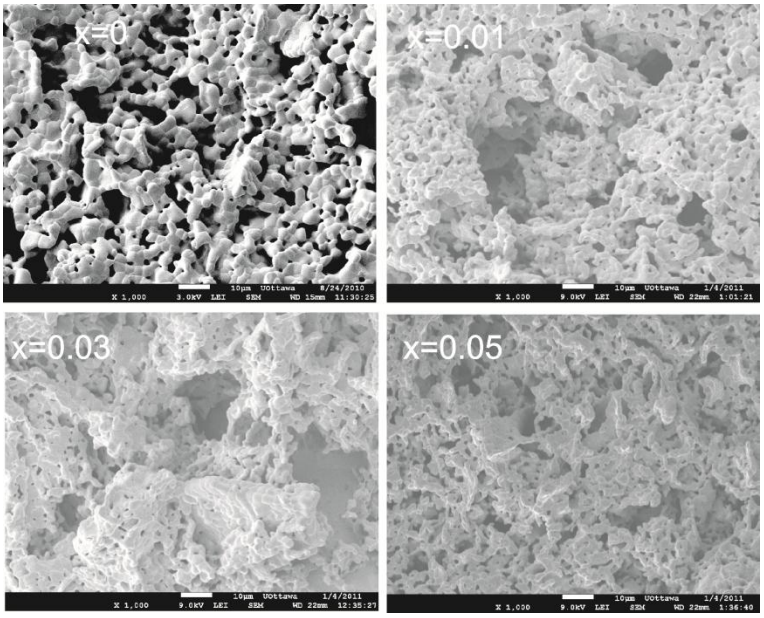

Figure 11.1. SEM micrographs of $Sm_{0.95}Ce_{0.05}Fe_{1-x}Ni_xO_{3-\delta}$ (x=0-0.05) anodes before fuel cell operation.

Before performing any electrochemical measurement under methane, all cells were run with hydrogen for 2-3h. The purpose of this was to ensure a correct behaviour of the cell and to provide a reference for subsequent measurements with dry methane. The measured OCV values under hydrogen were lower than the theoretical Nernst potential values. As an example the theoretical Nernst potential values at 700^{o}C and 450^{o}C are 1.03V and 1.089V, respectively, but the experimental values were 0.88V (at 700^{o}C) and 1.0V (at 450^{o}C).This observation of lower OCV values using a SDC electrolyte has been previously linked to its lower densification [12], and its partial reduction near the surface of anodes under fuel cell conditions [13, 14]. The results of AC impedance analysis under hydrogen fuel are shown in Figure 11.2. The value of charge transfer resistances gradually increases as a function of Ni concentration which means that the performance of perovskite anode became worst on addition of Ni dopant. This behaviour matches well with the electrical conductivity trends under 5%v/v H_2/N_2 as previously reported (chapter 9, [15]). Briefly, the trend can be explained in terms of the p-type nature (hole-doping effect) of the Ni dopant. The n-type conductivity of the $Sm_{0.95}Ce_{0.05}FeO_{3-\delta}$ perovskite anode material decreases as function Ni concentration due to the titration of the electron-doping effect of Ce by the hole-doping

effect of Ni. This decrease in n-type electrical conductivity is responsible for the increase in R_{ct} values as a function of Ni concentration.

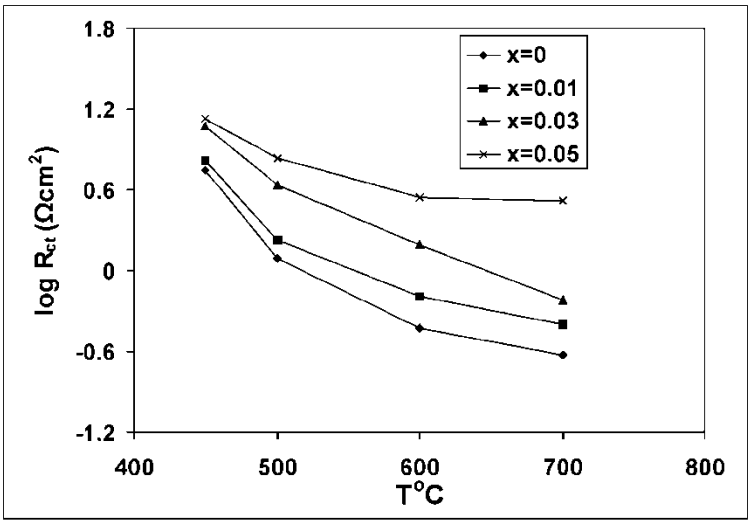

Figure 11.2. The charge transference resistances (R_{CT}) of $Sm_{0.95}Ce_{0.05}Fe_{1-x}Ni_xO_{3-\delta}$ (x=0-0.05) anodes at different temperatures under dry hydrogen

The performance of $Sm_{0.95}Ce_{0.05}Fe_{1-x}Ni_xO_{3-\delta}$ (x=0-0.05) perovskite anodes was evaluated under dry methane fuel. It was expected that performance of these perovskite anodes should increase as a function of Ni concentration because Ni has shown good catalytic activities towards methane oxidation [16]. However Ni-metal containing catalysts are easily poisoned due to formation of coking [17]. The electrocatalytic performance of Ni at the B-site depends on the reducibility of the M-O bond [18] and the oxide ion mobility in the perovskite system [6]. Additionally, the high oxide ion mobility in the perovskite plays a vital role in carbon cleaning mechanisms during methane oxidation [19]. This carbon cleaning mechanism prevents the deactivation of the catalyst via coke poisoning.

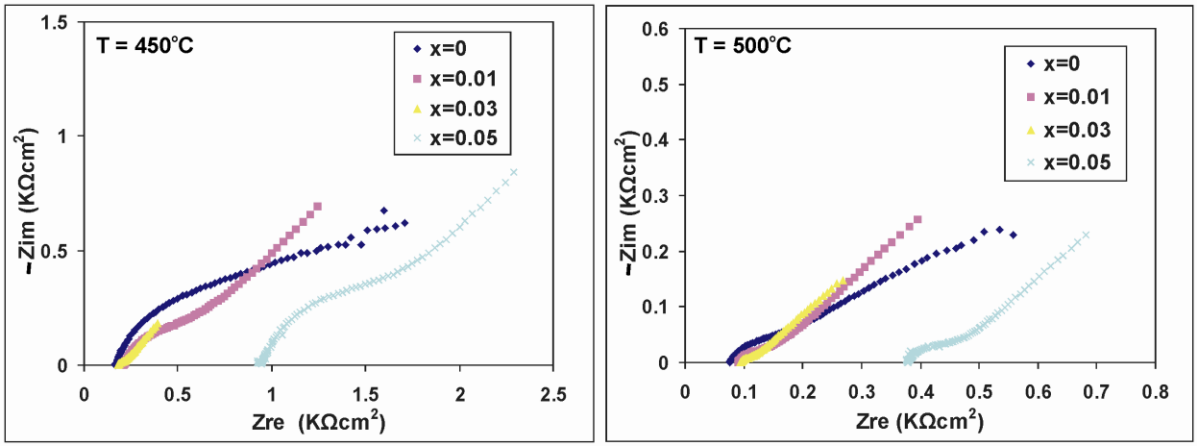

Figure 11.3. Nyquist plots of $Sm_{0.95}Ce_{0.05}Fe_{1-x}Ni_xO_{3-\delta}$ (x=0-0.05) at different temperatures in dry methane.

The values of R_{ct} for $Sm_{0.95}Ce_{0.05}Fe_{1-x}Ni_xO_{3-\delta}$ (x=0-0.05) perovskite anodes under dry methane are summarized in Table 11.1 and Nyquist plots are shown in Figure 11.3. The analysis revealed that performance does increase with increase in Ni concentration only up to x=0.03 which is indicated from a decrease in R_{ct} values. The performance of x=0.05 was the worst in the series with highest values of R_{ct}. Notably, the serial resistance for x=0.05 is highest amongst the series revealing also a bad contact (a poor interfacial match) between anode and electrolyte. The activation energy calculated from Arrhenius plots revealed the same trend i.e., the activation energy first decreases from x=0 to x=0.03 and then increases. The activation energies for x=0, 0.01, 0.03 and 0.05 are 214, 162 142 and 157 kJ/mol, respectively. This trend can easily be explained by considering the reducibility of M-O bond. As the Fe-O bond is stronger than the Ni-O bond [20, 21], the catalytic performance is expected to increase with increase in Ni concentration but addition of Ni also decreases the n-type conductivity of the anode. The combined effect is that the values of R_{ct} decreases from x=0 to x=0.03 and then increases at all temperatures.

Table 11.1: The charge transference resistances (R_{CT}) of $Sm_{0.95}C\ e_{0.05}Fe_{1-x}Ni_xO_{3-\delta}$ (x=0-0.05) anodes at different temperatures under dry methane.

T^oC	x=0	x=0.01	x=0.03	x=0.05
	R_{CT} (Ωcm^2)	R_{CT} (Ωcm^2)	R_{CT} (Ωcm^2)	R_{CT} (Ωcm^2)
450	2419.5 ± 360	954.9 ± 143	125.7 ± 19	1890 ± 283
500	247.2 ± 37	141.3 ± 21	61.1 ± 8	218.4 ± 32
550	49.5 ± 7	35.9 ± 5	27.8 ± 4	325.5 ± 49
600	4.5 ± 0.7	9 ± 1	1.65 ± 0.25	20.5 ± 3

To assess the degree of coking of the different anodes, SEM images of these anodes were obtained after performance. Figure 11.4 shows the SEM micrographs of anodes after performance under dry methane fuel at 700°C. The x=0, x=0.01 and x=0.05 materials did not show significant coking. The presence of carbon wires in the x=0.03 anode indicates that there is a balance between the reactivity toward oxidation and the ability of the material to eliminate carbon deposits. The x=0.03 material achieved the best balance in this series of materials producing the lowest R_{ct} and showing no change in performance over 24h of operation. Long term test are required to assess the degree of coking over time and the ability of the material to remove coking by different pulse techniques if required.

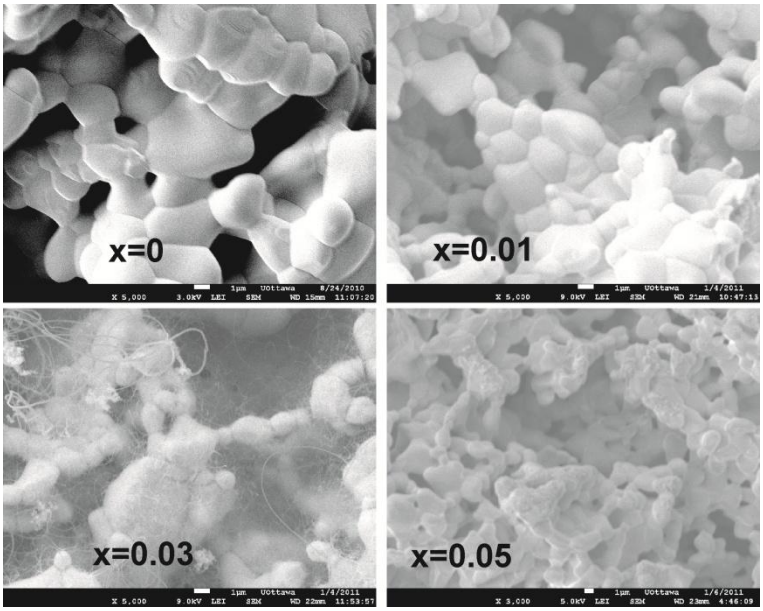

Figure 11.4. SEM micrographs of $Sm_{0.95}Ce_{0.05}Fe_{1-x}Ni_xO_{3-\delta}$ (x=0-0.05) anodes after performance under methane at 700^0C.

11.4. Conclusions

A new series of candidates for Low Temperature Solid Oxide Fuel Cell (LT-SOFC) anode materials based on $Sm_{0.95}Ce_{0.05}Fe_{1-x}Ni_xO_{3-\delta}$ (x=0-0.05) perovskite materials were evaluated for dry methane fuel. These materials were stable under reducing condition below 800^oC and their n-type electrical conductivity decreases with increase in Ni concentration which is due to the hole-dopant nature of Ni. Fuel cell test under hydrogen revealed that values of charge transfer resistance increases with increase in Ni concentration. The electrochemical impedance measurements made under dry methane indicated that performance does improve on Ni doping only up to x=0.03. In spite of the fact that light coking occurred in the case of x=0.03, it exhibited the lowest values of charge transfer resistance amongst the series. These results suggested that SOFCs can be operated at the low temperature of 450^oC under dry methane with reasonably good performance.

11.5. References

[1] N.Q. Minh, J. Am. Ceram. Soc. 76 (1993) 563-588.
[2] S.P.S. Badwal, K. Foger, Ceram. Int. 22 (1996) 257-265.
[3] A. Ovalle, J.C. Ruiz-Morales, J. Canales-Vázquez, D. Marrero-López, J.T.S. Irvine, Solid State Ionics. 177 (2006) 1997-2003.
[4] G. Pudmich, B.A. Boukamp, M. Gonzalez-Cuenca, W. Jungen, W. Zipprich, F. Tietz, Solid State Ionics. 135 (2000) 433-438.
[5] M.A. Pena, J.L.G. Fierro, Chem. Rev. 101 (2001) 1981-2017.
[6] S.M. Lima, J.M. Assaf, M.A. Pena, J.L.G. Fierro, Appl. Catal. A. 311 (2006) 94-104.
[7] K. Urasaki, Y. Sekine, S. kawabe, E. Kikuchi, M. Matsukata, Appl. Catal. A. 286 (2005) 23-29.
[8] S.M. Bukhari, J.B. Giorgi, Solid State Ionics. 180 (2009) 198-204.
[9] S.M. Bukhari, J.B. Giorgi, ECS Trans. 28 (2010) 19-29.
[10] S.M. Bukhari, J.B. Giorgi, ECS Trans. 33 (2010) 81-91.
[11] S.M. Bukhari, J.B. Giorgi, Solid State Ionics. 181 (2010) 392-401.
[12] H. Shi, W. Zhou, R. Ran, Z. Shao, J. Power Sources. 195 (2010) 393-401.
[13] T. Miyashita, J. Mater. Sci. 40 (2005) 6027.
[14] T. Miyashita, The Open Materials Science Journal. 3 (2009) 33-39.
[15] S.M. Bukhari, J.B. Giorgi, Sens. Actuators B. 155 (2010) 524-537.
[16] Y. Matsumura, T. Nakamori, Appl. Catal. A. 258 (2004) 107-114.
[17] Ase Slagtern, U. Olsbye, Appl. Catal. A. 110 (1994) 99-108.
[18] J.R. Mawdsley, T.R. Krause, Appl. Catal. A. 334 (2008) 311-320.
[19] S.M.d. Lima, J.M. Assaf, Catalysis Letters. 108 (2006) 63-70.
[20] X. Zhu, H. Wang, W. Yang, Solid State Ionics. 177 (2006) 2917-2921.
[21] D. Klissurski, R. Dimtrova, Bull. Chem. Soc. Jpn. 63 (1990) 590-591.

12. Synthesize and characterization of $Sm_{0.95}Ce_{0.05}Fe_{1-x}Cr_xO_{3-\delta}$ (x=0-0.10) perovskite materials

The contents of this chapter have been accepted for the publication in Journal of The Electrochemical Society

Abstract

This work examines the relative REDOX stability and conductivity of new Cr-doped perovskite materials ($Sm_{0.95}Ce_{0.05}Fe_{1-x}Cr_xO_{3-\delta}$, x=0-0.10) for potential use as anode materials and sensors for reducing gases at low temperatures. These perovskite materials were characterized by XRD, XPS and SEM. A reduction stability test revealed that these perovskites are stable at temperatures below 800^oC under reducing conditions. The introduction of Cr in the lattice was found to be in the form of Cr^{+3} and Cr^{+6}. As a function of Cr content, the ratio of Cr^{+3}/Cr^{+6} was found to increase. The reduction treatment tended to decrease the concentration of lattice oxygen but the surface adsorbed oxygen was found to be higher in reduced samples as compared to fresh samples. This observation suggested that these materials have a tendency to recapture oxygen when exposed to air after the reduction treatment. The reduction treatment improved the electrical conductivity due to the formation of nanoparticles. The x=0.03 perovskite has highest electrical conductivity under both air and reducing atmospheres and shows the greatest promise for use in sensor applications for reducing gases at low temperatures.

12.1. Introduction

Perovskite type oxides (ABO_3) have shown great technological versatility due to their very flexible and easily tailored properties [1]. These properties include but are not limited to good redox and thermal stabilities; tuneable mixed electronic and ionic conductivities; and resistance to sulphur and coke poisoning under a wide range of operational temperatures [2-4]. These tunable properties make them suitable for use in solid oxide fuel cells (SOFCs) and sensor applications.

$SmFeO_3$ is a p-type semiconducting perovskite oxide which has been investigated as a candidate for sensing oxidizing gases [5, 6]. However, some of its characteristics have precluded its use in other related applications such as fuel cell technology or sensing of reducing gases. These undesirable characteristics include reduction instability, poor catalytic activity for hydrocarbon oxidation, and very low electrical conductivity under reducing conditions. The reduction instability issue can be ameliorated by introducing an electron

donor dopant which is larger than Sm at the A-site. Previous work in our group has shown that doping cerium at the A-site in $SmFeO_3$ is effective in improving its reduction instability and electrical conductivity under reducing conditions [2]. The resulting cerium doped materials ($Sm_{1-x}Ce_xFeO_{3-\delta}$, x=0.01-0.05) are stable under reducing conditions up to 900^oC with n-type electrical behaviour and are resistant to coking.

Doping at the B-site has traditionally been used for fine tuning catalytic properties. This was traditionally done by the incorporation of reactive transition metals. For this reason, we have previously fine tuned and improved the catalytic properties of $Sm_{0.95}Ce_{0.05}Fe_1O_{3-\delta}$ perovskite by incorporating nickel and cobalt dopants [7-11]. The resulting materials ($Sm_{0.95}Ce_{0.05}Fe_{1-x}M_xO_{3-\delta}$, M=Ni, Co, x=0-0.10) have shown improvements in catalytic activity toward methane oxidation, and the ability to detect reducing gases at various temperatures. Significantly, the multi-substituted perovskites do not show any phase segregation under reducing atmospheres up to reasonably high temperatures (800^oC), but the metal atoms undergo a series of changes in oxidation state, with the appropriate release of oxygen atoms and the formation of vacancies. The net result is a change in conductivity which can be used to sense specific reducing gases (H_2, CH_4 and CO have been reported).

These observations suggested that the introduction of a more REDOX-active dopant should enhance the sensing performance. Chromium was selected as it can achieve multiple oxidation states up to +6. This work will explore the redox stability and conductivity of a newly developed series of perovskite oxides with formula $Sm_{0.95}Ce_{0.05}Fe_{1-x}Cr_xO_{3-\delta}$ (x=0-0.10). The results will be discussed in terms of their potential as anode materials and sensors for reducing gases at low temperatures.

12.2. Experimental

12.2.1. Powder preparation

$Sm_{0.95}Ce_{0.05}Fe_{1-x}Cr_xO_{3-\delta}$ (x=0-0.10) composite oxides were synthesized via the decomposition of citrate precursors. To achieve a particular composition, the necessary quantities of cerium nitrate [$Ce(NO_3)_3 \cdot 6H_2O$, Alfa Aesar, 99.5%], samarium nitrate [$Sm(NO_3)_3 \cdot 6H_2O$, Alfa Aesar, 99.9%], iron nitrate [$Fe(NO_3)_3 \cdot 9H_2O$, Alfa Aesar, minimum 98%] and chromium nitrate [$Cr(NO_3)_2 \cdot 6H_2O$, Alfa Aesar, 99%] were dissolved in deionized water and then were mixed together in the appropriate ratio. Citric acid monohydrate [Alfa Aesar, minimum 99.0%] was prepared separately such that the ratio of total metal to citric

acid was 1:1. This citric acid solution was added to the solution of metals as a complexing agent. The resulting solution was evaporated to obtain a gel, which on further firing yielded a solid amorphous citrate precursor. This solid precursor was calcined at 850^{o}C for 24h under air to achieve a single perovskite phase structure.

12.2.2. Material characterization

Phase composition, lattice parameters and crystallite sizes of $Sm_{0.95}Ce_{0.05}Fe_{1-x}Cr_xO_{3-\delta}$ (x=0-0.10) were determined by powder X-ray diffraction (PXRD, Phillips PW 1830) analysis using CuK_α radiation. The crystalline phase was assigned by using a powder diffraction file database (ICDD/JCPDS, 2001, Dataset 1-99). LaB_6 was used as an internal standard to calibrate theta values. Peak refinements were performed by using the Jade 6.1 software. To test the perovskite phase stability, these materials were reduced in a cylindrical quartz chamber at 800^{o}C for 1h under flow of 5%v/v H_2/N_2. After the treatment, the samples were cooled to room temperature under the same atmosphere. These reduced samples were also analyzed by powder X-ray diffraction for phase composition and lattice parameters.

A Quantachrome Autosorb 1-C instrument was used to measure the BET surface areas of all as synthesized powder samples. The surface morphology of powder samples, fresh pellets and pellets reduced at 1000^{o}C for 1h under 5%v/v H_2/N_2 was observed by scanning electron microscopy (SEM, JEOL JSM-7500F). The surface composition and oxidation states of each species were identified for fresh powder samples, powders reduced at 800^{o}C for 1h under 5%v/v H_2/N_2, fresh pellets and pellets reduced at 1000^{o}C for 1h under 5%v/v H_2/N_2 by X-ray photoelectron spectroscopy (XPS; Kratos AXIS Ultra^{DLD} 39-306l), using a monochromatic Al anode. Quantification and identification of oxidation states was performed using the peaks of $Sm3d_{5/2}$, $Ce3d_{5/2}$, $Fe2p_{3/2}$, $Cr2p_{3/2}$ and O1s core levels. The Casa Software [12] was used for the analysis and quantification of XP spectra. Pass energy of 80eV and 20eV was used for complete surveys and individual regions respectively. The calibration of the B.E. scale of all spectra was done with the B.E. of the C1s level set at 284.8eV. A nonlinear background subtraction (Shirley) was used to fit all peaks.

12.2.3. Electrical conductivity measurements

The electrical conductivity of all perovskites was measured using rectangular pellets by the four probe method. Pellets were prepared by uniaxially pressing 2.0g of powder to 15000lbs in order to form a disc which was sintered at 1350^{o}C for 4h. The sintered disc was

chopped into a rectangular shape pellet. Electrical conductivities of $Sm_{0.95}Ce_{0.05}Fe_{1-x}Cr_xO_{3-\delta}$ (x=0-0.10) perovskites were measured under both air (oxidising atmosphere) and 5%v/v H_2/N_2 (reducing atmosphere). For electrical conductivity measurements under a reducing atmosphere, two kinds of samples were used: one kind of sample was partially reduced and a second kind was fully reduced. Partially reduced samples were previously treated for 1h at 700^oC prior to measurement while fully reduced samples were treated to 1000^oC for 1h before conductivity measurements.

12.3. Results and discussions

12.3.1. Bulk structure

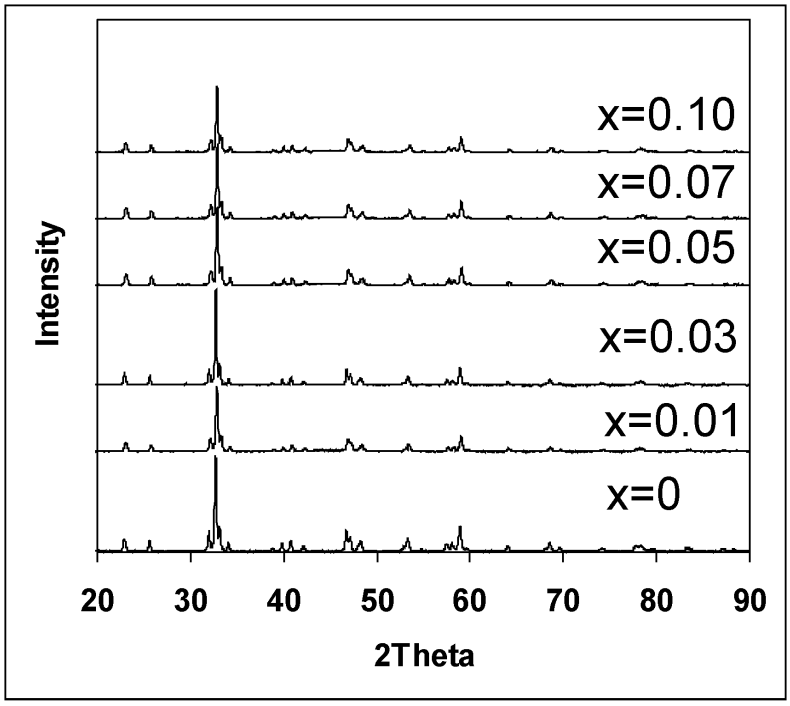

Figure 12.1. XRD pattern of as synthesized $Sm_{0.95}Ce_{0.05}Fe_{1-x}Cr_xO_{3-\delta}$ (x=0-0.10) powders.

Room temperature XRD patterns of the fresh $Sm_{0.95}Ce_{0.05}Fe_{1-x}Cr_xO_{3-\delta}$ (x=0-0.10) powders are shown in Figure 12.1. These patterns were compared with the standard JCPDS card number 39-1490 ($SmFeO_3$). All the Cr doped perovskite materials possess the same structure as $SmFeO_3$, namely orthorhombic symmetry belonging to the Pnma (62) space group. Importantly, all these Cr doped perovskite materials showed only a single phase. Cell

parameters and crystallite sizes were calculated from peak positions and full-width-half-maxima using the Scherrer equation [13]. Table 12.1 presents the cell parameters, crystallite sizes and tolerance factors for this series of perovskite oxides. The comparison of cell parameters revealed that lattice volumes decrease as Cr is doped into the lattice at the Fe site. This suggests that the size of the Cr ion is smaller than the Fe^{+3} (0.645Å[14]) ion. A comparison with tabulated values suggests that Cr is either in the form of Cr^{+3} (0.615Å[14]) or Cr^{+6}(0.44Å[14]) in the lattice.

Table 12.1. Cell parameters, cell volumes, crystallite sizes and Goldschmidt tolerance factors of as synthesized and reduced powders of $Sm_{0.95}Ce_{0.05}Fe_{1-x}Cr_xO_{3-\delta}$ (x =0-0.10).

$Sm_{0.95}Ce_{0.05}Fe_{1-x}Cr_xO_{3-\delta}$	Crystallite Size (Å)	a (Å)	b (Å)	c (Å)	Volume ($Å^3$)	Tolerance factor (t)
x=0	667 (563)[a]	5.591 (5.590)	7.719 (7.743)	5.400 (5.4)	233.05 (233.73)	0.8584
x=0.01	792 (787)	5.586 (5.590)	7.714 (7.713)	5.404 (5.406)	232.86 (233.08)	0.8593
x=0.03	853 (838)	5.574 (5.590)	7.686 (7.724)	5.392 (5.394)	231.00 (232.90)	0.8610
x=0.05	621 (833)	5.576 (5.581)	7.682 (7.705)	5.383 (5.419)	230.58 (233.02)	0.8627
x=0.07	539 (703)	5.569 (5.588)	7.699 (7.719)	5.368 (5.409)	230.16 (233.31)	0.8645
x=0.10	500 (581)	5.557 (5.579)	7.677 (7.706)	5.360 (5.391)	228.66 (231.77)	0.8671

[a] The values in parenthesis are for samples reduced at 800°C for 1h under 5%v/v H_2/N_2

The tolerance factors for this Cr doped series were calculated by using the standard formula proposed by Goldschmidt [15], equation 12.1, and assuming Cr^{+3} in the lattice.

$$t = \frac{r_A + r_O}{\sqrt{2}(r_B + r_O)} \qquad (12.1)$$

In the formula, r_A, r_B and r_O are ionic radii of the A-cation, the B-cation and the oxygen anion present in the lattice. A stable perovskite structure has a tolerance factor in the range of 1 to 0.77, with 1 being for a perfect cubic structure [15]. The tolerance factors for this series

were around 0.86, consistent with the orthorhombic structure determined by XRD (Pnma (62) space group). The increase in tolerance factor as a function of chromium content indicates an increase in stability and a more cubic structure upon chromium doping. To be noted is that if Cr^{+6} is present, then the tolerance factor would be expected to be even larger, based upon ionic radii, indicating a more stable structure.

The thermal stability of these Cr doped materials was tested by exposing them to a reducing atmosphere (5%v/v H_2/N_2) at high temperature. The temperature was increased in 100^o intervals, with the materials being exposed for 1h to each temperature. The experiments show a consistently stable XRD pattern corresponding to a single perovskite phase (identical to those in Figure 12.1) up to 700^oC. Above this temperature, additional peaks appear which is indicative of a phase separation. Figure 12.2 shows the XRD pattern of samples reduced at 800^oC. At this temperature, only the x=0.01 and 0.03 samples show a separate Sm_2O_3 phase. This indicates that these samples are more easily reduced due to presence of Cr^{+6} in the lattice, as discussed below. The lattice volumes and crystallite sizes of reduced samples are summarized in Table 12.1. The lattice volumes of reduced samples are bigger than those of fresh samples, indicating that the metals ions are being reduced ($Fe^{+3} \rightarrow Fe^{+2}$ and $Cr^{+6} \rightarrow Cr^{+3}$) and consequently, their ionic radii are larger.

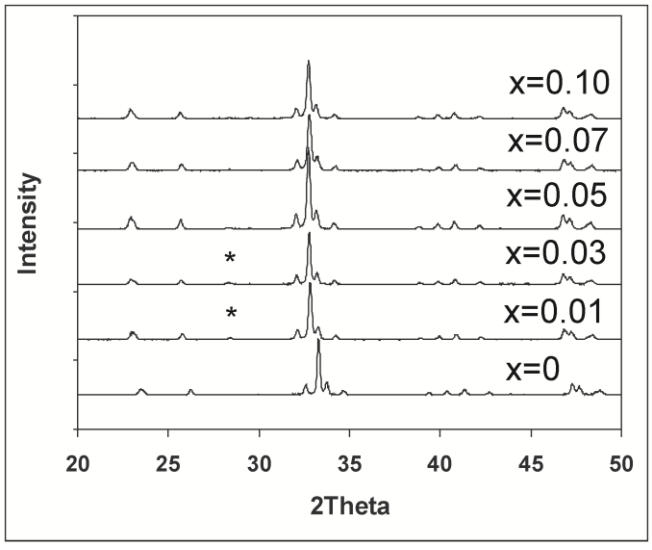

Figure 12.2. XRD patterns of $Sm_{0.95}Ce_{0.05}Fe_{1-x}Cr_xO_{3-\delta}$ (x=0-0.10) powders reduced at 800^oC for 1h under 5%v/v H_2/N_2. The * symbol indicates peaks corresponding to a separate Sm_2O_3 phase.

At temperatures above 800°C, the remaining samples start to show a separation of the Sm_2O_3 phase. Figure 3 shows the XRD patterns of pellets reduced at 1000°C for 1h under 5%v/v H_2/N_2. All samples showed Sm_2O_3 as a separated phase, but after an initial increase, the intensity of the Sm_2O_3 peak is seen to gradually decrease as a function of Cr concentration. These observations suggest that upon introduction of chromium into the lattice, there is a destabilization of the $Sm_{0.95}Ce_{0.05}FeO_{3-\delta}$ lattice making it more reducible, but the reduction stability of the Cr doped perovskite oxides increases thereafter. That the x=0.01 sample is the least stable one in the series is also demonstrated by the appearance of an additional iron phase (Fe or Fe_2O_3, which cannot be distinguished in this case) in the XRD pattern, but only for this concentration.

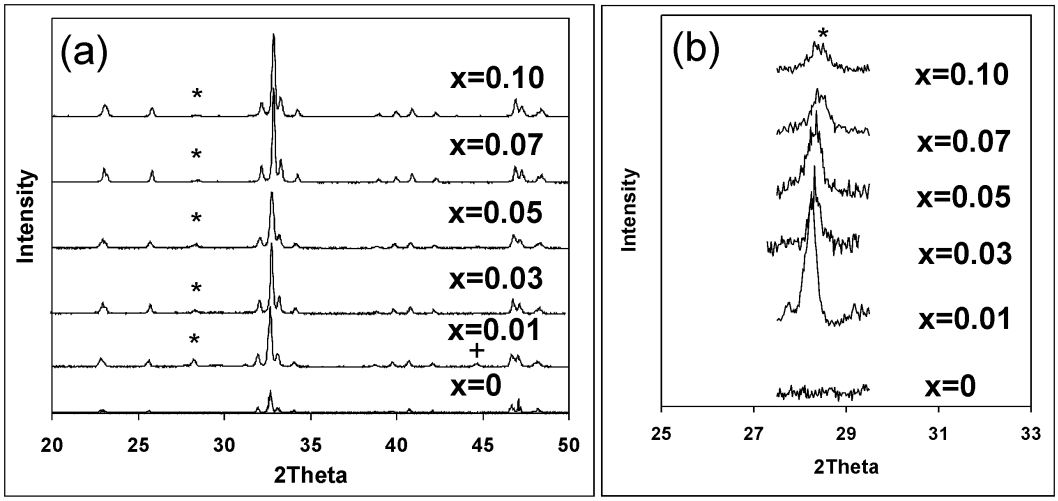

Figure 12.3. XRD pattern of $Sm_{0.95}Ce_{0.05}Fe_{1-x}Cr_xO_{3-\delta}$ (x=0-0.10) pellets after reduction at 1000°C for 1h under 5%v/v H_2/N_2. The * symbol indicates peaks corresponding to a separate Sm_2O_3 phase. The insert indicates the normalized intensity of this samaria phase. The + symbol indicates peaks corresponding to a separate Fe or Fe_2O_3 phase.

12.3.2. Surface Chemical composition

X-ray photoelectron spectroscopy (XPS) was used to determine the oxidation states and relative surface atomic ratios of all metals and oxygen in the $Sm_{0.95}Ce_{0.05}Fe_{1-x}Cr_xO_{3-\delta}$ series. For quantification of the elemental composition and identification of the oxidation states of Sm, Ce, Fe, Cr and O, the core level peaks for $Sm3d_{5/2}$, $Ce3d_{5/2}$, $Fe2p_{3/2}$, $Cr2p_{3/2}$ and O1s were used. The $Sm3d_{5/2}$, $Ce3d_{5/2}$, $Fe2p_{3/2}$, $Cr2p_{3/2}$ and O1s core level peaks for all the as-

synthesized Cr doped materials are shown in Figure 12.4. In all fresh samples, the positions of the $Sm3d_{5/2}$ and $Fe2p_{3/2}$ peaks were ~1082.9eV and ~710.5eV, respectively. These positions indicate that the oxidation state of both Sm and Fe is +3. For Cr, there are two peaks, one at 576.8eV which corresponds to Cr^{+3} and another at 578.8eV which corresponds to Cr^{+6}. Relative quantification of Cr^{+3} and Cr^{+6} was performed by fitting the $Cr2p_{3/2}$ core level peaks. The ratio Cr^{+3}/Cr^{+6} increases as a function of chromium content (ratio = 0.06, 0.18, 0.30, 0.45, and 0.68, for x=0.01-0.10). This trend indicates that after an initial destabilization of the structure by the introduction of the highly reducible Cr^{+6} species, the reducibility of the new series decreases with higher Cr content. This observation matches well with the XRD trend of reduced powders and pellets as discussed above.

We can rationalize the observations by considering the charge of the chromium ions. That is, upon initial doping, the oxide environment allows the presence of Cr^{+6}, in fact Cr^{+6} should be favoured according to the tolerance factor. However, as the concentration of chromium increases, Cr^{+6} becomes de-stabilizing due to the high charge, and the material favours Cr^{+3} to replace the Fe^{+3} ion in the lattice. Because Cr^{+6} is highly reducible, the shift toward Cr^{+3} as a function of chromium content makes the material more stable.

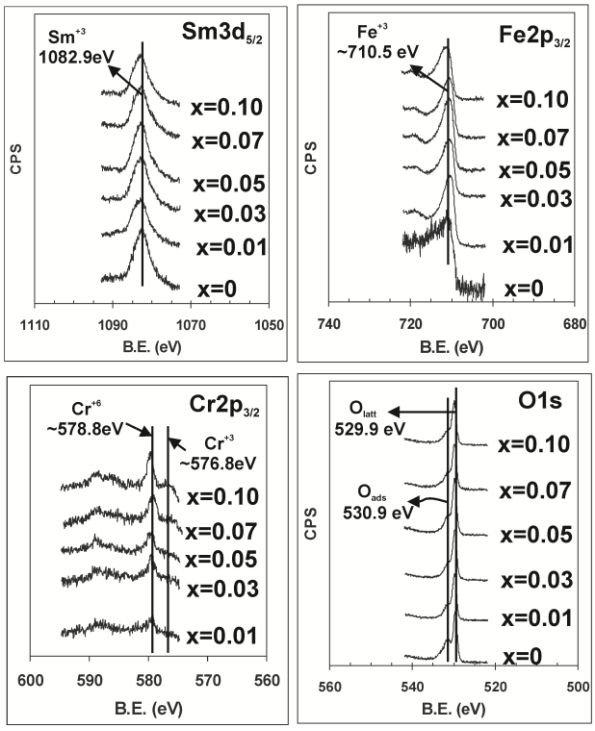

Figure 12.4. $Sm3d_{5/2}$, $Fe2p_{3/2}$,$Cr2p_{3/2}$ and O1s peaks of as synthesized $Sm_{0.95}Ce_{0.05}Fe_{1-x}Cr_xO_{3-\delta}$ (x=0-0.10).

For powders reduced at 800°C and pellets reduced at 1000°C, the position of the $Sm3d_{5/2}$ core level peak was not changed; the oxidation state of Sm remains +3. However, the oxidation states for iron and chromium change significantly upon sample reduction (Figure 12.5). After reduction, there is only one $Cr2p_{3/2}$ peak (~576eV) instead of two for the oxidized sample, which indicates that Cr is present only as Cr^{+3} in both reduced powders and reduced pellets (Figure 12.5).

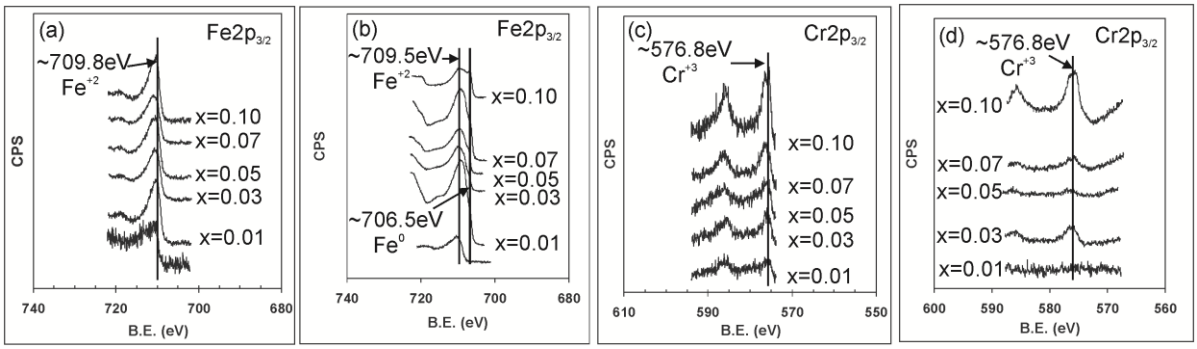

Figure 12.5. (a), (b) show the $Fe2p_{3/2}$ peaks for powder samples reduced at 800°C and pellets reduced at 1000°C, respectively; (c), (d) show the $Cr2p_{3/2}$ peaks for powder samples reduced at 800°C and pellets reduced at 1000°C, respectively.

The effect of reduction upon iron can be followed by the shifts in the $Fe2p_{3/2}$ peaks. Upon treatment to 800°C the $Fe2p_{3/2}$ core level peak shifted to lower B.E. (~709.8eV) indicating the $Fe^{+3} \rightarrow Fe^{+2}$ reduction. Further treatment to 1000°C in the reducing atmosphere yields an additional peak/shoulder at 706.5eV which indicates the presence of metallic Fe. This shoulder is more prominent at higher Cr concentration suggesting that the introduction of Cr in the lattice has increased the reducibility of Fe in the $Sm_{0.95}Ce_{0.05}Fe_{1-x}Cr_xO_{3-\delta}$ (x=0-0.10) system. This observation is inconsistent with the previous XRD results (Figure 12.3), however the discrepancy can be explained as the difference between surface species (as seen by XPS) and bulk species (as seen by XRD). Nevertheless, the presence of metallic Fe at the surface of the pellets will certainly play a role in the conductivity measurements described below. The determination of the oxidation state of Ce was not possible due to the very broad and low intensity peaks of the $Ce3d_{5/2}$ core level.

Relative surface atomic ratios of Sm, Ce, Fe and Cr were calculated by using the overall area of each peak. The results are displayed in Figure 12.6. In fresh samples, the increase in

Cr concentration lowers the Sm content on the surface in favour of Fe. Upon reduction treatment of the powders at 800^{o}C, Sm segregates to the surface in concentrations well above the expected stoichiometric values. Chromium itself segregates to the surface in both oxidized and reduced forms of the perovskites. The concentration of Ce on the surface for fresh samples was lower than the stoichiometric values and did not change upon reduction treatment.

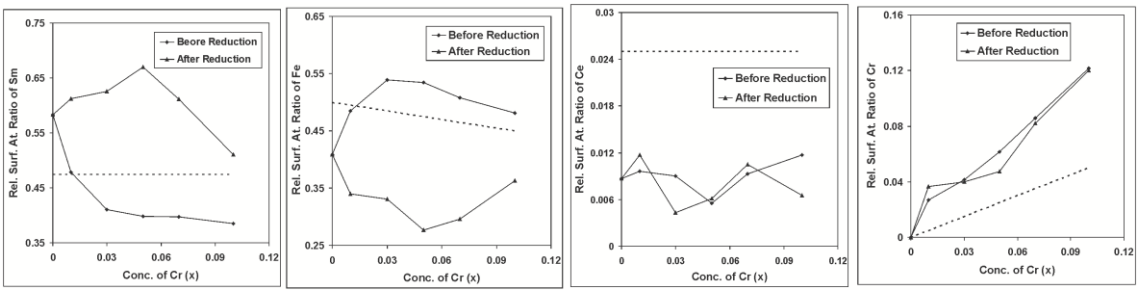

Figure 12.6. Relative surface atomic ratios of Sm, Ce, Fe and Cr calculated from $Sm3d_{5/2}$, $Ce3d_{5/2}$, $Fe2p_{3/2}$ and $Cr2p_{3/2}$ peak intensities for fresh powder samples and powders reduced at 800^{o}C for 1h under 5%v/v H_2/N_2. The dash lines represent stoichiometric concentrations of the $Sm_{0.95}Ce_{0.05}Fe_{1-x}Cr_xO_{3-\delta}$ perovskites.

For $Sm_{0.95}Ce_{0.05}Fe_{1-x}Cr_xO_{3-\delta}$ (x=0-0.10) materials, the O1s core level consists of two components, as observed for $SmFeO_3$ [16]. The low B.E. component has been assigned to lattice oxygen ($O^{-2}_{lattice}$) while the high B.E. component corresponds to surface adsorbed oxygen (O^{-}_{ads}). The B.E. values of $O^{-2}_{lattice}$ and O^{-}_{ads} in this Cr doped series are ~530eV and ~531eV, respectively (Figure 12.4), in good agreement with the reported values for $SmFeO_3$ [16]. Table 12.2 summarizes the concentration and the ratio of lattice to adsorbed oxygen for fresh and reduced powders. It is important to remember that XPS is a surface sensitive technique and the measurements are limited to a depth of ~ 1nm into the material and therefore the stoichiometries reported correspond to this portion of the material.

The expected bulk oxygen stoichiometry for ABO_3 perovskites is 3, that is an oxygen to metal ratio of 1.5. Although fresh samples showed a single perovskite phase by XRD, it is unclear if the perovskite structure is maintained at the surface, particularly in view of the segregation of different metals. The segregation of different metals at the surface is consistent with the variations in oxygen stoichiometry, reported as O^{-2}/total-metal to

minimize errors in quantification from XPS data. We used the general perovskite formula and its oxygen vacancy parameter (δ, $Sm_{0.95}Ce_{0.05}Fe_{1-x}Cr_xO_{3-\delta}$, obtained directly from the oxygen to metal ratio) to assess the excess (or deficiency) in surface lattice oxygen. Positive values of the vacancy parameter indicate oxygen deficiency, and negative values of δ indicate oxygen excess in the lattice.

Table 12.2. Oxygen composition of fresh and reduced powders as a function of Cr concentration.

	Experimental Surface Lattice Stoichiometry $\frac{O^{-2}}{Sm+Ce+Fe+Ni}$		**Surface Vacancy Parameter (δ)**		$\frac{O^{-2}_{lattice}}{O^{-}_{ads}}$	
	Fresh	**Reduced**	**Fresh**	**Reduced**	**Fresh**	**Reduced**
x=0	1.06	1.24	0.88	0.52	0.75	0.62
x=0.01	2.78	1.29	-2.56	0.43	0.99	0.58
x=0.03	2.46	0.75	-1.93	1.51	1.01	0.50
x=0.05	2.62	0.71	-2.23	1.58	1.09	0.38
x=0.07	3.14	0.55	-3.28	1.91	1.13	0.31
x=0.10	2.99	0.54	-2.99	1.92	1.14	0.29

For fresh powders, the vacancy parameter for all Cr substituted perovskites showed a large excess of lattice oxygen. The concentration of lattice oxygen increases as a function of Cr concentration, likely due to presence of Cr^{+6}, maintaining charge neutrality. This is in agreement with the data presented in Figure 4; the total intensity of the Cr^{+6} peak increases despite the increase of the Cr^{+3}/Cr^{+6} ratio. The large oxygen content is a further indication that the perovskite structure is not maintained at the surface.

Upon reduction, it is expected that both lattice and adsorbed oxygen concentrations should decrease. This was not experimentally observed for this perovskite series. The lattice oxygen concentration in reduced samples is lowered as compared to fresh samples, as expected. However, the ratio of lattice oxygen to adsorbed oxygen appears to be lower than in the fresh samples. At first glance this would indicate that reduction preferentially removes

lattice oxygen. This is not the case. Exposure to air in the transfer between the reduction chamber and the XPS setup results in the recapturing of oxygen, which preferentially occurs at the surface (hence O^-_{ads} increases). This behaviour was corroborated by selective in-situ reductions at the XPS setup, and has been previously reported for Ni doped $Sm_{0.95}Ce_{0.05}FeO_{3-\delta}$ [10]. A quick re-oxidation behaviour is very important and desirable for many technological applications including sensors and SOFCs.

12.3.3. Microstructure

SEM micrographs of as synthesized powders of this Cr doped series are displayed in Figure 12.7. Careful comparison of these micrographs revealed that the introduction of Cr in the composition prevents the grain growth and also decreases the surface porosity. These observations match well with the fact that the BET surface area of these powders decreases as a function of Cr concentration. The BET surface areas of $Sm_{0.95}Ce_{0.05}Fe_{1-x}Cr_xO_{3-\delta}$ (x=0-0.10) perovskite materials are in the range of 6.937-1.946 m^2/g.

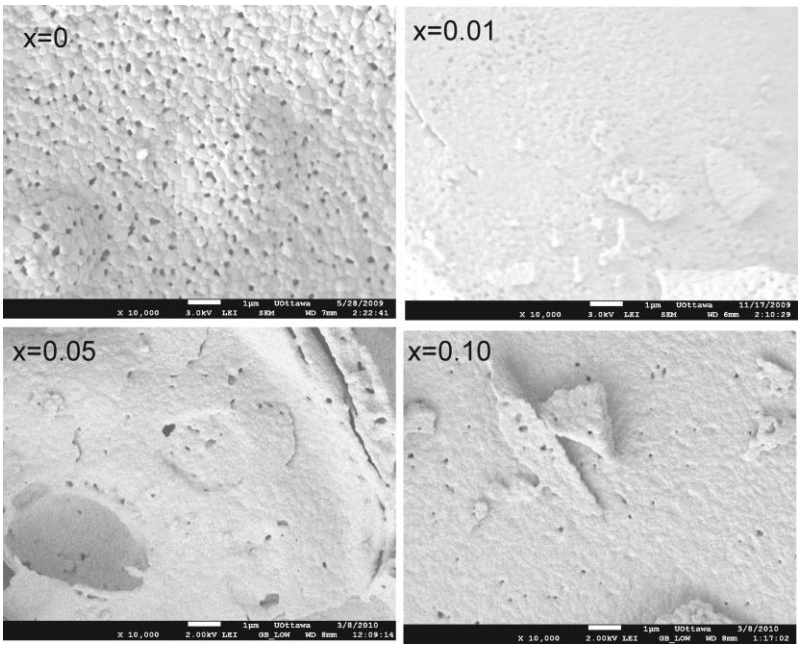

Figure 12.7. Surface morphology of fresh $Sm_{0.95}Ce_{0.05}Fe_{1-x}Cr_xO_{3-\delta}$ powders. Typical particle sizes of as-synthesized powders is in the order of 20-30μm.

Images of the surface of reduced pellets were also obtained by SEM. A change in surface morphology is observed between oxidized and reduced pellets that may be correlated with the change in electrical conductivities discussed below. Figure 12.8 shows the surface

morphologies of pellets reduced at 1000^{o}C under 5%v/v H_2/N_2 for 1h. All samples developed nanoparticles on the surface due to a combination of surface segregation and phase separation (as discussed in terms of XPS and XRD data). The images show that at low chromium concentrations the roughening of the surface is more pronounced. In contrast, at high Cr content the images indicate a large amount of smaller particles. These observations help to bridge the apparent contradiction discussed above between the XRD and the XPS data, namely a small concentration of chromium destabilizes the lattice of the parent $Sm_{0.95}Ce_{0.05}FeO_{3-\delta}$ perovskite, but at high chromium concentrations reduction may be more pronounced, albeit limited to the surface.

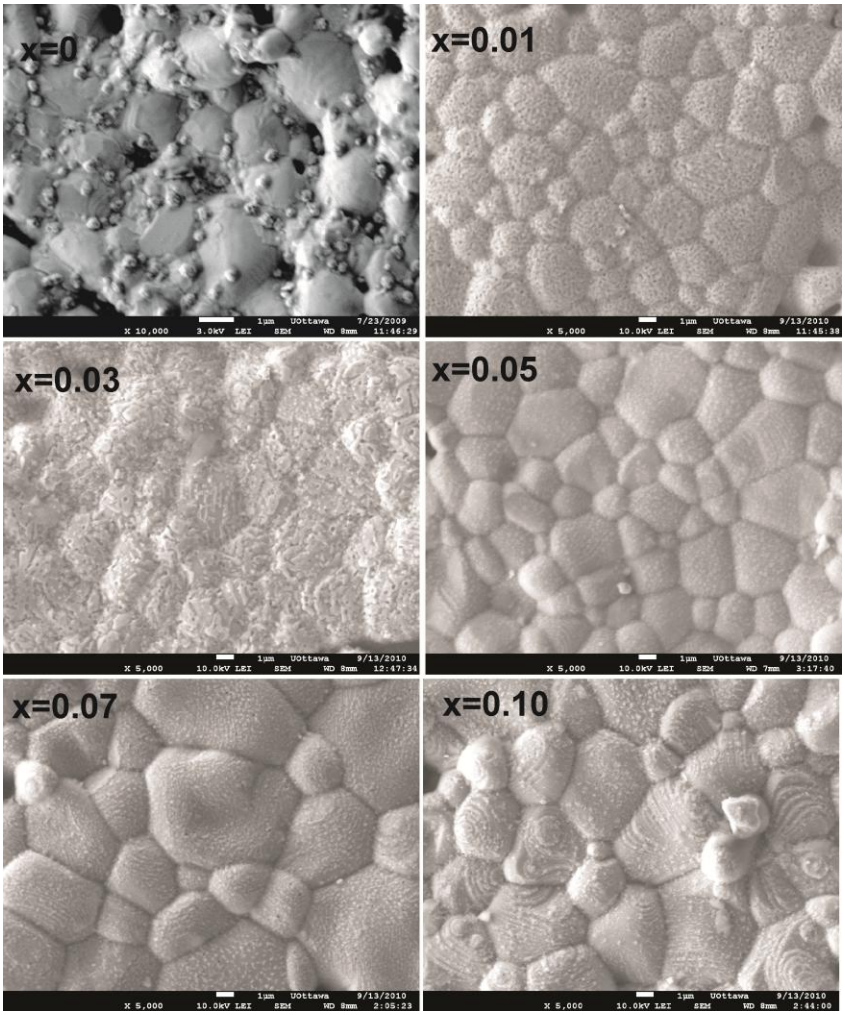

Figure 12.8. Surface morphology of $Sm_{0.95}Ce_{0.05}Fe_{1-x}Cr_xO_{3-\delta}$ pellets reduced at 1000^{o}C for 1h under 5%v/v H_2/N_2.

12.3.4. Electrical conductivity

Electrical conductivities were measured under air (oxidizing conditions) and 5%v/v H_2/N_2 (reducing conditions). Under reducing conditions, the electrical conductivity measurements were made with two types of samples: i) partially reduced samples that were treated to 700^{o}C for 1h under 5%v/v H_2/N_2; and ii) fully reduced samples that were treated to 1000^{o}C for 1h under 5%v/v H_2/N_2. The electrical conductivity of partially reduced samples was measured from 25^{o}C to 700^{o}C (through several heat/cool cycles). Because these materials are stable under reducing conditions up to 700^{o}C, no phase separations are observed and the conductivity measurements reflect the conductivity of the pure perovskite phase. In contrast, fully reduced samples consist of the bulk perovskite structure with surface nanoparticles containing different phases as described above. Since these samples have been treated to 1000^{o}C already, conductivity measurements are also performed up to that temperature.

Under air, the electrical conductivity of the $Sm_{0.95}Ce_{0.05}Fe_{1-x}Cr_xO_{3-\delta}$ series increases as a function of temperature indicating that all these materials are semiconductors (Figure 12.9a). However, the conductivity as a function of Cr concentration, has a maximum at x=0.03 for all temperatures (Figure 12.9d). Partially reduced and fully reduced samples show similar behaviour under 5%v/v H_2/N_2; the conductivity increases as a function of temperature although the dependence on Cr concentration is less pronounced (Figure 12.9). The conductivity values under reducing conditions are higher than those in air for all samples, which suggests that these materials, in single phase structure as well as after surface segregation and phase separation, behave like a n-type conductor. However, the specific charge carrier and/or conducting species could not be identified. As expected by the formation of highly reduced surface species, the conductivity of fully reduced samples is higher than that of partially reduced samples.

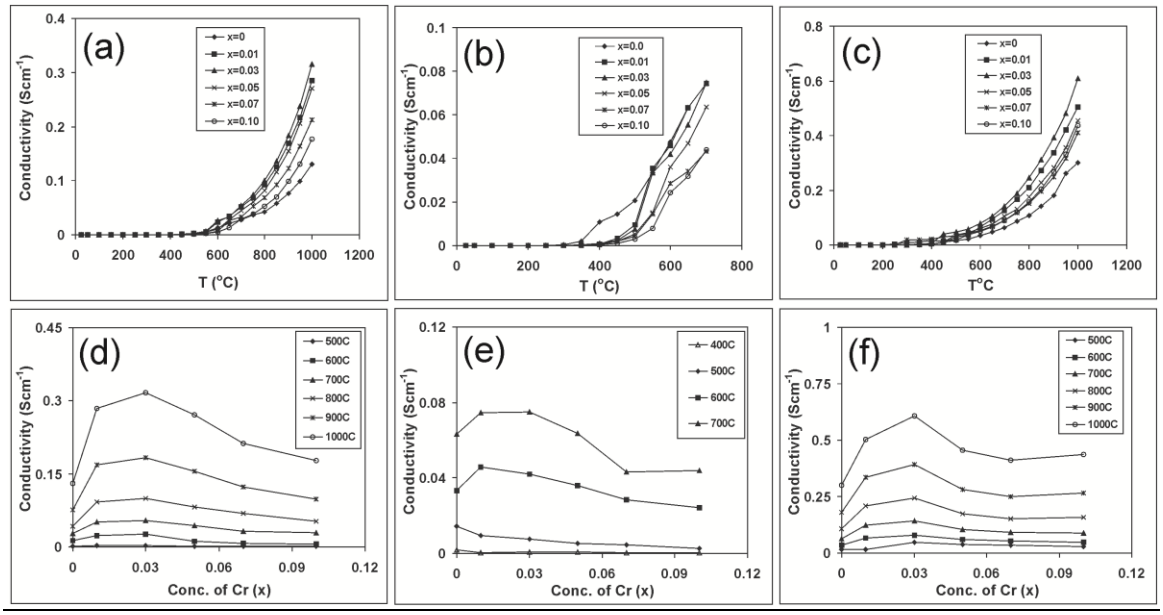

Figure 12.9. Electrical conductivities of fresh pellets in air (a and d), partially reduced pellets under 5%v/v H_2/N_2 (b and e), and fully reduced pellets under 5%v/v H_2/N_2 (c and f).

As a function of Cr concentration (Figure 12.9d-f), the trends are more difficult to explain due to the multiple redox couples that result from introduction of Cr in the lattice. The reduction processes ($Cr^{+6} \rightarrow Cr^{+3}$, $Fe^{+3} \rightarrow Fe^{+2} \rightarrow Fe^{0}$) observed upon exposure to hydrogen at high temperature compete to yield a maximum in conductivity at x=0.03 in most cases, except for the partially reduced samples at low temperatures. Additionally, the surface segregation observed upon reduction further confounds any trend.

12.4. Conclusions

Complex perovskites with general formula $Sm_{0.95}Ce_{0.05}Fe_{1-x}Cr_xO_{3-\delta}$ (x=0-0.10) were prepared via a citrate precursor route. The resulting materials showed a single phase in X-ray diffraction with orthorhombic symmetry. Lattice volumes decreased as a function of Cr concentration suggesting the presence of Cr^{+3}/Cr^{+6}. Surface analysis by XPS shows the presence of Cr^{+3} and Cr^{+6}, and importantly the concentration of Cr^{+6} increases with Cr content in the series. These materials are stable in air up to 1400°C and no phase separation was observed after exposure to 5%v/v H_2/N_2 at 700°C for 1 hour. The onset of phase separation without deterioration of the perovskite phase was found to be at 800°C. XRD of samples reduced at 800°C for 1 hour under 5%v/v H_2/N_2 showed that lattice volumes increased upon reduction indicating that some metal species has reduced to lower oxidation

states. Consistently, XPS shows metal atoms in lower oxidation states, including metallic Fe upon reduction at 1000^{o}C. Reduced samples have a lower concentration of O^{-2}_{latt} as compared to fresh samples (as expected) but the concentration of O^{-}_{ads} was found to be higher than expected. A possible explanation for this behaviour is the oxygen recapturing ability of the material upon exposure to air. This behaviour suggested that these materials have reversible redox properties. The electrical conductivity of all the materials in this series increases upon reduction of the perovskite partly due to the formation of nanoparticles on the surface as a result of surface segregation and phase separation. The change in conductivity suggests that these materials have the potential to be used as sensors for reducing gases.

12.5. References

[1] M.A. Pena, J.L.G. Fierro, Chem. Rev. 101 (2001) 1981-2017.
[2] S.M. Bukhari, J.B. Giorgi, Solid State Ionics. 180 (2009) 198-204.
[3] X. Li, H. Zhao, N. Xu, X. Zhou, C. Zhang, N. Chen, International Journal of Hydrogen Energy. 34 (2009) 6407-6414.
[4] B.A. Boukamp, Nature Materials. 2 (2003) 294-296.
[5] H. Aono, E. Traversa, M. Sakamoto, Y. Sadaoka, Sens. Actuators B. 94 (2003) 132-139.
[6] M.C. Carotta, G. Martinelli, Y. Sadaoka, P. Nunziante, E. Traversa, Sens. Actuators B. 48 (1998) 270-276.
[7] S.M. Bukhari, J.B. Giorgi, ECS Trans. 33 (2010) 81-91.
[8] S.M. Bukhari, J.B. Giorgi, ECS Trans. 28 (2010) 19-29.
[9] S.M. Bukhari, J.B. Giorgi, Sens. Actuators B. 155 (2010) 524-537.
[10] S.M. Bukhari, J.B. Giorgi, Solid State Ionics (2010) submitted.
[11] S.M. Bukhari, J.B. Giorgi, J. Electrochem. Soc. 158 (2011) J159-J164.
[12] N. Fairley, Casa XPS version 2.3.13 Dev73 (2007).
[13] I. MDI Jade 6.1 Software Materials Data. Serial#MDI-R97738 (2002).
[14] R.D. Shanon, Acta cryst. A32 (1976) 751-767.
[15] V.M. Goldschmidt, Oslo, Naturwissenschaften. 14 (1926) 477.
[16] H. Aono, M. Sato, E. Traversa, M. Sakamoto, Y. Sadaoka, J. Am. Ceram. Soc. 84 (2001) 341-347.

13. Potential of $Sm_{0.95}Ce_{0.05}Fe_{1-x}Cr_xO_{3-\delta}$ Perovskite Materials for Gas Sensing

The contents of this chapter have been published as: Syed M. Bukhari and Javier B. Giorgi, Electrochemical Society Trans., 33(8) (2010) 117-130

Abstract

Reducing-gas sensors based on $Sm_{0.95}Ce_{0.05}Fe_{1-x}Cr_xO_{3-\delta}$ (x=0-0.05) perovskites were prepared in the form of pellets. The sensor's surface is enriched with Cr due to surface segregation, and the Sm surface concentration varies along the series. The introduction of Cr in the perovskite lattice produces a rearrangement of charge within the perovskite structure, as indicated by changes in concentration of the different Fe species. The concentration of lattice and surface-adsorbed oxygen as a function of Cr concentration were found to be correlated with different Fe species. The electrical conductivity responses toward H_2, CO and CH_4 (1-5%v/v) were measured in air at different temperatures. All sensors showed good sensitivity towards the target gases at 200^{o}C and 300^{o}C but only x=0.01 was able to detect H_2, CO and CH_4 at 25^{o}C. Response and recovery time are dependent on surface chemical composition and surface morphology.

13.1. Introduction

The methods which are currently approved for environmental monitoring require the use of very costly and bulky analytical equipment, thus currently preventing a wide distribution of environmental monitoring locations. This problem can be resolved by using devices based on solid-state gas sensors because their usage will reduce the cost dramatically as these are much cheaper than other analytical equipment. However, the performance of available solid-state gas sensors is not up to the desired level. So there is a great demand of developing new materials for reliable and selective solid-state gas sensors. There are different types of solid-state gas sensors but simplest of them are those which are based on changes in electrical parameters. These types of sensors use semiconducting materials as active elements. Amongst the semiconducting materials, ABO_3 type perovskite oxides are very attractive candidates for this application because of their stability under various thermal and chemical stresses and their mixed ionic and electronic conductivity.

$SmFeO_3$ is a perovskite oxide with p-type semiconducting behaviour that has been used for sensing gases like NO_2, O_3 and CO [1-3]. Ce doping at the A-site of $SmFeO_3$ ($Sm_{1-x}Ce_xFeO_3$) not only improved its electrical conductivity under reducing conditions but also changed its behaviour from p-type to n-type, thus making the doped material an interesting candidate for detection of reducing gases [4]. Further improvement in electrical conductivity and sensitivity of $Sm_{0.95}Ce_{0.05}FeO_{3-\delta}$ under reducing gases has been achieved by substituting Co at the B-site [5, 6]. In this work, we report a new series of perovskite oxides with formula $Sm_{0.95}Ce_{0.05}Fe_{1-x}Cr_xO_{3-\delta}$. These Cr doped materials are n-type semiconductors with fairly high electrical conductivity under both oxidizing and reducing conditions. This work will show the potential of these newly developed Cr doped materials for detection of reducing gases like H_2, CO and CH_4 in air (1-5%v/v), at different temperatures i.e., 25^{o}C, 200^{o}C and 300^{o}C.

13.2. Experimental

13.2.1. Powder Preparation and Sensor Fabrication

The precursor powders of $Sm_{0.95}Ce_{0.05}Fe_{1-x}Cr_xO_{3-\delta}$ (x=0-0.05) were synthesized via the sol gel method because it (i) allows homogeneous mixing of components; (ii) lowers the calcination temperature; and (iii) helps in improving the surface area of the final product. In the sol gel method, iron nitrate [$Fe(NO_3)_3{\cdot}9H_2O$, AlfaAesar, >98%], chromium nitrate [$Cr(NO_3)_3.6H_2O$, AlfaAesar, 99%], samarium nitrate [($Sm(NO_3)_3{\cdot}6H_2O$, AlfaAesar, 99.9%], cerium nitrate [$Ce(NO_3)_3{\cdot}6H_2O$, AlfaAesar, 99.5%], and citric acid monohydrate (minimum 99.0%) were used as precursors. Following the desired stoichiometry ($Sm_{0.95} + Ce_{0.05} : Fe_{(1-x)} + Cr_x = 1:1$), the four metal nitrate solutions were separately prepared in de-ionized water. These metal nitrate solutions were mixed with a citric acid solution such that a total metal content to citric acid ratio was 1:1. The resulting solution was evaporated to dryness at 100^{o}C to form amorphous citrate precursors which were further ground and calcined at 850^{o}C for 24h to produce the perovskite phase.

Pellets were formed by uniaxial pressing of powders and then sintered in air at 1350^{o}C for 4h. The rectangular shape sensors were fabricated by chopping sintered pellets. Four notches were made on each sensor and Pt wires were wrapped around the notches to make four contacts. A DC power supply, a source of current, was connected to the two outer Pt

wires. A digital multimeter was connected to the two inner Pt wires for the measurement of voltage.

13.2.2. Characterization of Materials and Sensors

Powder X-ray diffraction analysis of as synthesized powders, reduced powders under 5% v/v H_2/N_2 for one hour at different temperatures, and sintered pellets, was used to determine the crystal structure and phase composition. Surface morphology of each solid state sensor was explored by Scanning electron microscopy (SEM, JEOL JSM-7500F) while the surface chemical states and composition were measured by X-ray photoelectron spectroscopy (XPS; Kratos AXIS Ultra^{DLD} 39-306l), using a monochromatic Al anode.

Gas sensing experiments were carried out in a test chamber made up of a quartz tube with rubber septa on both ends, which sits in a furnace connected to a temperature controller. Figure 13.1 shows a schematic representation of the 4 probe sensing experiment.

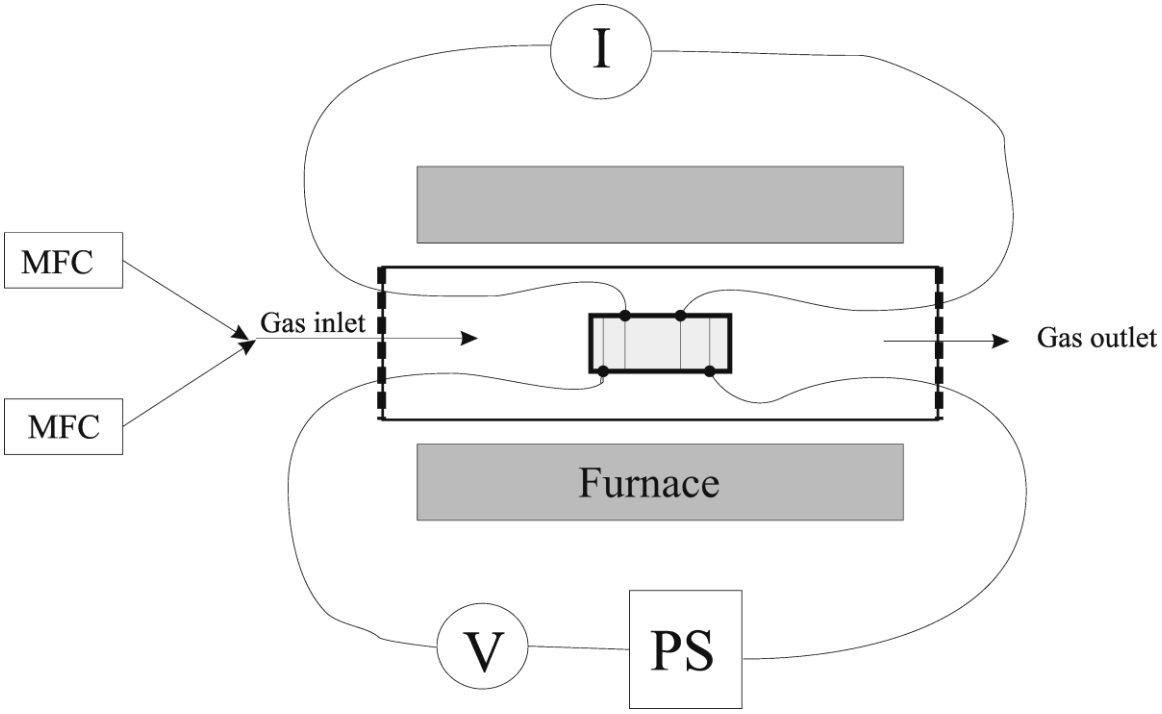

Figure 13.1. Schematic of the sensor setup.

The electrical conductivity of each sensor was measured under air, 1%H_2/air, 1%CO/air and 1%CH_4/air in the temperature range of 25-400^oC and an effective activation energy for the conductivity change was determined. The electrical conductivity responses of these sensors were then measured for H_2, CO and CH_4 in air using a concentration range (1-

5%v/v), at different temperatures i.e., 25°C, 200°C and 300°C. Sensor response, S, at a particular temperature was evaluated using the relation:

$$S(\%) = 100 \times \left(\frac{\sigma_{gas} - \sigma_{Air}}{\sigma_{Air}} \right) \quad (13.1)$$

13.3. Results and discussions

13.3.1. Phase Composition and Surface Morphology

X-ray diffraction of the as-synthesized powders (Figure 13.2) showed that $Sm_{0.95}Ce_{0.05}Fe_{1-x}Cr_xO_{3-\delta}$ (x=0-0.05) materials have a single phase with orthorhombic symmetry belonging to space group Pnma (62). The introduction of Cr into the lattice shifts the XRD peak to larger 2Θ values and therefore a decreasing trend of lattice volumes was observed. This observation suggested that Cr is entering into the lattice as Cr^{+3} and/or Cr^{+6}, which are smaller ions than the nominally Fe^{+3} ions being replaced. The reduction stability of these materials was also tested by treating with 5 %v/v H_2/N_2 for one hour at different temperatures. The results showed that they are stable up to 700°C and phase separation without deterioration of perovskite phase does occur at 800°C and above. The comparison of diffractograms of sintered pellets also revealed that the perovskite phase does not decompose nor does phase separation occurs on heating in air up to 1350°C for 4h.

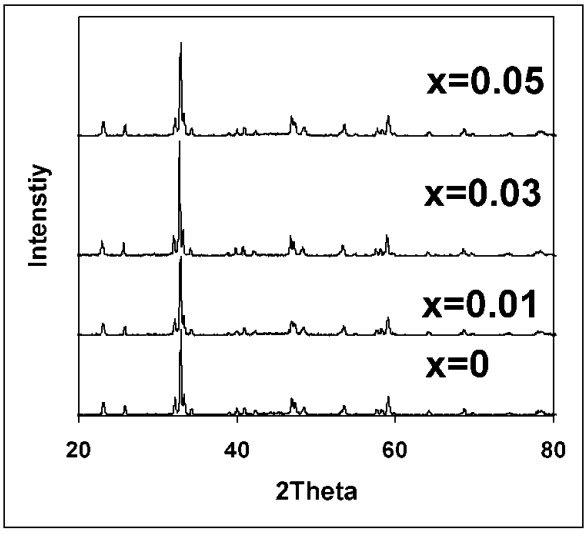

Figure 13.2. XRD pattern of as synthesized $Sm_{0.95}Ce_{0.05}Fe_{1-x}Cr_xO_{3-\delta}$ (x=0-0.05) perovskite materials.

The surface morphology of each solid state sensor was explored by scanning electron microscopy. Figure 13.3 shows the microstructure of each sensor. The particle size of the perovskite in the pellets grows sharply as a function of chromium concentration up to x=0.03 and then decreases. In all sensors, particles on the surface have well defined grain boundaries.

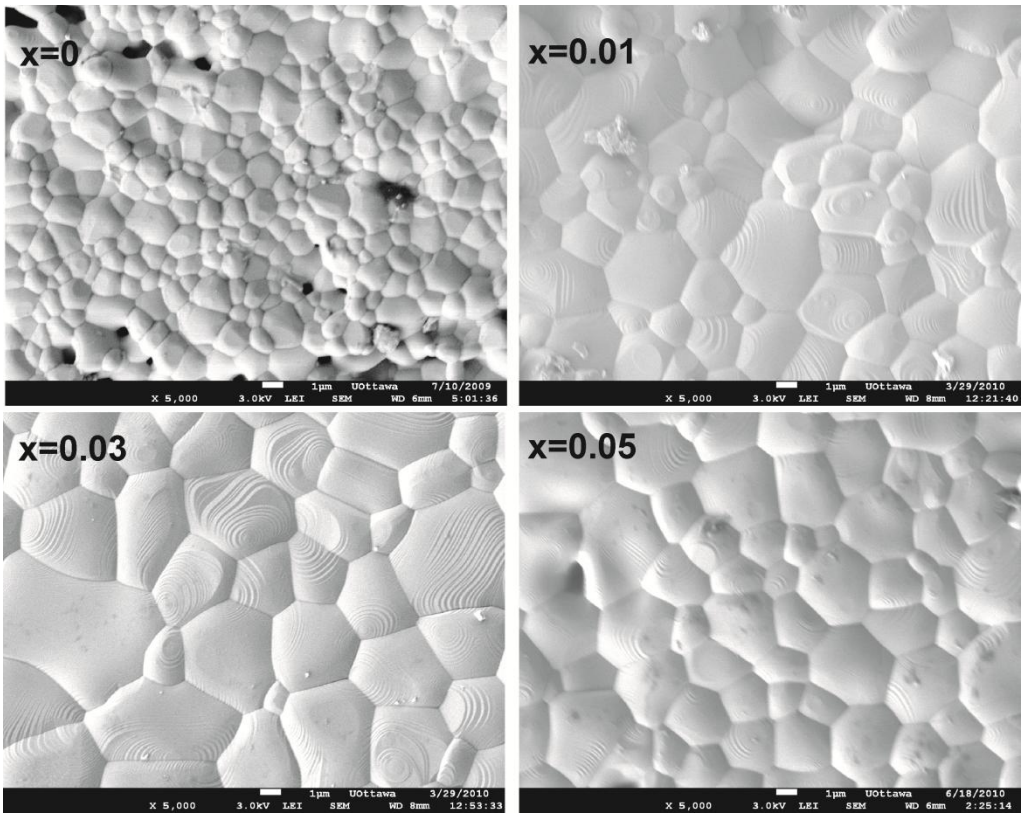

Figure 13.3. SEM images of $Sm_{0.95}Ce_{0.05}Fe_{1-x}Cr_xO_{3-\delta}$ (x=0-0.05) sensors showing the surface morphology.

13.3.2. XPS and Surface Chemical Composition

X-ray photoelectron spectroscopy was used to determine the chemical state and relative abundance of the elements on the surface of each sensor. For the purpose of quantification and identification of oxidation states, peaks of $Sm3d_{5/2}$, $Ce3d_{5/2}$, $Fe2p_{3/2}$, $Cr2p_{3/2}$ and O1s core levels were used. The energy scale was calibrated by setting the adventitious C1s peak at 284.8 eV. Casa XPS software [7] was used to analyze and quantify the XP spectra. In all samples, the position of the $Sm3d_{5/2}$ peak was ~1082eV which indicates that Sm is in the +3

oxidation state [8]. The peaks of $Ce3d_{5/2}$ and $Cr2p_{3/2}$ core levels were of very low intensity and thus determination of exact oxidation state of Ce and Cr was not possible.

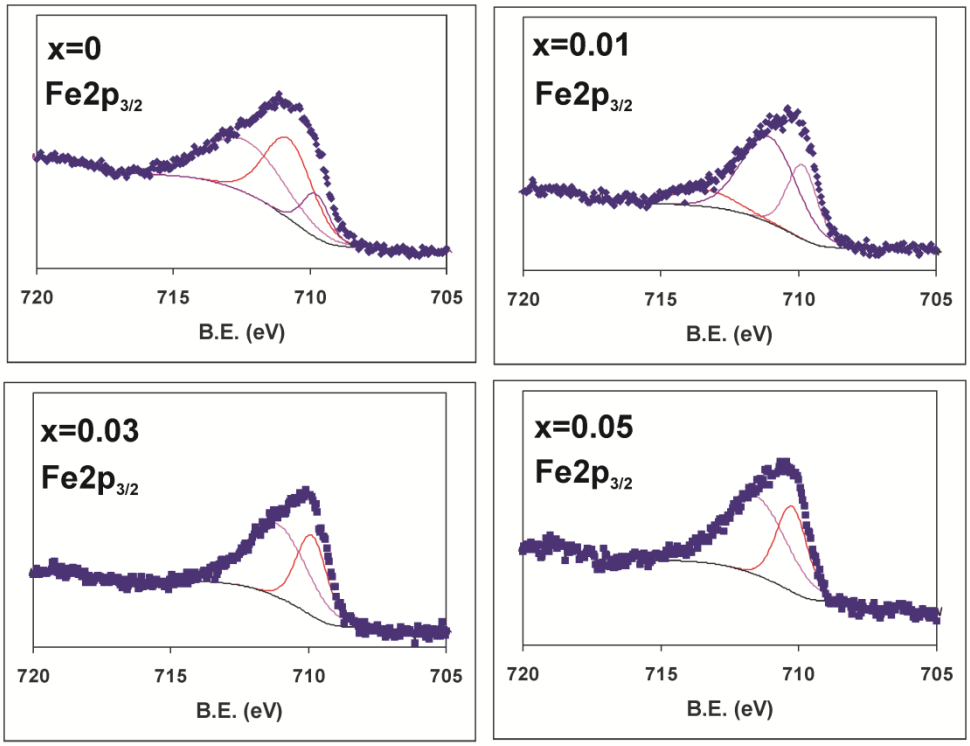

Figure 13.4. Fitting results of $Fe2p_{3/2}$ peaks for $Sm_{0.95}Ce_{0.05}Fe_{1-x}Cr_xO_{3-\delta}$ (x=0-0.05).

In all sensors, the $Fe2p_{3/2}$ peak was quite broad and thus, multiple peaks can easily be fitted, showing the multiple oxidation states of Fe in the lattice. Figure 13.4 shows peak fitting of $Fe2p_{3/2}$ for the four sensors. Sensors built with the x=0 and x=0.01 materials showed three peaks while the x=0.03 and x=0.05 materials showed only two peaks. The oxidation state of Fe species in each case can easily be identified by comparing with literature reported photoelectron positions. The reported B.E. for Fe^{+2} and Fe^{+3} are 709.3eV and 710.5eV, respectively [9]. In this work the peaks in the range of 709.5-710eV and 710.5-711eV have been ascribed to Fe^{+2} and $Fe^{+3,}$ respectively, while the peak at ~ 713.2±3eV is assigned to Fe^{+4}, consistent with previous results [6]. Thus, it is clear that x=0 and x=0.01 have three kind of Fe species i.e., Fe^{+2}, Fe^{+3} and Fe^{+4} while x=0.03 and x=0.05 have two kind of Fe species i.e., Fe^{+2} and Fe^{+3} in their lattice. Percentages of the three Fe species as a function of Cr concentration are given in Table 13.1. Introduction of Cr into the lattice decreases the concentration of Fe^{+2} and Fe^{+4} species present in the undoped

$Sm_{0.95}Ce_{0.05}FeO_{3-\delta}$ perovskite, which suggests a charge rearrangement between Cr and Fe in the lattice.

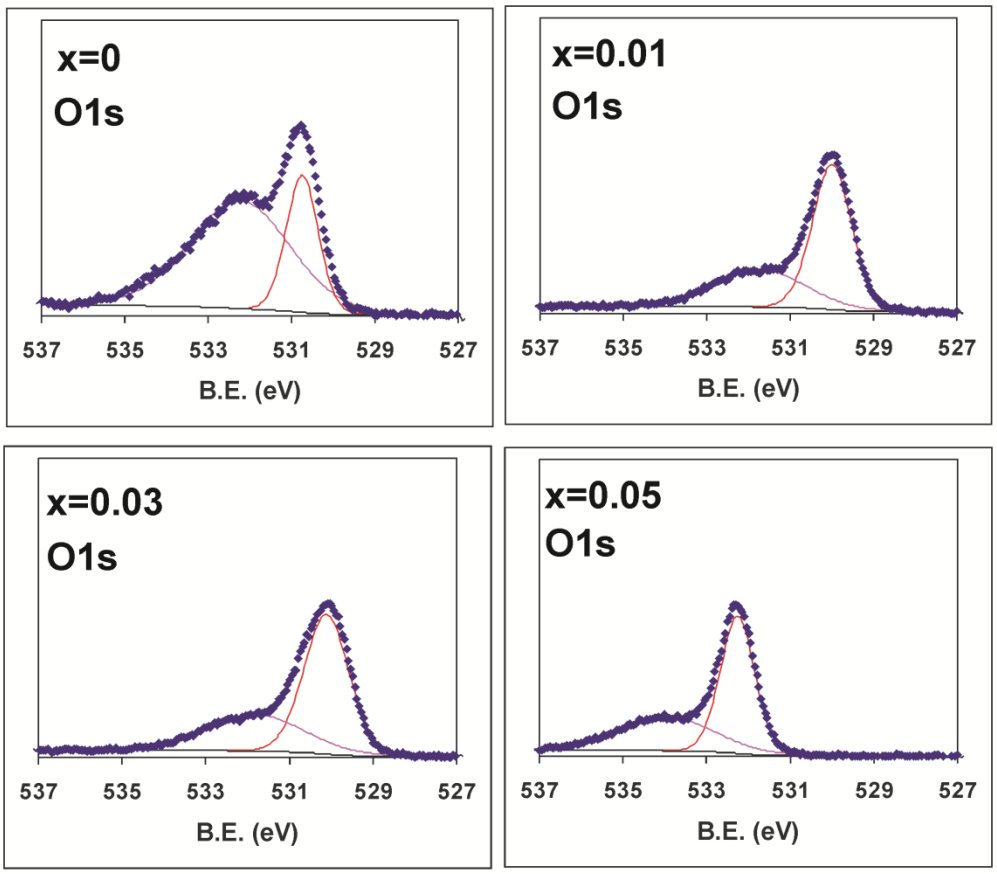

Figure 13.5. Fitting results of O1s peaks for $Sm_{0.95}Ce_{0.05}Fe_{1-x}Cr_xO_{3-\delta}$ (x=0-0.05).

Figure 13.5 shows the XPS data for the oxygen region. The O1s peak in all sensors consist of two components, as previously observed in different perovskite oxide materials [4, 5, 8, 10]. The low binding energy component (~529eV) has been assigned to lattice oxygen (O_{latt}) while the high binding energy component (~531eV) corresponds to adsorbed oxygen (O_{ads}). Table 13.1 summarizes the ratios of O_{latt} to total metal contents and O_{ads} as a function of Cr concentration. The percentage of O_{latt} increases while that of O_{ads} decreases up to x=0.03 and the trend is reverse beyond that chromium content. This can be explained qualitatively in terms of changes in concentration of the different Fe species as a function of Cr concentration, although the exact oxidation state of Cr is not measurable from the spectra because of the low intensity and breadth of the peak. The concentration of Fe^{+4} decreases and

becomes zero in x=0.03 while Fe^{+2} gradually increases up to x=0.03. As the concentration of lattice oxygen is high for the doped materials, a decrease in positive charge localized at the iron ions in the lattice implies the presence of a high oxidation state metal to maintain charge neutrality. That is, some of the Cr ions present must be in a high oxidation state, i.e. +6.

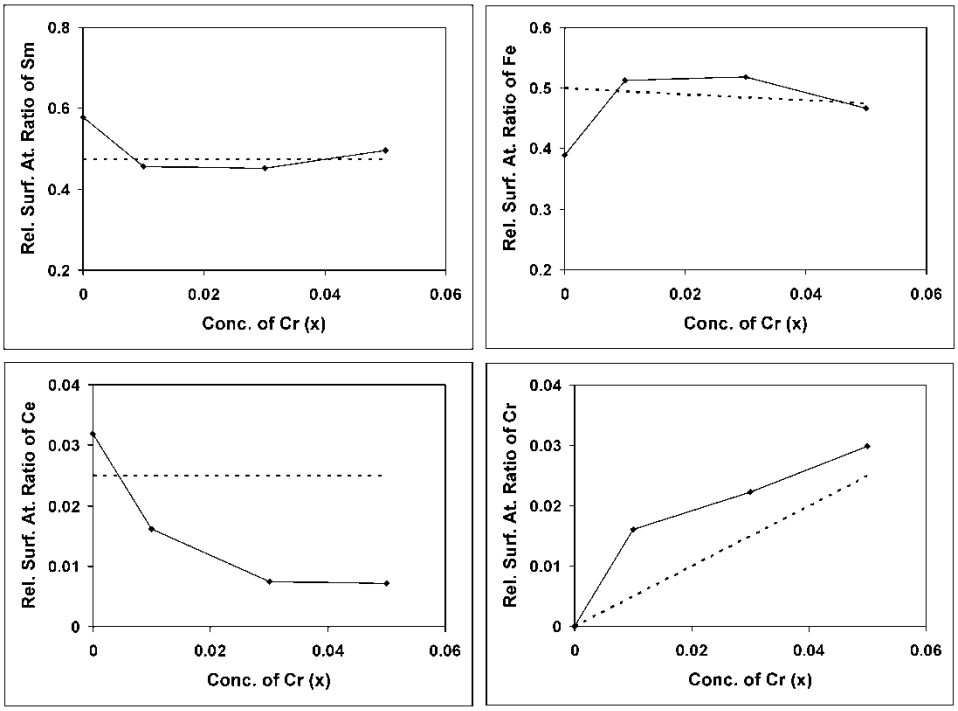

Figure 13.6. Surface atomic ratios of metal atoms in $Sm_{0.95}Ce_{0.05}Fe_{1-x}Cr_xO_{3-\delta}$ sensors as calculated from peak fitting of the $Sm3d_{5/2}$, $Ce3d_{5/2}$, $Fe2p_{3/2}$ and $Co2p_{3/2}$ core levels. The dotted lines represent the expected bulk atomic ratios.

Relative surface atomic ratios of the four metals, Sm, Ce, Fe and Co, were also determined from peak fittings of the $Sm3d_{5/2}$, $Ce3d_{5/2}$, $Fe2p_{3/2}$ and $Co2p_{3/2}$ core levels. The results of surface metal quantification are shown in Figure 13.6. The surfaces of all sensors were enriched with Cr due to surface segregation, pushing the cerium ions away from the surface. The results show that upon the introduction of Cr, the initially Sm rich surface decreases in Sm concentration, approaching the stoichiometric value. Similarly, the Fe concentration increases to stoichiometric values. The trend of surface adsorbed oxygen is found to correlate with the surface atomic ratio of Sm. For example, for the x=0 sensor, which contains a high concentration of surface Sm, the O_{ads} concentration is high as shown by the O_{latt}/O_{ads} ratio in Table 13.1. In general, at a high concentration of Sm on the surface,

there are more active sites for interaction with gas molecules due to the high coordination number of Sm (12).

Table 13.1. Quantification results obtained from peak fittings of O1s and $Fe2p_{3/2}$ peaks.

Chromium conc.(x)	Iron (Fe)			Oxygen	
	Fe^{+2}	Fe^{+3}	Fe^{+4}	$\frac{O_{latt}}{Sm+Ce+Fe+Co}$	$\frac{O_{latt}}{O_{ads}}$
0	20.73	45.86	33.41	0.86	0.66
0.01	28.44	58.57	12.99	2.73	1.69
0.03	36.06	63.94	0	2.66	1.78
0.05	34.88	65.12	0	2.59	1.68

13.3.3. Electrical properties and response

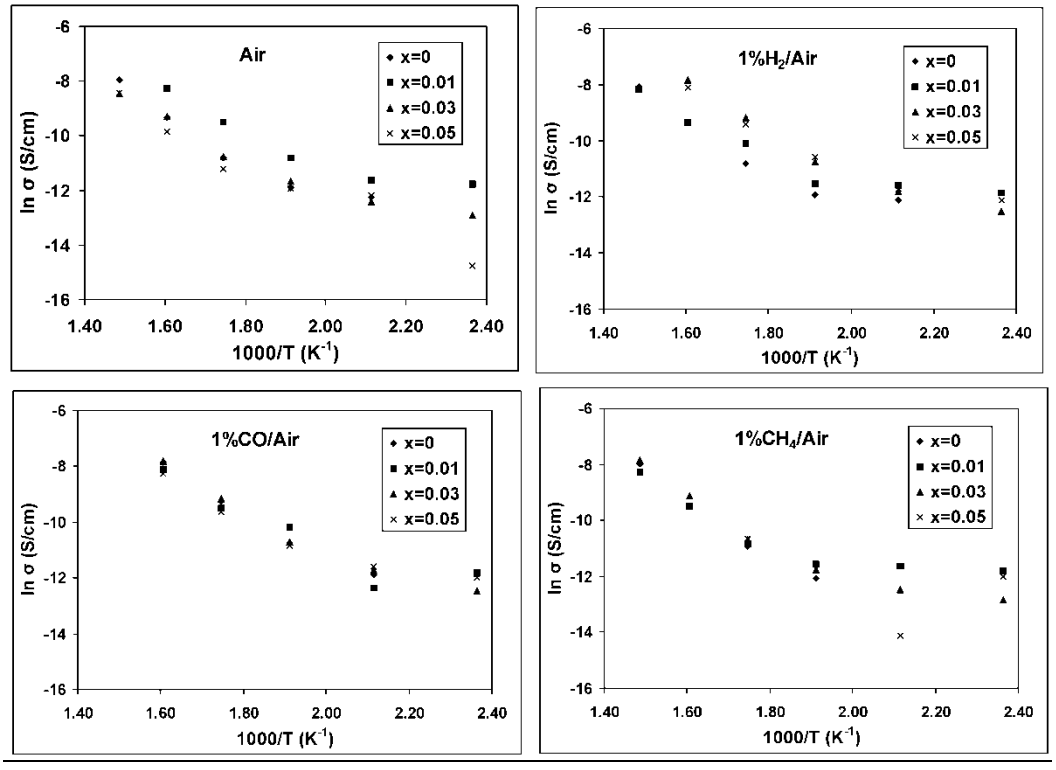

Figure 13.7. Electrical conductivity of $Sm_{0.95}Ce_{0.05}Fe_{1-x}Cr_xO_{3-\delta}$ (x=0-0.05) sensors in air, 1%H_2/air, 1%CO/air and 1%CH_4/air.

Arrhenius plots of electrical conductivities of all sensors under air, 1%H_2/air, 1%CO/air and 1%CH_4/air are shown in Figure 13.7. Qualitatively, the analysis shows that the electrical conductivity increases with an increase in temperature, indicating the semiconducting nature of all compositions (x=0-0.05). This dependency also indicates that the process is thermally activated and an activation energy for the process can be calculated from the Arrhenius type relation: $\sigma(T)=Aexp(-Ea/RT)$ [11]. It is clear from the graphs that there are two regions with different slopes. The activation energies calculated from the slopes in the higher temperature regime (250-400°C) are given in Table 13.2. Additionally, the higher electrical conductivities under 1%H_2/air, 1%CO/air and 1%CH_4/air as compared to air shows the n-type nature of all the sensors.

Table 13.2. Activation energies calculated from the slopes of Arrhenius plots.

Chromium conc.(x)	Activation Energies (kJ/mol)			
	Air	1% H_2	1% CO	1% CH_4
0	77.00	75.70	79.12	79.17
0.01	65.89	63.38	68.52	65.23
0.03	64.21	78.84	77.22	77.60
0.05	68.18	69.89	64.94	64.81

Sensors with increasing Cr concentration were tested for reducing gases including hydrogen, carbon monoxide and methane in air from 1-5%v⁄v at three different temperatures 25^{o}C, 200^{o}C and 300^{o}C. The electrical conductivity responses of these sensors for hydrogen are shown in Figure 13.8. All sensors showed a linear and reversible response for hydrogen under all testing temperatures. Indeed x=0.01 showed a detectable response at room temperature. At 200^{o}C, the optimal response was shown by x=0. But at 300^{o}C the response towards hydrogen was found to increase with increase in Cr concentration and thus x=0.05 has optimal sensitivity for hydrogen.

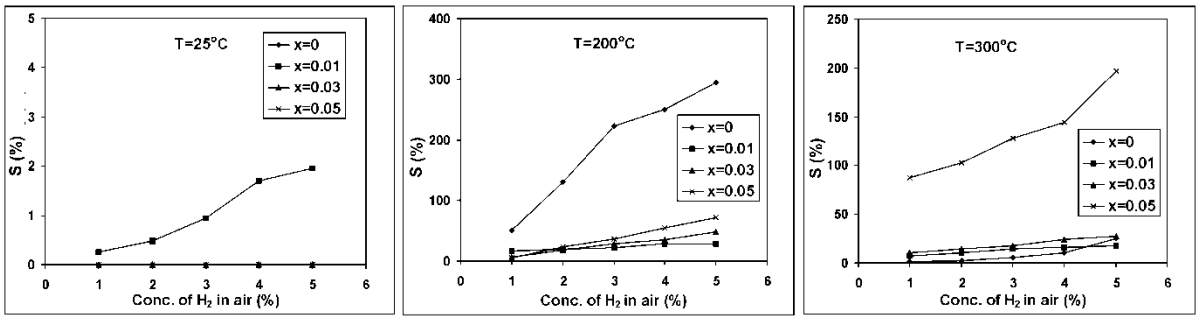

Figure 13.8. Concentration dependence of the electrical conductivity response of $Sm_{0.95}Ce_{0.05}Fe_{1-x}Cr_xO_{3-\delta}$ (x=0-0.05) for hydrogen in air at different temperatures.

Experiments for methane detection in air were also performed with these sensors at different temperatures. Electrical conductivity responses of $Sm_{0.95}Ce_{0.05}Fe_{1-x}Cr_xO_{3-\delta}$ (x=0-0.05) sensors for CH_4 in air are shown in Figure 13.9. The most active sensor for CH_4 at room temperature was found to be x=0.01. The sensor response towards methane at 200°C was found to increase with an increase in Cr concentration and thus x=0.05 was one of the most effective sensors for methane sensing at this temperature. At higher temperature, 300°C, the optimal sensor response was shown by x=0.05.

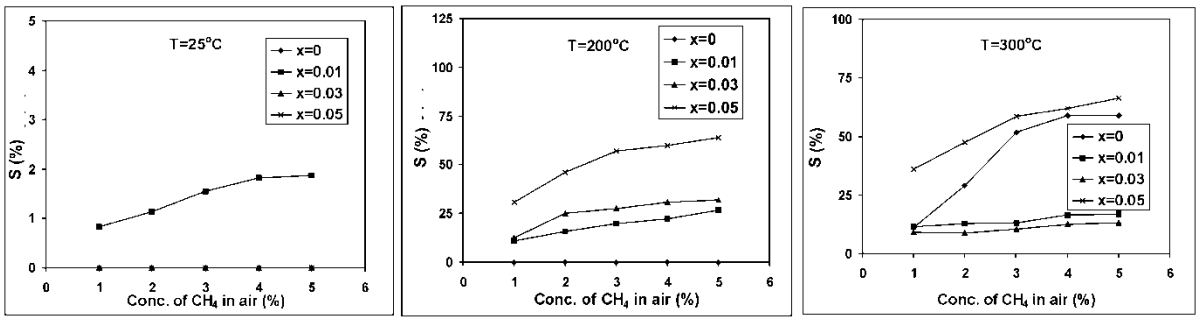

Figure 13.9. Concentration dependence of the electrical conductivity response of $Sm_{0.95}Ce_{0.05}Fe_{1-x}Cr_xO_{3-\delta}$ (x=0-0.05) for methane at different temperatures.

Figure 13.10 shows the response of these sensors towards different concentration of carbon monoxide in air at different temperatures. All sensors were able to detect CO at both 200°C and 300°C. At 300°C, the optimal sensor response was exhibited by x=0.05 as responses were also found to increase with increase in Cr concentration. The most efficient sensor at 200°C was x=0 but only x=0.01 was able to detect carbon monoxide at room temperature (25°C).

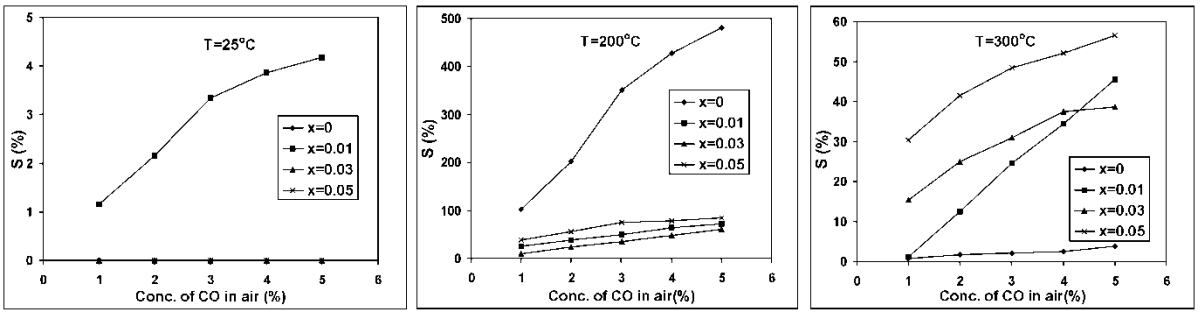

Figure 13.10. Concentration dependence of the electrical conductivity response of $Sm_{0.95}Ce_{0.05}Fe_{1-x}Cr_xO_{3-\delta}$ (x=0-0.05) for carbon monoxide (CO) at different temperatures.

13.3.4. Sensing Mechanism

Perovskite type oxides can be selectively doped to generate materials and devices with desired properties [12]. The resulting material could be n- or p-type depending on the relative concentration of electrons and holes (the charge carriers). If the concentration of electrons is greater than that of holes, the resulting material will be n-type and if the concentration of holes is greater than that of electrons then the new material will be p-type. Since the $Sm_{0.95}Ce_{0.05}FeO_{3-\delta}$ perovskite material is n-type, it has relatively high concentration of electron. When Cr is doped at Fe site in $Sm_{0.95}Ce_{0.05}FeO_{3-\delta}$, the resulting $Sm_{0.95}Ce_{0.05}Fe_{1-x}Cr_xO_{3-\delta}$ (x=0-0.05) perovskite materials are n-type too and have significantly higher electrical conductivities under both oxidizing and reducing conditions. This improved electrical conductivity can be ascribed to an increase in electron-charge carrier and oxygen vacancy concentration, nominally creating an extrinsic point defect.

In general, the electrical conductivity of n-type sensors is relatively low under air but high under reducing conditions. This is because under oxidizing conditions, oxygen being an oxidizing agent removes electrons from the conduction band (equation 13.2) and decreases the concentration of electron.

$$O_{ads} + 2e^- \rightarrow O^{-2} + 2\dot{h} \qquad (13.2)$$

On the other hand, upon exposure to a reducing gas (like H_2, CO and CH_4), the concentration of electrons increases in the conduction band due to an electron releasing effect (equation 13.3-13.5).

$$H_2 + O^{-2} + 2\dot{h} \rightarrow H_2O + V_O^{\bullet\bullet} + 2e^- \quad (13.3)$$

$$CO + O^{-2} + 2\dot{h} \rightarrow CO_2 + V_O^{\bullet\bullet} + 2e^- \quad (13.4)$$

$$CH_4 + 3O^{-2} + 6\dot{h} \rightarrow CO + 2H_2O + 3V_O^{\bullet\bullet} + 6e^- \quad (13.5)$$

This is a bulk type mechanism. But there is also a possibility of surface reaction type mechanism as explained in Chapter 6 (equation 13.6). According to which, the reducing gas (which may be pre-adsorbed) reacts with surface oxygen species (O_2, O_2^- or O^-). As a result, the electrons release to the conduction band of the material.

$$R + xO_{ads}^{y} \rightarrow RO_x + |xy|e^- \quad (13.6)$$

where R is reducing gas.

In the present case, the sensors are n-type, the carrier gas is air (oxidizing agent) and the target gases are H_2, CO and CH_4 (reducing agents). When a target gas is introduced in the stream of air flowing through the testing chamber the electrical conductivity increases due to the interaction between the target gas molecules and the surface of the sensor. Similarly, when the flow of the target gas is interrupted, the electrical conductivity of sensor decreases to its original value due to reoxidation of the sensor surface (i.e., hole concentration increases).

13.3.5. Concentration dependence and quality of the sensors

The concentration dependence of the sensitivity is usually analyzed using a power law (equation 13.7, where S_g and C_g are the sensitivity and concentration of a gas while K and α are fitting constants). In this relationship, values of α are used to compare different sensor materials, including the traditional SnO_2 based sensors [13-15]. A linearized form of this equation has been used here by plotting $\ln S_g$ versus $\ln C_g$.

Table 13.3 summarizes the values of α for $Sm_{0.95}Ce_{0.05}Fe_{1-x}Cr_xO_{3-\delta}$ based sensors at 25°C, 200°C and 300°C. Generally, a sensor is considered of good quality, if it has high values of α, meaning strong concentration dependence. The values of α obtained for these $Sm_{0.95}Ce_{0.05}Fe_{1-x}Cr_xO_{3-\delta}$ based sensors can be compared with those based on tin oxide. The reported values of α for SnO_2 base sensors, for hydrogen detection range between 1/6 and 1/2

[13, 16]. The comparison shows that the sensors under study have reasonably high value α for hydrogen, carbon monoxide and methane.

$$S_g = KC_g^{-\alpha} \tag{13.7}$$

Table 13.3. The values of α for $Sm_{0.95}Ce_{0.05}Fe_{1-x}Cr_xO_{3-\delta}$ (x=0-0.05) based sensors

Temperature(°C)	**Cr Conc. (x)**	α_{H_2}	α_{CO}	α_{CH_4}
25°C	0	--[a]	--[a]	--[a]
	0.01	1.3209	0.8336	0.5343
	0.03	--[a]	--[a]	--[a]
	0.05	--[a]	--[a]	--[a]
200°C	0	1.0997	1.0019	--[a]
	0.01	0.3638	0.654	0.5344
	0.03	1.2371	1.1146	0.5807
	0.05	1.613	0.4582	0.4582
300°C	0	1.759	0.9714	1.1007
	0.01	0.5976	1.3989	0.4805
	0.03	0.6014	0.562	0.3658
	0.05	0.4755	0.3823	0.4655

[a] The conductivity of the sensors under these conditions was below the detection limit, and therefore values of sensitivity were not obtainable.

The response time for these sensors is defined as the time it takes to achieve 95% of the stable response values after injection of the target gas. Similarly, recovery time has been defined as the time required to achieve 105 % of the original conductivity upon removal of the target gas. These values are summarized in Table 13.4. All the tested sensors have shorter recovery times than response times, which suggest that the oxidation process is faster than the reduction process. The comparison of data reveals that response and recovery times decrease as a function of increasing temperature as one would expect for activated processes. The response time increases as a function of Cr concentration up to x=0.03, which can be ascribed to a decrease in grain boundaries due to increased particle sizes, a decrease in the number of active sites due to a decrease in the surface atomic ratio of Sm (high coordination number, more active sites for adsorption) and a decrease in surface adsorbed oxygen (available for interaction of target gas molecules) while from x=0.03 to 0.05 the response time decreases which can be explained in terms of an increase in grain boundaries due to

decrease in particle size and an increase in the number of active sites due to increase in surface atomic ratio.

Table 13.4. Response and recovery times for $Sm_{0.95}Ce_{0.05}Fe_{1-x}Cr_xO_{3-\delta}$ (x=0-0.05) sensors.

T°C	Cr conc. (x)	Response time (minutes)			Recovery time (minutes)		
		1%H_2/air	1%CO/air	1%CH_4/air	1%H_2/air	1%CO/air	1%CH_4/air
25	0	--[a]	--[a]	--[a]	--[a]	--[a]	--[a]
	0.01	26	23	34	22	19	30
	0.03	--[a]	--[a]	--[a]	--[a]	--[a]	--[a]
	0.05	--[a]	--[a]	--[a]	--[a]	--[a]	--[a]
200	0	3	4	--[a]	2	2	--[a]
	0.01	9	8	14	6	7	12
	0.03	12	14	16	9	12	9
	0.05	7	9	12	6	8	11
300	0	2	2	4	1	2	3
	0.01	7	7	9	5	9	8
	0.03	9	11	10	7	8	7
	0.05	6	8	5	5	6	4

[a] The conductivity of the sensors under these conditions was below the detection limit, and therefore values of sensitivity were not obtainable.

13.4. Conclusions

$Sm_{0.95}Ce_{0.05}Fe_{1-x}Cr_xO_{3-\delta}$ (x=0-0.05) are n-type semiconductor sensors. The activation energies toward electrical conductivity for these sensors were found to change as a function of Cr concentration. XPS analysis reveals that the surfaces of the sensors are enriched with Cr due to surface segregation. Furthermore Cr concentration in the lattice greatly affects the amounts of both surface adsorbed oxygen species and lattice oxygen. The change in concentration of different species of Fe as function of Cr concentration suggested a redox reaction upon introduction of Cr into lattice. A linear and reversible response is observed by all Cr doped $Sm_{0.95}Ce_{0.05}FeO_{3-\delta}$ sensors towards H_2, CO and CH_4 at 25°C, 200°C and 300°C. The response time of these sensors was strongly dependent on surface morphology and surface chemical composition. High values of the fitting constant "α ", suggested that these sensors are strongly concentration dependent. Indeed x=0.01 was able to detect H_2, CO and CH_4 at room temperature in the concentration range of 1-5% in air.

13.5. References

[1] H. Aono, E. Traversa, M. Sakamoto, Y. Sadaoka, Sens. Actuators B. 94 (2003) 132-139.

[2] G. Martinelli, M.C. Carotta, M. Ferroni, Y. Sadaoka, E. Traversa, Sens. Actuators B. 55 (1999) 99-110.

[3] M.C. Carotta, G. Martinelli, Y. Sadaoka, P. Nunziante, E. Traversa, Sens. Actuators B. 48 (1998) 270-276.

[4] S.M. Bukhari, J.B. Giorgi, Solid State Ionics. 180 (2009) 198-204.

[5] S.M. Bukhari, J.B. Giorgi, Solid State Ionics. 181 (2010) 392-401.

[6] S.M. Bukhari, J.B. Giorgi, ECS Trans. 28 (2010) 19-29.

[7] N. Fairley, Casa XPS version 2.3.13 Dev73 (2007).

[8] H. Aono, M. Sato, E. Traversa, M. Sakamoto, Y. Sadaoka, J. Am. Ceram. Soc. 84 (2001) 341-347.

[9] W. Cheng, X. Ma, J. Phys.: Conference Series. 152 (2009) 012039.

[10] S.M. Bukhari, J.B. Giorgi, Sens. Actuators B. 155 (2010) 524-537.

[11] S.P. Jiang, L. Liu, K.P. Ong, P. Wu, J. Li, J. Pu, J. Power Sources. 176 (2008) 82-89.

[12] B.G. Yacobi, Semiconductor Materials: An introduction to Basic Principles, SRI International Menlo Park, California, 2002.

[13] J. Watson, K. Ihokura, G.S.V. Coles, Meas. Sci. Technol. 4 (1993) 711-719.

[14] Y.C. Chen, Y.H. Chang, G.J. Chen, Y.L. Chai, D.T. Ray, Sens. Actuators B. 96 (2003) 82-87.

[15] P. Song, H. Qin, L. Zhang, X. Liu, S. Huang, J. Hu, M. Jiang, Physica B. 368 (2005) 204-208.

[16] P.K. Clifford, D.T. Tuma, Sens. Actuators B. 3 (1982) 233-254.

14. Conclusions and Recommendations

14.1. Conclusions

In this research project, we developed new perovskite oxide materials by doing partial substitution of Ce at the A-site in $SmFeO_3$ followed by doping of Co, Ni and Cr at the B-site. The resulting materials were characterized in terms of their crystalline phase, elemental quantification, chemical states of various metals, reduction stability at different temperatures and electrical conductivities under both air and dilute hydrogen (5%v/vH_2/N_2) in the temperature range of 25-1000^{o}C. After complete characterization, these perovskite oxides were tested as solid state gas sensors to detect reducing gases, H_2, CO and CH_4 in air (1-5%v/v) at different temperatures. On the basis of their reduction stability and electrical properties, some materials were selected and their electrochemical performances were evaluated as SOFC anodes under dry methane and dry hydrogen fuels. The main conclusions are as follows.

1. The solubility limit of Ce at the A-site in $SmFeO_3$ is limited to 5%. The Ce doping changed the $SmFeO_3$ from p-type to n-type, increased the electrical conductivity under reducing condition and solved the reduction instability issue. More importantly, these Ce doped materials are coke resistant. For these reasons, Ce doped materials showed very stable performance as SOFC anodes under both dry hydrogen and dry methane fuels. **The best anode material among these Ce doped materials is $Sm_{0.95}Ce_{0.05}FeO_{3-\delta}$.** However, this material did not work well at temperature lower than 550^{o}C under dry methane.
2. Co doping at the B-site of $Sm_{0.95}Ce_{0.05}FeO_{3-\delta}$ improved catalytic properties significantly due to an increase in reducibility. But due to the hole dopant nature of cobalt oxide, the electrical behaviour changed to p-type when the cobalt concentration increased beyond 5% in the series. Sensing experiments revealed that these cobalt doped materials can detect H_2, CO and CH_4 in air at different temperatures including room temperature. **As SOFC anode, the best performance is shown by $Sm_{0.95}Ce_{0.05}Fe_{0.97}Co_{0.03}O_{3-\delta}$ in the series under dry methane at all operational temperatures.** Nevertheless, light coking was observed at 700^{o}C

without significant degradation in performance while at the lower temperature of 500^{o}C there was no sign of coking even after 210h operation.

3. The Ni doped $Sm_{0.95}Ce_{0.05}FeO_{3-\delta}$ materials have the best performance as SOFC anodes under dry methane among all the perovskite oxides examined in this study. The performance trend was non linear as a function of Ni concentration due to a change in electrical behaviour from n-type to p-type. For this reason, **the best performance as anode in this series under dry methane oxidation is shown by $Sm_{0.95}Ce_{0.05}Fe_{0.97}Ni_{0.03}O_{3-\delta}$** despite of the fact that light coking occurred on $Sm_{0.95}Ce_{0.05}Fe_{0.97}Ni_{0.03}O_{3-\delta}$ anode at 600^{o}C as there was no significant degradation in the performance.
4. The sensing tests of Ni doped materials revealed that these are not good candidates as sensors. However, reduction treatment studies showed the formation of metallic nanoparticles on the surface which deeply influence their electrical conductivity as well as sensing ability. Consequently, this modification in surface structure and chemical composition enabled them to sense hydrogen gas at 300^{o}C very effectively. The response of sensors based on these reduced materials was measurable and reversible.
5. The study of Cr doped $Sm_{0.95}Ce_{0.05}FeO_{3-\delta}$ materials also showed some interesting results. Unlike Co and Ni doped materials, they do not show change in electrical behaviour as a function of Cr concentration. Sensors based on Cr doped materials can successfully detect target gases (H_2, CO and CH_4) in air at various temperatures, like cobalt doped materials.

14.1. Recommendations

As it has been demonstrated that Co and Cr doped $Sm_{0.95}Ce_{0.05}FeO_{3-\delta}$ perovskite oxides are capable of sensing target gases like H_2, CO and CH_4, thus, for practical applications, further research on these materials is recommended. Here are some important suggestions from the sensing applications point of view.

I. Effect of sensor thickness on sensor signal must be studied for commercial applications. Optimization of sensor design is required.

II. As the magnitude of response of each perovskite oxide materials towards each target gas is different, chemicals noses can be made and selectivity of each sensor can be studied on exposure to the various mixtures containing gases in different proportions.

III. Long term sensing experiments with repeated cycles must be performed because these can provide valuable information about the sensor life.

IV. Since the presence of water contents in the carrier gas has great impact on the performance of a sensor, it will be essential to do some experiments using humidified carrier gas.

V. In addition to H_2, CO and CH_4 some other target gases can be studied such as ethanol, NO_x, H_2S and O_3 to widen the practical applications of these perovskite oxide materials.

From this study, it is also quite obvious that newly developed $Sm_{0.95}Ce_{0.05}Fe_{1-x}M_xO_{3-\delta}$ perovskite oxides have reasonably high and stable performance as SOFC anodes under dry methane fuel. However, the cell power and cell current values are very low due to the very thick electrolyte used in this study. Therefore, to explore the commercial validity of these perovskite oxides, cells must be fabricated with a thinner electrolyte and their cell powers and cell currents must be measured and compared with the commercially available anode materials.

In regards to coke tolerance ability under dry methane fuel, their versatility and sustainability must be examined under other carbon enriched fuels like ethane, propane, butane and ethanol etc. Furthermore, it will be useful to study their sulphur tolerance by using fuels containing sulphur impurities which will give information about the possibility of using these perovskite oxides as anodes under complex fuel like biodiesels which are enriched with sulphur impurities.

In addition to Co, Ni and Cr, other dopants like Nb, Mn and V can be used to develop new materials and similar studies can be performed to evaluate their effects on enhancement of cell performance, reduction stability, coke and sulphur tolerance.

Appendix

1. Following materials were synthesized. However, their XRD patterns indicated multiple phases in the as-synthesized material. Further testing was not pursued.

- $PdCoO_3$
- $PdFeO_3$
- $CeCoO_3$
- $CeNiO_3$
- $CeFeO_3$
- $Sm_{0.95-x}Sr_xCe_{0.05}FeO_3$

2. $Sm_{0.95-x}Ba_xCe_{0.05}FeO_3$ perovskite oxides were synthesized as a single phase but further testing was not pursued due to their melting points (below 800^oC).